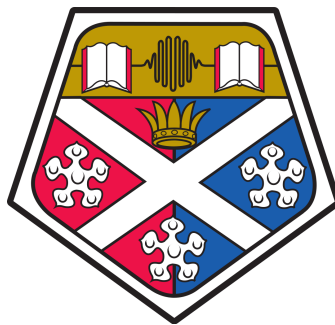


# Mathematical modelling of semiconductor photocatalysis

**Grant MacDonald**

A thesis presented for the degree of  
Doctor of Philosophy



The Department of Mathematics and Statistics

University of Strathclyde

June 2016

## Declaration of Authenticity and Author's Rights

This thesis is the result of the author's original research. It has been composed by the author and has not been previously submitted for examination which has led to the award of a degree.

The copyright of this thesis belongs to the author under the terms of the United Kingdom Copyright Acts as qualified by University of Strathclyde Regulation 3.50. Due acknowledgement must always be made of the use of any material contained in, or derived from, this thesis.

Signed:

Date:

## Acknowledgements

I am grateful to my primary supervisor Dr John Mackenzie for all of the help, support and guidance he has provided me with throughout my time here at Strathclyde. I would also like to take this opportunity to thank my second supervisor Prof. Andrew Mills for his invaluable input.

I also wish to express my gratitude to the Engineering and Physical Sciences Research Council (EPSRC) for making it financially possible for me to complete this thesis.

I would like to thank all the students who I shared an office with during my time as a PhD student. They all contributed to making my time at Strathclyde thoroughly memorable. I would like to thank Katy for keeping me sane during the final stages of the writing up process. You provided much needed respite.

Lastly, but most importantly, I wish to thank my parents. I owe every success I have ever had to the love, support and encouragement they have provided.

# Mathematical modelling of semiconductor photocatalysis

Grant MacDonald

## Abstract

Semiconductor photocatalysis can be extremely effective in the complete mineralisation of hundreds of organic materials and has been utilised in various different commercial systems, for example, self-cleaning glass, purification of water, the purification of air, sterilisation/disinfection and detecting oxygen in food packaging. The aim of this thesis is to further the understanding of semiconductor photocatalysis using mathematical models. One of the main issues considered is the applicability of assuming that reaction intermediates remain in a steady-state throughout the majority of any reactions taking place. We show that this assumption is not always valid.

First, we consider an intelligent ink that is used to test the effectiveness of self-cleaning glass. The system is modelled by a diffusion equation for the transport of dye molecules in the film coupled to an ordinary differential equation describing the photocatalytic reaction taking place at the glass surface. A finite difference method is introduced to solve the equations arising from the model. We are able to show that the proposed model can replicate experimental results well. The model also offers an explanation as to why the initial reaction rate is dependant on film thickness for several different reaction regimes considered.

Second, we consider models motivated by systems where photocatalytic reactions take place throughout the domain as opposed to exclusively at domain boundaries. We present a numerical method to solve such systems, and based on informal experimental results, explain the reasons behind the initial reaction rate

being dependent on the size of the domain.

Third, we consider four previously published models based on the removal of organic pollutants using semiconductor photocatalysis. We introduce more general mathematical models and demonstrate that by doing so there are a wider range of systems that the models can be applied to. One model involves an expanding domain and we present a moving mesh finite difference method that is used to solve such systems.

Fourth, we propose a moving mesh finite element method for coupled bulk-surface problems in two-dimensional time-dependant domains. These problems are motivated by a system where semiconductor photocatalysis is used to destroy organic dirt across a domain which is increasing in size.

Finally, we show how to determine the colour of a substance based on its absorbance spectrum. By comparing predictions made from experimental data to published photographs we are able to demonstrate that we can accurately predict the colour of a substance.

# Contents

<b>1</b>	<b>Introduction</b>	<b>1</b>
1.1	Heterogeneous catalysis . . . . .	1
1.2	Basic principles of semiconductor photochemistry . . . . .	2
1.3	Applications of semiconductor photocatalysts . . . . .	4
1.4	Need for models of semiconductor photocatalysis . . . . .	6
1.5	Modelling the reaction mechanism . . . . .	8
1.5.1	Langmuir-Hinshelwood slow-step model . . . . .	8
1.5.2	Pseudo-steady state assumption . . . . .	10
1.5.3	Evidence supporting a PSSA approach . . . . .	11
1.5.4	Quasi-steady state assumption . . . . .	12
1.5.5	Alternative surface reaction mechanisms . . . . .	13
1.6	Outline of thesis . . . . .	14
<b>2</b>	<b>Testing photocatalytic activity of self-cleaning glass</b>	<b>17</b>
2.1	General mathematical model . . . . .	18
2.1.1	Surface reaction mechanism . . . . .	19
2.1.2	Nondimensionalisation . . . . .	20
2.1.3	Boundary conditions . . . . .	21
2.1.4	Initial conditions . . . . .	22
2.1.5	Quasi-steady state assumption . . . . .	24
2.1.6	Analysis . . . . .	26
2.1.7	Analytical approximations . . . . .	28

2.1.8	Numerical method . . . . .	30
2.1.8.1	Solving the full system . . . . .	31
2.1.8.2	Conservation of reactant molecules for the full system	34
2.1.8.3	Solving the QSSA system . . . . .	37
2.1.8.4	Conservation of reactant molecules for the QSSA system . . . . .	39
2.1.8.5	Accuracy of the numerical scheme used to solve the full system . . . . .	40
2.1.8.6	Accuracy of the numerical scheme used to solve the QSSA system . . . . .	44
2.1.9	Typical concentration profiles . . . . .	48
2.1.9.1	Diffusion-limited regime . . . . .	49
2.1.9.2	Reaction-limited regime . . . . .	53
2.1.9.3	Adsorption-limited regime . . . . .	57
2.1.9.4	Intermediate regime . . . . .	61
2.2	Experimental procedure and results . . . . .	64
2.3	Mathematically modelling resazurin case . . . . .	72
2.3.1	Estimating the initial reaction rate . . . . .	73
2.3.2	Interpreting experimental results . . . . .	73
2.3.3	Numerical simulations . . . . .	75
2.3.4	Experimenting with film thickness . . . . .	84
2.4	Conclusions . . . . .	88
<b>3</b>	<b>Photocatalytic reactions occurring throughout a domain</b>	<b>89</b>
3.1	Simple model for photocatalytic reactions occurring throughout a domain . . . . .	89
3.1.1	Experimental data . . . . .	91
3.2	General model for photocatalytic reactions occurring throughout a domain . . . . .	92

3.2.1	Immobile reactant . . . . .	93
3.2.2	Numerical method - Solving the full system . . . . .	95
3.2.3	Simulations . . . . .	95
3.3	Oxygen diffusion in an indicator/polymer matrix . . . . .	102
3.3.1	A model for reaction-diffusion kinetics in a polymer film . .	103
3.3.2	Nondimensionalisation . . . . .	106
3.3.3	Numerical method . . . . .	108
3.3.3.1	Accuracy of the numerical scheme . . . . .	110
3.3.4	Numerical simulations . . . . .	112
3.3.4.1	Replicating existing results . . . . .	112
3.3.4.2	Further results . . . . .	113
3.3.4.3	Experimenting with film thickness . . . . .	115
3.4	Reactant activated by diffusion of gas . . . . .	122
3.4.1	Initial model . . . . .	122
3.4.2	Boundary and initial conditions . . . . .	125
3.4.3	Nondimensionalisation . . . . .	126
3.4.4	Pre-reaction concentrations . . . . .	127
3.4.5	Quasi-steady state assumption . . . . .	129
3.4.6	Measuring the initial reaction rate . . . . .	129
3.4.7	Numerical method . . . . .	130
3.4.8	Accuracy of numerical scheme . . . . .	136
3.4.9	Typical concentration profiles . . . . .	140
3.4.10	Experimenting with film thickness . . . . .	142
3.5	Conclusions . . . . .	146

**4 A kinetic model for the photocatalysed removal of organic pollutants** **148**

4.1	Introduction . . . . .	148
4.2	Case 1: Non-absorbing film overlayer on a photocatalyst . . . . .	149

4.2.1	Experimental results . . . . .	152
4.3	Proposed model . . . . .	152
4.4	Numerical method . . . . .	157
4.4.1	Solving the full system . . . . .	161
4.4.2	Solving the QSSA system . . . . .	164
4.4.3	Accuracy of the numerical scheme . . . . .	166
4.4.4	General model . . . . .	170
4.5	Case 2: Absorbing film overlayer on a photocatalyst . . . . .	174
4.5.1	Ollis model . . . . .	174
4.5.2	Experimental results . . . . .	175
4.5.3	Generalised model . . . . .	175
4.5.4	Simulations . . . . .	176
4.6	Case 3: Film adjacent to a photocatalyst layer . . . . .	179
4.6.1	Ollis model . . . . .	179
4.6.2	Experimental data . . . . .	182
4.6.3	Generalised model . . . . .	183
4.6.4	Simulations . . . . .	183
4.7	Conclusions . . . . .	186
<b>5</b>	<b>A moving mesh finite element method for surface catalysed reactions in two-dimensional time-dependant domains</b>	<b>190</b>
5.1	Model system equations . . . . .	191
5.1.1	ALE reformulation . . . . .	193
5.1.2	A conservative weak ALE formulation . . . . .	194
5.2	Moving finite element discretisation . . . . .	196
5.2.1	Spatial semi-discretisation . . . . .	196
5.2.2	Temporal integration . . . . .	199
5.2.3	A model bulk-surface problem in a stationary domain . . . . .	200
5.3	Practical evaluation of ALE mapping . . . . .	202

5.3.1	Bulk domain mesh generation . . . . .	203
5.3.2	Boundary mesh generation . . . . .	205
5.4	The complete algorithm . . . . .	205
5.5	Application to Langmuir-Hinshelwood surface reaction mechanism .	206
5.5.1	Stationary domains . . . . .	207
5.5.1.1	Circular domain . . . . .	207
5.5.1.2	Non-circular domain . . . . .	211
5.5.2	Expanding circular domains . . . . .	215
5.5.3	Expanding domain with boundary source of reactant . . . . .	221
5.6	Conclusions . . . . .	224
<b>6</b>	<b>Conclusion</b>	<b>225</b>
6.1	Summary of main contributions . . . . .	225
6.2	Future work . . . . .	227
<b>A</b>	<b>Colour prediction</b>	<b>230</b>
A.1	Calculating CIE tristimulus values . . . . .	230
A.2	Making colour predictions using published data . . . . .	233
A.3	Making colour predictions using experimental data . . . . .	238
A.4	Conclusions and further work . . . . .	240

# Chapter 1

## Introduction

### 1.1 Heterogeneous catalysis

Catalysis is a term which describes the property of substances that facilitate chemical reactions without being consumed during the reaction [17]. Although a broad definition includes materials which limit the rate of a chemical reaction, usually catalysis involves increasing the rate of a reaction. The difference between homogeneous catalysis and heterogeneous catalysis is the phase of the catalyst used in a reaction. Homogeneous catalysts are present in the same phases as the reactant and products taking part in a reaction, whereas, heterogeneous catalysts are present in a different phase to the reactants and products present [17]. Generally, heterogeneous catalysts are solid, while the reactants are gases or liquids. One of the main advantages of using heterogeneous catalysts, as opposed to homogeneous catalysts, is the fact that the catalysts are either automatically removed in the process, or are easily separated from reactants and products using simple methods [29]. Deutschmann *et al.* [19] report that, in 2008, the catalyst global market reached a turnover of 13 billion U.S dollars. This demonstrates the wide use and applicability of catalysts in industry. Hence, gaining a better understanding of heterogeneous catalysts and how they work could be incredibly valuable.

Herrman [30] gives a brief summary of the overall process of heterogeneous

photocatalysis. This involves transport of reactants in the fluid phase to the photocatalyst surface followed by adsorption of at least one of the reactants onto the surface. Once adsorbed, the reactant will be converted into products. These products will then be desorbed from the surface and removed from the interface region. The difference between heterogeneous photocatalysis and traditional heterogeneous catalysis is the mode of activation of the catalyst. In the photocatalysis case photonic activation replaces thermal activation, which occurs in traditional catalysis [30].

## 1.2 Basic principles of semiconductor photochemistry

The energy levels of a semiconductor correspond to a large number of discrete quantum states of electrons. Close to the atomic nucleus, energy levels are filled with electrons and are referred to as the valence band (VB). Higher energy levels of a semiconductor will be mostly empty and are referred to as the conduction band (CB). The difference in energy between these two bands is called the bandgap energy ( $E_{BG}$ ). Figure 1.1 illustrates the basic electron energy features of a semiconducting material [54].

The absorption of a photon of ultra-bandgap light, i.e.  $h\nu \geq E_{BG}$ , will cause an electron to be promoted from the valence band to the conduction band, where  $h$  represents Planck's constant and  $\nu$  represents the frequency of light. Excited electrons leave behind electron holes, i.e. unoccupied states in the valence band. This process is illustrated in the insert diagram of Figure 1.1. Although the holes themselves do not physically move, neighbouring electrons can move and will fill existing holes leaving new holes behind. This gives the impression that the holes are moving and positively charged.

What happens to the electron-hole pair, ( $e^-$ ,  $h^+$ ), will determine the photoac-

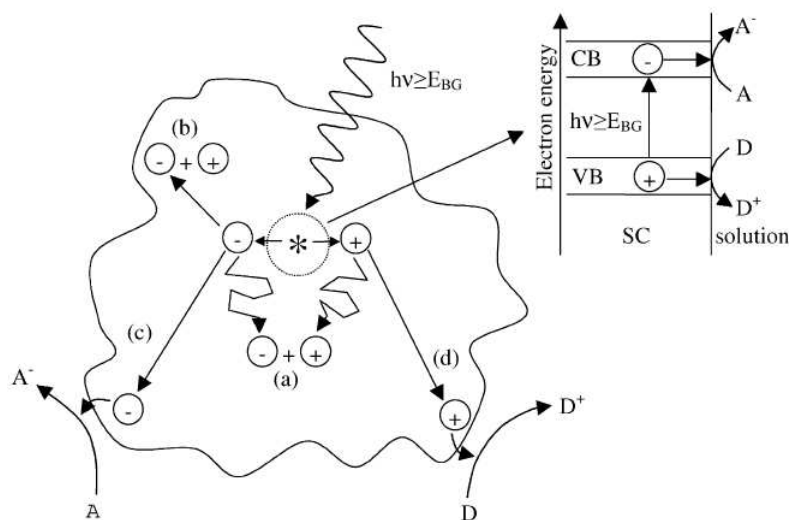
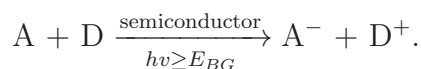


Figure 1.1: Illustration of the major processes that occur on a semiconductor particle upon absorption of a photon of ultra-bandgap light (diagram copied from [54]).

tivity of the semiconductor. If the electron-hole pairs merely recombine, they will generate heat (processes (a) and (b) in Figure 1.1), and the semiconductor will show no photoactivity. On the other hand, if the electron and hole can make their separate ways to the surface of the semiconducting material, it is possible that an interaction with a surface species could occur. For example, if an electron donor, D, is present at the surface, then the photo-generated hole can react with D to generate an oxidised product,  $D^+$  (process (d) in Figure 1.1). Also, if there is an acceptor, A, present at the surface, the electron promoted from the valence band to the conduction band can react with A to produce a reduced product,  $A^-$  (process (c) in Figure 1.1). The overall reaction can be summarised as follows:



Electron-hole recombinations usually dominate the photocatalytic process. In designing efficient photocatalytic systems, one aim is often to improve the reaction efficiency by the introduction of sacrificial electron donors to prevent electron-hole recombinations.

The semiconductor photocatalyst most commonly used is titania,  $\text{TiO}_2$ , as it is chemically and biologically inert, photocatalytically active, easy to produce and use, activated by sunlight and inexpensive. Titania does have one substantial limitation in that it does not absorb visible light; however, it does absorb UV light. For anatase titania  $E_{BG} = 3.2$  eV [53]. Hence, if  $E_{BG} \leq h\nu$ , after converting frequency  $\nu$  into wavelength  $\lambda$ , we must have that  $\lambda < 388$  nm. Since visible light corresponds to a wavelength range of 400 to 700 nm, UV light is required to ensure that  $E_{BG}$  is large enough to allow sufficient electrons to be promoted to the valance band. For both research and commercial applications,  $\text{TiO}_2$  is the preferred semiconducting material to use in the field of semiconductor photochemistry [54].

### 1.3 Applications of semiconductor photocatalysts

One reason for the commercial interest in semiconductor photocatalysis is how effective it can be in the complete mineralisation of hundreds of organic materials. Semiconductor photocatalysis has been used for various different commercial systems. Mills and Lee [54] give examples of numerous companies involved in the development of semiconductor photocatalyst systems which can be used in the purification of water, the purification of air, sterilisation/disinfection and many other commercial applications.

Pilkington Glass are the producers of the world's first self-cleaning glass, Activ<sup>TM</sup>, which is available in numerous countries throughout the world [5]. Several other companies have developed, or are developing, similar products [54], and a considerable amount of research has been performed in this area [11, 27, 70, 72].

Figure 1.2 shows the main steps involved in self-cleaning glass. A thin nano-coating is applied to a piece of glass, as shown in Figure 1.2 (a). The coating consists of a thin film of  $\text{TiO}_2$  and is usually 15-20 nm thick [58]. When UV light reaches the glass, the  $\text{TiO}_2$  is activated. This causes surface reactions to take place which help break down organic dirt on the glass, as shown in Figure 1.2 (b). This

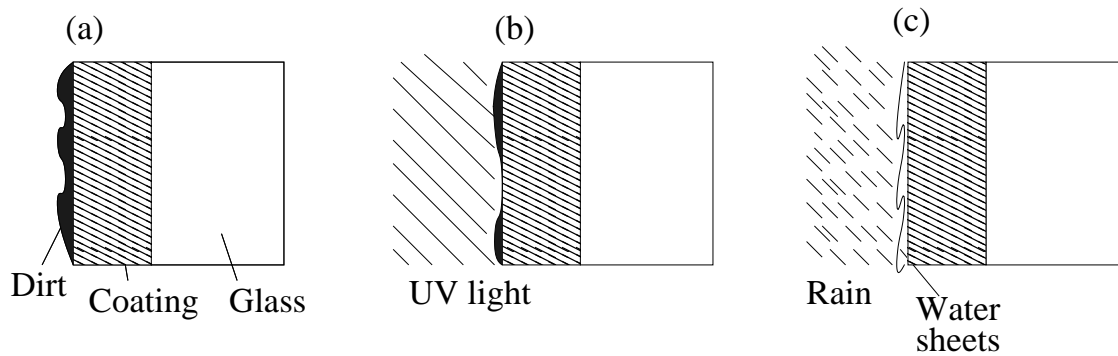


Figure 1.2: Illustration of the processes of self-cleaning glass [5].

effectively loosens any dirt which is on the glass. Rain water is then able to wash away dirt particles on the surface. Due to the hydrophilic nature of the coating, water droplets will spread across the surface forming sheets, as demonstrated in Figure 1.2 (c). This prevents streaks from forming after the water has left the surface [5].

There are many areas where the presence of a particular gas is undesirable and the detection of this gas is important. One example is oxygen in food packaging. By minimising the amount of oxygen in food packaging, the shelf-life of many foods is greatly increased. Therefore, it is useful to know if a particular package of food has been contaminated with an excessive amount of oxygen. Lee *et al.* [40] have devised a semiconductor film which, under UV illumination, will change colour irreversibly under an atmosphere of nitrogen, air and oxygen. Several other groups have considered the use of oxygen indicators in food packaging [38, 48, 51, 89].

Semiconductor photocatalysis technology has been used to create self-cleaning and antibacteric ceramic tiles [28, 43, 85, 86]. One key difference in these products, in comparison to self-cleaning glass, is the lack of UV light available to activate the photocatalyst. One solution to this issue is to create a coating which contains both  $\text{TiO}_2$  and silver (Ag). Several authors have found that Ag-doped titania coatings were significantly more photocatalytically active than titania coatings in the absence of UV light [18, 64, 69]. These kinds of products could be particularly

useful in hospitals and other care facilities.

Catalytic clothing is a recent project which is investigating how clothing coated with semiconductor photocatalysts can be used to help break down air-borne pollutants [6]. Research into how semiconductor photocatalysis can be used in self-cleaning cotton has also been undertaken by several groups [73, 90, 93].

## 1.4 Need for models of semiconductor photocatalysis

Performing physical experiments can prove to be expensive and time consuming. Mathematical models can be used to try and further understand the key limiting steps of the overall reaction mechanism involved in semiconductor photocatalysis. This information can then be used to optimise the systems under consideration. The interaction between the transport of reactant in the bulk region, coupled to the surface bound reactions, create challenges when modelling semiconductor photocatalysis. Furthermore, for some applications of semiconductor photocatalysis, the domain of the chemical system may be time dependent. This presents additional challenges when attempting to model these systems and solve the associated equations.

In this thesis, we will focus on systems where the transport of reactant in the bulk is via diffusion. Coupled with the diffusive transport of reactant, we consider situations where the photocatalysed reactions take place in the bulk or on surfaces. Hence, modelling these systems will result in having reaction-diffusion systems to solve.

Chapwanya *et al.* [14] consider non-standard finite difference methods for solving Michaelis-Menten type reaction-diffusion equations. Hisaka and Sugiyama [31] also consider reaction-diffusion equations with Michaelis-Menten type reaction terms. An explicit finite difference method was presented where the time step

used was automatically adjusted to ensure a sufficiently accurate solution was being calculated. Singh *et al.* [79] consider similar systems to Hisaka and Sugiyama [31] and propose both finite difference and finite element methods.

Several groups have considered the solution of coupled bulk-surface reaction-diffusion equations in two and three dimensions. Madzvamuse *et al.* [45] formulate models for systems of bulk reaction-diffusion equations coupled to surface reaction-diffusion equations via linear Robin-type boundary conditions. The bulk-surface finite element method introduced by Elliot and Ranner [23] is used to numerically solve the coupled system of equations. Rätz and Röger [74] consider a problem where a system of reaction-diffusion equations on a boundary is coupled to a diffusion equation in the bulk via a Robin-type boundary condition. A diffuse-interface method is used to numerically solve the arising equations. A description of this method can be found in [41]. In chapter 2 we will introduce a diffusion equation with non-linear boundary conditions which arises when the quasi-steady state assumption (QSSA) is invoked. Douglas and Dupont [21] consider Galerkin methods for solving these kind of systems.

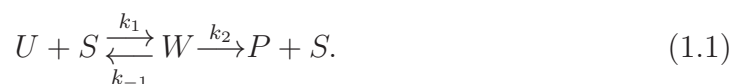
Skakauskas and Katauskis [80, 81, 82] have studied two dimensional mathematical models of the kinetics of unimolecular heterogeneous reactions. Alternating direction implicit finite difference methods were used to solve these systems [76]. Ambrazevicius [9] considers the solvability of the coupled systems of equations considered by Skakauskas and Katauskis. Vijayendran *et al.* [88] consider similar systems to Skakauskas and Katauskis. The systems are explicitly solved by the method of lines, where the time derivatives were integrated using a fifth-order Runge-Kutta-Fehlberg algorithm and spatial derivatives were approximated using second-order finite difference methods.

## 1.5 Modelling the reaction mechanism

In this section we consider reaction mechanisms which arise from semiconductor photocatalysis. Within this section we will ignore limiting effects such as bulk diffusion. However, this limitation is relaxed in the rest of the thesis where diffusion as a bulk transport mechanism will be considered in conjunction with the surface reaction mechanisms discussed in this section.

### 1.5.1 Langmuir-Hinshelwood slow-step model

Ollis [68] gives a comprehensive list of studies which have made use of the Langmuir-Hinshelwood kinetics model within the heterogeneous photochemistry field. The Langmuir-Hinshelwood (LH) rate form has frequently been used to describe liquid-phase kinetics for suspended or immobilized solid photocatalysts. If a reactant  $U$  is being adsorbed onto a surface, it is assumed that it is being adsorbed to a free site  $S$  at a rate  $k_1$  to form the complex  $W$ . After  $W$  is formed, it can be desorbed at a rate  $k_{-1}$  or can form a product,  $P$ , at the reaction rate  $k_2$ . Hence, the overall reaction involves at least three steps:



Let  $u$ ,  $w$  and  $p$  represent the concentrations of  $U$ ,  $W$  and  $P$ , respectively, and let  $s_{tot}$  represent the concentration of the total number of adsorption sites at the photocatalyst surface. Assuming the law of mass action kinetics, we have that

$$\frac{dw(t)}{dt} = k_1 u(t) s_{tot} - (k_1 u(t) + k_{-1} + k_2) w(t).$$

The rate of reaction  $-r$  is given by

$$-r = k_2 w(t).$$

Ollis gives a brief description of the simplest form of the Langmuir-Hinshelwood approach, which is referred to as the slow-step model. The LH rate form involves assuming one relatively rapid reaction achieving adsorption equilibrium, followed by a single, slow surface reaction step which is rate determining [68]. This involves making the assumption that  $w(t)$  remains constant throughout the reaction, i.e.  $\frac{dw}{dt} = 0$ , after an initial rapid reaction, which gives

$$w(t) = \frac{K s_{tot} u}{K u + \frac{k_{-1} + k_2}{k_{-1}}}, \quad (1.2)$$

where  $K = \frac{k_1}{k_{-1}}$ . Note that this assumption is often referred to as the quasi-steady state assumption (QSSA). Additionally, it is assumed that  $k_2$  is small relative to  $k_{-1}$ . This results in the approximation

$$-r = \frac{k_2 K_{a,app} s_{tot} u}{K_{a,app} u + 1}, \quad (1.3)$$

where  $K_{a,app} = K$  in this particular case. From this approximation, if  $K u \gg 1$ , we have that  $-r \approx k_2 s_{tot}$ , i.e. the reaction rate is approximately zeroth-order. Similarly, if  $K u \ll 1$ , we have that  $-r = k_2 K s_{tot} u$ , i.e. the reaction rate is first-order.

In their review of the applications of semiconductor photocatalysis, Hoffmann *et al.* [32] considered nine studies of photocatalytic systems utilising titania for phenol and 4-chlorophenol degradation. For each of the studies, the parameters  $k_2$  and  $K$  were estimated and, by plotting  $\frac{1}{K}$  against  $k_2$ , it was shown that  $k_2$  and  $K$  have positive correlations. The slow-step model does not incorporate this correlation. Also, several studies [25, 47, 92] have found that the rate constants,  $k_2$  and  $K$ , are both light intensity dependent. Again, the slow-step model does not include this dependency. Ollis points out that experimental results have suggested that the dark adsorption equilibrium constant,  $K$  in (1.2), is not equal to the apparent adsorption constant,  $K_{a,app}$  in (1.3). This is at variance with the slow-

step model, as (1.3) follows directly from (1.2).

### 1.5.2 Pseudo-steady state assumption

As an alternative to the slow-step model, Ollis [68] proposes a PSSA (pseudo-steady state approach) model. This involves assuming that pseudo-steady state analysis can be applied to reaction intermediates involved in the photocatalytic reaction process. A significant difference between the PSSA model and the slow-step model is that the PSSA approach does not necessarily assume that  $k_2$  is small relative to  $k_1u$  and  $k_{-1}$ . Additionally, Ollis assumes that the surface reaction rate  $k_2$  is light intensity dependent. As mentioned earlier, when a semiconductor is illuminated with sufficient energetic photons, electron-hole pairs are produced. These pairs migrate to the surface and may react with an absorbed reactant directly or produce active oxygen species. We therefore expect the concentration of active oxygen species to be dependent on photon flow. These hydroxyl radicals will interact with reactants in the system. Hence, we have  $k_2 = k'_2(\text{OH})$ , where  $(\text{OH})$  represents the concentration of surface hydroxyl radicals and  $k'_2$  is a reaction rate constant. The intensity dependence arises because the photon adsorption rate is the ultimate driver for the formation of hydroxyl radicals. In [68] it is assumed that  $k'_2(\text{OH}) = \alpha I^n$ , where  $\alpha$  and  $n$  are constants and  $I$  is the intensity of light illuminating the reactant. There are two circumstances which commonly arise; low intensity where  $k_2$  varies with  $I^{1.0}$ , and high intensity where  $k_2$  varies with  $I^{0.5}$  [68].

By invoking the QSSA, i.e.  $\frac{dw}{dt} = 0$ , the equivalent of (1.2) for the PSSA model is

$$w(t) = \frac{K s_{tot} u}{K u + \frac{k_{-1} + \alpha I^n}{k_2}},$$

which in turn gives

$$-r = \frac{\alpha I^n K_{a,app} u s_{tot}}{K_{a,app} u + 1}, \quad (1.4)$$

where  $K_{a,app} = \frac{k_1}{k_{-1} + \alpha I^n}$ . Note that both  $k_2$  and  $K_{a,app}$  depend on intensity and that  $k_2$  and  $K_{d,app}$  (where  $K_{d,app} = \frac{1}{K_{a,app}}$ ) depend on the intensity raised to the power  $n$ . The slow-step model predicted that the rate equation would only depend on intensity through  $k_2$ .

### 1.5.3 Evidence supporting a PSSA approach

Ollis [68] cites several papers which support the PSSA approach. Emeline *et al.* [25] recently reported on the photocatalyzed oxidation of phenol in water and found that both  $k_2$  and  $K_{d,app}$  varied with  $I^{1.0}$ . Xu and Langford [92] studied the photocatalytic rate of disappearance of a reactant, acetophenone, and found that estimates obtained for  $k_2$  show that it could plausibly fit either a first or half order dependence on intensity. From the data it is possible that  $k_2$  and  $K_{d,app}$  have the same dependency on  $I$  as predicted. Another study was carried out by Martyanov and Savinov [47] who explored oxidation of methyl viologen (MV) in TiO<sub>2</sub> slurries. The curves for MV oxidation rate versus MV concentration fit the LH form and the experimental results are consistent with the hypothesis that  $K_{d,app}$  should vary as intensity to a power (either 0.5 or 1.0 depending on the regime). Mills *et al.* [59] attempted to further validate the steady-state model by reanalysing previous results from a study of the photo-assisted mineralization of 4-chlorophenol (4-CP) by titania films and dispersions as a function of incident light intensity [56]. It was found that the kinetics of 4-CP removal appear to depend on  $I^\beta$  (where  $\beta = 0.6$  or 1 when the TiO<sub>2</sub> is in dispersed or film form). It was shown that the PSSA model is a fairly good fit for the experimental data. The same year, Mills *et al.* [60] made use of the PSSA model proposed by Ollis [68] to explain the kinetics of organic removal by semiconductor photocatalysis in aqueous solution. In this study, Mills *et al.* [60] use the model to explain the kinetics of concomitant reduction by oxygen. The study found that this model provides a simple explanation for the observed kinetics associated with the oxidation of the organic and the reduction of oxygen. Brosilion *et al.* [13] have reported that photocatalytic degradation of metolachlor

in water and butyric acid in air displayed the same intensity dependence predicted by Ollis. This claims to be the first study where this result was observed in gas phase (as opposed to liquid phase).

Ollis [68], as well as several other groups, find several flaws with the widely used slow-step model. The model proposed by Ollis [68] can be used to fit several sets of experimental data fairly well. A fundamental step in the PSSA model proposed by Ollis is assuming that the surface coverage  $\theta$  is constant. This assumption allows Ollis to find an analytical expression for  $\theta$ , and subsequently, an analytical expression for the initial reaction rate. An additional assumption is that the transport of reactant, i.e. diffusion, does not play a role in determining the overall reaction rate.

We will make use of the PSSA model proposed by Ollis to model reactions taking place at the photocatalyst surface. However, we will not make the assumption that the surface coverage  $\theta$  is constant. Additionally, we will consider the transport of reactant throughout the domain via linear diffusion. By adding these two complexities to the model proposed by Ollis, we have a significantly more challenging system to model.

#### 1.5.4 Quasi-steady state assumption

As discussed in the previous section, it is common practice to assume that the concentration of intermediates (in this case  $w(t)$ ) is constant throughout the majority of a reaction. This is commonly known as the quasi-steady state assumption (QSSA).

Any experimental measurements which are explained using the QSSA are performed after an initial, relatively short pre-steady state period before the reactant concentration decays appreciably. After this initial period of time, if the rate of production of products is constant, then the concentration of intermediates must be constant (in our case the intermediate is  $W$ ). Applying the QSSA to our pro-

posed reaction scheme leads to the assumption that

$$\frac{dw(t)}{dt} = 0.$$

This assumption is made in the slow-step model and the PSSA model discussed previously. Considerable research has been done to determine the applicability of the QSSA [36, 77, 78] and in particular a considerable amount of research has been carried out for systems where there is a continuous supply of reactant [12, 26].

### 1.5.5 Alternative surface reaction mechanisms

Ollis [68] briefly explains that other mechanisms are available and specifically references the Eley-Rideal (ER) mechanism considered by Emeline *et al.* [25]. An ER mechanism involves a bimolecular reaction, whereas the model proposed by Ollis [68] involves a unimolecular reaction. However, a Langmuir-Hinshelwood (LH) mechanism can also be used to describe bimolecular reactions, and in fact, traditionally, the term LH mechanism is used to describe the bimolecular case, as opposed to the unimolecular case which we have considered in this introduction [66]. The main difference between a LH mechanism and an ER mechanism is that a LH mechanism involves two adsorbed molecules reacting together, whereas an ER mechanism involves one adsorbed species reacting directly with another reactant which has not been adsorbed [17]. Several groups have used ER mechanisms when modelling semiconductor photocatalysis [13, 24], including an often cited paper by Turchi and Ollis [87].

Monllor-Satoca *et al.* [63] propose a “Direct-Indirect” model. Their model is based on the degree of electronic interaction of the semiconductor surface with dissolved reactant molecules. This approach is fundamentally different to all mechanisms we have considered. One major difference is that Monllor-Satoca *et al.* do not believe that OH radicals, photo generated from OH<sup>-</sup> groups adsorbed on terminal Ti atoms, behave as active species in interfacial oxidational reactions. This

is due to their opinion that adsorbed  $\text{OH}^-$  groups cannot be photo-oxidized with valence band holes.

Throughout this thesis we will assume a reaction mechanism based on the PSSA model. However, when modelling surface reactions (and bulk reactions later in the thesis), we will not necessarily invoke the QSSA. This adds a level of complexity to the model and will allow us to determine whether or not the QSSA is an appropriate assumption to make for any given parameter regime of a particular system. Additionally, we will consider the transport of reactant throughout the domain and couple this with reactions taking place at the boundary (or throughout the domain).

## 1.6 Outline of thesis

We have presented a basic introduction to semiconductor photocatalysis and its applications. We then explored the literature outlining how these kinds of reactions can be modelled. One commonly used modelling technique involves assuming that a steady-state of intermediates exists (QSSA). We will investigate the validity of this assumption throughout this thesis. Finally, we looked at the numerical methods which can be used to solve the mathematical models which we will present in this thesis. We now turn our attention to the work presented in this thesis.

Chapter 2 discusses current and possible future methods of testing the photocatalytic activity of self-cleaning glass. After presenting a general model, we go on to apply this model to a resazurin-based ink. We present a numerical method which allows us to efficiently and accurately solve the model equations, where we have a reactant diffusing throughout a domain and reacting exclusively at the boundary. Note that all numerical methods discussed in this thesis were implemented using Matlab. Additionally, Matlab was used to present all simulation results. We use experimental data to verify the model presented. In particular, we focus on the dependency of the reaction rate on the film thickness, where numerical predictions

agree well with experimental data. An abbreviated explanation of the dependence of the kinetics on the film thickness, based on the numerical experiments in this chapter, appears in [62].

In Chapter 3 we consider several systems where catalysed reactions take place throughout the bulk domain. After considering a couple of previously published models ([46] and [67]), we consider a system where gas diffuses into a domain and reacts with a reactant distributed uniformly throughout the domain. We use a similar numerical technique to that presented in Chapter 2. As in Chapter 2, we use our model to investigate the effect that film thickness has on the reaction rate. For two of the models considered, we are able to explain interesting results which are observed when the film thickness is varied.

Chapter 4 discusses three simplified models presented by Ollis [67] for the photocatalysed removal of carbonaceous and sulfur films on self-cleaning surfaces. We present more general models in each case and demonstrate that we can replicate the results found by Ollis using these more general models. Our proposed models involve solving a diffusion equation over an expanding or contracting domain, where novel numerical techniques are used to solve these models.

In Chapter 5 we consider a two-dimensional version of one of the general models presented in Chapter 4. We present a computational framework for the solution of coupled bulk-surface reaction-diffusion equations in two dimensions based on a conservative finite element Arbitrary Lagrangian-Eulerian (ALE) scheme to approximate the solution of the PDEs. A description of the numerical method and its application to a model bulk-surface problem on a stationary domain appears in the publication [42]. In this publication, the numerical method is utilised by one of the co-authors to model biological cell migration.

In Chapter 6 we consider what future work could be undertaken to further explore the topics considered in this thesis.

Finally, in Appendix A we consider the problem of converting adsorbance spectrum data into a colour. We then apply the technique to experimental data we

considered in Chapter 2. The colours predicted compare well to published photographs of the colours observed during experiments.

## Chapter 2

# Testing photocatalytic activity of self-cleaning glass

It is important to have a quick and easy way to determine whether or not a piece of glass is self-cleaning. This would not only be useful to ensure that the glass is still displaying photocatalytic activity, but is vital to ensure that any glass sold as self-cleaning genuinely is.

Mills and McFarlane [55] describe several methods which are currently used to test the activity of semiconductor photocatalysts. The stearic acid (SA) test works by applying a thin layer of SA to a photocatalytic film and monitoring the disappearance of SA to determine the activity of the film. This method is currently very popular for a number of reasons. Firstly, the SA being applied to films provides a reasonable model for the types of compounds likely to deposit on self-cleaning surfaces. Secondly, SA is stable under UVA illumination when not applied to a photocatalytic surface. This will ensure that any disappearance of SA can be attributed to the photocatalytic activity of the film it is applied to. Thirdly, the kinetics of the disappearance of SA are straightforward and do not depend on the thickness of the photocatalytic film being tested. This removes one factor when interpreting experimental results. Finally, there are numerous different ways to monitor the progress of the reaction, although the most common

method used is infra-red absorbance spectroscopy.

One fundamental problem with the SA test is the difficulty making measurements in the field. Due to the need for trained technicians and expensive equipment, this test is not particularly easy to perform. Additionally, it can take hours for a SA film to completely disappear when applied to self-cleaning glass due to the very thin nature of photocatalytic films used in self-cleaning glass.

Mills *et al.* [57] have devised an ink, containing resazurin (Rz), which when applied to a photocatalytic film (for example self-cleaning glass) changes colour from blue to pink rapidly and irreversibly within minutes. After the ink has changed colour it will be completely bleached, however this bleaching takes place over a larger time scale than the initial colour change. There are several ways of applying the Rz based ink to a surface, for example, the ink could be included in a felt-tip pen [58]. The ability to test the photocatalytic activity of a surface quickly and easily without the need for any expensive equipment or personnel makes this test attractive compared to the SA test and other alternatives [50].

## 2.1 General mathematical model

We consider a general situation where we have a reactant  $U$  which forms a layer over a semiconductor photocatalyst surface. At the surface, if illuminated with sufficient photons of light, the photocatalyst will interact with the reactant causing the concentration to decrease. Figure 2.1 shows the initial setup, where the photocatalyst can be illuminated from the front or back.

We let the reactant layer be of thickness  $L$  and assume that the concentration of reactant  $U$  is given by  $u(x, t)$ , where  $x$  represents position and  $t$  represents time. At  $x = L$  assume that no reactant can pass through the boundary and at  $x = 0$  (i.e. the surface of the photocatalyst) the concentration of reactant depends on the surface reaction kinetics. Within the reactant layer molecules are free to diffuse throughout the domain. We will assume that molecules of  $U$  are transported

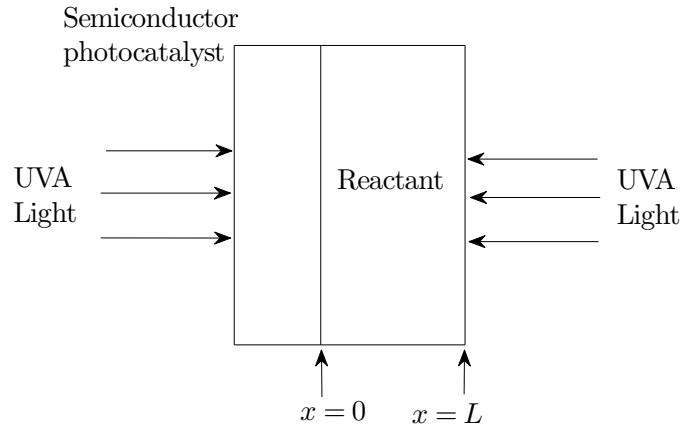


Figure 2.1: Diagram of the initial set-up.

through the reactant layer via the linear diffusion equation

$$\frac{\partial u}{\partial t} = D \frac{\partial^2 u}{\partial x^2}, \quad (2.1)$$

where  $D$  is the diffusion coefficient of the reactant.

### 2.1.1 Surface reaction mechanism

We begin with the same three reaction steps shown in (1.1) of Section 1.5.1. At the surface of the photocatalyst, molecules of  $U$  are adsorbed to unoccupied adsorption sites at a rate  $k_1$  to form the complex  $W$ . Once  $W$  is formed, molecules of  $U$  can be desorbed at a rate  $k_{-1}$  or can go on to form a product  $P$  at the reaction rate  $k_2$ .

Let  $s_{tot}$  represent the concentration of the total number of adsorption sites at the catalyst surface and let  $w(t)$  represent the concentration of bound reactant molecules at a time  $t$ . Hence, assuming the law of mass action kinetics, the following differential equation describes the kinetics of  $u(0, t)$  and  $w(t)$ ;

$$\frac{dw(t)}{dt} = k_1 u(0, t) s_{tot} - (k_1 u(0, t) + k_{-1} + k_2) w(t). \quad (2.2)$$

Similarly, we have

$$\frac{dp(t)}{dt} = k_2 w(t), \quad (2.3)$$

where  $p(t)$  represents the concentration of product being formed at the photocatalyst surface.

Recall, from Section 1.5.2, that Ollis [68] assumes that the surface reaction is dependent on light intensity reaching the surface. Hence, we assume that  $k_2 = k'_2 I^\beta$ , where  $k'_2$  is a reaction rate constant,  $I$  is the intensity of light reaching the surface, and  $\beta$  represents an exponent which is thought to vary between 0 and 1 [50] (or 0 and 0.5 [68]).

If the film is irradiated from behind, we will assume that the intensity of light reaching the photocatalyst surface is constant throughout the reaction. Alternatively, if the photocatalyst is illuminated from the front, the intensity of light reaching the photocatalyst will increase as the concentration of reactant decreases.

This model of the surface reaction mechanism is very similar to the model presented in Section 1.5.2, however there is a substantial difference. In this case we do not assume that the concentration of the intermediate species  $w(t)$  is constant. We will go on to investigate the applicability of this assumption throughout this chapter.

### 2.1.2 Nondimensionalisation

We nondimensionalise (2.1), (2.2) and (2.3) using the following scalings:

$$\hat{t} = \frac{t}{T}, \quad \hat{u} = \frac{u}{u_0}, \quad \hat{x} = \frac{x}{L}, \quad (2.4)$$

where  $u_0$  represents the initial concentration of reactant which we assume is evenly distributed throughout the layer, and we let the characteristic time be  $T = \frac{L^2}{D}$ .

Additionally, we have

$$\hat{k}_1 = k_1 u_0 \frac{L^2}{D}, \quad \hat{k}_{-1} = k_{-1} \frac{L^2}{D}, \quad \hat{k}_2 = k_2 \frac{L^2}{D}, \quad (2.5)$$

$$\hat{w} = \frac{w}{Lu_0}, \quad \hat{s}_{tot} = \frac{s_{tot}}{Lu_0}, \quad \hat{p} = \frac{p}{Lu_0}. \quad (2.6)$$

The nondimensional version of (2.1) therefore takes the form

$$\frac{\partial u}{\partial t} = \frac{\partial^2 u}{\partial x^2}, \quad 0 < x < 1, \quad (2.7)$$

where the hat notation has been dropped for convenience. Similarly we can nondimensionalise (2.2) and (2.3) where, once the hat notation has been dropped, the nondimensional version is identical to the dimensional version. From this point forward, unless stated otherwise, all equations and parameters are nondimensional.

### 2.1.3 Boundary conditions

At  $x = 1$  we have zero flux which simply means that no reactant can pass through the boundary. Hence, by Fick's first law, we have  $\frac{\partial u}{\partial x}(1, t) = 0$ . At  $x = 0$  we assume we have reaction kinetics as described in Section 2.1.1.

Given the global conservation of reactant molecules and a reactant layer of cross sectional area  $dA$  we have

$$\begin{aligned} & \underbrace{dA w(t)}_{\text{Molecules bound to the surface}} + dA \underbrace{\int_0^1 u(x, t) dx}_{\text{Molecules in the bulk}} + \underbrace{dA k_2 \int_0^t w(a) da}_{\text{Molecules transformed into products}} \\ & = dA \underbrace{\int_0^1 u(x, 0) dx}_{\text{Total initial molecules}}. \quad (2.8) \end{aligned}$$

Differentiating (2.8) with respect to  $t$  we find that

$$\frac{dw(t)}{dt} + \int_0^1 \frac{\partial u(x, t)}{\partial t} dx + k_2 w(t) = 0,$$

where we assume that  $w(0) = 0$  (i.e. initially there are no molecules bound to the surface). Making use of (2.7) and the zero flux boundary condition at  $x = 1$  gives an expression for the rate of change of  $u$  at the boundary given by

$$\left. \frac{\partial u}{\partial x} \right|_{x=0} = \frac{dw(t)}{dt} + k_2 w(t). \quad (2.9)$$

Substituting for  $\frac{dw(t)}{dt}$  from (2.2), our boundary condition for  $u$  at  $x = 0$  is given by

$$\left. \frac{\partial u}{\partial x} \right|_{x=0} = k_1 u(0, t) s_{tot} - (k_1 u(0, t) + k_{-1}) w(t). \quad (2.10)$$

#### 2.1.4 Initial conditions

We assume that initially  $u(x, 0) = 1$  and  $w(0) = 0$ , i.e. the instant after the reactant is applied to the photocatalyst all reactant is evenly distributed throughout the domain and there is no reactant bound to the photocatalyst surface. Prior to the system being illuminated by UVA light, molecules are free to diffuse across the domain and free to adsorb onto and desorb from the photocatalyst surface until the system is in equilibrium. Before the system is illuminated we have  $k_2 = 0$ , since  $k_2$  is intensity dependent. If the surface concentrations are in equilibrium, we must have  $\frac{\partial w}{\partial t}(t) = 0$  for all  $t > T_0$ , where  $T_0$  is the time it takes the system to reach equilibrium, and will depend upon the adsorption/desorption rates as well as the rate of diffusion and the thickness of the film. Note that when the system is in equilibrium we have  $\frac{\partial u(x, t)}{\partial x} = \frac{\partial u(x, t)}{\partial t} = 0$ . We define  $u_q$  and  $w_q$  as the equilibrium concentrations of  $u(x, t)$  and  $w(t)$  when  $t > T_0$  and  $k_2 = 0$ . Assuming the system

is in equilibrium, solving (2.2) for  $w_q$  gives

$$w_q = \frac{k_1 u_q s_{tot}}{k_1 u_q + k_{-1}}. \quad (2.11)$$

Assuming a global conservation of reactant, substituting  $k_2 = 0$  into (2.8) and simplifying gives

$$w_q + u_q = 1. \quad (2.12)$$

By substituting  $w_q$  from (2.11) into (2.12) we find that  $u_q$  is a solution of the quadratic equation

$$K u_q^2 + (K s_{tot} + 1 - K) u_q - 1 = 0, \quad (2.13)$$

where  $K = \frac{k_1}{k_{-1}}$ . It can be shown that (2.13) has only one positive solution, namely

$$u_q = \frac{-(K s_{tot} + 1 - K) + \sqrt{(K s_{tot} + 1 - K)^2 + 4K}}{2K}.$$

Substituting  $u_q$  into (2.11) will give  $w_q$ .

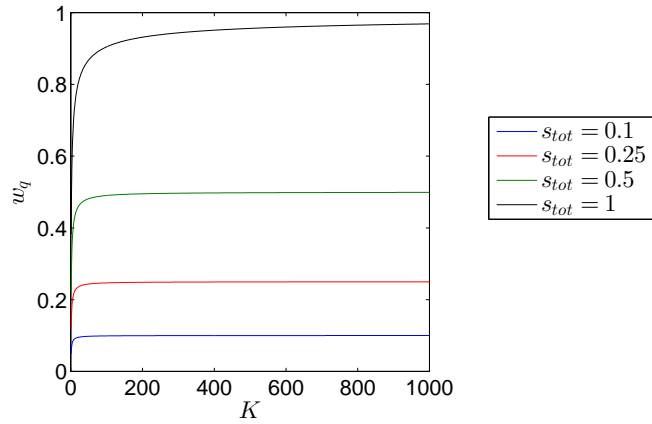


Figure 2.2: Initial equilibrated value of the surface bound reactant  $w_q$  as a function of the association constant  $K$  for several choices of the concentration of adsorption sites  $s_{tot}$ .

Figure 2.2 shows, for four different values of  $s_{tot}$ , how  $w_q$  varies with  $K$ . For all

$s_{tot}$  values considered, as  $K$  is increased,  $w_q$  tends to  $s_{tot}$ . This is hardly surprising, by increasing  $K$  the rate at which molecules can be adsorbed to the surface will be far higher than the rate at which they are desorbed, hence, if  $K$  is large enough, approximately all available sites will be occupied.

From this point forward we will let  $t = 0$  refer to a time when the film is first illuminated and the system is initially in equilibrium. The full system therefore evolves according to the equations

$$\left\{ \begin{array}{l} \frac{\partial u}{\partial t} = \frac{\partial^2 u}{\partial x^2}, \\ \frac{\partial u}{\partial x}(0, t) = k_1 u(0, t) s_{tot} - (k_1 u(0, t) + k_{-1}) w(t), \\ \frac{\partial u}{\partial x}(1, t) = 0, \\ u(x, 0) = u_q, \end{array} \right. \quad \begin{array}{l} 0 < x < 1, \\ \\ \\ 0 \leq x \leq 1, \end{array} \quad (2.14)$$

$$\left\{ \begin{array}{l} \frac{dw}{dt} = k_1 u(0, t) s_{tot} - (k_1 u(0, t) + k_{-1} + k_2) w(t), \\ w(0) = w_q, \end{array} \right. \quad (2.15)$$

$$\left\{ \begin{array}{l} \frac{dp}{dt} = k_2 w(t), \\ p(0) = 0. \end{array} \right. \quad (2.16)$$

### 2.1.5 Quasi-steady state assumption

As discussed in Chapter 1, it is common practice to assume that the concentration of intermediates (in this case  $w(t)$ ) is constant throughout the majority of a reaction. This is commonly known as the quasi-steady state assumption (QSSA).

Any experimental measurements which are explained using the QSSA are per-

formed after an initial, relatively short pre-steady state period before the reactant concentration decays appreciably. After this initial period of time, if the rate of production of products is constant, then the concentration of intermediates must be constant (in our case the intermediate is  $W$ ). Applying the QSSA to our proposed reaction scheme leads to the assumption that

$$\frac{dw(t)}{dt} = 0.$$

Segel and Slemrod [78] use singular perturbation theory to show that the QSSA is valid if  $\epsilon$  is small where

$$\epsilon = \frac{s_{tot}}{K_m + u}, \quad (2.17)$$

$u$  is the concentration of reactant at the surface and  $K_m = \frac{k_{-1}+k_2}{k_1}$ . Segel and Slemrod [78] do not consider transport of reactant in their analysis, hence we will investigate the applicability of (2.17) to the system we are considering.

We will consider two extreme cases. Firstly, if the rate of diffusion is quick enough to ensure that there is a constant supply of reactant at the photocatalyst surface (reaction-limited regime), then we effectively have that there is a continuous supply of reactant ready to react at the surface for the majority of the reaction. Hence, the equivalent to  $u$  in this case will be the total concentration of reactant in the bulk at  $t = 0$ . Due to our choice of nondimensionalisation this total concentration will be  $u_q$ . Hence, for our particular system, assuming we are in a reaction-limited regime, the QSSA is valid if  $\epsilon_Q$  is small where

$$\epsilon_Q = \frac{s_{tot}}{K_m + u_q}. \quad (2.18)$$

On the other hand, if we assume that diffusion is the limiting factor in our system, we will have that the concentration of reactant at  $x = 0$  is very small throughout the reaction (after some initial rapid decrease). This means that the other parameters ( $s_{tot}$ ,  $K_m$  and the initial concentration of reactant) are largely

irrelevant in terms of predicting the validity of the QSSA. We would expect that in a completely diffusion-limited regime, the QSSA is a valid assumption to make. This is because if  $u(0, t)$  remains small throughout the reaction, there will be very little reactant available to bind to the surface, and any bound molecules will react quicker than they can be replaced. This implies that  $w(t)$  would remain close to zero throughout the reaction.

Hence, for a completely reaction-limited regime we can use (2.18) to estimate whether the QSSA holds, and for an entirely diffusion-limited regime we expect the QSSA to hold. In an intermediate regime it is not immediately clear how we can approximate whether the QSSA is a valid assumption to make or not.

Assuming that the QSSA is a valid assumption to make, we can solve (2.2) for the steady-state concentration  $w_Q(t)$ . By substituting  $\frac{dw(t)}{dt} = 0$  and  $w_Q(t)$  into (2.9) we can define a new boundary condition at  $x = 0$ . This allows us to simplify the coupled system of equations (2.14) and (2.15) into the following differential equation

$$\left\{ \begin{array}{l} \frac{\partial u}{\partial t} = \frac{\partial^2 u}{\partial x^2}, \quad 0 < x < 1, \\ \frac{\partial u}{\partial x}(0, t) = \frac{k_1 k_2 u(0, t) s_{tot}}{k_1 u(0, t) + k_{-1} + k_2}, \\ \frac{\partial u}{\partial x}(1, t) = 0, \\ u(x, 0) = u_q, \quad 0 \leq x \leq 1. \end{array} \right. \quad (2.19)$$

Additionally, by replacing  $w(t)$  with  $w_Q(t)$  in (2.16) we have

$$\frac{dp}{dt} = \frac{k_1 k_2 u(0, t) s_{tot}}{k_1 u(0, t) + k_{-1} + k_2}. \quad (2.20)$$

### 2.1.6 Analysis

Adsorbance data can be used to estimate the average concentration of a sample. To investigate the kinetics of the average concentration we integrate both sides of

(2.7) from  $x = 0$  to  $x = 1$  and hence

$$\int_0^1 \frac{\partial u}{\partial t} dx = \left( \frac{\partial u}{\partial x} \Big|_{x=1} - \frac{\partial u}{\partial x} \Big|_{x=0} \right).$$

The average of the concentration of  $U$  over the  $x$  region from 0 to 1 is

$$\bar{u}(t) = \int_0^1 u(x, t) dx.$$

Hence, making use of the boundary condition at  $x = 1$  we find that

$$\frac{d\bar{u}}{dt} = - \frac{\partial u}{\partial x} \Big|_{x=0}, \quad (2.21)$$

which shows how the boundary condition and the overall rate of reaction are related. From (2.10) and (2.21) we have that

$$\frac{d\bar{u}}{dt} = -k_1 u(0, t) s_{tot} + (k_1 u(0, t) + k_{-1}) w(t). \quad (2.22)$$

This expression gives an indication of how the overall concentration of reactant in the bulk decreases with respect to the concentration of reactant at the boundary. It is difficult to immediately draw any conclusions from (2.22) as to how the concentration may decrease due to the presence of  $w(t)$  in this expression. However, assuming we are in a regime where the QSSA is valid, from (2.19) and (2.21), we have

$$\frac{d\bar{u}}{dt} = - \frac{k_1 k_2 u(0, t) s_{tot}}{k_1 u(0, t) + k_{-1} + k_2}. \quad (2.23)$$

This expression can be used to predict how  $\frac{d\bar{u}}{dt}$  behaves for different parameter regimes. For example, if we have a  $k_2$  value which is significantly larger than  $k_1 u(0, t)$  and  $k_{-1}$  we would have

$$\frac{d\bar{u}}{dt} \approx -k_1 u(0, t) s_{tot},$$

which is clearly first-order with respect to concentration. Similarly, if we have an extremely large  $k_1$  value we have that the denominator of (2.23) is dominated by  $k_1 u(0, t)$  (assuming  $u(0, t)$  is not extremely small) and

$$\frac{d\bar{u}}{dt} \approx -k_2 s_{tot},$$

which is clearly zeroth-order. However, as  $u(0, t)$  approaches zero,  $k_{-1}$  and/or  $k_2$  could start to dominate the denominator and we would have

$$\frac{d\bar{u}}{dt} \approx -\frac{k_1 k_2 u(0, t) s_{tot}}{k_{-1} + k_2},$$

which is once again first-order. Hence the kinetics of the overall reaction would initially be zeroth-order before transitioning to first-order towards the end of the reaction.

Note that the right hand side of (2.23) can be re-written as

$$\frac{k_{LH} K_a u(0, t)}{1 + K_a u(0, t)},$$

where  $K_a = \frac{k_1}{k_{-1} + k_2}$  and  $k_{LH} = k_2 s_{tot}$ , which is of the same form as the right hand side of (1.4).

### 2.1.7 Analytical approximations

Analytical solutions of the model equations can be obtained in certain limiting situations. We first consider the situation that we are in a reaction-limited regime. A reaction-limited regime could refer to a situation where the adsorption/desorption rate is very slow, or a regime where the adsorbed species is being converted into product very slowly. Within this regime we can assume that concentration profiles of  $u(x, t)$  are approximately flat, or equivalently,  $\frac{\partial u(x, t)}{\partial x} \approx 0$ . If, in addition, we assume that the QSSA is valid we can solve (2.23) analytically for  $\bar{u}(t)$ , with the initial condition  $\bar{u}(0) = u_g$ . Chapwanya *et al.* [14] illustrate how (2.23) can be

solved. Using the separation of variables method, we find that

$$\bar{u}(t) + K_m \ln(\bar{u}(t)) = u_q + K_m \ln(u_q) - k_2 s_{tot} t. \quad (2.24)$$

Dividing (2.24) by  $K_m$ , taking exponentials of both sides and again dividing by  $K_m$  we have

$$\frac{\bar{u}(t)}{K_m} \exp\left(\frac{\bar{u}(t)}{K_m}\right) = \frac{u_q}{K_m} \exp\left(\frac{u_q}{K_m} - \frac{k_2 s_{tot} t}{K_m}\right). \quad (2.25)$$

We can now solve (2.25) to give

$$\bar{u}(t) = K_m W\left(\frac{u_q}{K_m} \exp\left(\frac{u_q}{K_m} - \frac{k_2 s_{tot} t}{K_m}\right)\right), \quad (2.26)$$

where  $W$  represents the Lambert W function [15]. Hence, when in a reaction-limited regime, assuming the QSSA is valid, we have an analytic approximation to the solution of (2.19).

We will now assume that the overall reaction rate is limited by the transport of reactant to the photocatalyst surface, i.e. diffusion-limited. For systems in this regime, the rate of reaction at the surface is far quicker than the diffusion process. Hence, as soon as molecules reach the photocatalyst surface they will react, leaving behind an empty site. Due to the slow rate of diffusion, these vacant sites will not be immediately filled and will remain almost entirely empty for the duration of the reaction.

If we assume that the surface reaction is quick enough to ensure that  $u(0, t) = 0$ , after some initial short period of time, we can analytically solve an approximation of (2.7) for  $u(x, t)$ . Hence, our fully coupled system of equations (2.14) and (2.15)

can be simplified into the following system

$$\left\{ \begin{array}{l} \frac{\partial u}{\partial t} = \frac{\partial^2 u}{\partial x^2}, \quad 0 < x < 1, \\ u(0, t) = 0, \\ \frac{\partial u}{\partial x}(1, t) = 0, \\ u(x, 0) = u_q, \quad 0 \leq x \leq 1. \end{array} \right. \quad (2.27)$$

Due to the assumption that diffusion is the limiting factor in the overall process (and due to our choice of nondimensionalisation) we have that the approximate solution of (2.27) will be independent of all parameters, other than  $u_q$ . Crank [16] gives the solution of (2.27) as

$$u(x, t) = \frac{4u_q}{\pi} \sum_{n=1}^{\infty} \frac{(-1)^n}{2n+1} \exp\left(- (2n+1)^2 \pi^2 t\right) \cos\left((2n+1)\pi x\right). \quad (2.28)$$

Hence, we have shown that for two extreme parameter regimes we can find an approximation to our solution analytically. This will allow us to compare our numerical results with analytic solutions for both regimes. However, when the parameters are such that we are outside of both extreme regimes, an alternative way of approximating the solution to our system is required.

### 2.1.8 Numerical method

A finite difference method is used to find a numerical solution to the systems of equations introduced in this chapter. We divide the spatial domain  $(0, 1)$  into  $N$  equal intervals, and the temporal domain  $(0, T)$  into  $NT$  equal intervals, with mesh spacings  $\Delta x$  and  $\Delta t$ , respectively. We will find approximations of  $u$  at all grid points, denoted by  $u_j^n = u(j\Delta x, n\Delta t)$ . Additionally, when solving the full system of equations (2.14) and (2.15) we need to approximate  $w$  at each time step,

denoted by  $w^n$ .

To solve the nondimensional system of equations given by (2.14) and (2.15) and the system given by (2.19) a Crank-Nicolson scheme is proposed. A Crank-Nicolson discretisation of both diffusion equations in (2.14) and (2.19) is given by

$$\frac{u_j^{n+1} - u_j^n}{\Delta t} = \frac{1}{2(\Delta x)^2} \left( (u_{j+1}^{n+1} - 2u_j^{n+1} + u_{j-1}^{n+1}) + (u_{j+1}^n - 2u_j^n + u_{j-1}^n) \right),$$

for  $j = 0, 1, 2, \dots, N$  and  $n = 0, 1, 2, \dots, NT - 1$ . If we let  $V = \frac{\Delta t}{2(\Delta x)^2}$  we have

$$-Vu_{j+1}^{n+1} + (1 + 2V)u_j^{n+1} - Vu_{j-1}^{n+1} = Vu_{j+1}^n + (1 - 2V)u_j^n + Vu_{j-1}^n. \quad (2.29)$$

At  $x = 1$ , i.e.  $x = x_N$ , we have a zero flux boundary condition. Using a central difference approximation at  $x = 1$  we discretise in the following way:

$$\frac{u_{N+1}^n - u_{N-1}^n}{2\Delta x} = 0 \quad \forall n, \quad (2.30)$$

where  $u_{N+1}^n$  is a ghost node which will not appear explicitly in the numerical scheme. Hence

$$u_{N+1}^n = u_{N-1}^n \quad \forall n. \quad (2.31)$$

Evaluating (2.29) with  $j = N$ , making use of (2.31) gives

$$(1 + 2V)u_N^{n+1} - 2Vu_{N-1}^{n+1} = (1 - 2V)u_N^n + 2Vu_{N-1}^n. \quad (2.32)$$

How we proceed at this point is dependent on what system of equations we aim to solve.

### 2.1.8.1 Solving the full system

The diffusion equation in (2.14) is discretised by a Crank-Nicolson method for nodes  $j = 0, \dots, N$  with a ghost node approach from Section 2.1.8 being imple-

mented at both boundaries. Additionally, (2.15) is discretised in time by the Crank-Nicolson method. Hence, at each time step we need to solve for  $u$  (at all  $N + 1$  nodes) and  $w$  (at  $x = 0$ ). This gives a system of  $N + 2$  nonlinear algebraic equations to solve at each time step. Note that the system is nonlinear due to a product of  $w(t)$  and  $u(0, t)$  appearing in the boundary condition of (2.14). We refer to this as the full system.

At  $x = 0$  we have the flux boundary condition shown in (2.14) which can be discretised using a central difference approximation to give

$$\frac{u_1^n - u_{-1}^n}{2\Delta x} = k_1 u_0^n s_{tot} - (k_1 u_0^n + k_{-1}) w^n \quad \forall n, \quad (2.33)$$

where  $u_{-1}^n$  is a ghost node which will not be explicitly present in our numerical scheme. Rearranging (2.33) gives

$$u_{-1}^n = u_1^n - 2\Delta x(k_1 u_0^n s_{tot} - (k_1 u_0^n + k_{-1}) w^n). \quad (2.34)$$

Hence, evaluating (2.29) with  $j = 0$ , and making use of (2.34) gives

$$\begin{aligned} & -2V u_1^{n+1} + (1 + 2V + 2V\Delta x k_1 (s_{tot} - w^{n+1})) u_0^{n+1} \\ & = 2V u_1^n + (1 - 2V - 2V\Delta x k_1 (s_{tot} - w^n)) u_0^n + 2V\Delta x k_{-1} (w^n + w^{n+1}). \end{aligned} \quad (2.35)$$

Using (2.29), (2.32) and (2.35) we can solve for  $u^{n+1}$  at all grid points assuming we have an estimate for  $w^{n+1}$ .

Our approach involves finding an estimate of  $w^{n+1}$ , which is then used to find an estimate of  $u^{n+1}$  at all grid points. We will refer to the initial estimate of  $w^{n+1}$  as  $w^{[n+1,1]}$ , which we obtain by discretising (2.15) using a forward Euler method to give

$$\frac{w^{[n+1,1]} - w^n}{\Delta t} = k_1 u_0^n s_{tot} - (k_1 u_0^n + k_{-1} + k_2) w^n,$$

which can be rearranged to give

$$w^{[n+1,1]} = w^n + \Delta t(k_1 u_0^n s_{tot} - (k_1 u_0^n + k_{-1} + k_2)w^n). \quad (2.36)$$

We can now use the approximation  $w^{[n+1,1]}$  to solve (2.29), (2.32) and (2.35) for  $u$  at the following time step, which we will refer to as  $u^{[n+1,1]}$ .

By discretising (2.15) using a Crank-Nicolson method, we can make use of  $u^{[n+1,1]}$  to update our approximation to  $w^{n+1}$ . We will refer to this improved approximation as  $w^{[n+1,2]}$ . Hence, we have

$$\begin{aligned} \frac{w^{[n+1,2]} - w^n}{\Delta t} = \frac{1}{2} \left( \left( k_1 u_0^{[n+1,1]} s_{tot} - (k_1 u_0^{[n+1,1]} + k_{-1} + k_2)w^{[n+1,2]} \right) \right. \\ \left. + \left( k_1 u_0^n s_{tot} - (k_1 u_0^n + k_{-1} + k_2)w^n \right) \right), \end{aligned} \quad (2.37)$$

which can be rearranged to give

$$w^{[n+1,2]} = \frac{w^n + \frac{\Delta t}{2} \left( k_1 u_0^{[n+1,1]} s_{tot} + k_1 u_0^n s_{tot} - (k_1 u_0^n + k_{-1} + k_2)w^n \right)}{1 + \frac{\Delta t}{2} \left( k_1 u_0^{[n+1,1]} + k_{-1} + k_2 \right)}. \quad (2.38)$$

At this stage we have obtained approximations for  $u^{n+1}$  and  $w^{n+1}$ , given by  $u^{[n+1,1]}$  and  $w^{[n+1,2]}$ , by solving one system of  $N + 1$  linear algebraic equations and two scalar linear algebraic equations. We can either: set  $u^{n+1} = u^{[n+1,1]}$  and  $w^{n+1} = w^{[n+1,2]}$  and move onto the next time step, repeat the process a predetermined number of times or, finally, repeat the process as many times as required until

$$\max \left\{ \max (|u^{[n+1,it-1]} - u^{[n+1,it-2]}|), |w^{[n+1,it]} - w^{[n+1,it-1]}| \right\} < tol, \quad (2.39)$$

where  $it$  represents the number of iterations required for the solution of  $u^{n+1}$  and  $w^{n+1}$  to converge within some defined tolerance,  $tol$ . Solving to convergence

involves solving a  $N + 1$  system of linear algebraic equations  $it$  times, and a single linear algebraic equation  $it + 1$  times.

In summary, we can use the following scheme to solve for  $u^{n+1}$  and  $w^{n+1}$  until convergence at each time step; In practice we do not propose solving until conver-

---

**Algorithm 1** Solving the full system until convergence at each time step

---

- 1: Approximate  $w^{[n+1,1]}$  using a forward Euler method as shown in (2.36);
  - 2: Calculate the approximation  $u^{[n+1,1]}$  using a Crank-Nicolson scheme by solving the system of equations given by (2.29), (2.32) and (2.35) using the approximation  $w^{[n+1,1]}$ ;
  - 3: Using the approximation  $u^{[n+1,1]}$  calculate  $w^{[n+1,2]}$  using a Crank-Nicolson scheme as shown in (2.38);
  - 4: For  $m = 2:it$ , repeat steps 2 and 3 using the estimates  $u^{[n+1,m-1]}$  and  $w^{[n+1,m]}$  to find the improved approximations  $u^{[n+1,m]}$  and  $w^{[n+1,m+1]}$  using (2.39) to monitor the difference in each subsequent approximation.
  - 5: Set  $u^{n+1} = u^{[n+1,it]}$  and  $w^{n+1} = w^{[n+1,it+1]}$  and proceed to the following time step.
- 

gence at each time step. We instead propose performing steps 1 to 3 of Algorithm 1 at each time step.

### 2.1.8.2 Conservation of reactant molecules for the full system

Recall that (2.8) gives an expression which equates the total number of reactant molecules within our system to the sum of molecules within the bulk, molecules bound to the surface and molecules which have been converted into product. It is important that any numerical scheme we propose maintains this global conservation of molecules. We will show that the discrete analogue of (2.8) holds. Note that throughout this analysis we assume that the iterative process described in Section 2.1.8.1 is carried out until convergence at each time step.

If we consider the conservation of reactant given by (2.8), cancelling by a factor  $dA$  and letting  $p(t)$  represent the concentration of product formed, we have

$$w(t) + \int_0^1 u(x, t) \, dx + p(t) = \int_0^1 u(x, 0) \, dx, \quad \forall t > 0. \quad (2.40)$$

For  $\Delta t > 0$ , we therefore have

$$w(t + \Delta t) - w(t) + \int_0^1 (u(x, t + \Delta t) - u(x, t)) \, dx + p(t + \Delta t) - p(t) = 0. \quad (2.41)$$

If we can establish a discrete equivalent to (2.41) satisfied by our numerical method, then this will imply that our numerical scheme maintains the continuous result that the total number of molecules in our system remains constant throughout the reaction.

If we define the discrete equivalent of  $\bar{u}(t^n) = \int_0^1 u(x, t^n) \, dx$  as

$$\bar{u}^n \equiv \frac{\Delta x}{2} \sum_{j=0}^{N-1} (u_{j+1}^n + u_j^n),$$

then, the discrete analogue of  $\int_0^1 (u(x, t^n + \Delta t) - u(x, t^n)) \, dx$  is given by

$$\begin{aligned} \bar{u}^{n+1} - \bar{u}^n &= \frac{\Delta x}{2} \sum_{j=0}^{N-1} \left( (u_{j+1}^{n+1} + u_j^{n+1}) - (u_{j+1}^n + u_j^n) \right) \\ &= \frac{\Delta x}{2} \sum_{j=0}^{N-1} \left( (u_{j+1}^{n+1} - u_{j+1}^n) + (u_j^{n+1} - u_j^n) \right). \end{aligned} \quad (2.42)$$

From the Crank-Nicolson discretisation (2.29) we have that

$$u_{j+1}^{n+1} - u_{j+1}^n = V(u_{j+2}^{n+1} - 2u_{j+1}^{n+1} + u_j^{n+1} + u_{j+2}^n - 2u_{j+1}^n + u_j^n), \quad j = -1, \dots, N-1,$$

and similarly

$$u_j^{n+1} - u_j^n = V(u_{j+1}^{n+1} - 2u_j^{n+1} + u_{j-1}^{n+1} + u_{j+1}^n - 2u_j^n + u_{j-1}^n), \quad j = 0, \dots, N.$$

Hence, we have

$$\begin{aligned} & (u_{j+1}^{n+1} - u_{j+1}^n) + (u_j^{n+1} - u_j^n) \\ = & V \left( u_{j+2}^{n+1} - u_{j+1}^{n+1} - u_j^{n+1} + u_{j-1}^{n+1} + u_{j+2}^n - u_{j+1}^n - u_j^n + u_{j-1}^n \right). \end{aligned} \quad (2.43)$$

Substituting (2.43) into (2.42) we find that almost all terms cancel with each other and

$$\begin{aligned} \bar{u}^{n+1} - \bar{u}^n = & \frac{\Delta x}{2} V \left( (u_{-1}^{n+1} - u_1^{n+1}) + (u_{-1}^n - u_1^n) \right. \\ & \left. + (u_{N+1}^{n+1} - u_{N-1}^{n+1}) + (u_{N+1}^n - u_{N-1}^n) \right). \end{aligned} \quad (2.44)$$

From (2.30) we have that  $u_{N+1}^n - u_{N-1}^n = 0 \quad \forall n$ , and from (2.34) we have that

$$u_1^n - u_{-1}^n = 2\Delta x \left( k_1 u_0^n s_{tot} - (k_1 u_0^n + k_{-1}) w^n \right).$$

Hence, substituting into (2.44), we have

$$\begin{aligned} \bar{u}^{n+1} - \bar{u}^n = & -V(\Delta x)^2 \left( k_1 u_0^{n+1} s_{tot} - (k_1 u_0^{n+1} + k_{-1}) w^{n+1} \right. \\ & \left. + k_1 u_0^n s_{tot} - (k_1 u_0^n + k_{-1}) w^n \right). \end{aligned} \quad (2.45)$$

From (2.37) we have that the discrete analogue of  $w(t^n + \Delta t) - w(t^n)$  is given by,

$$\begin{aligned} w^{n+1} - w^n = & \frac{\Delta t}{2} \left( k_1 u_0^{n+1} s_{tot} - (k_1 u_0^{n+1} + k_{-1} + k_2) w^{n+1} \right. \\ & \left. + k_1 u_0^n s_{tot} - (k_1 u_0^n + k_{-1} + k_2) w^n \right). \end{aligned} \quad (2.46)$$

Similarly, if we discretise (2.3) using a Crank-Nicolson method we have that the discrete analogue of  $p(t^n + \Delta t) - p(t^n)$  is given by

$$p^{n+1} - p^n = \frac{\Delta t}{2} k_2 \left( w^{n+1} + w^n \right). \quad (2.47)$$

Using (2.45), (2.46) and (2.47) we therefore have

$$\begin{aligned} & (w^{n+1} - w^n) + (\bar{u}^{n+1} - \bar{u}^n) + (p^{n+1} - p^n) \\ &= \frac{\Delta t}{2} \left( k_1 u_0^{n+1} s_{tot} - (k_1 u_0^{n+1} + k_{-1}) w^{n+1} + k_1 u_0^n s_{tot} - (k_1 u_0^n + k_{-1}) w^n \right) \\ & - V(\Delta x)^2 \left( k_1 u_0^{n+1} s_{tot} - (k_1 u_0^{n+1} + k_{-1}) w^{n+1} + k_1 u_0^n s_{tot} - (k_1 u_0^n + k_{-1}) w^n \right) = 0, \end{aligned}$$

since  $V(\Delta x)^2 = \frac{\Delta t}{2}$ . Hence, we have shown that the discretisation of the full system of equations, (2.14), (2.15) and (2.16), maintains the conservation of molecules as in the continuous case. Note that conservation of molecules will only apply if Algorithm 1 is used to calculate the surface and bulk concentrations, where the solutions converge at each time step.

### 2.1.8.3 Solving the QSSA system

By invoking the QSSA we eliminate the equation for the evolution of the concentration of the complex  $W$  on the boundary. Hence, we have a slightly different system to solve, given by (2.19). We now only have to solve an equation for  $u$  in the bulk with a nonlinear boundary condition. Hence, we have a  $N + 1$  system of nonlinear algebraic equations to solve at each time step. Although in one respect we have simplified our equation system, we have an additional complication due to the existence of a nonlinear boundary condition.

Discretising the left hand boundary condition from (2.19), we have

$$\frac{u_1^n - u_{-1}^n}{2\Delta x} = \frac{k_1 k_2 u_0^n s_{tot}}{k_1 u_0^n + k_{-1} + k_2},$$

which can be rearranged to give

$$u_{-1}^n = u_1^n - 2\Delta x \left( \frac{k_1 k_2 u_0^n s_{tot}}{k_1 u_0^n + k_{-1} + k_2} \right).$$

Substituting into (2.29) with  $j = 0$  we have

$$\begin{aligned} -2Vu_1^{n+1} + (1 + 2V)u_0^{n+1} + 2V\Delta x \left( \frac{k_1 k_2 u_0^{n+1} s_{tot}}{k_1 u_0^{n+1} + k_{-1} + k_2} \right) \\ = 2Vu_1^n + (1 - 2V)u_0^n - 2V\Delta x \left( \frac{k_1 k_2 u_0^n s_{tot}}{k_1 u_0^n + k_{-1} + k_2} \right). \end{aligned} \quad (2.48)$$

As there is only one nonlinear equation in our entire system, we attempt to linearise (2.48) using  $u_0^n$  as an estimate for  $u_0^{n+1}$ . The only term which we approximate using this method is the  $u_0^{n+1}$  term in the denominator of the final term of the left hand side of (2.48). Hence, we have

$$\begin{aligned} -2Vu_1^{n+1} + \left( 1 + 2V + 2V\Delta x \left( \frac{k_1 k_2 s_{tot}}{k_1 u_0^n + k_{-1} + k_2} \right) \right) u_0^{n+1} \\ = 2Vu_1^n + (1 - 2V)u_0^n - 2V\Delta x \left( \frac{k_1 k_2 u_0^n s_{tot}}{k_1 u_0^n + k_{-1} + k_2} \right). \end{aligned} \quad (2.49)$$

We can now solve (2.29), (2.32) and (2.49) for an approximation of  $u^{n+1}$ , which we will refer to as  $u^{[n+1,1]}$ . Using this improved estimate of  $u_0^{n+1}$  we can solve again for an improved approximation of  $u^{n+1}$  at all nodes. Hence, using  $u_0^{[n+1,1]}$  as an estimate for  $u_0^{n+1}$  in (2.48), we have

$$\begin{aligned} -2Vu_1^{n+1} + \left( 1 + 2V + 2V\Delta x \left( \frac{k_1 k_2 s_{tot}}{k_1 u_0^{[n+1,1]} + k_{-1} + k_2} \right) \right) u_0^{n+1} \\ = 2Vu_1^n + (1 - 2V)u_0^n - 2V\Delta x \left( \frac{k_1 k_2 u_0^n s_{tot}}{k_1 u_0^n + k_{-1} + k_2} \right), \end{aligned} \quad (2.50)$$

and we can solve (2.29), (2.32) and (2.50) for an improved approximation of  $u^{n+1}$ , which we will refer to as  $u^{[n+1,2]}$ . Similar to our previous approach, we can either set  $u^{n+1} = u^{[n+1,2]}$  and proceed to the following time step, perform a predetermined number of iterations or, finally, we can repeat this process as many times

as required until

$$\max(|u^{[n+1,it]} - u^{[n+1,it-1]}|) < tol, \quad (2.51)$$

where  $it$  represents the number of iterations required for the solution of  $u^{n+1}$  to converge within a specified tolerance,  $tol$ , at each time step.

In summary, we will use the following scheme to solve for  $u^{n+1}$  until convergence at each time step;

---

**Algorithm 2** Solving the QSSA system until convergence at each time step

---

- 1: Solve (2.29), (2.32) and (2.49) for  $u^{[n+1,1]}$ ;
  - 2: Using  $u_0^{[n+1,1]}$  as an approximation to  $u_0^{n+1}$  solve (2.29), (2.32) and (2.50) for an improved approximation to  $u^{n+1}$  which we will refer to as  $u^{[n+1,2]}$ .
  - 3: For  $m = 3$  :  $it$  repeat Step 2 as many times as necessary using  $u_0^{[n+1,m-1]}$  to find the improved approximation  $u_0^{[n+1,m]}$  using (2.51) to monitor the difference in each subsequent approximation.
  - 4: Set  $u^{n+1} = u^{[n+1,m]}$  and proceed to the next time step.
- 

As in our approach to solving the full system, we will investigate whether it is necessary to solve until convergence at each time step to maintain accuracy in our numerical solutions.

#### 2.1.8.4 Conservation of reactant molecules for the QSSA system

Using a similar technique to that used in Section 2.1.8.2 we can show that conservation of reactant also holds for the QSSA system. When we assume the QSSA, (2.44) remains valid. Hence, with the adapted boundary conditions (2.19), we have that the equivalent to (2.45) when the QSSA is invoked is given by

$$\bar{u}^{n+1} - \bar{u}^n = -V(\Delta x)^2 \left( \frac{k_1 k_2 u_0^{n+1} s_{tot}}{k_1 u_0^{n+1} + k_{-1} + k_2} + \frac{k_1 k_2 u_0^n s_{tot}}{k_1 u_0^n + k_{-1} + k_2} \right).$$

By invoking the QSSA we are assuming that  $w(t)$  remains constant, hence the equivalent to (2.46) will simply be

$$\bar{w}^{n+1} - \bar{w}^n = 0.$$

In terms of the product, if we discretise (2.20) using a Crank-Nicolson method we have that the equivalent of (2.47) is given by

$$\bar{p}^{n+1} - \bar{p}^n = -\frac{\Delta t}{2} \left( \frac{k_1 k_2 u_0^{n+1} s_{tot}}{k_1 u_0^{n+1} + k_{-1} + k_2} + \frac{k_1 k_2 u_0^n s_{tot}}{k_1 u_0^n + k_{-1} + k_2} \right).$$

Hence, it is straightforward to show that

$$(w^{n+1} - w^n) + (\bar{u}^{n+1} - \bar{u}^n) + (p^{n+1} - p^n) = 0,$$

as was the case for the full system.

### 2.1.8.5 Accuracy of the numerical scheme used to solve the full system

We will define the error in the approximation of  $u$  at each time step  $n$  ( $1 \leq n \leq NT$ ) as

$$E_u^n = \max\{|u_j^n - u(x_j, t^n)|, j = 0, 1, \dots, N\}, \quad (2.52)$$

and the error in approximating  $w$  at each time step as

$$E_w^n = |w^n - w(t^n)|. \quad (2.53)$$

For the systems we are solving we do not have an exact solution. To allow us to determine the convergence rates of our proposed numerical methods we will calculate a reference solution using a large number of time steps and as many iterations of the iterative process outlined above as required to ensure that our solutions are converging at each time step. When we are investigating temporal accuracy we will keep the number of spatial grid points constant for all numerical

experiments. Similarly, when we are testing for spatial accuracy we will keep the number of time steps used constant.

To ensure that our proposed method of solving our system is effective across a range of different parameters, we will consider four different regimes. Namely, we will consider a diffusion-limited regime, a surface reaction-limited regime, an adsorption-limited regime and an intermediate regime. In Section 2.1.9 we present several plots for each regime demonstrating how the spatial profiles and average concentrations vary between different regimes.

Ideally, we want to perform as few iterations as possible of our proposed method at each time step. Hence, we will consider two different methods of solving our full system, both of which involve solving one  $(N + 1)$  system of linear equations at each time step.

- Method 1 - Perform steps 1 to 3 of Algorithm 1 at each time step, i.e. predict  $w^{n+1}$ , solve for  $u^{n+1}$  once before correcting the initial approximation to  $w^{n+1}$ .
- Method 2 - Perform steps 1 to 2 of Algorithm 1 at each time step, i.e. predict  $w^{n+1}$  and solve for  $u^{n+1}$ .

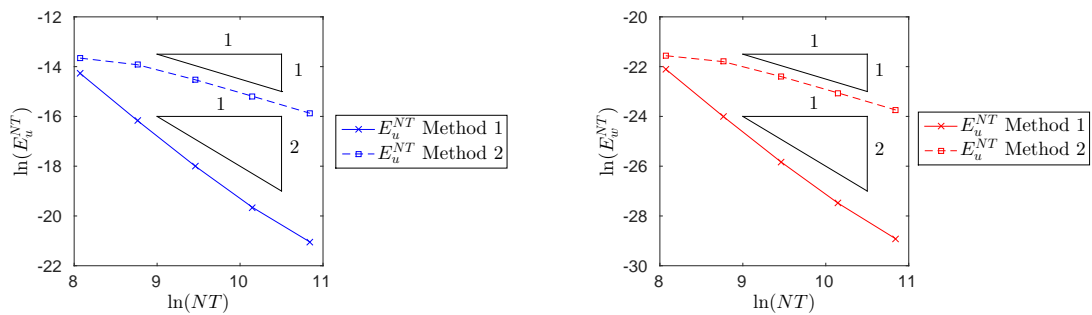


Figure 2.3: Temporal convergence results of  $u$  and  $w$  for a diffusion-limited regime showing that Method 1 is second-order convergent in time.

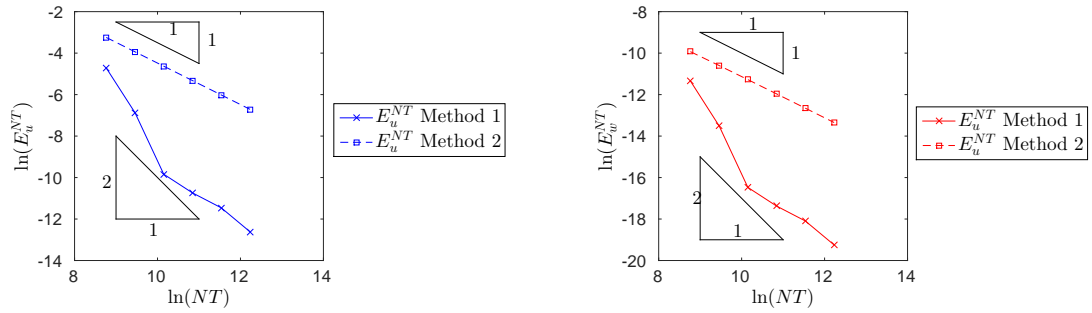


Figure 2.4: Temporal convergence results of  $u$  and  $w$  for a reaction-limited regime showing that Method 1 is second-order convergent in time.

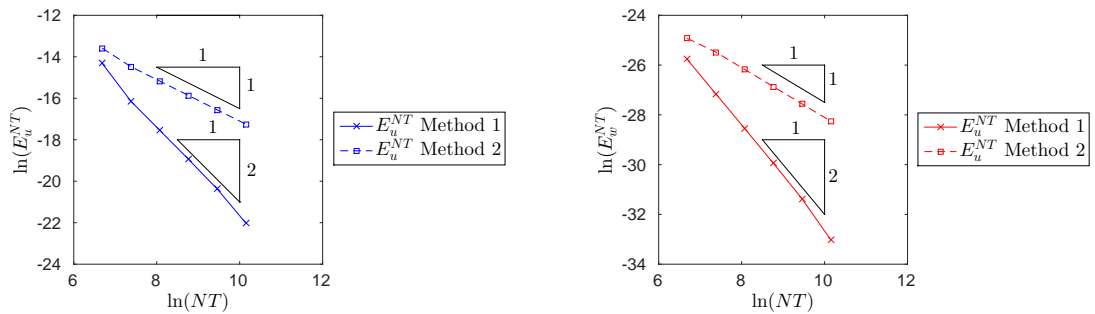


Figure 2.5: Temporal convergence results of  $u$  and  $w$  for an adsorption-limited regime showing that Method 1 is approximately second-order convergent in time.

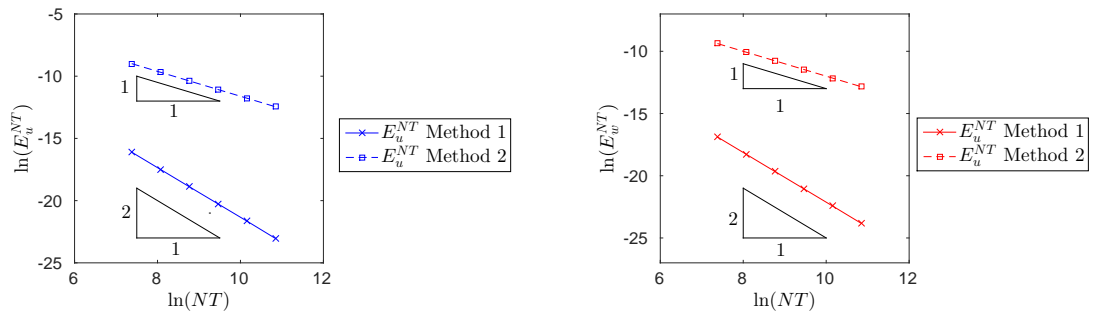


Figure 2.6: Temporal convergence results of  $u$  and  $w$  for an intermediate regime showing that Method 1 is second-order convergent in time.

Figure 2.3 shows temporal convergence results when parameters are chosen such that we are in a diffusion-limited regime. The following parameters were used;  $k_1 = 500, k_{-1} = 0.01, k_2 = 5000, s_{tot} = 0.2, T = 0.2, N = 1600$ . For our most accurate solution  $NT = 1.4 \times 10^6$  with  $tol = 1 \times 10^{-15}$ . To test the accuracy of

our scheme a range of time steps from  $NT = 3.2 \times 10^3$  to  $NT = 5.12 \times 10^4$  were used. From both plots of Figure 2.3 we can see that Method 1 converges far more quickly than Method 2 for  $u$  and  $w$ . Additionally, the error is considerably smaller for all  $NT$  values considered. With Method 1 we have second-order temporal convergence, whereas Method 2 only gives first-order convergence.

Figure 2.4 shows the results when we have chosen parameters such that we are in a reaction-limited regime. The following parameters were used;  $k_1 = 250, k_{-1} = 1, k_2 = 0.01, s_{tot} = 0.1, T = 10, N = 400$ . For our most accurate solution  $NT = 6.4 \times 10^6$  with  $tol = 1 \times 10^{-15}$ . The number of time steps used varied from  $NT = 8 \times 10^2$  to  $NT = 2.56 \times 10^4$ . The results are very similar to the previous case.

Figure 2.5 shows the results when we have chosen parameters such that we are in an adsorption-limited regime;  $k_1 = 5 \times 10^{-3}, k_{-1} = 10, k_2 = 50, s_{tot} = 1, T = 10, N = 400$ . For our most accurate solution  $NT = 5.12 \times 10^6$  with  $tol = 1 \times 10^{-15}$ . To test the accuracy of our scheme the number of time steps used varied from  $NT = 800$  to  $NT = 2.05 \times 10^5$ . The results presented in Figure 2.5 are very similar to the previous two regimes.

Figure 2.6 show the results when we have chosen parameters such that we are not in any of the previous regimes considered and are instead in an intermediate regime. The following parameters were used;  $k_1 = 1, k_{-1} = 1, k_2 = 1, s_{tot} = 1, T = 1, N = 400$ . For our most accurate solution  $NT = 1.2 \times 10^6$  with  $tol = 1 \times 10^{-15}$ . To test the accuracy of our scheme a range of time steps from  $NT = 1.6 \times 10^3$  to  $NT = 5.12 \times 10^4$  were used. Figure 2.6 shows that the results are similar to those presented for the three previous regimes.

By looking at four different parameter regimes we have demonstrated that Method 1 is consistently far more accurate than Method 2 and is second-order convergent in time. In reality we would not suggest using Method 2, as it is only marginally less expensive than Method 1, but gives significantly less accurate results.

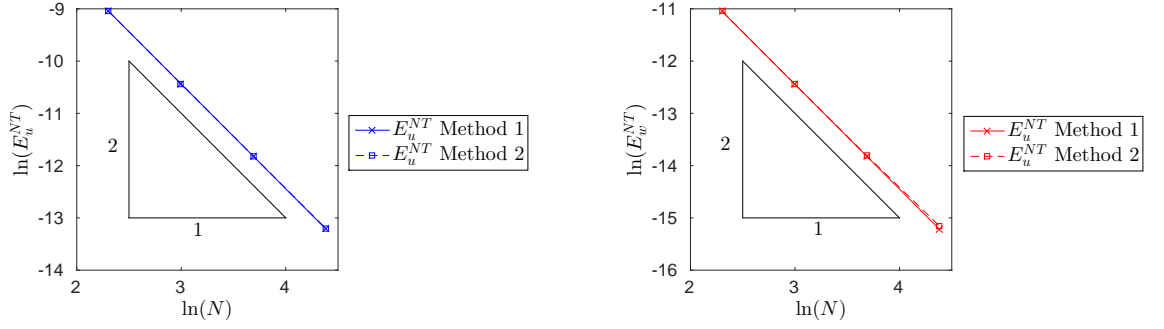


Figure 2.7: Spatial convergence results of  $u$  and  $w$  for an intermediate regime showing that Methods 1 and 2 are second-order convergent in space.

Figure 2.7 shows spatial convergence results when parameters are chosen such that we are in an intermediate regime. For our most accurate solution  $N = 1000$  with  $tol = 1 \times 10^{-15}$ . To test the accuracy of our scheme a range of spatial grid points from  $N = 10$  to  $N = 80$  were used. For all spatial convergence simulations  $NT = 9 \times 10^6$ . The results show that, spatially, both Method 1 and 2 are second-order convergent. The plots show that for this particular set of parameters the errors are almost identical. This is due to the large number of time steps used. This means that the benefit of using Method 1 over Method 2 is negated. These results are consistent across the four different regimes considered above during the temporal convergence tests.

#### 2.1.8.6 Accuracy of the numerical scheme used to solve the QSSA system

We will now perform similar convergence tests for all four parameter regimes when we invoke the QSSA. Our approach of calculating reference solutions and errors is the same as the approach outlined in the previous section. We will consider two different methods of solving the QSSA system based on the algorithm presented earlier.

- Method 1<sub>Q</sub> - Perform steps 1 and 2 of Algorithm 2 once at each time step i.e. solve for  $u^{n+1}$  twice at each time step.

- Method  $2_Q$  - Perform step of Algorithm 2 once at each time step i.e. solve for  $u^{n+1}$  once each time step.

For each number of time steps chosen, and for each method, we compared  $u$  at the final time step with the reference solution at the final time step, and calculated the error using (2.52). Throughout our tests we will use similar parameters to those used when testing our method of solving the full system.

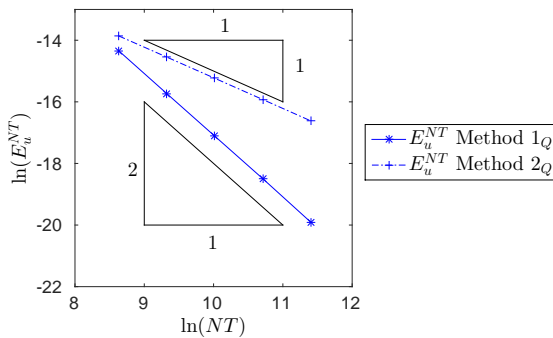


Figure 2.8: Temporal convergence results of  $u$  for a diffusion-limited regime when the QSSA is invoked showing that Method  $1_Q$  is second-order convergent in time.

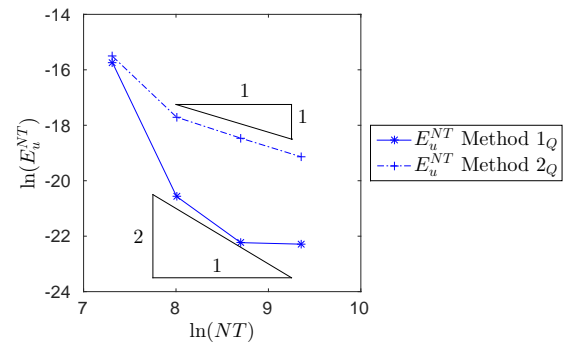


Figure 2.9: Temporal convergence results of  $u$  for a reaction-limited regime when the QSSA is invoked showing the difference in errors obtained when Methods  $1_Q$  and  $2_Q$  are used.

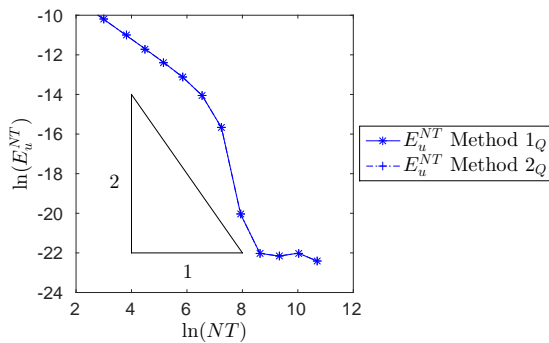


Figure 2.10: Temporal convergence results of  $u$  for an adsorption-limited regime when the QSSA is invoked showing a comparison between the errors obtained when Methods  $1_Q$  and  $2_Q$  are used.

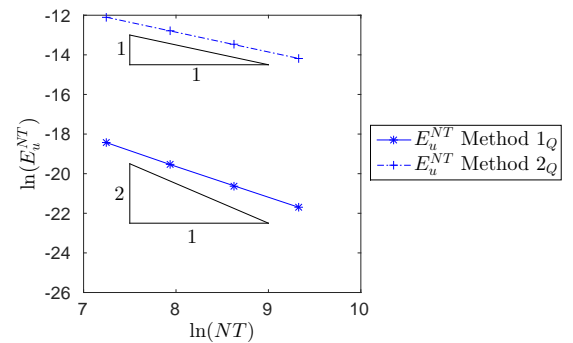


Figure 2.11: Temporal convergence results of  $u$  for an intermediate regime when the QSSA is invoked showing the difference in errors obtained when Methods  $1_Q$  and  $2_Q$  are used.

Figure 2.8 shows the results when we have chosen parameters such that we are in a diffusion-limited regime. The following parameters were used;  $k_1 = 500, k_{-1} = 0.01, k_2 = 5000, s_{tot} = 0.2, T = 0.2, N = 1600$ . For our most accurate solution  $NT = 1.4 \times 10^6$  with  $tol = 1 \times 10^{-15}$ . To test the accuracy of our scheme a range of time steps from  $NT = 5.6 \times 10^3$  to  $NT = 8.96 \times 10^4$  were used. Figure 2.8 shows the temporal convergence results for Methods  $1_Q$  and  $2_Q$ . As was the case when solving the full system, Method  $1_Q$  gives second-order convergence whereas Method  $2_Q$  only gives first-order convergence.

Figure 2.9 shows the results when we have chosen parameters such that we are in a reaction-limited regime. The following parameters were used;  $k_1 = 250, k_{-1} = 1, k_2 = 0.01, s_{tot} = 0.1, T = 10, N = 400$ . For our most accurate solution  $NT = 6.4 \times 10^6$  with  $tol = 1 \times 10^{-15}$ . To test the accuracy of our scheme a range of time steps from  $NT = 6.4 \times 10^3$  to  $NT = 2.05 \times 10^5$  were used.

From Figure 2.9 we can see that, as in the previous case Method  $1_Q$  gives a more accurate result than Method  $2_Q$ . However, in this case the error obtained from Method  $1_Q$  is not reducing at a constant rate. Instead it decreases rapidly before slowing down considerably. This could be due to the relatively simple system we are aiming to solve. Due to the choice of parameters, the spatial profiles of  $u$  are likely to be almost flat and varying very slowly in time. Hence, very few time steps are required to approximate the solution accurately. This may make it difficult to demonstrate second-order convergence for Method  $1_Q$  with this particular set of parameters.

Figure 2.10 shows the results when we have chosen parameters such that we are in an adsorption-limited regime. The following parameters were used;  $k_1 = 5 \times 10^{-3}, k_{-1} = 10, k_2 = 50, s_{tot} = 1, T = 10, N = 400$ . For our most accurate solution  $NT = 1.4 \times 10^6$  with  $tol = 1 \times 10^{-15}$ . To test the accuracy of our scheme a range of time steps from  $NT = 800$  to  $NT = 2.56 \times 10^4$  were used. We can see that both Method  $1_Q$  and Method  $2_Q$  give identical results. Like the previous case, the solution of  $u$  will vary very little in space and time. This may make it

difficult to demonstrate second-order convergence. In this case we see that the error decreases very quickly before tailing off as  $NT$  is increased further. There is no benefit of using Method  $1_Q$  over Method  $2_Q$ . This could be because, even with relatively small  $NT$  values, our scheme is able to approximate the solution fairly accurately.

Figure 2.11 shows the results when we have chosen parameters such that we are in an intermediate regime. For all simulations the following parameters were used;  $k_1 = 1, k_{-1} = 1, k_2 = 1, s_{tot} = 1, T = 1, N = 400$ . For our most accurate solution  $NT = 1.2 \times 10^6$  time steps were used with  $tol = 1 \times 10^{-15}$ . To test the accuracy of our scheme a range of time steps from  $NT = 1.6 \times 10^3$  to  $NT = 5.12 \times 10^4$  were used. We see similar results to those presented in Figure 2.8, however in this instance Method  $1_Q$  is not quite second-order (the gradient of the straight line fitted to the data points is approximately 1.6). However, Method  $1_Q$  does perform considerably better than Method  $2_Q$ .

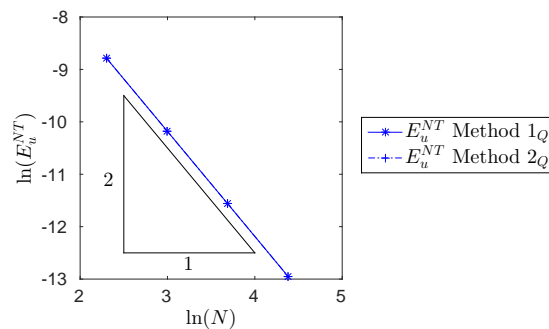


Figure 2.12: Spatial convergence results of  $u$  for an intermediate regime showing that Methods  $1_Q$  and  $2_Q$  are second-order convergent in space.

Figure 2.12 shows spatial convergence results when parameters are chosen such that we are in an intermediate regime. For our most accurate solution  $N = 1000$  with  $tol = 1 \times 10^{-15}$ . To test the accuracy of our scheme a range of spatial grid points ranging from  $N = 10$  to  $N = 80$  were used. For all simulations testing spatial convergence,  $NT = 9 \times 10^6$ . The results presented in Figure 2.12 are the same as those presented when the full system was solved. Spatially both

Method  $1_Q$  and  $2_Q$  are second-order. The plots show that for this particular set of parameters the errors are almost identical. This is due to using such a large number of time steps, which negates the benefit of using Method  $1_Q$  over Method  $2_Q$ . These results are replicated across all four regimes considered.

For the four parameter regimes considered we have shown that for two cases Method  $1_Q$  is significantly more accurate than Method  $2_Q$ . However, for the adsorption-limited and reaction-limited cases our results are slightly less convincing. We found that when we have relatively flat concentration profiles of  $u$ , Method  $1_Q$  is less convincing. However, in seven of the eight cases we considered (when testing the full system and the QSSA system) we found that Method 1 and Method  $1_Q$  give a considerable improvement over using Method 2 and Method  $2_Q$ , however the improvement is far better when the full system is being solved.

### 2.1.9 Typical concentration profiles

In this section we present plots showing concentration profiles, and average concentrations when we choose parameters such that we are in the four regimes considered earlier in the chapter.

For each set of parameters we will solve our full system, (2.14), (2.15) and (2.16), numerically and plot concentration profiles of  $u(x, t)$  against  $x$  at 10 uniform times ranging from  $t = 0$  to  $t = T$  along with plots of  $w(t)$  against  $t$  and  $\bar{u}(t)$  against  $t$ . Additionally, we will present plots for each regime to confirm that our earlier analysis in Section 2.1.8.2 holds, i.e. that we have conservation of reactant. Note that at  $t = 0$  molecules absorbed onto the surface and in the bulk are in a steady-state, as discussed in Section 2.1.4.

With the same sets of parameters, we will solve the QSSA system (2.19) and, if appropriate, we will compare the analytic approximations found earlier with results from the other two systems. We will plot  $\bar{u}(t)$  obtained from both, or all three if applicable, methods used to solve the system. This will allow us to directly compare all three methods and will give an indication of whether or not the QSSA

is valid and whether the assumptions made which allow us to analytically solve our system within certain regimes are valid.

### 2.1.9.1 Diffusion-limited regime

To demonstrate a diffusion-limited regime, the following parameters were used;  $s_{tot} = 0.2$ ,  $k_1 = 500$ ,  $k_{-1} = 0.01$ ,  $k_2 = 5000$  and  $T = 2$ . Due to choosing a very high adsorption to desorption ratio, i.e.  $k_1/k_{-1}$ , any available reactant molecules present at the boundary will quickly bind to the reaction sites. Furthermore, we have chosen a relatively large value of  $k_2$ . As the diffusion coefficient is effectively equal to one due to our nondimensionalisation, we are in a regime where the adsorption and subsequent reaction taking place at the surface happens far more quickly than the diffusion process which transports reactant throughout the domain. Choosing  $s_{tot} = 0.2$  in this instance has little impact on the overall kinetics, as due to  $k_2$  being large, there will not be a large amount of reactant able to bind to the surface at any one time. By performing additional simulations with similar parameters, we were able to confirm that the following results were typical of a diffusion-limited regime. Additionally, by slightly varying a selection of the parameters used, we confirmed that our results were not sensitive to slight changes in the parameter values chosen. To solve the full system, Method 1 was used with  $N = 100$  and  $NT = 1 \times 10^4$ . Similarly, when solving the QSSA system, Method 1<sub>Q</sub> was used with  $N = 100$  and  $NT = 1 \times 10^4$ .

Figure 2.13 shows the results when the full coupled system (2.14) and (2.15) is solved. From the first plot of Figure 2.13 we can see that, close to  $x = 0$ ,  $u(x, t)$  is very small. This is due to the reaction taking place at the surface being far quicker than the rate of diffusion. These types of profiles are typical of a diffusion-limited parameter regime. Additionally, this plot shows that the equilibrated concentration of reactant at  $t = 0$  is significantly smaller than 1. This is due to the high  $k_1$  to  $k_{-1}$  ratio coupled with the relatively large value of  $s_{tot}$  (which equals 0.2). The second plot of Figure 2.13 shows how  $w(t)$  varies with time for this particular set of

parameters. Note that for this plot the  $y$ -axis has been converted to a logarithmic scale. The plot shows that  $w(t)$  decreases rapidly and remains very small for the remainder of the reaction. This is unsurprising, considering that at  $t = 0$  there is a significant amount of reactant already absorbed onto the surface which is ready to react. The very large size of  $k_2$  means that any reactant bound to the surface will react very quickly, leaving vacant sites behind. However, due to the relatively slow nature of the diffusion process, there is little reactant available to bind to the surface, which is required for the reaction to proceed.

The final plot of Figure 2.13 shows how the average concentration  $\bar{u}(t)$  varies with time. It appears that the reduction of  $\bar{u}(t)$  is first-order with respect to time, i.e.  $\frac{d\bar{u}(t)}{dt} = C\bar{u}(t)$ , where  $C$  is some constant. Plotting  $\ln(\bar{u}(t))$  against  $t$  produces a straight line which confirms that this is the case.

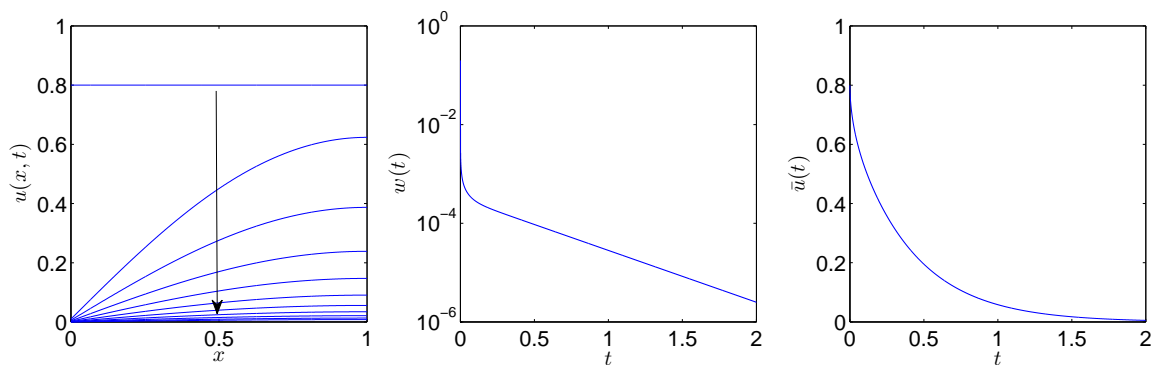


Figure 2.13: Simulation results obtained by solving the full system in a diffusion-limited parameter regime.

Figure 2.14 shows a comparison of the average concentration when all three methods are used to solve our system. The average concentration obtained by invoking the QSSA is very similar to the plot produced when the full system is solved. This suggests that the QSSA is a valid assumption to make in this parameter regime. Note that the  $\epsilon_Q$  value calculated from (2.18) is 0.5553, which is relatively large. Hence, if we were to base our prediction of whether the QSSA was valid or not entirely on  $\epsilon_Q$ , we would assume that the QSSA would not be valid.

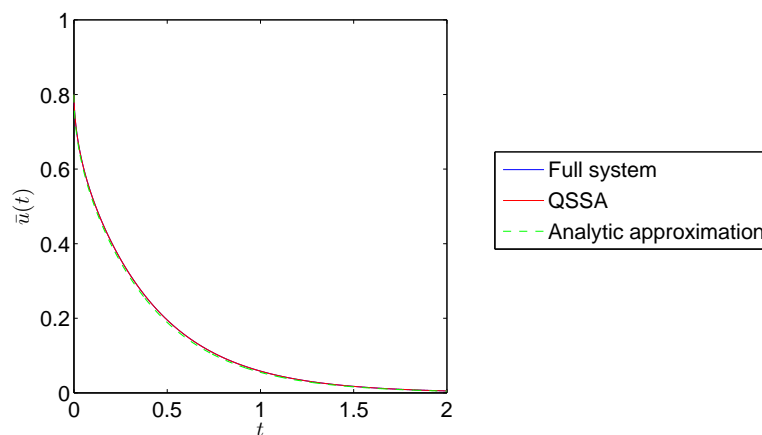


Figure 2.14: A plot showing a comparison between the average concentration predicted from all three methods.

However, as the results in Figures 2.14 demonstrate, with this set of parameters the QSSA is a fair assumption to make. As was discussed earlier in Section 2.1.5, this is due to being in a regime which is diffusion-limited.

The results obtained using the approximate analytic solution (2.28) presented in Figure 2.14 are also very similar to results obtained from the full system. This suggests that the analytic solution is accurate for this particular set of parameters. Note that, although not shown here, the concentration profiles obtained from the QSSA system and the analytic solution are almost identical to those obtained when solving the full system.

Figure 2.15 shows that the conservation of reactant holds when our full system is solved numerically for this particular set of parameters. We can see that there is a substantial amount of product formed for  $t$  close to zero. This corresponds to the substantial concentration of reactant which is initially bound to the photocatalyst surface being converted into product.

To test that conservation of reactant holds for the full system we calculate a discrete equivalent of the left hand side of (2.40) and compare it to a discrete equivalent of the right hand side of (2.40). The error in the total amount of reactant in the system is defined as the difference between these values at each

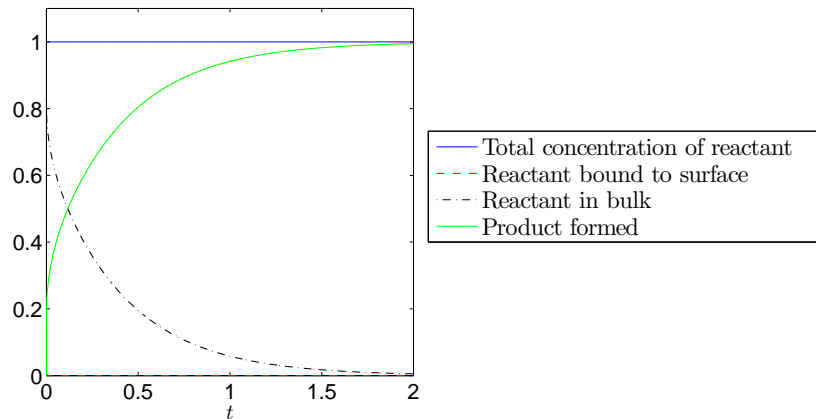


Figure 2.15: A plot showing that the conservation of reactant holds throughout the simulation using the fully coupled system.

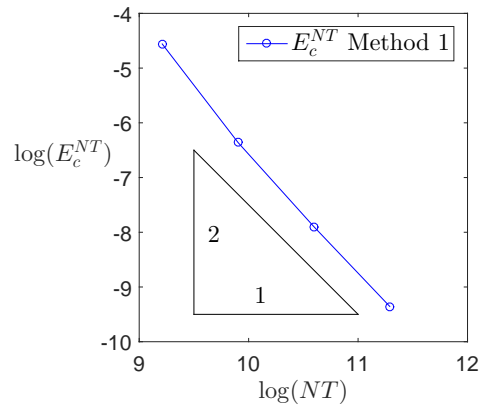


Figure 2.16: Convergence results for the error in the total concentration of reactant  $E_c$  showing that Method 1 is second-order convergent.

time step. We define the error in the total concentration of reactant  $E_c$  as the maximum difference between the total concentration calculated at each time step and the total concentration at  $t = 0$ . We found that if the fully convergent method described in Algorithm 1 is used, conservation holds to machine zero. However, when Method 1 is used, the error in the conservation is of order  $(\Delta t)^2$ . This is shown in Figure 2.16, where a range of time steps from  $NT = 1 \times 10^4$  to  $NT = 8 \times 10^4$  were used. This was also the case for conservation of reactant when the QSSA was invoked. Note that convergence results of this kind will be omitted for the remainder of regimes considered.

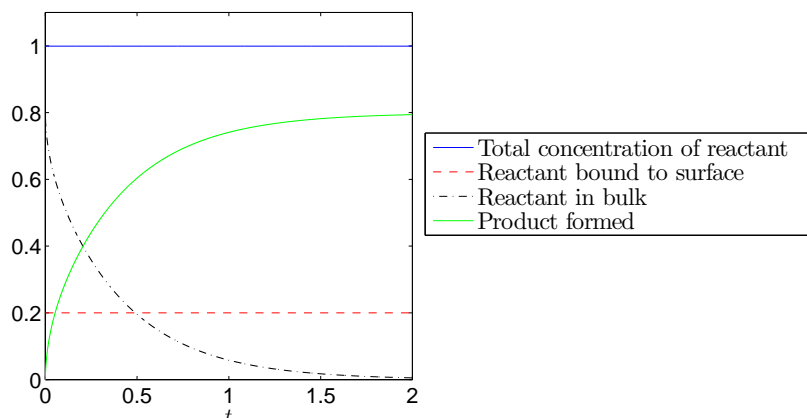


Figure 2.17: A plot showing that the conservation of reactant holds throughout the simulation when the QSSA system is solved.

Figure 2.17 demonstrates that the conservation of reactant holds when the QSSA is invoked for this particular case. The total reactant in the bulk is very similar to the results obtained when solving the full system, however there is a significant difference in both the total concentration formed and the reactant bound to the surface. By invoking the QSSA we are assuming that  $\frac{dw}{dt} = 0$ , hence  $w(t)$  must remain constant throughout. This means that we constantly have some reactant bound to the surface, and hence, the amount of product formed will not tend to one in this case.

### 2.1.9.2 Reaction-limited regime

We next consider a reaction-limited regime where the following parameter values were used;  $s_{tot} = 0.1$ ,  $k_1 = 250$ ,  $k_{-1} = 1$ ,  $k_2 = 0.01$  and  $T = 1500$ . By choosing a very high adsorption to desorption ratio, we ensure that any available molecules of reactant will quickly bind to any free surface reaction sites. Additionally, the small value of  $k_2$ , relative to the diffusion coefficient, ensures we are in a regime where the conversion of bound species to products taking place at the surface is far slower than the transportation of reactant to the surface, and slower than the adsorption process. Hence, there is a constant supply of bound reactant at the

surface until the reactant is exhausted. By setting  $s_{tot} = 0.1$ , we are limiting the maximum amount of bound species on the surface, which will have an impact on the overall kinetics of the system. By performing additional simulations with similar parameters, we were able to confirm that the following results were typical of a surface reaction-limited regime. Additionally, by slightly varying a selection of the parameters used, we confirmed that our results were not sensitive to slight changes in the parameter values. To solve the full system, Method 1 was used with  $N = 100$  and  $NT = 1.5 \times 10^5$ . Similarly, when solving the QSSA system, Method  $1_Q$  was used with the same values of  $N$  and  $NT$ .

Figure 2.18 shows the results when the full coupled system (2.14) and (2.15) is solved. From the first plot we can see that the concentration profiles are approximately flat. This is because diffusion is quick enough to ensure that any reactant which binds to the surface is immediately replaced, and, simultaneously, all remaining reactant in the bulk is evenly distributed throughout the domain. These types of profiles are typical of a reaction-limited parameter regime. Additionally, this plot shows that the equilibrated reactant concentration at  $t = 0$  is approximately 0.9. This is due to the high  $k_1$  to  $k_{-1}$  ratio coupled with the relatively small value of  $s_{tot}$  (which equals 0.1). Due to the size of  $s_{tot}$  the maximum concentration of  $w(t)$  is 0.1.

The second plot of Figure 2.18 shows how  $w(t)$  varies with time. Due to the slow surface reaction coupled with the reactant diffusing relatively quickly,  $w(t)$  initially remains approximately constant. The concentration of bound reactant starts to decrease when there is insufficient reactant left in the bulk to fill vacant surface reaction sites.

The final plot of Figure 2.18 shows how the average concentration  $\bar{u}(t)$  varies with time. It appears that the reduction of  $\bar{u}(t)$  is zeroth-order with respect to time, i.e.  $\frac{d\bar{u}(t)}{dt} = C$ , where  $C$  is some constant. This is evident due to the fact that the plot of  $\bar{u}(t)$  is a straight line for the vast majority of the simulation. Towards the end of the reaction the constant reduction of  $\bar{u}$  quickly tails off.

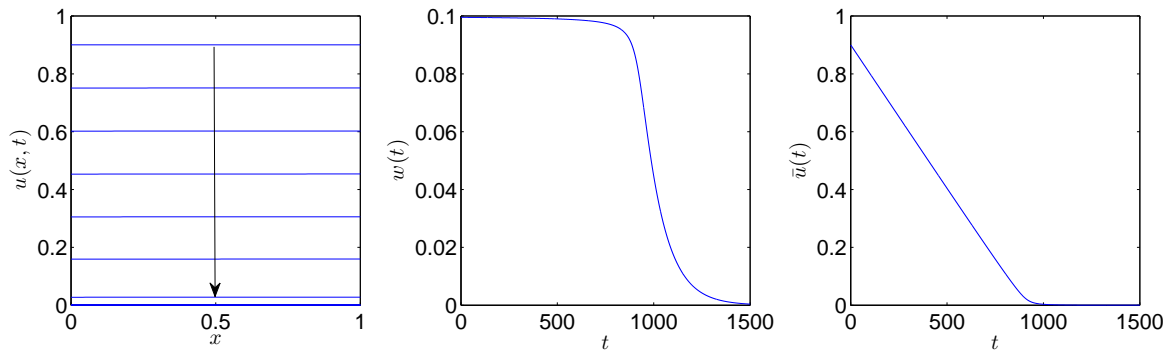


Figure 2.18: Simulation results obtained by solving the full system in a reaction-limited parameter regime.

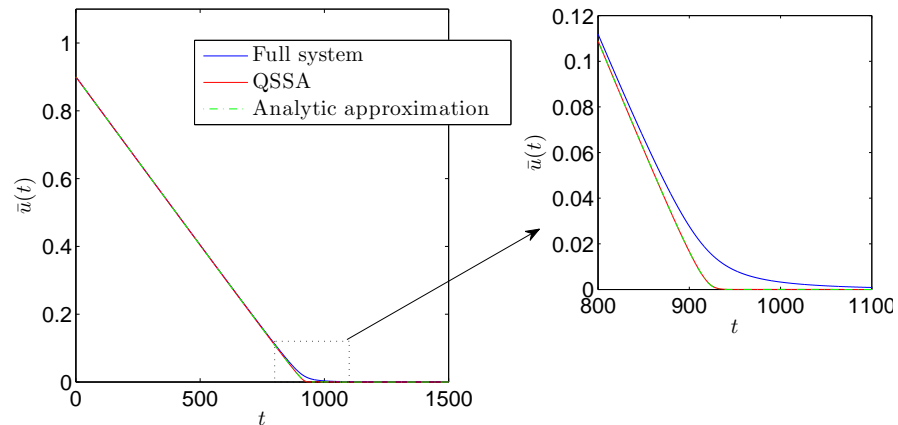


Figure 2.19: A plot showing a comparison between the average concentration predicted from the three methods. The right hand plot shows the same data as the left hand plot on a different axis.

Figure 2.19 shows a comparison of the average concentration when all three methods are used to solve our system. The results show that for the majority of the simulation, both the QSSA method and the analytic approximation (2.26) give a very similar average concentration to that obtained when the full system is solved. The  $\epsilon_Q$  value calculated from (2.18) is 0.0996, which is very small. Hence, if we were to base our prediction of whether the QSSA was valid or not entirely on  $\epsilon_Q$ , we would assume that the QSSA would be valid. In this particular regime, using  $\epsilon_Q$  as an estimate is appropriate as there is a constant supply of reactant at

the surface, until the reactant is exhausted.

Towards the end of reaction there is a slight difference between solving the full system and the other two systems (as demonstrated by the second plot of Figure 2.19). The period of time where there is a difference between the solution obtained from solving the full method and the solution obtained from other methods corresponds to the period of time where  $w(t)$  is no longer approximately constant. Hence, for this particular set of parameters the QSSA and the analytic solution give a fairly good approximation to the solution obtained from the full system for the vast majority of the reaction.

As in the previous case, the concentration profiles obtained from the QSSA system and the analytic approximation are qualitatively very similar to those obtained when solving the full system.

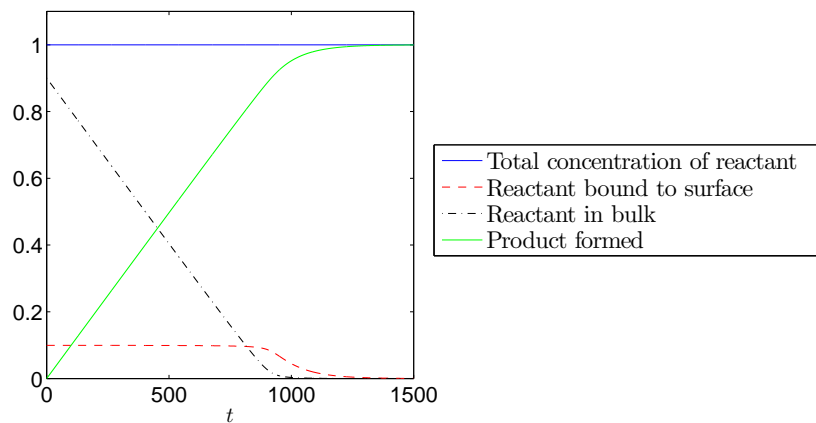


Figure 2.20: A plot showing that the conservation of reactant holds throughout the simulation using the fully coupled system.

Figure 2.20 shows that the conservation of reactant holds numerically for this particular set of parameters and reinforces the fact that  $w(t)$  remains relatively constant throughout the majority of the reaction. This suggests that the QSSA will be a valid approximation to make in this particular regime. The figure also demonstrates that the bulk concentration of reactant decreases at an approximately constant rate while the concentration of product is increasing at an approximately

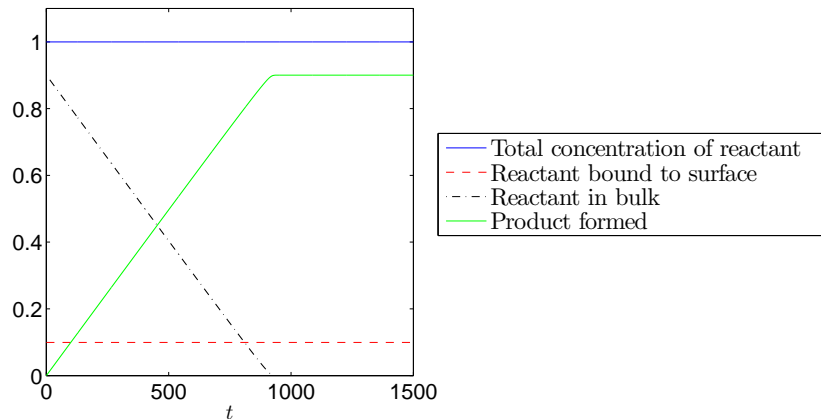


Figure 2.21: A plot showing that the conservation of reactant holds throughout the simulation when the QSSA system is solved.

constant rate.

Figure 2.21 shows that when the QSSA is invoked the conservation of reactant holds. Comparing Figure 2.21 with Figure 2.20 demonstrates well that the QSSA system gives a good approximation to the full system for the majority of the simulation. Towards the end of the reaction, when the full system is solved we find that the total reactant bound to the surface slowly tends to zero. By invoking the QSSA we assume that  $w(t)$  remains constant, hence the QSSA method does not predict this final reduction of  $w(t)$ . Also, because we have that there is still reactant bound to the surface we do not have the total product being formed tending to one, which we would expect.

### 2.1.9.3 Adsorption-limited regime

To demonstrate an adsorption-limited regime the following parameter values are used;  $s_{tot} = 1$ ,  $k_1 = 5 \times 10^{-3}$ ,  $k_{-1} = 10$ ,  $k_2 = 50$  and  $T = 1000$ . In this case, we have selected parameters such that  $k_1$  is much smaller than  $k_{-1}$ . By choosing  $k_2$  to be relatively large, the adsorption of reactant which is the rate-limiting step as opposed to the conversion of bound species into product, which was the rate-limiting step in the previous section. As in the previous case, the rate of diffusion

is far quicker than the reaction taking place at the surface. Due to the very low adsorption to desorption ratio, the choice of  $s_{tot}$  in this case does not play a role in limiting the overall reaction rate, assuming  $s_{tot}$  is not very small. By performing additional simulations with similar parameters, we were able to confirm that the following results were typical of an adsorption-limited regime. Additionally, by slightly varying a selection of the parameters used, we confirmed that our results were not sensitive to slight changes in the parameter values. To solve the full system, Method 1 was used with  $N = 100$  and  $NT = 1 \times 10^5$ . Similarly, when solving the QSSA system, Method 1<sub>Q</sub> was used with  $N = 100$  and  $NT = 1 \times 10^5$ .

Figure 2.22 shows the results when the full coupled system is solved. From the first plot of Figure 2.22 we can again see that the concentration profiles are approximately flat, as in the previous case. Additionally, this plot shows that the equilibrated concentration at  $t = 0$  is approximately 1. This is due to the small  $k_1$  to  $k_{-1}$  ratio. Note that, even though  $s_{tot}$  is fairly large, this fails to play a role due to the fact that reactant is being adsorbed to the surface far more slowly than it is being desorbed or converted into product. The second plot of Figure 2.22 shows how  $w(t)$  varies with time. The plot shows that  $w(t)$  remains very small throughout the simulation. This is due to  $k_1$  being considerably smaller than  $k_{-1}$  and  $k_2$ , which stops a substantial amount of reactant binding to the adsorption sites. The final plot of Figure 2.22 shows how the average concentration  $\bar{u}(t)$  varies with time. It appears that the reduction of  $\bar{u}(t)$  is first-order with respect to time. This can be demonstrated by plotting  $\ln(\bar{u}(t))$  versus  $t$ , which gives an approximately straight line.

Figure 2.23 shows that both the QSSA system and the analytic approximation (2.26) give very similar plots of  $\bar{u}(t)$  against  $t$  to those obtained when the full system is solved. This suggests that both the QSSA and the analytic approximation are valid for this regime. The  $\epsilon_Q$  value calculated from (2.18) is  $8.3326 \times 10^{-5}$ , which is extremely small. Hence, if we were to base our prediction of whether the QSSA was valid or not entirely on  $\epsilon_Q$ , we would assume that the QSSA would be valid. In this

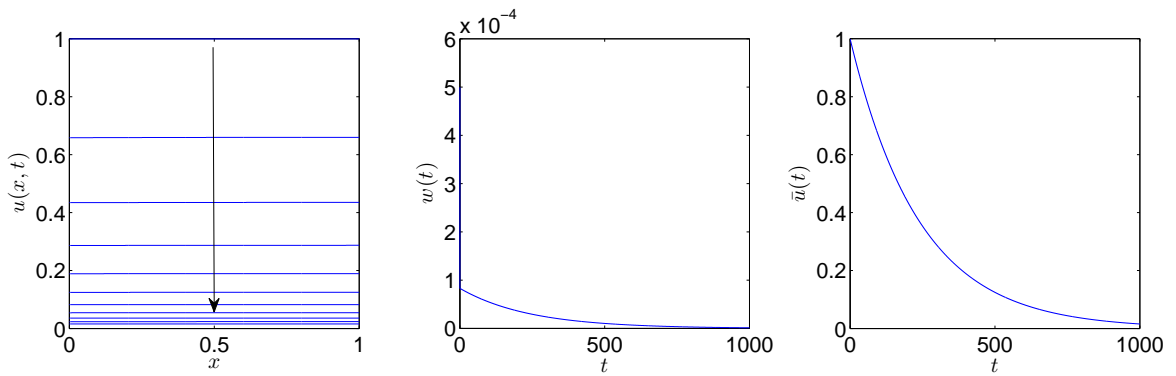


Figure 2.22: Simulation results obtained by solving the full system in an adsorption-limited parameter regime.

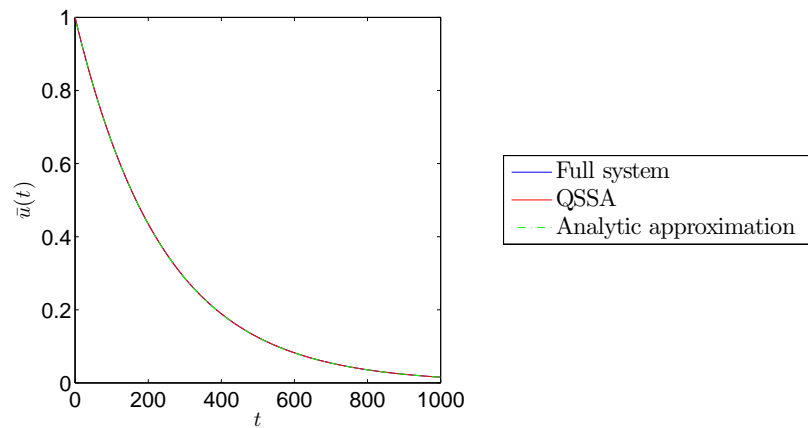


Figure 2.23: A plot showing a comparison between the average concentration predicted from the three methods in an adsorption-limited regime.

particular regime, using  $\epsilon_Q$  as an estimate is appropriate as  $w(t) \approx 0$  throughout the entire reaction.

Once again, the concentration profiles of  $\bar{u}$  obtained by solving the QSSA and using the analytic approximation are very similar, qualitatively and quantitatively, to those obtained by solving the full system.

Figure 2.24 shows that the conservation of reactant holds when our full system is solved numerically. Unsurprisingly, the plot also shows that the rate that product is being produced is very similar to the rate at which reactant in the bulk is

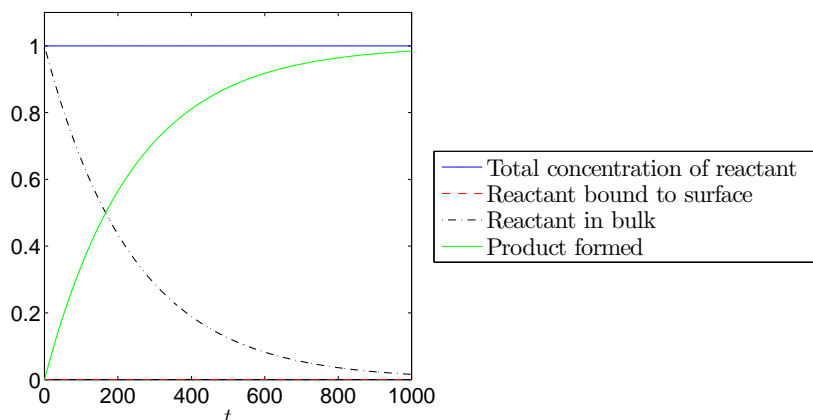


Figure 2.24: A plot showing that the conservation of reactant holds throughout the simulation using the fully coupled system.

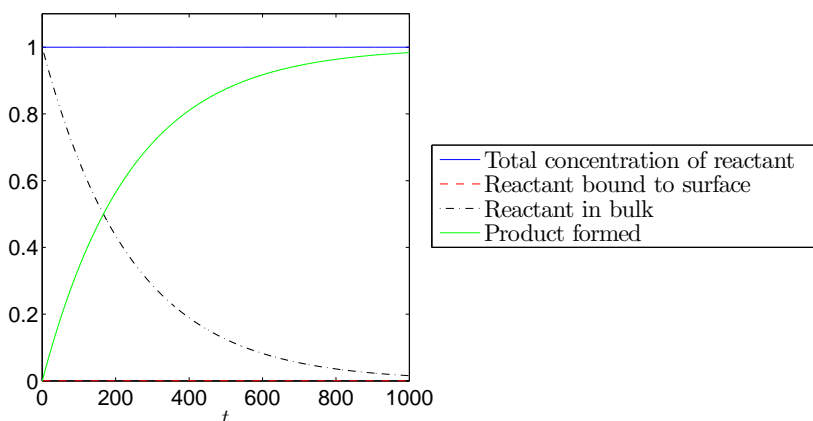


Figure 2.25: A plot showing that the conservation of reactant holds throughout the simulation when the QSSA system is solved.

decreasing. This is due to being in a regime where very little reactant is bound to the surface throughout the reaction. From this plot it is also clear that the concentration of reactant bound to the surface remains very small throughout the entire reaction.

Figure 2.25 shows that the conservation of reactant holds when our QSSA system is solved numerically. Additionally, by comparing Figure 2.25 with Figure 2.24 we see that the total concentrations of reactant in the bulk, reactant bound to the surface and product formed are very similar for both systems throughout

the simulation.

#### 2.1.9.4 Intermediate regime

With the following parameter values;  $s_{tot} = 1, k_1 = 1, k_{-1} = 1, k_2 = 1$  and  $T = 15$ , we would expect that no one process will entirely limit the overall reaction rate. By performing additional simulations with similar parameters, we were able to confirm that the following results were typical of an intermediate regime. Additionally, by slightly varying a selection of the parameters used, we confirmed that our results were not sensitive to slight changes in the parameter values. To solve the full system, Method 1 was used with  $N = 100$  and  $NT = 1 \times 10^4$ . Similarly, when solving the QSSA system, Method  $1_Q$  was used with  $N = 100$  and  $NT = 1 \times 10^4$ .

Figure 2.26 shows the results when the full coupled system is solved. From the first plot of Figure 2.26 we can see that the profiles have a slight gradient, which indicates that diffusion could be playing a role in the overall reaction rate. Additionally, the equilibrated concentration at  $t = 0$  is approximately 0.6. This is due to the ratio of  $k_1$  to  $k_{-1}$  equaling one and the fact that  $s_{tot} = 1$ , allowing a substantial amount of reactant to bind to the surface. The second plot of Figure 2.18 shows that  $w(t)$  varies considerably throughout the reaction. Without any further considerations this would suggest that the QSSA will not be valid in this parameter regime. The final plot of Figure 2.18 shows that the reduction of  $\bar{u}(t)$  is first-order with respect to time. As in previous cases this can be demonstrated by plotting  $\ln(\bar{u}(t))$  versus  $t$ , which gives a straight line.

Figure 2.27 shows the results obtained by solving the QSSA system are noticeably different to the results obtained from the full system. The  $\epsilon_Q$  value calculated from (2.18) is 0.3333, which is not particularly small. Hence, we would assume that the QSSA is invalid. Note we have not included an analytical solution in this comparison due to being in a region where neither analytic approximation is valid.

By looking at concentration profiles of  $u$ , we found that both methods give qualitatively similar results, however quantitatively they are quite different. This

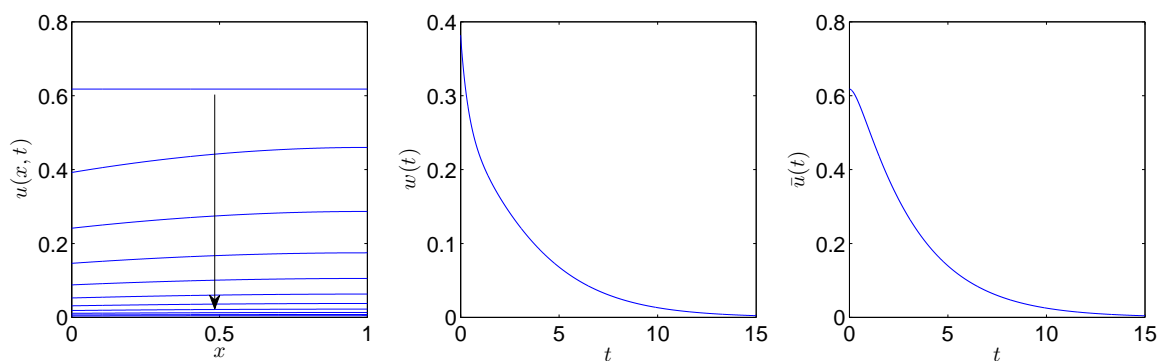


Figure 2.26: Simulation results obtained by solving the full system in an intermediate parameter regime.

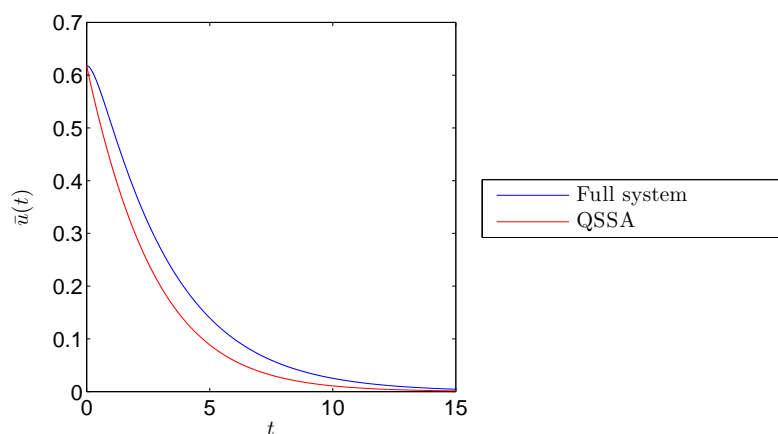


Figure 2.27: A plot showing a comparison between the average concentration predicted from the full system and the QSSA system for an intermediate regime.

suggests that, for this particular set of parameters, the QSSA is not valid.

Figures 2.28 and 2.29 show that the conservation of reactant holds when both our full system and our QSSA system are solved numerically. However, by comparing both plots we can see that there is a significant difference in the total concentration of reactant in the bulk, reactant bound to the surface and total amount of product formed.

By showing different sets of results for various parameter regimes we have shown two extreme parameter regimes where our analytic approximations are very close

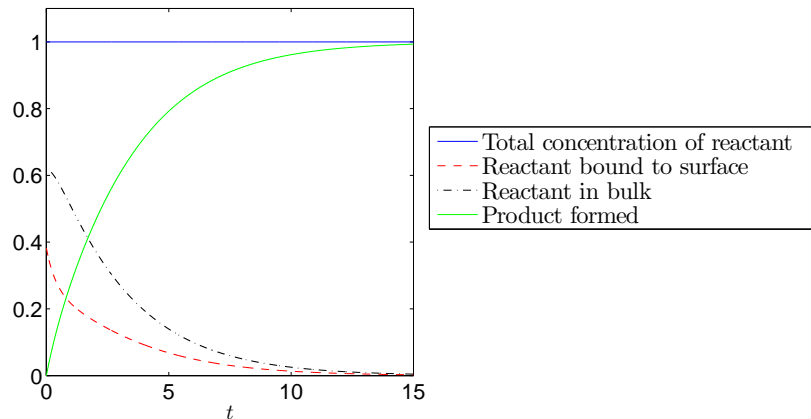


Figure 2.28: A plot showing that the conservation of reactant holds throughout the simulation using the fully coupled system.

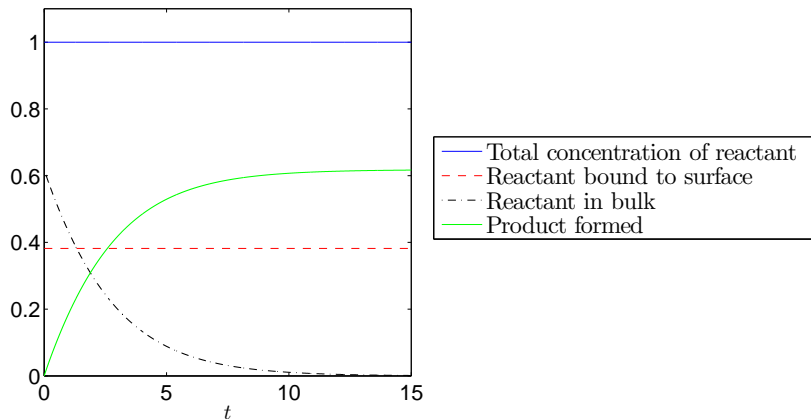
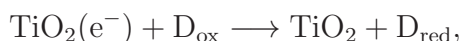


Figure 2.29: A plot showing that the conservation of reactant holds throughout the simulation when the QSSA system is solved.

to solutions obtained from solving our full system. Similarly, we have given several examples where the QSSA gives a very close approximation to the solutions obtained from solving the full system. Additionally, we have demonstrated that using  $\epsilon_Q$  from (2.18) to decide if the QSSA will hold (outwith a diffusion-limited parameter regime) is a fairly accurate approach. By giving an example of an intermediate case, we have demonstrated that for certain parameter regimes solving our full system is the only way to accurately solve the system due to the possible errors which may arise by invoking the QSSA.

## 2.2 Experimental procedure and results

The system used to assess the activity of self-cleaning glass is based on a water-based ink containing a redox dye, resazurin (Rz), mixed with a sacrificial electron donor (SED), glycerol, and a polymer, hydroxyethylcellulose (HEC) [50]. Once the ink is applied to the surface of a photocatalyst, if irradiated with sufficient energy to overcome the band gap, the  $\text{TiO}_2$  will react to produce holes and electrons. The photo-generated holes then oxidise the SED, which prevents the  $\text{TiO}_2$  electron-hole pairs recombining. This allows the photo-generated electrons  $\text{TiO}_2(e^-)$  to irreversibly reduce the dye,



where  $\text{D}_{\text{ox}}$  represents the dye Rz and  $\text{D}_{\text{red}}$  is the reduced form of the dye, resorufin (Rf). As the reduction occurs, the ink changes colour from blue to pink [58]. The colour change happens within a few minutes and after further irradiation the system completely bleaches the ink where the Rf is converted into its colourless form dihydroresorufin. Figure 2.30 shows the chemical structure of resazurin, resorufin and dihydroresorufin.



Figure 2.30: Chemical structure of resazurin, resorufin and dihydroresorufin.

Figure 2.31 shows typical absorbance spectra of the three chemicals. The blue arrows indicate how the absorbance peaks change with time as resazurin is converted to resorufin. For example, at approximately 582 nm the absorbance is increasing, whereas at 382 nm and 608 nm the absorbance is decreasing. Once the resorufin is completely exhausted the spectrum becomes almost flat for wave-

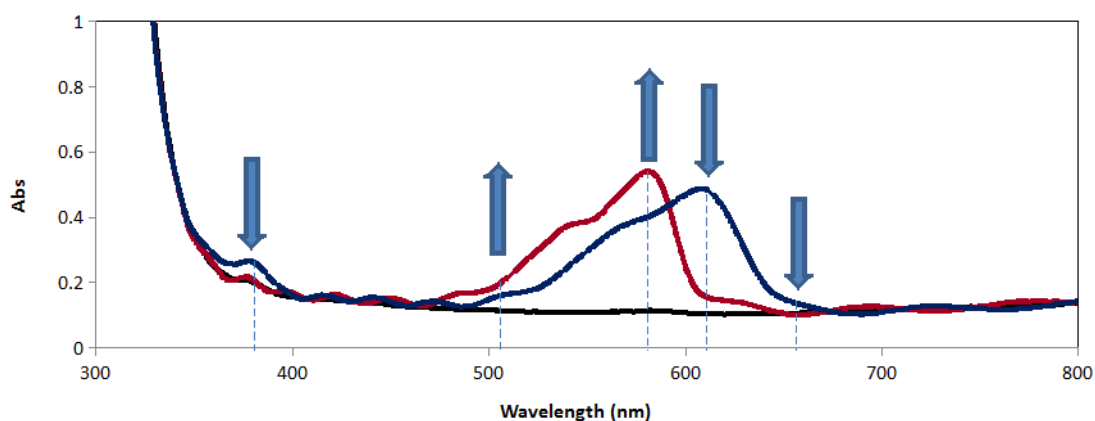


Figure 2.31: Typical absorbance spectra of resazurin (red line), resorufin (blue line) and dihydroresorufin (black line), where 608 nm and 582 nm refer to the wavelengths at which resazurin and resorufin have absorbance peaks, respectively.

lengths greater than approximately 400 nm.

Experiments were carried out by Nathan Wells and Professor Andrew Mills at Queen's University Belfast to determine the influence of film thickness on the initial reaction rate [62]. A total of seven film thicknesses were used ranging from 219 nm to 1483 nm. The ink used for experiments consisted of 1.5 g HEC (hydroxyethylcellulose) in 98.5 ml double distilled H<sub>2</sub>O. Additionally, 0.1333 g of resazurin sodium salt and 13.3333 g of glycerol were added. The ink was refrigerated, and stirred vigorously for 10 minutes immediately prior to use. Ink samples were prepared for irradiation by drawing down onto a 25 x 25 mm Activ<sup>TM</sup> glass plate. The sample was then purged in argon before being illuminated with UVA light through the back of the glass plate as shown in Figure 2.32.

Absorbance spectra were recorded at regular intervals until a perceived end point was reached for each thickness of film. The absorbance spectra for all films are shown in Figures 2.33 - 2.39. As the dye changes colour gradually from blue to pink, the initial absorbance spectrum has been plotted in blue and the final absorbance spectrum plotted in pink. The colour of the intermediate spectra give an estimate of how the colour of the dye may change throughout the reaction. Note that in Appendix A we explain how the absorbance spectrum of a substance

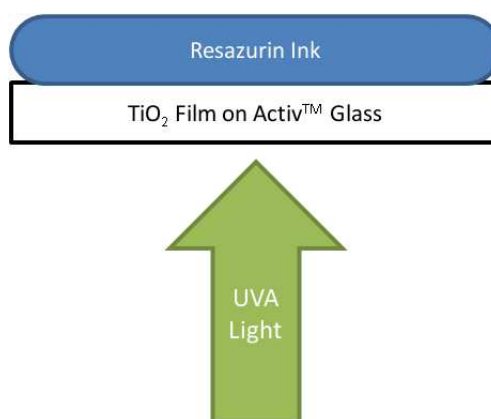


Figure 2.32: Diagram showing how the samples are illuminated with UVA light.

can be used to approximate its colour.

The Beer-Lambert law states that

$$\text{Abs}(\lambda) = \epsilon(\lambda)Lc, \quad (2.54)$$

where  $\lambda$  represents wavelength,  $\text{Abs}(\lambda)$  represents the absorbance,  $\epsilon(\lambda)$  is the molar absorptivity,  $L$  is the path length which light has to pass through and  $c$  is the concentration of the absorbing species in the material. It is assumed that  $c$  is constant throughout  $L$ . Since  $\epsilon(\lambda)$  is constant at a particular wavelength, absorbance is proportional to the concentration [83]. Hence, the concentration of Rz can be estimated based on the absorbance and thickness of the film. We are ultimately interested in the reaction rate of the reduction of Rz, i.e. the rate at which the concentration of Rz is decreasing. Hence, by measuring the absorbance at various times throughout the reaction we are able to estimate the reaction rate.

The absorbance was measured at 608 nm as this is where the greatest change in absorbance occurred. We define  $\text{Abs}_{608}(t)$  as the absorbance measured at 608 nm at time  $t$  after the initiation of UVA irradiation. The change in absorbance is measured by taking the final absorbance at 608 nm for each experiment and

subtracting it from the measured absorbance,

$$\Delta\text{Abs}_{608}(t) = \text{Abs}_{608}(t) - \text{Abs}_{608}(T),$$

where  $T$  is the time at the end of each experiment. Hence, in all cases  $\Delta\text{Abs}_{608}(t)$  will tend to zero as  $t \rightarrow T$ .

To determine the initial reaction rate from  $\Delta\text{Abs}_{608}(t)$ , a straight line is fitted through the data points corresponding to the period of time where the absorbance appears to be decreasing linearly with time. This straight line is plotted in Figures 2.33 - 2.39. The slope  $m$  of the straight line fit then gives an approximation of the initial reaction rate. As the initial absorbance is dependent on film thickness, to allow us to compare results from different films we divide  $m$  by the initial change in absorbance to calculate a normalised reaction rate

$$R_i = \frac{-m}{\Delta\text{Abs}_{608}(0)}.$$

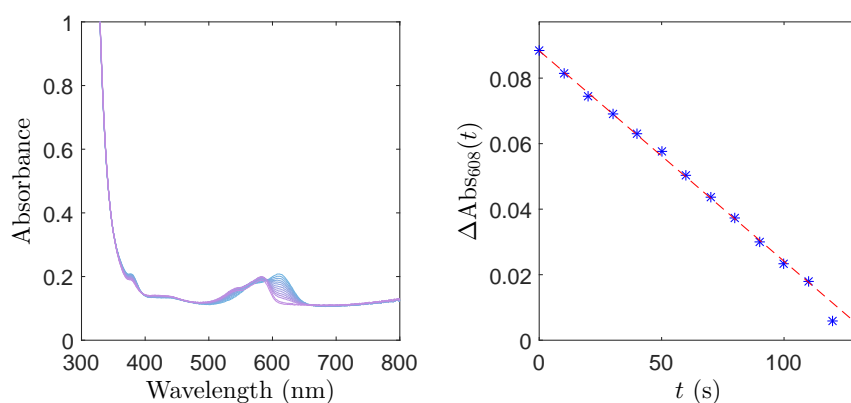


Figure 2.33: Experimental results using a 549 nm thick film. In the right hand plot the stars represent experimental data and the dashed line is a best fit straight line fitted to this data.

Figures 2.33 - 2.39 show very similar qualitative behaviour; the absorbance peak at 608 nm decreases whereas the peak at 582 nm increases. As  $L$  is increased, the experimental results show that the absorbance peak at 608 nm increases. This is

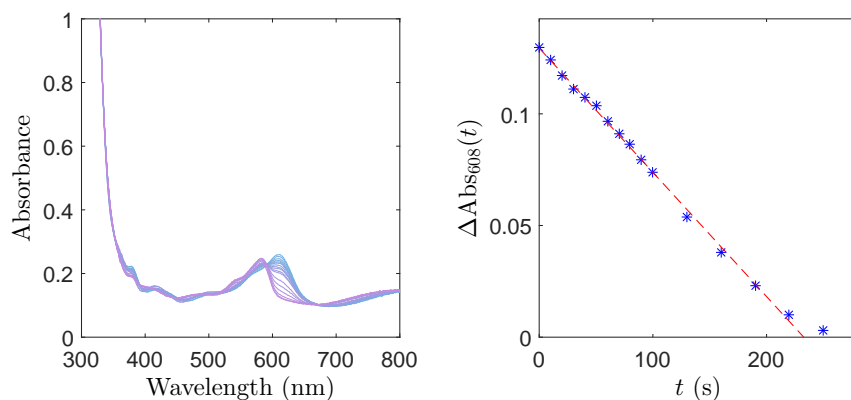


Figure 2.34: Experimental results using a 855 nm thick film. In the right hand plot the stars represent experimental data and the dashed line is a best fit straight line fitted to this data.

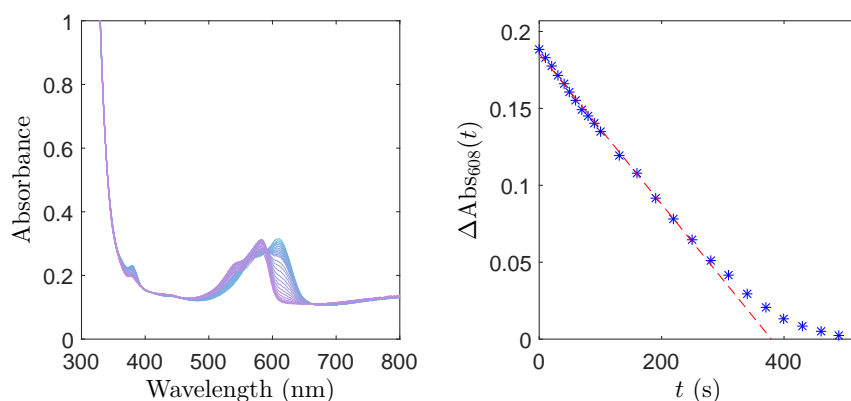


Figure 2.35: Experimental results using a 1217 nm thick film. In the right hand plot the stars represent experimental data and the dashed line is a best fit straight line fitted to this data.

unsurprising since from the Beer-Lambert law (2.54), if the concentration remains constant, as  $L$  is increased, the absorbance must increase. From all seven sets of data it is clear that  $\Delta\text{Abs}_{608}(t)$  decreases initially at an approximately constant rate. However, towards the end of the reaction it appears that the absorbance decreases at a slower rate.

Figure 2.40 shows the initial rate  $R_i$  plotted against film thickness  $L$  (blue stars). Figure 2.41 shows  $\ln(R_i)$  plotted against  $\ln(L)$  with a straight line fitted through the data. By calculating the equation of this straight line, we can calculate

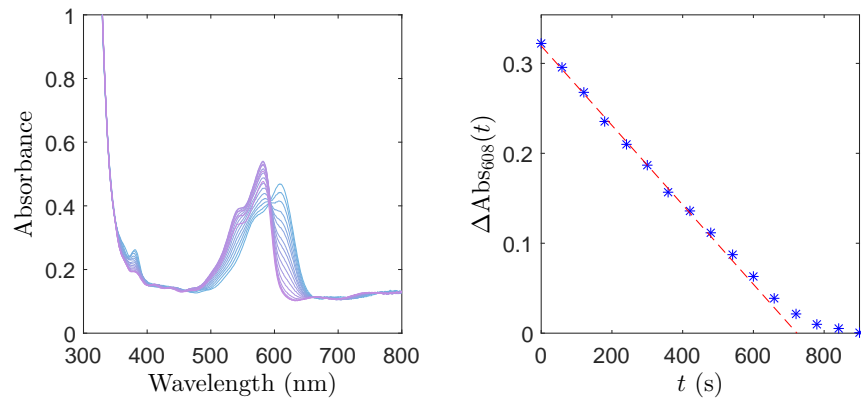


Figure 2.36: Experimental results using a 2140 nm thick film. In the right hand plot the stars represent experimental data and the dashed line is a best fit straight line fitted to this data.

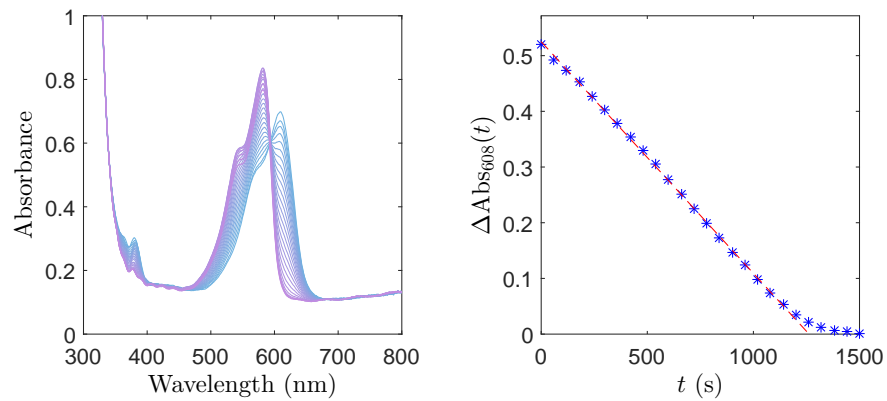


Figure 2.37: Experimental results using a 3418 nm thick film. In the right hand plot the stars represent experimental data and the dashed line is a best fit straight line fitted to this data.

the approximate relationship between  $R_i$  and  $L$  (which is plotted in red in Figure 2.40). The slope of this line is -1.1949. Hence we can deduce that the initial reaction rate is approximately first-order with respect to film thickness i.e.

$$R_i \propto \frac{1}{L}.$$

The diffusion coefficient for the dye in this system is estimated to be approxi-

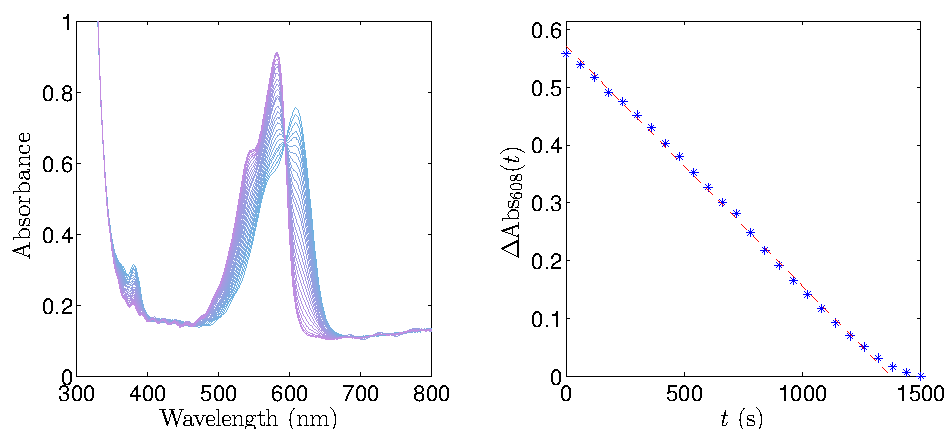


Figure 2.38: Experimental results using a 3614 nm thick film. In the right hand plot the stars represent experimental data and the dashed line is a best fit straight line fitted to this data.

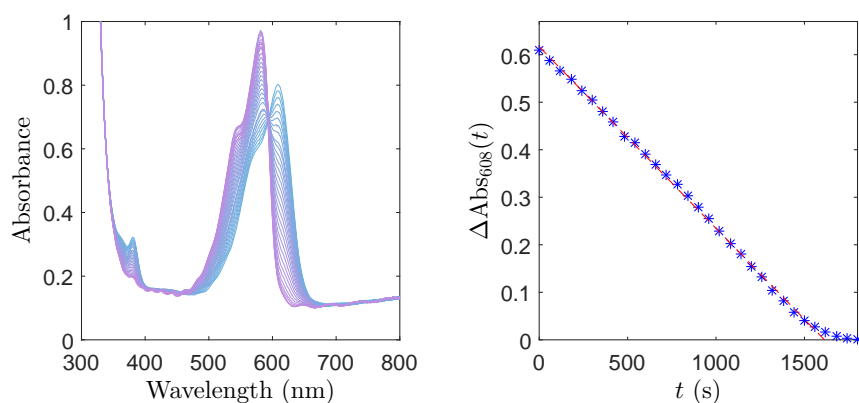


Figure 2.39: Experimental results using a 4014 nm thick film. In the right hand plot the stars represent experimental data and the dashed line is a best fit straight line fitted to this data.

mately  $10^{-13} \text{ m}^2 \text{ s}^{-1}$  [50]. The diffusive time scale is given by

$$t_D = \sqrt{\frac{L^2}{2D}}. \quad (2.55)$$

Hence, the time taken for a molecule of dye to diffuse across the ink layer will be approximately 1.5 s for the thinnest film and 9 s for the thickest film. However, the overall reaction takes place over a far longer time scale (over 100 s in the case of the thinnest film, and well over 1500 s for the thickest). This suggests that, for

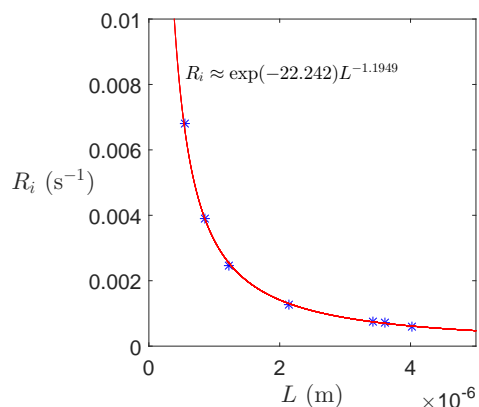


Figure 2.40: Experimentally observed initial reaction rate plotted against  $L$ .

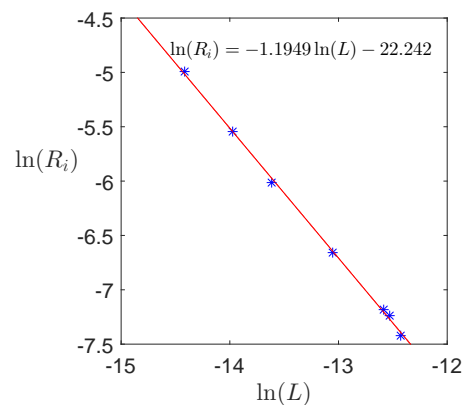


Figure 2.41: Experimental results showing  $\ln(R_i)$  plotted against  $\ln(L)$  with a straight line fitted through the data.

this particular system, the transport of dye molecules to the photocatalyst surface is not the process which limits the overall reaction rate.

Lachheb *et al.* [37] reported that many dyes are strongly adsorbed onto a photocatalyst surface. This suggests that the adsorption of Rz molecules onto the photocatalyst surface is not the process which limits the overall reaction rate.

It therefore seems likely that the one process likely to have the greatest impact on the overall reaction rate is the reaction taking place on the semiconductor surface which converts bound species into products. This is due to the low UVA irradiance which the semiconductor is illuminated with.

The usual expectation would then be that the initial reaction rate  $R_i$  should be independent of  $L$ . However, the experimental data presented in Figures 2.40 and 2.41 suggest that the initial reaction rate is approximately inversely proportional to film thickness. In the next section, we will apply our simple mathematical model to this particular system with the aim of explaining this apparent contradiction.

## 2.3 Mathematically modelling resazurin case

It is assumed that both glycerol and resazurin are required at the photocatalyst surface for the oxidation of resazurin to take place, which results in the dye changing colour. As there is a high concentration of glycerol in comparison to resazurin we will assume that there is enough glycerol to ensure that the surface reaction is never limited due to the lack of glycerol at the photocatalyst surface. Hence, we will not consider glycerol in our model. This assumption allows us to apply the model derived in the previous section.

Applying our model to this particular problem, our concentration of reactant  $u(x, t)$  represents the concentration of resazurin and  $w(t)$  represents the concentration of resazurin bound to the photocatalyst surface. The product  $p(t)$  represents the converted form of resazurin, resofurin. All other parameters are as described in the previous section. Figure 2.42 shows the initial setup for this particular system. We assume that we have a thin semiconductor photocatalyst applied to a piece of glass. An ink layer is applied directly to the  $\text{TiO}_2$ . Note that since the system is illuminated from behind, the surface reaction rate  $k_2$  will remain constant.

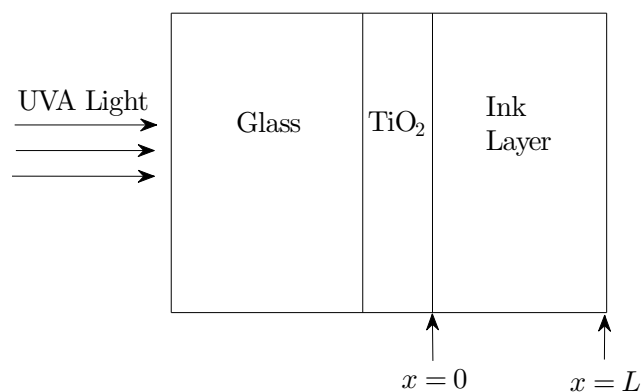


Figure 2.42: Diagram of the initial set-up.

To use our mathematical model we first need to convert any dimensional pa-

rameters into nondimensional form using (2.4)-(2.6). The predicted results then have to be expressed in terms of dimensional units to be compared with experimental data.

### 2.3.1 Estimating the initial reaction rate

To compare the results obtained from our model with experimental results we have to estimate the initial reaction rate  $R_i$ . This is done by calculating the average concentration  $\bar{u}(t)$  at each time step and determining the half-life ( $t_{1/2}$ ) of the reaction, which we define as the time taken for  $\bar{u}(t)$  to decrease by half. The half-life is a parameter which is simple and easy to measure for any kinetic system [50]. A straight line of slope  $m$  is then fitted to all data points corresponding to times ranging from zero to  $t_{1/2}$ . Dividing by the initial concentration  $u_q$ , we have that the normalised initial rate is given by

$$R_i = \frac{-m}{u_q}. \quad (2.56)$$

By applying this method of calculating the initial reaction rate to the experimental data from Section 2.2, we come to the same conclusions as those presented earlier, i.e. that  $R_i$  was approximately inversely proportional to  $L$ .

### 2.3.2 Interpreting experimental results

Assuming we are in a surface reaction-limited regime, we would expect  $k_2$  to be relatively small. Lachheb *et al.* [37] reported that many dyes are strongly absorbed onto a photocatalyst surface. Hence, we will assume that  $k_1 > k_{-1}$ . We have a dimensional equivalent of (2.23), given by

$$\frac{d\bar{u}}{dt} = -\frac{1}{L} \left( \frac{k_1 k_2 u(0, t) s_{tot}}{k_1 u(0, t) + k_{-1} + k_2} \right). \quad (2.57)$$

Due to the initial concentration being very large (as well as the small  $k_2$  value, and large  $k_1$  value relative to  $k_{-1}$ ), the denominator of (2.57) will be dominated initially by  $k_1 u(0, t)$ , and hence

$$\frac{d\bar{u}}{dt} \approx -\frac{1}{L} k_2 s_{tot}.$$

This implies that the initial reaction rate is zeroth-order and that it is inversely proportional to film thickness, i.e.

$$\frac{d\bar{u}}{dt} \propto \frac{1}{L}.$$

This is the approximate behaviour observed in the physical experiments.

As the concentration of dye decreases we will eventually be in a situation where  $k_1 u(0, t)$  no longer dominates the denominator. Hence, as  $u(0, t)$  approaches zero we have that

$$\frac{d\bar{u}}{dt} \approx -\frac{1}{L} \frac{k_1 k_2 u(0, t) s_{tot}}{k_{-1} + k_2},$$

which is first-order in time. This predicted change from zeroth-order to first-order kinetics is observed in the experimental data presented earlier.

If we assume that we are in a regime where the QSSA is valid, and that the surface reaction is the rate limiting process we clearly have that

$$R_i \propto \frac{1}{L}. \quad (2.58)$$

Before our system is able to find equilibrium we assume that  $u_0$  is constant for all films. This means that by increasing  $L$  we are increasing the total number of dye molecules. Although the rate at which product is being formed at the photocatalyst surface is independent of  $L$ , the total number of molecules still in the ink layer will increase with thickness. This means that although  $\frac{du(0,t)}{dt}$  is independent of film thickness, the rate at which  $\bar{u}(t)$  decreases must be dependent

on  $L$ . For example, a 10% drop in average concentration of dye within a thin film will occur far more quickly than a 10% reduction within a thick film. This is why, in this particular surface reaction-limited regime, the initial overall reaction rate is  $L$  dependent.

### 2.3.3 Numerical simulations

In this section we present results from numerical simulations which aim to replicate the experimental data presented earlier using physical parameters appropriate for this particular system. We have three options when solving our system: we can solve the full coupled system expressed in (2.14) and (2.15), we can assume the QSSA and solve the differential equation (2.19), or we can use the analytical solution (2.26) for an estimate of  $\bar{u}$  (assuming that we are in a surface reaction-limited regime).

When choosing which parameters to use in our model, we will make use of published data and data presented earlier in this chapter. For example, as was noted earlier, for this particular system we have that  $D = 10^{-13} \text{ m}^2 \text{ s}^{-1}$  [50]. We will also use the same range of film thicknesses used in the experimental results presented earlier, i.e.  $L$  ranges from  $5.49 \times 10^{-7} \text{ m}$  to  $4.014 \times 10^{-6} \text{ m}$ . Using the initial measured absorbance data, the thickness of each film, and a published estimate for  $\epsilon(\lambda)$  at 608 nm [50] we can use the Beer-Lambert law (2.54) to estimate the initial concentration. Hence, we estimate that  $u_0$  is equal to  $36.9 \text{ mol/m}^3$  for the entire range of films we consider.

This leaves us with several parameter values to estimate. As was shown earlier, with these particular physical parameters we have that the diffusive time scale will be 1.7 s for the thinnest film, and 12.7 s for the thickest. As we assume that diffusion is not rate limiting we must choose  $k_1$ ,  $k_{-1}$ ,  $k_2$  and  $s_{tot}$  to ensure that the adsorption/desorption and surface reaction timescales are appropriate. We also know that in these particular systems the reactant is strongly absorbed to the surface (i.e.  $k_1 > k_{-1}$ ) and that  $k_2$  must be relatively small due to the

low UVA irradiance which illuminates the photocatalyst surface. In the numerical simulations that follow we therefore set  $k_1 = 5.833 \times 10^{-3} \text{ m}^3/\text{mol s}^{-1}$ ,  $k_{-1} = 0.833 \times 10^{-3} \text{ s}^{-1}$ ,  $k_2 = 1.073 \times 10^{-2} \text{ s}^{-1}$  and  $s_{tot} = 1 \times 10^{-5} \text{ mol}/\text{m}^2$ .

Based on these parameters, we would expect to be in a regime where the transport of reactant to the photocatalyst surface is not the one process which slows down the overall reaction process. However, it is not immediately clear whether or not we will be in a regime where the overall reaction is entirely surface reaction-limited. By redefining (2.18) for dimensional systems, we can calculate  $\epsilon_Q$  values for this particular system. A dimensional version of  $\epsilon_Q$  is given by

$$\epsilon_Q = \frac{s_{tot}}{L(K_m + u_q)}. \quad (2.59)$$

This can give an indication of whether or not the QSSA is valid. However, as we may not be in a completely reaction-limited regime, it is uncertain whether  $\epsilon_Q$  will give an accurate indication of the validity of the QSSA. Figure 2.43 shows the  $\epsilon_Q$  values calculated from (2.59) for the range of  $L$  values which we are investigating. We can see that for the thinnest film,  $\epsilon_Q$  is almost equal to 0.5, which is fairly large. This suggests that the QSSA may not be valid for the thinnest films. However, for the thickest film,  $\epsilon_Q$  is less than 0.1 and hence the QSSA may be applicable. Using our model, we are able to test how accurate these predictions are for this particular system.

In addition to comparing results between the full system and the QSSA system, we will calculate the approximate analytical solution given in (2.26).

For each film we use all three solution methods. Figures 2.44 - 2.50 show the results for all seven films considered. As was previously mentioned, the numerical simulations were performed after converting dimensional parameters into nondimensional form. For all cases considered, when solving the nondimensional full system, Method 1 was used with  $N = 200$  and  $NT = 2 \times 10^4$ . Similarly, when solving the nondimensional QSSA system, Method  $1_Q$  was used with  $N = 200$

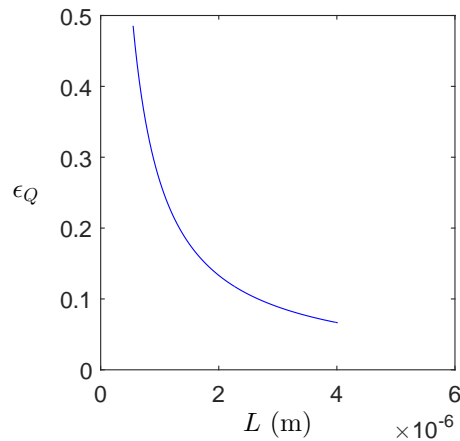


Figure 2.43: Variation in QSSA parameter  $\epsilon_Q$  (2.59) as a function of film thickness  $L$ .

and  $NT = 2 \times 10^4$ . Any results shown have been converted back to their dimensional form. In each figure, the first plot shows profiles of  $u(x, t)$  against  $x$  at 10 uniform times ranging from  $t = 0$  to  $t = T$ , where  $T$  is the time at which the simulation ends. The blue solid lines show the profiles when the full system, (2.14) and (2.15), is solved and the red dashed lines show the results when the QSSA is invoked (2.19). The second plot shows the concentration  $w(t)$  against  $t$  when the full system is solved. The third plot shows the average concentration  $\bar{u}$  against  $t$  when the full system is solved along with a straight line fitted to the initial data. The final plot shows a comparison of the normalised average concentration for all three methods. The average concentration obtained from solving the full system is plotted as a solid blue line, the concentration found by solving the QSSA system is plotted as a red dashed line, the approximate analytic solution is plotted in a dash-dot black line, and the normalised experimental data is plotted as red stars.

The first plot of Figures 2.44 - 2.50 show that the concentration profiles are approximately flat throughout the reaction for all seven films. However, for the final three films (Figures 2.48 - 2.50) there is a slight gradient in the profiles. This is reminiscent of the profiles shown in Figure 2.26 which corresponded to an intermediate regime. This is understandable, due to the films being thicker the

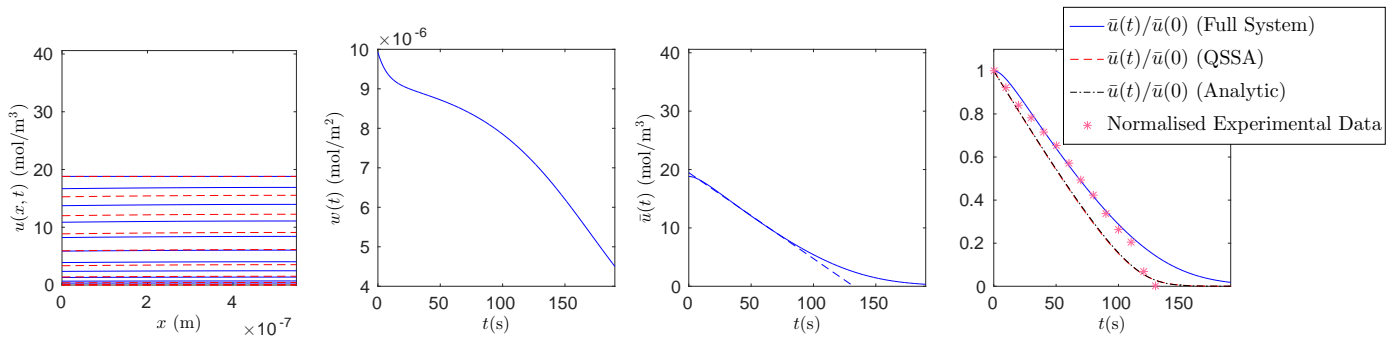


Figure 2.44: Simulation results obtained by solving the full system, the QSSA system and the analytical approximation for a reaction-limited parameter regime with  $L = 549$  nm. The final plot shows a comparison between simulation results and normalised experimental data.

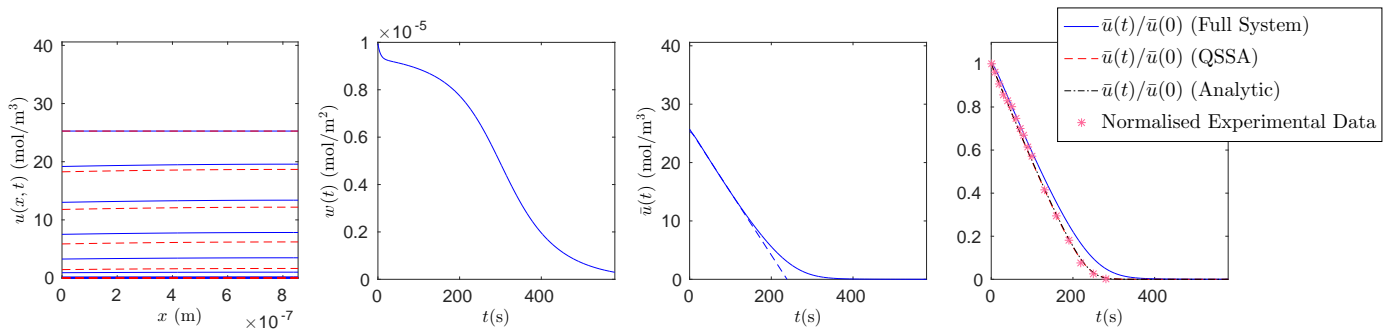


Figure 2.45: Simulation results obtained by solving the full system, the QSSA system and the analytical approximation for a reaction-limited parameter regime with  $L = 855$  nm. The final plot shows a comparison between simulation results and normalised experimental data.

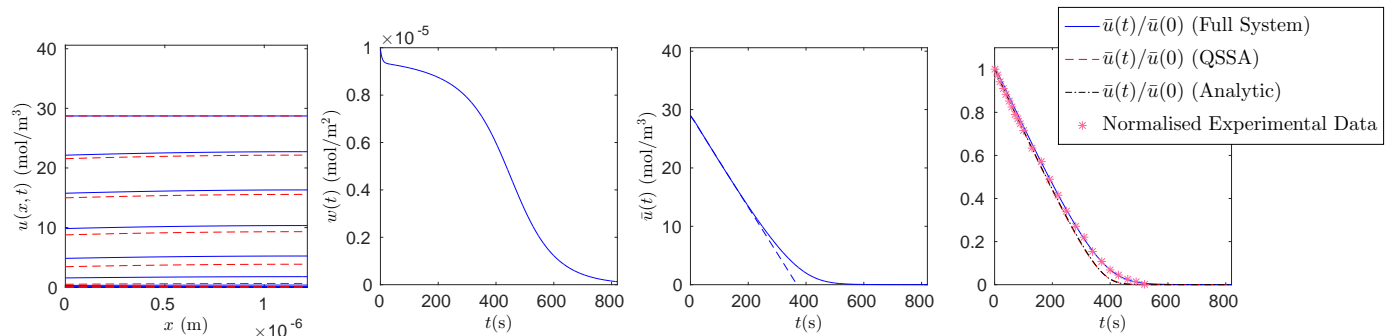


Figure 2.46: Simulation results obtained by solving the full system, the QSSA system and the analytical approximation for a reaction-limited parameter regime with  $L = 1217$  nm. The final plot shows a comparison between simulation results and normalised experimental data.

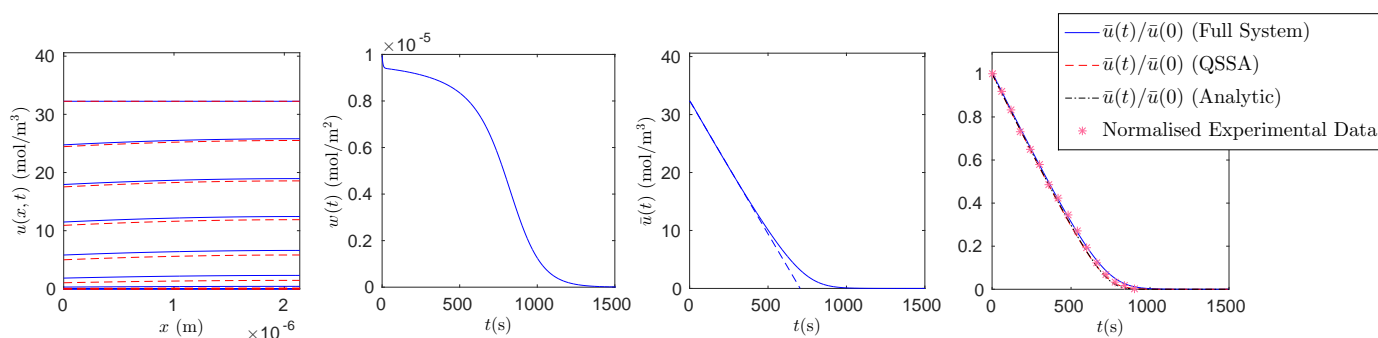


Figure 2.47: Simulation results obtained by solving the full system, the QSSA system and the analytical approximation for a reaction-limited parameter regime with  $L = 2140$  nm. The final plot shows a comparison between simulation results and normalised experimental data.

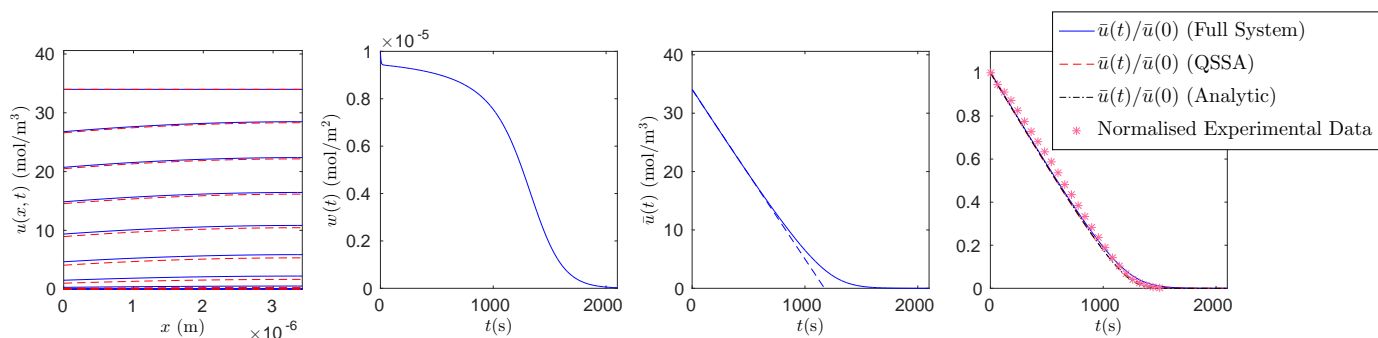


Figure 2.48: Simulation results obtained by solving the full system, the QSSA system and the analytical approximation for a reaction-limited parameter regime with  $L = 3418$  nm. The final plot shows a comparison between simulation results and normalised experimental data.

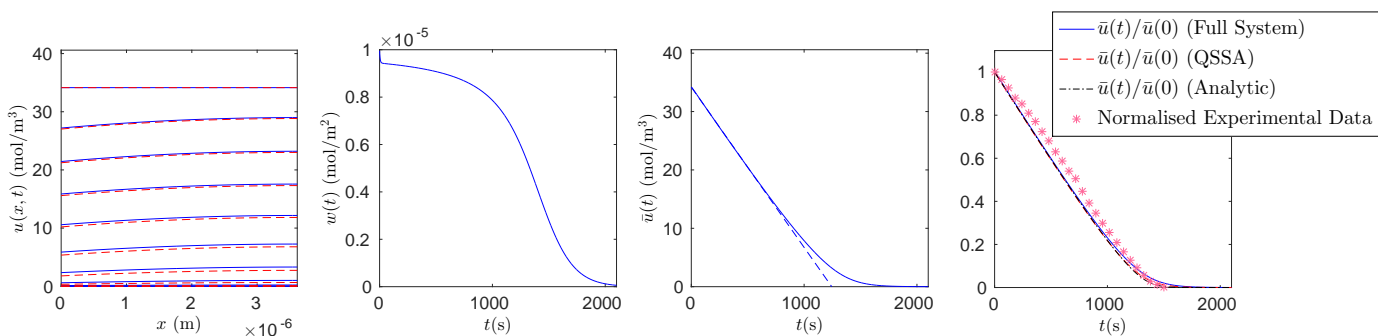


Figure 2.49: Simulation results obtained by solving the full system, the QSSA system and the analytical approximation for a reaction-limited parameter regime with  $L = 3614$  nm. The final plot shows a comparison between simulation results and normalised experimental data.

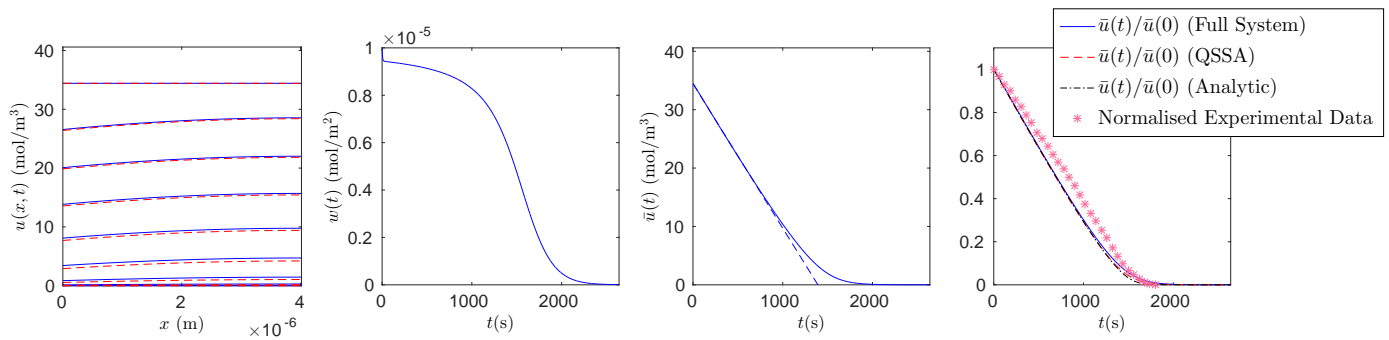


Figure 2.50: Simulation results obtained by solving the full system, the QSSA system and the analytical approximation for a reaction-limited parameter regime with  $L = 4014$  nm. The final plot shows a comparison between simulation results and normalised experimental data.

reactant will take longer to be transported through the domain. In terms of the validity of the QSSA, it is clear that as the film thickness is increased the QSSA becomes more accurate. This is in agreement with our earlier predictions made by calculating  $\epsilon_Q$  (Figure 2.43).

The second plots of Figures 2.44 - 2.50 show that the surface bound reactant concentration behaves in a similar way for all seven films. In all cases there is an initial rapid decrease in  $w(t)$ . This happens at roughly the same time for all films, however, as the figures all have different time scales this is not immediately obvious. In all cases, for the first half of the simulation  $w(t)$  is varying very little, before decreasing far more quickly in the latter stages of the reaction. As the film thickness is increased, the variation in  $w(t)$  during the first half of the reaction decreases. We would expect that during the first half of the simulations the QSSA will be more accurate as  $L$  increases.

The third plots of Figures 2.44 - 2.50 show the average concentration of reactant in the bulk when the full system is solved. The dashed blue line shows a straight line fitted to the data corresponding to  $t$  ranging from  $0$  to  $t_{1/2}$ . Qualitatively, all seven plots are very similar. Although, for the thinnest films,  $u_q$  is significantly smaller than for the largest films.

The final plots of Figures 2.44 - 2.50 shows a comparison between the three

methods used to solve our system and normalised experimental data. For all seven cases, by using the full system, we get very good agreement with the experimental data. Although, for the thinnest of films the prediction is not as convincing as the thicker films. In terms of the validity of the QSSA, the plots show that, as the film thickness is increased, the predictions using the QSSA becomes more accurate. The plots also demonstrate that there is very little difference between using the QSSA and the analytic approximation. Although, for the thickest of films, there is a slight difference between the two plots. This is not surprising, as the profiles of  $u$  are no longer completely flat for the thickest film (as shown in Figure 2.50).

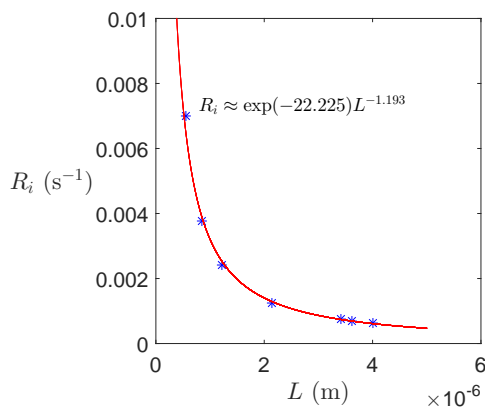


Figure 2.51: Model simulation results showing  $R_i$  plotted against  $L$  when the full system is solved.

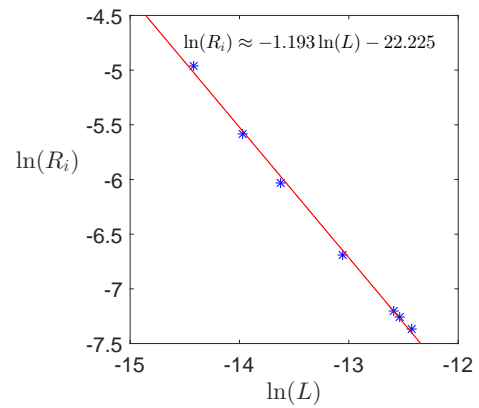


Figure 2.52: Model simulation results showing  $\ln(R_i)$  plotted against  $\ln(L)$  when the full system is solved.

Figure 2.51 shows the initial reaction rate  $R_i$  plotted against film thickness  $L$  for each of the seven films obtained by solving the full system. Figure 2.52 shows a plot of  $\ln(R_i)$  versus  $\ln(L)$ . By fitting a straight line through the  $\ln - \ln$  data, we can determine an approximate relationship between  $R_i$  and  $L$ . Re-arranging the equation of this straight line allows us to find a function which fits the  $R_i$  versus  $L$  data shown in Figure 2.51 and plotted in red. From the equation of the best fit straight line we have that the gradient is approximately -1.193. This is very similar to the corresponding value calculated from the experimental data (which was -1.1949). This implies that  $R_i$  is approximately inversely proportional to  $L$

and is in agreement with the experimental data.

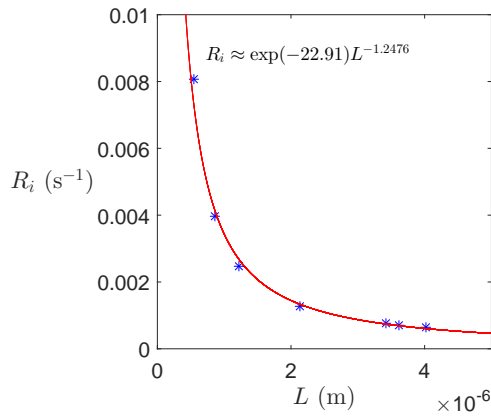


Figure 2.53: Model simulation results showing  $R_i$  plotted against  $L$  when the QSSA is invoked.

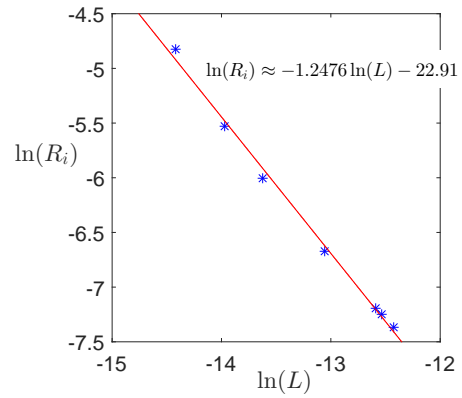


Figure 2.54: Model simulation results showing  $\ln(R_i)$  plotted against  $\ln(L)$  when the QSSA is invoked.

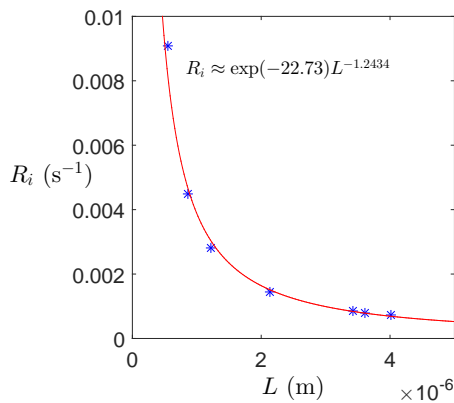


Figure 2.55: Model simulation results showing  $R_i$  plotted against  $L$  when the analytical approximation is used.

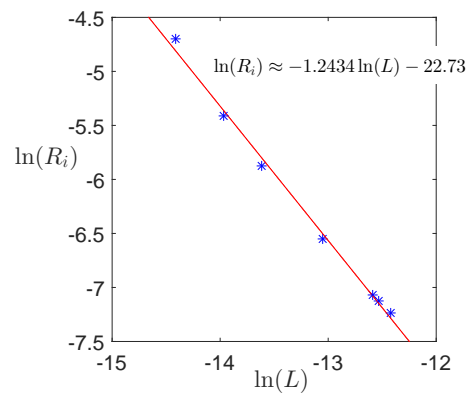


Figure 2.56: Model simulation results showing  $\ln(R_i)$  plotted against  $\ln(L)$  when the analytical approximation is used.

Figures 2.53 and 2.54 show the same results presented in Figures 2.51 and 2.52 when the QSSA has been invoked. Similarly, Figures 2.55 and 2.56 show the results when the approximate analytic solution is used to solve the system. When the QSSA system is solved, the gradient of the best fit straight line is approximately -1.2476. Similarly, the approximate analytic solution gives a gradient

of approximately -1.2434. This demonstrates that these two methods give very similar results.

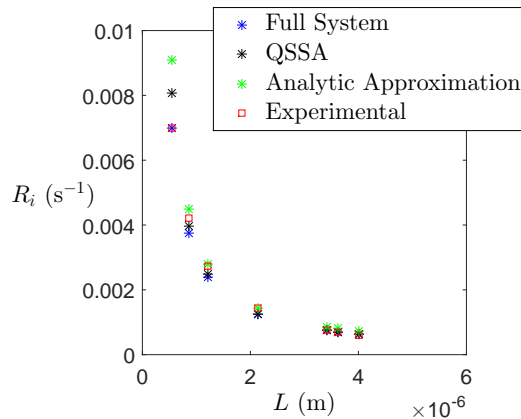


Figure 2.57: Model simulation results showing  $R_i$  plotted against  $L$  when all three methods are used to solve the system.

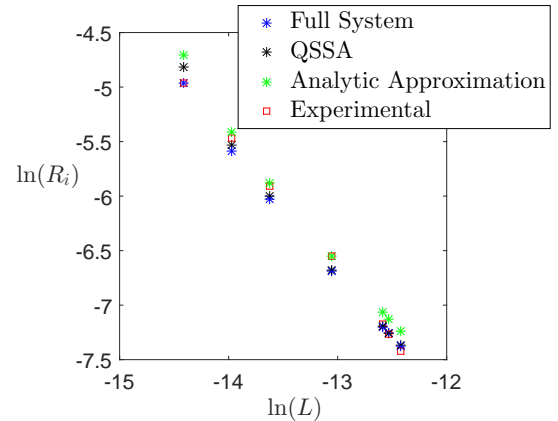


Figure 2.58: Model simulation results showing  $\ln(R_i)$  plotted against  $\ln(L)$  when all three methods are used to solve the system.

All three methods give similar results in term of approximating the initial reaction rate  $R_i$  as shown in Figures 2.57 and 2.58. From this comparison it is clear that solving the full system gives the best results in terms of replicating the experimental data.

We have shown that, using physically realistic parameters, our model can replicate the experimental results fairly well. Additionally, our earlier finding that, for particular regimes, the initial reaction rate is inversely proportional to the film thickness holds in this case. However neither the experimental results or the simulation results give the exact relationship predicted. The experimental results and our model results suggest that

$$R_i \propto L^{-a},$$

where  $a$  is approximately equal to -1.2, as opposed to the -1 value predicted from our analysis.

Recall that when arriving at the relationship (2.58) between  $R$  and  $L$  we assumed that the QSSA was valid. However, by calculating  $\epsilon_Q$  and comparing nu-

merical results obtained when the QSSA was and was not assumed, we have shown that the QSSA is not particularly accurate for the entire range of films we have considered. This perhaps explains why the relationship between  $R_i$  and  $L$  is not exactly what our analysis suggests it should be. For the larger films, we see that diffusion is starting to play a role and is no longer quick enough to ensure a constant supply of reactant at the photocatalyst surface. This contradicts an assumption made in Section 2.3.2, that within this regime the overall rate was entirely reaction-limited. Were our parameters to fall within a regime where the QSSA is valid and the overall reaction rate is completely reaction-limited, we would expect to find that our simulation results would be far closer to what was predicted earlier in Section 2.3.2.

### 2.3.4 Experimenting with film thickness

We can further study the relationship between  $R_i$  and  $L$  by expanding the region of  $L$  values which we consider. When defining the initial reaction rate we have previously used the half-life in our approximations. For the previous regime this was an appropriate measure, as the initial reduction of  $\bar{u}$  was approximately constant. However, over a wider range of  $L$  values, this is not always the case. For example, in a diffusion-limited regime, fitting a straight line through initial data ranging from  $t = 0$  to  $t = t_{1/2}$  is not appropriate. For this reason, we will now replace  $t_{1/2}$  with  $t_{1/10}$  when considering the initial reaction rate as defined in Section 2.3.1.

For all cases considered, to solve the nondimensional full system, Method 1 was used with  $N = 320$  and  $NT = 4 \times 10^5$ . The  $L$  values considered range from  $L = 1.16 \times 10^{-10}$  m to  $L = 3.5 \times 10^{-3}$  m ( $\ln(L)$  ranges from approximately -22.9 to -5.7 for this range of  $L$  values). The first plot of Figure 2.59 shows  $\ln(R_i)$  plotted against  $\ln(L)$ . From this plot there appears to be three distinct regimes. In the left hand plot, we have fitted three straight lines to different ranges of data points. Each straight line represents a regime where we have, approximately,  $R_i \propto L^m$ , where  $m = 0, -1$  and  $-2$ . The second plot reinforces the existence of these three

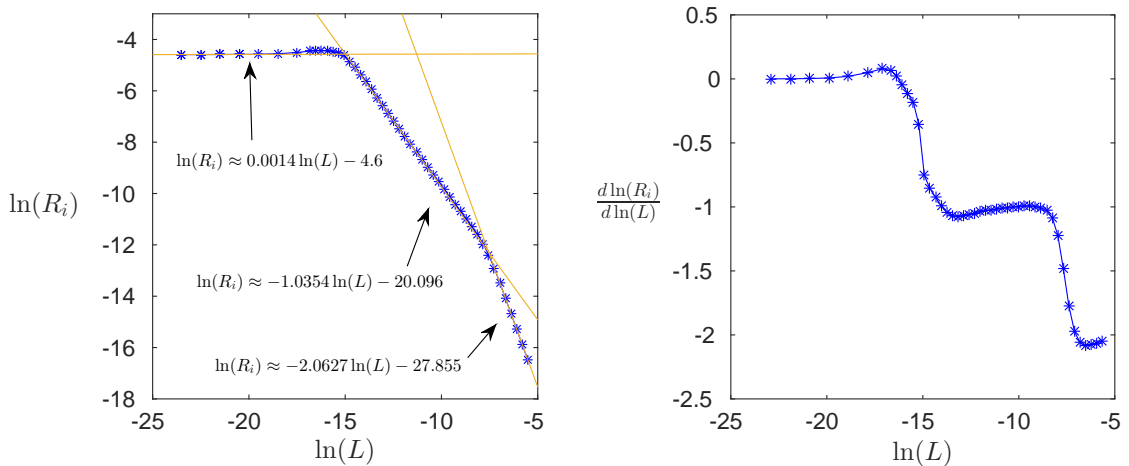


Figure 2.59: The left hand plot shows  $\ln(R_i)$  versus  $\ln(L)$ . Within this figure there are three clear regimes. Straight lines have been fitted to each of the three regimes. The right hand plot shows the rate of change of  $\ln(R_i)$  with respect to  $\ln(L)$  plotted against  $\ln(L)$ . This plot confirms the existence of three distinct regimes.

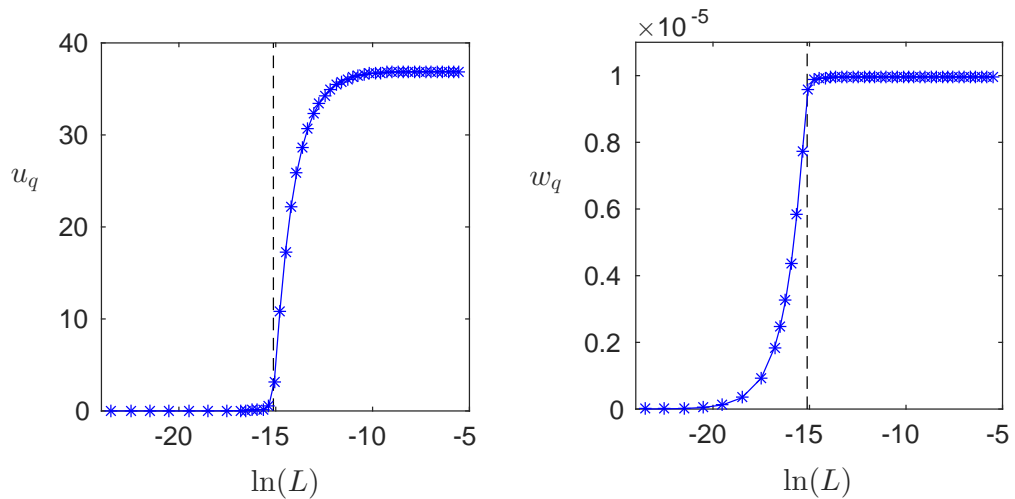


Figure 2.60: The first plot shows  $u_q$  plotted against  $\ln(L)$  and demonstrates that for  $L$  large enough  $u_q$  is approximately equal to  $u_0$ , and for  $L$  small enough,  $u_q$  is approximately zero. The second plot shows  $w_q$  plotted against  $\ln(L)$  and demonstrates that  $w_q$  tends to  $s_{tot}$  for large  $L$ , and tends to zero for small  $L$ . The vertical dotted black line in each plot represents the  $L$  value where the total reactant in the system ( $u_0 L$ ) equals  $s_{tot}$ .

distinct regimes. By plotting the derivative of  $\ln(R_i)$  with respect to  $\ln(L)$  against  $\ln(L)$ , we are able to show the there are three distinct regimes where the derivative is approximately 0, -1 and -2.

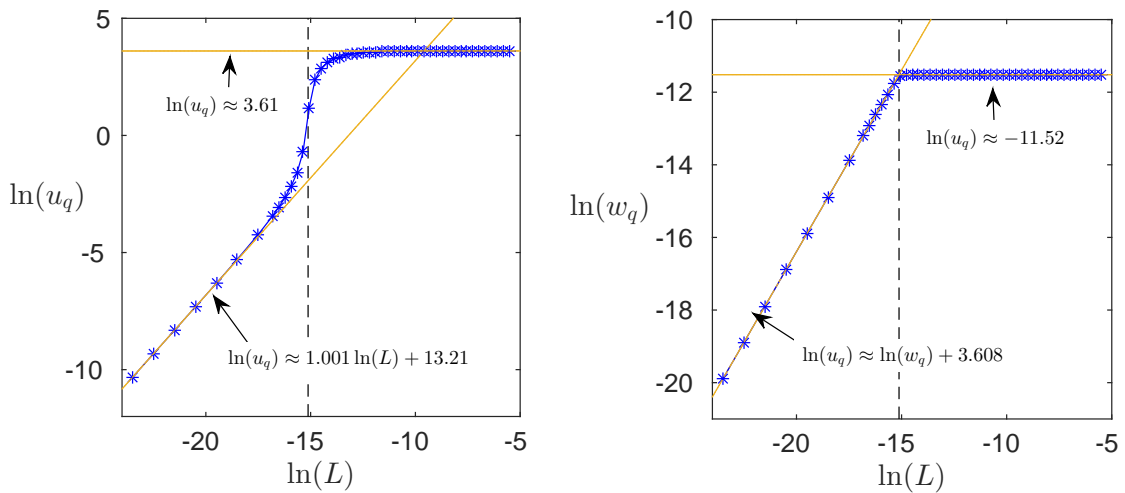


Figure 2.61: The first plot shows  $\ln(u_q)$  plotted against  $\ln(L)$  with straight lines fitted to the data points corresponding to the four largest  $L$  values considered and the four smallest  $L$  values considered. The first plot shows  $\ln(w_q)$  plotted against  $\ln(L)$  with straight lines fitted to data points corresponding to the four largest  $L$  values considered and the four smallest  $L$  values considered. The vertical dotted black line in each plot represents the  $L$  value where the total reactant in the system ( $u_0L$ ) equals  $s_{tot}$ .

Figure 2.60 shows how  $u_q$  and  $w_q$  vary over a wide range of  $L$  values. For very small  $L$  values,  $u_q$  is almost zero, as when  $L$  becomes very small the total concentration of reactant, in comparison to  $s_{tot}$ , is small. Hence, practically all reactant in the system is able to bind to the surface. For very large  $L$ , the total amount of reactant in the system will be large compared to  $s_{tot}$ , meaning that even if all surface reaction sites are saturated with reactant,  $u_q$  will remain very close to  $u_0$ . The second plot demonstrates that for large enough  $L$  values, the surface sites will be completely saturated, and  $w_q$  tends to  $s_{tot}$ . The plot also shows that  $w_q$  tends to zero as  $L$  decreases. By plotting the point at which  $u_0L = s_{tot}$  ( $L = 2.71 \times 10^{-4}$  m), we have shown that there is a clear difference in how both  $u_q$  and  $w_q$  vary with  $L$ . For  $u_q$ , when  $L$  is smaller than this value, we have that  $u_q$  quickly tends to zero. When  $L$  is larger than this value,  $u_q$  tends to  $s_{tot}$ . The change in  $w_q$  is similar, but due to the ratio of  $k_1$  to  $k_{-1}$ , we have that for any  $L$  value greater than  $L = 2.71 \times 10^{-4}$  m,  $w_q$  is approximately equal to  $s_{tot}$ . Due

to the presence of  $u_q$  in the definition of  $R_i$  (2.56), it is important to consider  $u_q$  when discussing the results presented in Figure 2.59.

For the largest  $L$  values considered, we have, from both plots of Figure 2.59, that  $R_i$  is approximately proportional to  $\frac{1}{L^2}$ . This is typical of a diffusion-limited regime. For large  $L$  values, we have, from Figure 2.60, that  $u_q$  remains constant. Hence,  $u_q$  is not having an influence in determining  $R_i$  for this particular regime.

For the intermediate regime, we have, from both plots of Figure 2.59, that  $R_i$  is approximately inversely proportional to  $L$ . Our explanation behind this result is as previously explained. The rate at which the total amount of reaction is reducing is constant. However, as  $L$  is decreasing, the total amount of reactant in the system is decreasing. Hence, although the rate that the total amount of  $u$  is being reduced remains independent of  $L$ , the rate that the average of  $u$  is decreasing must be dependent on  $L$ . However, this explanation is dependent on  $u_q$  being constant, due to the presence of  $u_q$  in the definition of  $R_i$ . For the range of  $L$  values corresponding to  $\ln(L)$  ranging from approximately -17 to -12.5,  $u_q$  is varying significantly. This corresponds to the region where Figure 2.59 shows a transition between the region where  $R_i \propto L^0$  and  $R_i \propto L^{-1}$ .

For very small  $L$  values, we have the perhaps surprising result, that  $R_i$  is approximately independent of  $L$ . We have, from the first plot of Figure 2.61, that for the smallest  $L$  values considered, that  $u$  is proportional to  $L$ . In almost all cases we have previously considered, we had that  $\frac{d\bar{u}}{dt}$  would decrease as  $u$  decreased. Hence, for this regime, because  $u_q$  is decreasing with  $L$ , we would have that  $\frac{d\bar{u}}{dt}$  at  $t = 0$  would decrease with  $L$  (this can be shown numerically). So for this regime, the rate at which the total amount of  $u$  is decreasing is proportional to  $L$  (this can be shown numerically). However, as  $u_q$  is also decreasing proportionally with  $L$ , we find that  $R_i$  is constant.

By performing similar simulations with different sets of parameters, we confirmed that the results described above are not unique to this particular set of parameters. For each simulation performed we found that there were, as above,

three distinct regions where  $R_i$  was proportional to 0,1 and 2. However, for each additional set of parameters we tested, the values of  $L$  where the observed kinetics transitioned from one region to the next varied for each set of parameters. Quantifying, for a given set of parameters, exactly where we expect the observed kinetics to transition from one region to another would be an interesting extension of the work presented in this chapter.

## 2.4 Conclusions

In this chapter we have shown that our mathematical model is able to replicate existing data fairly well using physically realistic parameter values. This was the case for results showing how the concentration of resazurin decreases with time for seven different films and the results showing how the initial reaction rate varies with  $L$ . Additionally, we have given an explanation as to why experimental results show a  $\frac{1}{L}$  dependence in the initial reaction rate.

For the parameter regime used to replicate the experimental results considered in this chapter, the validity of the QSSA is questionable. Hence, solving the full system for this particular regime would be advisable.

# Chapter 3

## Photocatalytic reactions occurring throughout a domain

For all the systems considered in this chapter we assume that reactions are taking place throughout the domain. This is significantly different to the model presented in the previous chapter, where a reaction was taking place exclusively at a photocatalyst surface. The work in this chapter was motivated by informal experimental results for a system where gas diffuses into a polymer film before reacting with a dye throughout the film. We propose a model which could be used to approximate such systems.

### 3.1 Simple model for photocatalytic reactions occurring throughout a domain

Ollis [67] considers a transparent organic substance distributed throughout a porous photocatalyst. A discrete model is proposed which splits the photocatalyst into five layers and assumes that the intensity of light able to reach each layer decreases as the depth of the layers increases. It is assumed that the intensity which reaches the first layer is equal to  $I_0$  and the intensity which reaches each subsequent layer

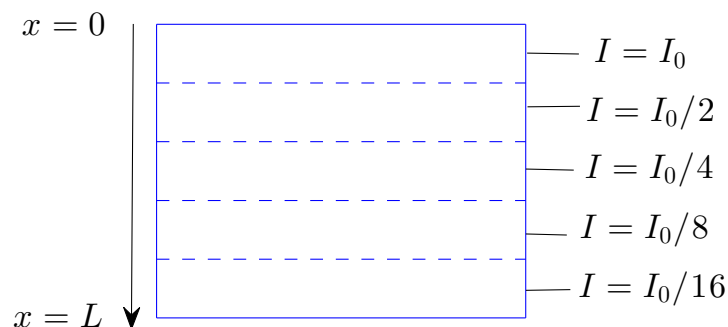


Figure 3.1: Diagram of the initial set-up of a discrete model proposed by Ollis [67] showing how  $I$  varies with  $x$ .

is halved (as shown in Figure 3.1). Treating each layer independently, Ollis calculates the mass of the reactant remaining in each layer and sums to find the total mass remaining. Ollis assumes a zero order rate constant  $k_0$  and effectively treats the photocatalyst layer as five separate layers where the zeroth-order rate constant is halved for each successive layer. Hence, letting  $M_i(t)$  ( $i = 1, \dots, 5$ ) represent the mass of reactant at time  $t$  in each layer, Ollis derived the following equations

$$\begin{aligned} \text{Layer 1 : } M_1(t) &= \frac{M_0}{5} - k_0 t \\ \text{Layer 2 : } M_2(t) &= \frac{M_0}{5} - \frac{k_0}{2} t \\ \text{Layer 3 : } M_3(t) &= \frac{M_0}{5} - \frac{k_0}{4} t \\ \text{Layer 4 : } M_4(t) &= \frac{M_0}{5} - \frac{k_0}{8} t \\ \text{Layer 5 : } M_5(t) &= \frac{M_0}{5} - \frac{k_0}{16} t, \end{aligned}$$

where  $M_0$  represents the initial total mass of reactant. From these five equations it is straightforward to calculate the total mass  $M_{tot}(t) = \sum_{i=1}^5 M_i(t)$  remaining

at any time. Figure 3.2 shows a replication of the plots presented by Ollis, demonstrating how  $\frac{M_{tot}}{M_0}$  varies with  $k_0t$  and how  $\ln\left(\frac{M_{tot}}{M_0}\right)$  varies with  $k_0t$ . Additionally, by plotting a best fit straight line in the second plot of Figure 3.2, we can see that the reduction of  $M_{tot}(t)$  is approximately first-order.

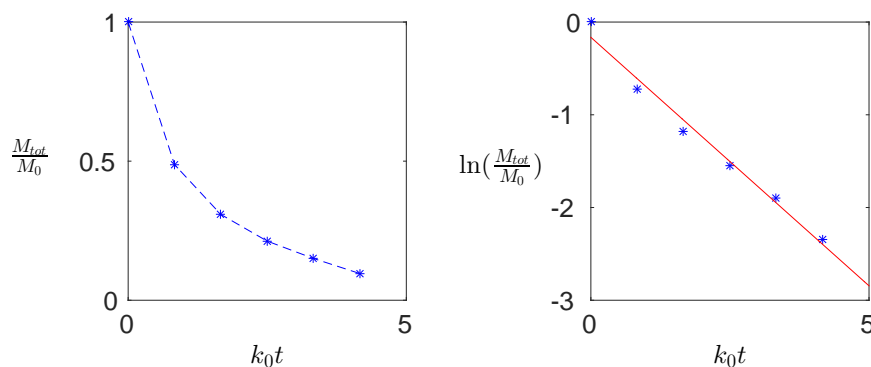


Figure 3.2: A replication of the results presented by Ollis [67] showing how  $\frac{M_{tot}}{M_0}$  varies with  $k_0t$  (left hand plot) and how  $\ln\left(\frac{M_{tot}}{M_0}\right)$  varies with  $k_0t$ , where the red line shows the best linear fit (right hand plot).

### 3.1.1 Experimental data

Allain *et al.* [8] show a first-order relationship between the absorbance of a stearic acid film and irradiation time. As the thickness of the film remains constant, assuming the Beer-Lambert law, the absorbance of the film must be proportional to the concentration of reactant [83]. Hence, the model proposed by Ollis can help rationalize the apparent first-order rate dependence. Figure 3.2 was produced using the model proposed by Ollis and is qualitatively very similar to the experimental data produced by Allain *et al.*

### 3.2 General model for photocatalytic reactions occurring throughout a domain

We initially consider a reactant distributed throughout a porous photocatalyst. In this case we expect the reactions to occur throughout the domain, as opposed to only taking place at the photocatalyst surface as in the systems considered in the previous chapter. We initially assume the photocatalyst is porous, hence, the absorbance by the photocatalyst will cause the intensity of light to depend on  $x$  (where  $x$  ranges from 0 to  $L$ , the thickness of the porous photocatalyst). At the surface of the photocatalyst ( $x = 0$ ) the intensity will equal  $I_0$ , and as  $x$  increases we expect the intensity to decrease as shown in Figure 3.3.

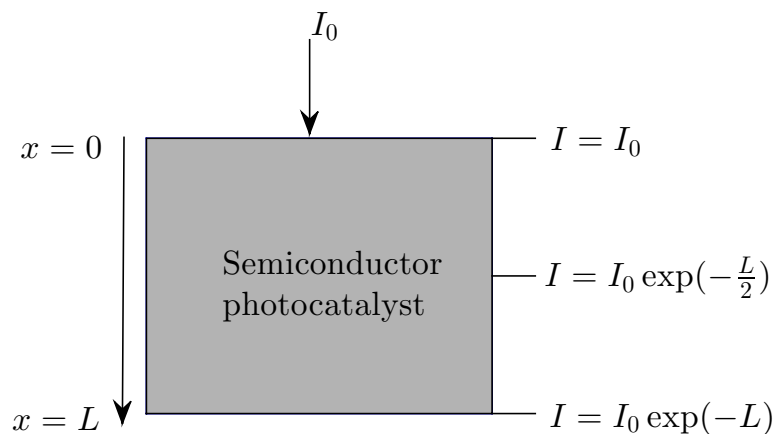


Figure 3.3: Diagram of the initial set-up showing how the light intensity varies with  $x$ .

Let  $u(x, t)$  represent the concentration of reactant at time  $t$  and position  $x$ . We assume that the light intensity is dependent on  $x$  but independent of  $t$ . Assuming the same intensity dependence proposed by Ollis [67], we have

$$I(x) = I_0 \exp(-\beta x),$$

where  $\beta$  is the absorbance coefficient.

We assume the same reaction mechanism considered in Section 2.1.1; however, in this case we have reactions taking place throughout the domain, hence

$$\frac{\partial u}{\partial t} = D \frac{\partial^2 u}{\partial x^2} - k_1 s_{tot} u + (k_1 u + k_{-1}) w, \quad (3.1)$$

$$\frac{\partial w}{\partial t} = k_1 u s_{tot} - (k_1 u + k_{-1} + k_2(x)) w, \quad (3.2)$$

$$\frac{\partial p}{\partial t} = k_2(x) w, \quad (3.3)$$

where  $u$  and  $w$  represent the free and absorbed concentrations of reactant throughout the layer and  $p$  represents the concentration of product being formed. As we assume that reaction sites are immobile, there will be no transport of  $w$  or  $p$  via diffusion. The parameters  $k_1$ ,  $k_{-1}$  and  $k_2$  are as previously defined, although in this case they are defined throughout the domain as opposed to being defined purely at the boundary. Recall from Section 2.1.1 that we defined our surface reaction constant as  $k_2 = k'_2 I$ . In this case we have

$$k_2(x) = k'_2 I(x) = k'_2 I_0 \exp(-\beta x),$$

where  $k'_2$  is a rate constant.

If we assume the QSSA is valid then we have

$$\frac{\partial u}{\partial t} = D \frac{\partial^2 u}{\partial x^2} - \frac{k_1 k_2(x) s_{tot} u}{k_1 u + k_{-1} + k_2(x)},$$

$$\frac{\partial p}{\partial t} = \frac{k_1 k_2(x) u s_{tot}}{k_1 u + k_{-1} + k_2(x)}.$$

### 3.2.1 Immobile reactant

We will now apply the model we introduced in Section 3.2 to the problem presented in Section 3.1. Ollis assumed that the reactant remains stationary and hence, we

will apply our model with the diffusion coefficient  $D$  equal to zero. In this case (3.1) will become

$$\frac{du}{dt} = -k_1 s_{tot} u + (k_1 u + k_{-1}) w, \quad (3.4)$$

and (3.2) and (3.3) will continue to define the evolution of  $w$  and  $p$ .

Prior to any reactions taking place we assume that the concentration of reactant  $u$  is uniformly distributed throughout the domain. We will refer to this pre-reaction concentration as  $u_0$ . As in Section 2.1.4, we assume that molecules of reactant are free to adsorb onto and desorb from the photocatalyst surface until the system is in equilibrium. We define the equilibrium concentrations of  $u$  and  $w$  as  $u_q$  and  $w_q$ , respectively. The method used to calculate  $u_q$  and  $w_q$  is similar to the method described in Section 2.1.4. At  $t = 0$  we assume that  $u(x, 0) = u_q$ ,  $w(x, 0) = w_q$  and  $p(x, 0) = 0$ . We will refer to this as the full system.

Alternatively, assuming the QSSA we have

$$\frac{\partial u}{\partial t} = -\frac{k_1 k_2(x) s_{tot} u}{k_1 u + k_{-1} + k_2(x)} = -\frac{k_2(x) s_{tot} u}{u + K_m}, \quad (3.5)$$

where  $K_m = \frac{k_{-1} + k_2}{k_1}$ . Rearranging (3.5) and integrating with respect to  $t$  gives

$$u + K_m \ln(u) = u_0 + K_m \ln(u_0) - k_2(x) s_{tot} t.$$

Hence, solving for  $u$  we have

$$u = K_m W \left( \frac{u_0}{K_m} \exp \left( \frac{u_0}{K_m} - \frac{k_2(x) s_{tot} t}{K_m} \right) \right). \quad (3.6)$$

Note the similarities between (3.6) and (2.26) [14]. The only major difference being that in this case  $u$  is defined throughout the domain, hence, (3.6) will have to be solved for all  $x$  where a solution is required.

To nondimensionalise the full system (3.1)-(3.3) we use a similar scaling to that presented in Section 3.4.3. However, in this case, diffusion does not occur and we

only consider one reactant, as opposed to two in Section 3.4.3. The same scaling is used to nondimensionalise the QSSA system.

### 3.2.2 Numerical method - Solving the full system

We discretise (3.2) using a forward Euler method to find an approximation of  $w$  at the forward time step. This allows us to discretise (3.4) using a Crank-Nicolson method to find an approximation of  $u$  at the forward time step. We can then correct our initial approximation of  $w$  at the forward time step by discretising (3.2) using a Crank-Nicolson method, which makes use of our approximation of  $u$  at the forward time step. Using the most recent approximation of  $w$  at the forward time step, (3.3) can be discretised using a Crank-Nicolson method to find an approximation of  $p$  at the forward time step.

### 3.2.3 Simulations

In this section we present simulations when both the full system and QSSA system are considered. When choosing which parameters to use  $L$ ,  $u_0$  and  $I_0$  were kept equal to one due to our choice of nondimensionalisation. Figures 3.4 - 3.8 show profiles of  $u(x, t)$  against  $x$  for 10 uniform times between 0 and  $T$ ,  $k_2(x)$  against  $x$ ,  $u_{ave}(t)$  (where  $u_{ave}(t) = \int_0^1 u(x, t) dx$ ) against  $t$  and  $\ln(u_{ave})$  against  $t$  (which will show if the reaction is first-order with respect to  $u$ ). The red line in the final plot of each figure shows the best linear fit of  $\ln(u_{ave})$  against  $t$ . We solve both the full system and the QSSA system for each set of parameters. When the full system is solved we show profiles of  $w(x, t)$  and the average concentration of  $w$  versus  $t$ . For all simulations presented, when solving the full system we have  $N = 100$  and  $NT = 5 \times 10^4$ .

Figures 3.4 and 3.5 show the results when we have  $k_1 = 100$ ,  $k_{-1} = 1$ ,  $k'_2 = 10$ ,  $\beta = 3.2$  and  $s_{tot} = 0.1$ . These parameters were chosen to replicate the results presented by Ollis. By choosing the  $k_1$  to  $k_{-1}$  ratio to be large relative to  $k_2(x)$ , we

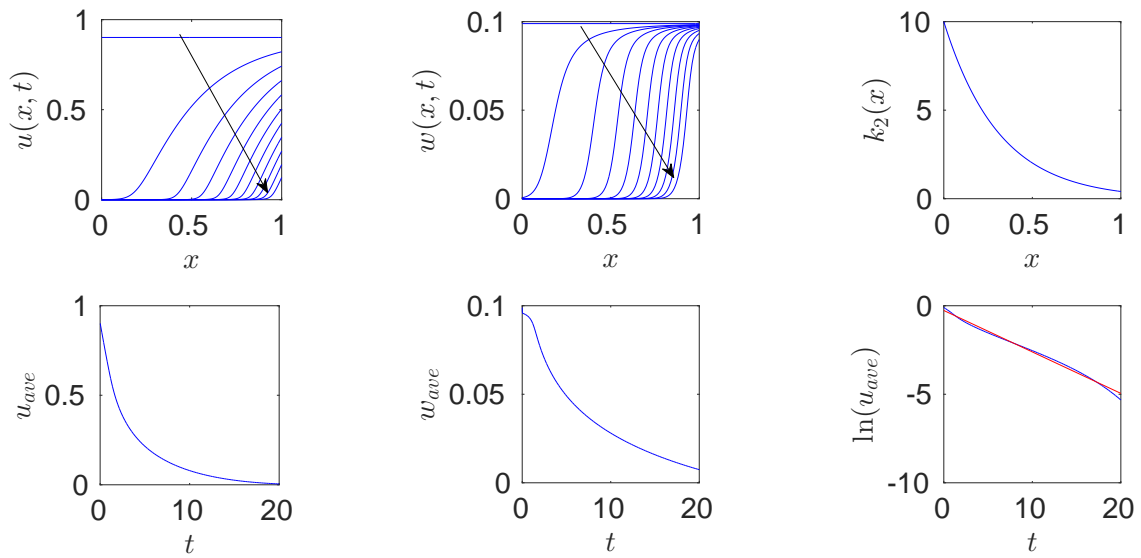


Figure 3.4: Results when the full system is solved with  $k_1 = 100$ ,  $k_{-1} = 1$ ,  $k'_2 = 10$ ,  $\beta = 3.2$  and  $s_{tot} = 0.1$ .

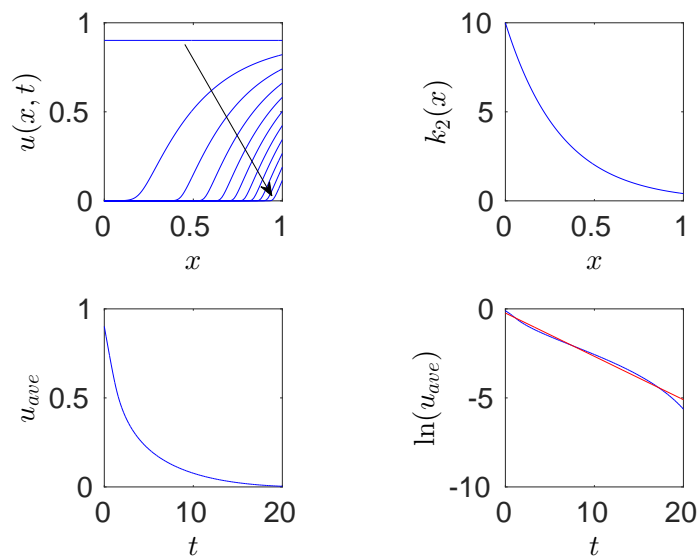


Figure 3.5: Results when the QSSA system is solved with  $k_1 = 100$ ,  $k_{-1} = 1$ ,  $k'_2 = 10$ ,  $\beta = 3.2$  and  $s_{tot} = 0.1$ .

have that the surface reaction will be rate-limiting as opposed to the adsorption process. Note that in this case, choosing  $s_{tot} = 0.1$  will limit the amount of reactant able to bind to reaction sites. Furthermore,  $\beta$  and  $k'_2$  are chosen to ensure that

$k_2(x)$  is much larger at  $x = 0$  than at  $x = 1$ . The chosen parameter regime is representative of all regimes where the adsorption/desorption process is not the rate-limiting step, and  $k_2(x)$  varies significantly from  $x = 0$  to  $x = 1$ . Figure 3.4 shows the results when the full system is solved and Figure 3.5 shows the results when the QSSA system is solved. The first plot of both figures shows that at  $x = 0$ ,  $u(x, t)$  decreases far more quickly than at  $x = 1$ ; this is not surprising when looking at how  $k_2(x)$  varies with  $x$ . In this case  $k_1$  is very large in comparison to  $k_{-1}$  and  $k_2$ , hence molecules of reactant will be very quickly adsorbed onto reaction sites. Once the reactant is adsorbed onto sites, the rate of reaction will be limited by the reaction rate  $k_2$ , which is why we see a significant difference between the overall reaction rate at  $x = 0$  and  $x = 1$ .

Using (2.18) we can calculate  $\epsilon$  for each set of parameters used. For the first set of parameters used (Figures 3.4 and 3.5),  $\epsilon(x)$  ranges from 0.099 to 0.11, where  $\epsilon$  is dependent on  $x$  due to  $k_2$  varying with  $x$ . Hence, in this parameter regime, we would expect the QSSA to be an accurate approximation. Our results show that there is very little difference between the two sets of results to plotting accuracy.

The parameters used during this simulation were chosen to replicate the discrete prediction made by Ollis (as shown in Figure 3.2). As the QSSA is valid for this regime we must have that (3.5) is a valid approximation. As  $k_1 u$  is significantly larger than  $k_{-1}$  and  $k_2(x)$  throughout the domain for the majority of the reaction, we have, from (3.5), that

$$\frac{\partial u}{\partial t} \approx -k_2(x) s_{tot} u = -k_2' I_0 s_{tot} \exp(-\beta x) u.$$

Hence, the reduction of  $u$  is controlled by  $k_2(x)$ , where  $k_2(x)$  decreases as  $x$  increases. For this set of parameters we have demonstrated that our continuous model predicts the same first-order reduction of the total amount of  $u$  as the discrete model proposed by Ollis.

Figures 3.6 and 3.7 show the results when we are in an adsorption-limited

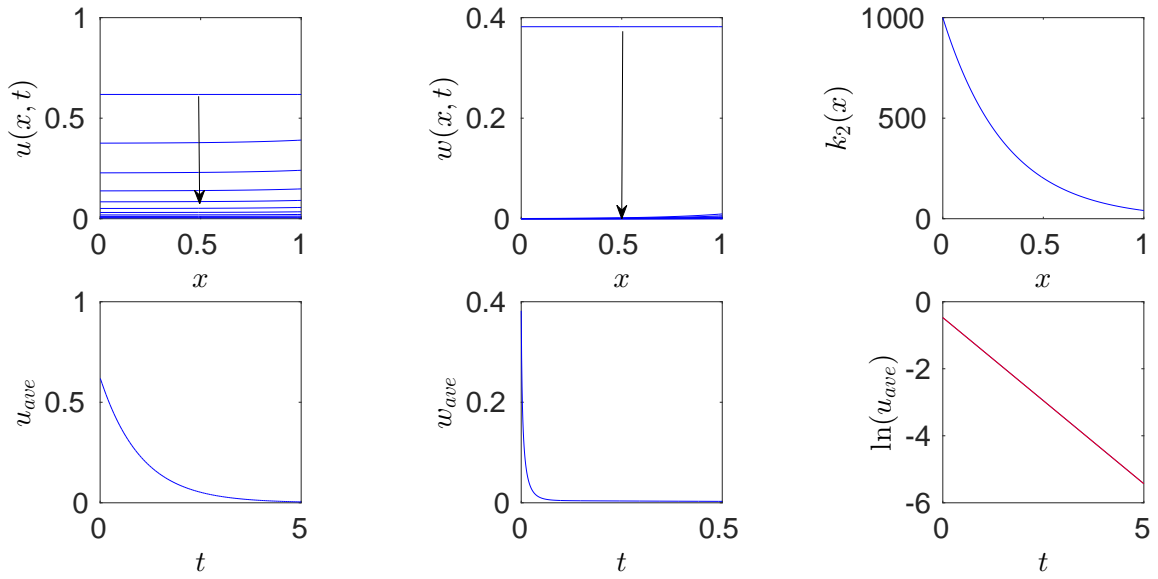


Figure 3.6: Results when the full system is solved with  $k_1 = 1, k_{-1} = 1, k'_2 = 1000, \beta = 3.2$  and  $s_{tot} = 1$ .

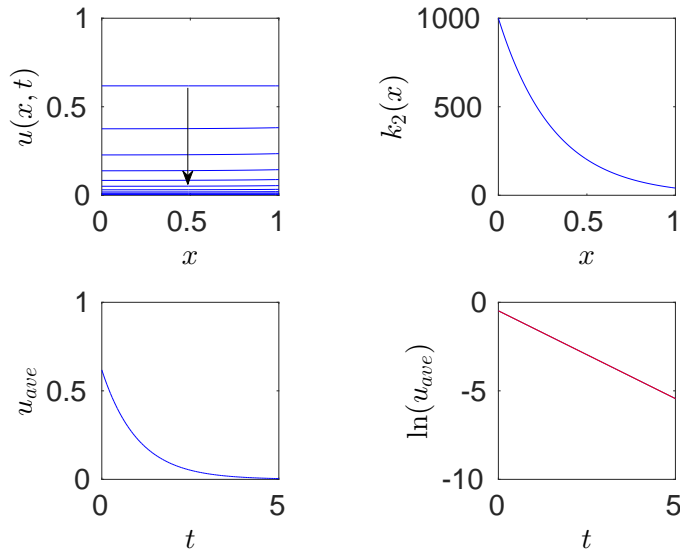


Figure 3.7: Results when the QSSA system is solved with  $k_1 = 1, k_{-1} = 1, k'_2 = 1000, \beta = 3.2$  and  $s_{tot} = 1$ .

regime, with  $k_1 = 1, k_{-1} = 1, k'_2 = 1000, \beta = 3.2$  and  $s_{tot} = 1$ . These parameters were chosen such that  $k_2(x)$  is large enough throughout the domain, relative to the adsorption/desorption rate constants, to ensure that the adsorption process is

rate-limiting throughout the domain. Note that, as  $s_{tot}$  is relatively large, it will not play a role in determining the overall reaction rate. The following results are representative of all parameter regimes where  $k_2(x)$  is much larger than  $k_1$  and  $k_{-1}$  throughout the domain and is not sensitive to small changes in parameters. Figure 3.6 shows the results when the full system is solved and Figure 3.7 shows the results when the QSSA system is solved. Note that the fifth plot of Figure 3.6 shows  $w_{ave}$  against  $t$  for  $t$  ranging from 0 to 0.5 as opposed to from 0 to 5. This was done to demonstrate how quickly  $w_{ave}$  approaches zero.

The first plot of both figures shows that the profiles of  $u$  are almost flat throughout the simulation. When the full system is solved,  $w(x, t)$  decreases rapidly and remains zero for the remainder of the simulation. This is due to  $k_2(x)$  being far larger than both  $k_1$  and  $k_{-1}$  throughout the domain. In this regime, the fact that  $k_2(x)$  decreases as  $x$  increases, does not play a role in the overall reaction rate. This is because it is the adsorption process which slows down the overall reaction.

For the second set of parameters (Figures 3.6 and 3.7)  $\epsilon(x)$  ranges from  $1.0 \times 10^{-3}$  to  $2.4 \times 10^{-2}$ , and hence, we would expect the QSSA to be an accurate approximation. As in the last case, our results show almost identical results when the QSSA is and is not used. The final plot, of each figure, shows a very convincing first-order fit of  $u_{ave}$  with respect to time.

As the QSSA is valid for this regime, (3.5) is a valid approximation. As  $k_2(x)$  is significantly larger than  $k_1u$  and  $k_{-1}$  throughout the domain for the entirety of the reaction, from (3.5) we have that

$$\frac{du}{dt} \approx -k_1us_{tot}.$$

Hence, the overall reduction of  $u$  is first-order, with respect to  $u$ . We have demonstrated that even in a completely different regime to the previous case, we still predict a first-order reduction of  $u$ .

Figures 3.8 and 3.9 show the results when we have  $k_1 = 5, k_{-1} = 1, k'_2 = 0.1,$

$\beta = 3.2$  and  $s_{tot} = 1$ . These parameters were chosen to ensure that  $\epsilon(x)$  is large for all  $x$  considered. The following plots are merely one example of an instance where the QSSA is not valid, there are numerous other regimes which show similar results. Figure 3.8 shows the results when the full system is solved and Figure 3.9 shows the results when the QSSA system is solved. The results are qualitatively similar to the case shown in Figures 3.4 and 3.5 in that the reactions taking place at  $x = 0$  are far quicker than the reactions taking place at  $x = 1$ . Similar to the previous case, the plots of  $\ln(u_{ave})$  versus  $t$  show a fairly convincing first-order fit. However, in this case there is a distinct difference between the full system results and the QSSA system results. Although qualitatively the results are similar, quantitatively they are significantly different. This is demonstrated in Figure 3.10, which shows how  $u_{ave}$  differs when the full and QSSA systems are solved. The  $\epsilon(x)$  values corresponding to this set of parameters range from 1.73 to 1.79.

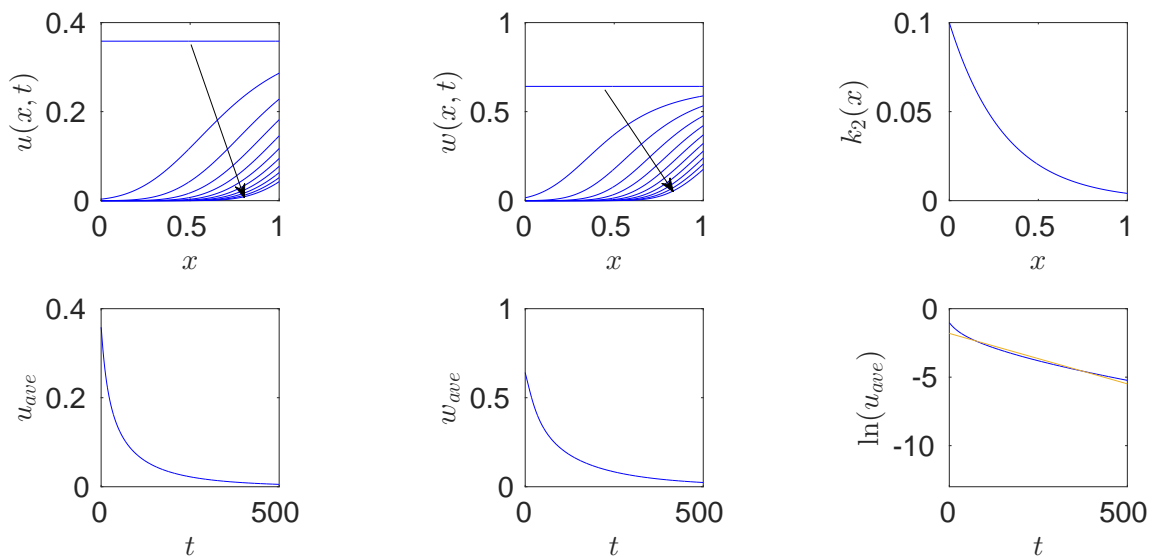


Figure 3.8: Results when the full system is solved with  $k_1 = 5$ ,  $k_{-1} = 1$ ,  $k'_2 = 0.1$ ,  $\beta = 3.2$  and  $s_{tot} = 1$ .

We have shown that the general model we introduced in Section 3.2 can be applied to the problem described in Section 3.1. Our model agrees with the findings made by Ollis (which agreed with experimental results) that the reduction of  $u$

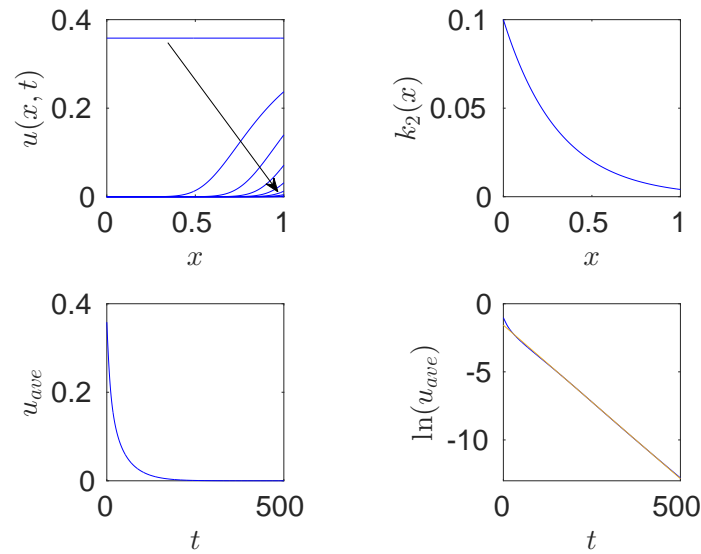


Figure 3.9: Results when the QSSA system is solved with  $k_1 = 5$ ,  $k_{-1} = 1$ ,  $k'_2 = 0.1$ ,  $\beta = 3.2$  and  $s_{tot} = 1$ .

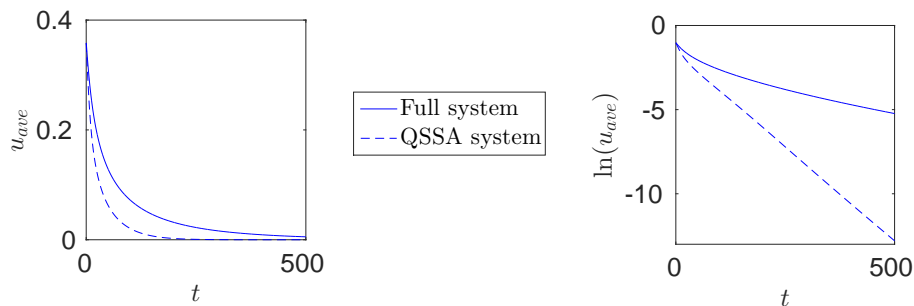


Figure 3.10: Comparison of  $u_{ave}$  versus  $t$  when the full system and QSSA system are solved with  $k_1 = 5$ ,  $k_{-1} = 1$ ,  $k'_2 = 0.1$ ,  $\beta = 3.2$  and  $s_{tot} = 1$ . In both plots the solid lines show the results when the full system is solved, and the dashed lines show the results when the QSSA system is solved.

is approximately first-order. This was the case for all three cases considered. However, our general model shows that there are different regimes where a first order reduction of the total amount of  $u$  occurs. By choosing parameters such that  $k_2(x)$  does not play a role in the overall reaction rate we were able to demonstrate that a fundamentally different regime can still predict a first-order reduction in concentration. Additionally, by choosing parameters such that  $\epsilon(x)$  was large, we

were able to show that the QSSA is not valid for all parameter regimes, meaning that, for certain regimes, solving the full system is necessary.

### 3.3 Oxygen diffusion in an indicator/polymer matrix

Modified-atmosphere packaging (MAP) is a method of packaging which decreases the oxygen content of a package by flushing the package volume with nitrogen or carbon dioxide. It is a common technology used by both the wholesale and retail food packaging industry due to its ability to prolong the shelf-life of foods by a factor of 3-4 times that in air [40].

Current methods of detecting and monitoring the oxygen concentration in food packaging are expensive and require the package to be destroyed [46]. Oxygen indicators placed inside a food package can monitor the presence of oxygen within the package. One possible solution is the use of UV or visible light activated redox indicators which change colour in the presence of oxygen. This gives a cheap and easy way of determining whether a food substance within a package has been exposed to oxygen since it has been packaged.

Although considerable research has focused on the development and characterisation of indicators, the embedding of such indicators has not been sufficiently examined [46]. Oxygen indicators are often contained in sachets or tablets which act as oxygen scavengers. However, oxygen scavengers have to be stored under anaerobic conditions and are relatively expensive. Integrating oxygen indicators into polymer foils could enable cheap, large-scale production of food packages which can detect the presence of oxygen.

Marek *et al.* [46] consider the use of oxygen indicators as a time-monitoring sensor. Such an indicator changes colour irreversibly once exposed to oxygen. This not only shows that a package has been damaged, and hence exposed to oxygen,

but shows how long a package has been exposed to oxygen. Oxygen passes through a diffusion channel within the package causing a colour change after a desired time (which will depend on the shelf-life of the product).

The proposed oxygen sensor is based on methylene blue (MB) and riboflavin. Both riboflavin and MB are dissolved in water where they both exist in an oxidised state, which we will refer to as  $Rb^+$  and  $MB^+$ , respectively. The overall system is green due to the colour of  $MB^+$  (blue) and  $Rb^+$  (yellow). The system is activated by UV-light irradiation. The riboflavin acts as an electron donor towards MB resulting in the colourless leuco methylene blue (LMB) and the oxidised form of riboflavin (which is yellow, as is the overall system at this stage). In the presence of oxygen, LMB is oxidised back to MB, which will result in a green colour of the overall system. Hence, the system will be yellow if no oxygen is present in the system and green if oxygen is present.

### 3.3.1 A model for reaction-diffusion kinetics in a polymer film

Marek *et al.* [46] present a model describing the simultaneous diffusion of oxygen and reaction between oxygen and LMB. Oxygen diffusion coefficients and kinetic parameters were determined experimentally. Marek *et al.* were able to demonstrate that their proposed model could accurately replicate experimental results. In this section we will present a numerical method which could be used to solve the system of equations arising from the model proposed by Marek *et al.* After demonstrating that our proposed method can accurately replicate the results presented by Marek *et al.*, we perform simulations to determine how the initial reaction rate will vary with film thickness for this particular system.

It is assumed that the polymer film has a rectangular geometry, as shown in Figure 3.11, with oxygen diffusing into the system at both sides. Hence, it is assumed that the system is symmetrical which allows us to consider only half the

total domain.

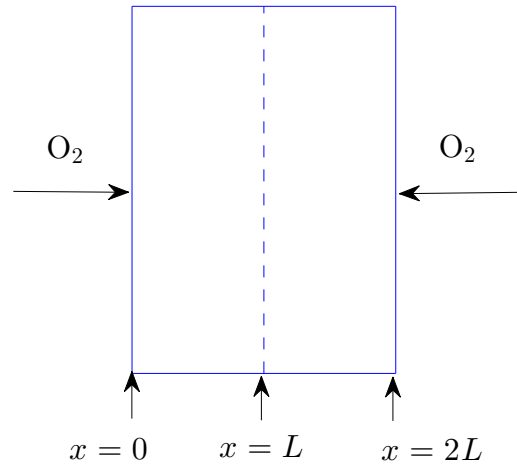


Figure 3.11: Model of oxygen diffusing into a water-swollen polymer film from two sides. The oxygen can penetrate the film only from the surface in  $x$ -direction at  $x = 0$  and  $x = 2L$  [46].

Marek *et al.* [46] have proposed the following model which describes the consumption of diffusing oxygen by the oxidation of LMB. By Fick's second law, the change in oxygen concentration with respect to time is given by

$$\frac{\partial[O_2]}{\partial t} = D \frac{\partial^2[O_2]}{\partial x^2} - k[O_2]^p[LMB]^m,$$

where  $x$  represents position,  $t$  represents time,  $[O_2]$  represents the concentration of  $O_2$ ,  $[LMB]$  represents the concentration of LMB,  $k$  represents a reaction rate constant,  $D$  represents the diffusion coefficient of oxygen in a polymer matrix,  $p$  is the order of reaction with respect to oxygen concentration and  $m$  is the order of reaction with respect to LMB concentration. When considering the change in concentration of LMB and MB with respect to time, it is assumed that neither

diffuse throughout the domain, hence we have

$$\frac{\partial[\text{LMB}]}{\partial t} = -k[\text{O}_2]^p[\text{LMB}]^m = -\frac{\partial[\text{MB}]}{\partial t},$$

where  $[\text{MB}]$  represents the concentration of MB. In this case MB is the product being formed by the system.

Initially, it is assumed that the oxygen concentration in the film is zero everywhere except at the film surface where the concentration remains equal to  $[\text{O}_2]_0$ . Hence, at  $x = 0$  we have

$$[\text{O}_2](0, t) = [\text{O}_2]_0.$$

At the middle of the film, a no-flux boundary condition is assumed due to the system being symmetric. Hence, at  $x = L$  (where  $L$  represents half of the total film thickness) we have

$$\frac{\partial[\text{O}_2]}{\partial x}(L, t) = 0.$$

It is also assumed that initially  $[\text{LMB}](x, 0) = [\text{LMB}]_0$  everywhere except at  $x = 0$ , where any LMB has been completely converted to MB. Similarly,  $[\text{MB}](x, 0) = 0$  everywhere except at  $x = 0$  where  $[\text{MB}](0, 0) = [\text{LMB}]_0$ .

The system is therefore modelled by the following equations

$$\left\{ \begin{array}{l} \frac{\partial[\text{O}_2]}{\partial t} = D \frac{\partial^2[\text{O}_2]}{\partial x^2} - k[\text{O}_2]^p[\text{LMB}]^m, \quad 0 < x < L, \\ [\text{O}_2](0, t) = [\text{O}_2]_0, \\ \frac{\partial[\text{O}_2]}{\partial x}(L, t) = 0, \\ [\text{O}_2](x, 0) = 0, \end{array} \right. \quad 0 < x \leq L, \quad (3.7)$$

$$\left\{ \begin{array}{l} \frac{\partial[\text{LMB}]}{\partial t} = -k[\text{O}_2]^p[\text{LMB}]^m, \quad 0 \leq x \leq L, \\ [\text{LMB}](0, 0) = 0, \\ [\text{LMB}](x, 0) = [\text{LMB}]_0, \quad 0 < x \leq L, \end{array} \right. \quad (3.8)$$

$$\left\{ \begin{array}{l} \frac{\partial[\text{MB}]}{\partial t} = k[\text{O}_2]^p[\text{LMB}]^m, \quad 0 \leq x \leq L, \\ [\text{MB}](0, 0) = [\text{MB}]_0, \\ [\text{MB}](x, 0) = 0, \quad 0 < x \leq L. \end{array} \right. \quad (3.9)$$

As  $[\text{MB}]$  is only present in (3.9), it does not play a role in the evolution of  $[\text{O}_2]$  or  $[\text{LMB}]$ .

This system is similar to the model introduced in Section 3.2 in that reactions are taking place throughout the domain. However, in this case we do not have adsorption/desorption taking place and we now have two reactants which are required to react together to form products. The reaction is also non-linear due to  $[\text{O}_2]$  and  $[\text{LMB}]$  being raised to the power of  $p$  and  $m$ , respectively.

### 3.3.2 Nondimensionalisation

We nondimensionalise (3.7), (3.8) and (3.9) using the following scaling:

$$\hat{t} = \frac{t}{T}, \quad \hat{x} = \frac{x}{L}, \quad u = \frac{[\text{O}_2]}{[\text{LMB}]_0},$$

$$w = \frac{[\text{LMB}]}{[\text{LMB}]_0}, \quad v = \frac{[\text{MB}]}{[\text{LMB}]_0}, \quad \hat{k} = T \frac{[\text{LMB}]_0^{p+m}}{[\text{LMB}]_0} k,$$

$$u_0 = \frac{[\text{O}_2]_0}{[\text{LMB}]_0}, \quad v_0 = \frac{[\text{MB}]_0}{[\text{LMB}]_0},$$

where we let the characteristic time be  $T = \frac{L^2}{D}$ . Hence, our nondimensional version of the system is given by

$$\left\{ \begin{array}{l} \frac{\partial u}{\partial t} = \frac{\partial^2 u}{\partial x^2} - ku^p w^m, \quad 0 < x < 1, \\ u(0, t) = u_0, \\ \frac{\partial u}{\partial x}(1, t) = 0, \\ u(x, 0) = 0, \quad 0 < x \leq 1, \end{array} \right. \quad (3.10)$$

$$\left\{ \begin{array}{l} \frac{\partial w}{\partial t} = -ku^p w^m, \quad 0 \leq x \leq 1, \\ w(0, 0) = 0, \\ w(x, 0) = 1, \quad 0 < x \leq 1, \end{array} \right. \quad (3.11)$$

$$\left\{ \begin{array}{l} \frac{\partial v}{\partial t} = ku^p w^m, \quad 0 \leq x \leq 1, \\ v(0, 0) = v_0, \\ v(x, 0) = 0, \quad 0 < x \leq 1. \end{array} \right. \quad (3.12)$$

where the hat notation has been dropped for convenience. In the following section we will present the numerical method which is used to solve the nondimensional system (3.10) - (3.12). For all simulation results which we present in this chapter, the dimensional system is converted into a nondimensional form, before being converted back to the original dimensional form to present the results.

### 3.3.3 Numerical method

A finite difference method is used to find a numerical solution to the nondimensional system of equations (3.10) - (3.12). We will not include details of how  $v$  is approximated as it is very similar to how  $w$  is approximated. We divide the nondimensional spatial domain  $(0, 1)$  into  $N$  equal intervals, and the temporal domain  $(0, T)$  into  $NT$  equal intervals, with mesh spacings  $\Delta x$  and  $\Delta t$ , respectively. We will find approximations of  $u$  and  $w$  at all grid points, denoted by  $u_i^n = u(i\Delta x, n\Delta t)$  and  $w_i^n = w(i\Delta x, n\Delta t)$ , respectively.

We use a forward Euler method to discretise the non-linear reaction term of (3.10) and a Crank-Nicolson method to discretise the diffusion term, which gives

$$\frac{u_j^{n+1} - u_j^n}{\Delta t} = \frac{1}{2(\Delta x)^2} \left( (u_{j+1}^{n+1} - 2u_j^{n+1} + u_{j-1}^{n+1}) + (u_{j+1}^n - 2u_j^n + u_{j-1}^n) \right) - k(u_j^n)^p (w_j^n)^m,$$

for  $j = 0, 1, 2, \dots, N$  and  $n = 0, 1, 2, \dots, NT - 1$ . If we let  $V = \frac{\Delta t}{2(\Delta x)^2}$  we have

$$-Vu_{j+1}^{n+1} + (1 + 2V)u_j^{n+1} - Vu_{j-1}^{n+1} = Vu_{j+1}^n + (1 - 2V)u_j^n + Vu_{j-1}^n - \Delta t k(u_j^n)^p (w_j^n)^m. \quad (3.13)$$

At  $x = 0$  we have that  $u = u_0$ . At  $x = 1$ , i.e.  $x = x_N$ , we have a zero flux boundary condition. Using a central difference approximation at  $x = 1$  we discretise in the following way:

$$\frac{u_{N+1}^n - u_{N-1}^n}{2\Delta x} = 0 \quad \forall n,$$

where  $u_{N+1}^n$  is a ghost node which will not appear explicitly in the numerical scheme. Hence

$$u_{N+1}^n = u_{N-1}^n \quad \forall n. \quad (3.14)$$

Evaluating (3.13) with  $j = N$  and making use of (3.14) gives

$$(1 + 2V)u_N^{n+1} - 2Vu_{N-1}^{n+1} = (1 - 2V)u_N^n + 2Vu_{N-1}^n - \Delta t k(u_N^n)^p (w_N^n)^m. \quad (3.15)$$

Hence, using (3.13) and (3.15), we can solve for  $u^{[n+1,1]}$ , which represents our first approximation of  $u$  at the forward time step.

We now discretise (3.11) using a forward Euler method, which, after rearranging, gives

$$w_j^{n+1} = w_j^n - \Delta t k(u_j^n)^p (w_j^n)^m. \quad (3.16)$$

Hence, (3.16) can be solved for  $w_j^{n+1}$  at all grid points. We will refer to this initial estimate as  $w_j^{[n+1,1]}$ . As we now have estimates of  $u$  and  $w$  at the forward time step, we discretise both (3.10) and (3.11) using a Crank-Nicolson method. Using  $u^{[n+1,1]}$  and  $w^{[n+1,1]}$  as an approximation of  $u^{n+1}$  and  $w^{n+1}$ , respectively, a revised discretisation of (3.10) is given by

$$\begin{aligned} -Vu_{j+1}^{n+1} + (1+2V)u_j^{n+1} - Vu_{j-1}^{n+1} &= Vu_{j+1}^n + (1-2V)u_j^n + Vu_{j-1}^n \\ &\quad - \frac{\Delta t}{2} \left( k(u_j^n)^p (w_j^n)^m + k(u_j^{[n+1,1]})^p (w_j^{[n+1,1]})^m \right). \end{aligned} \quad (3.17)$$

Similarly, a revised discretisation of (3.15) is given by

$$\begin{aligned} (1+2V)u_N^{n+1} - 2Vu_{N-1}^{n+1} &= (1-2V)u_N^n + 2Vu_{N-1}^n - \\ &\quad \frac{\Delta t}{2} \left( k(u_N^n)^p (w_N^n)^m + k(u_N^{[n+1,1]})^p (w_N^{[n+1,1]})^m \right). \end{aligned} \quad (3.18)$$

We now solve (3.17) and (3.18) for an improved estimate of  $u^{n+1}$ , denoted by  $u^{[n+1,2]}$ . Similarly, a revised discretisation of (3.8) is given by

$$w_j^{n+1} = w_j^n - \frac{\Delta t}{2} \left( k(u_j^n)^p (w_j^n)^m + k(u_j^{[n+1,2]})^p (w_j^{[n+1,1]})^m \right), \quad (3.19)$$

which can be solved for an improved estimate of  $w^{n+1}$ , denoted by  $w^{[n+1,2]}$ .

### 3.3.3.1 Accuracy of the numerical scheme

We will now perform convergence tests using the method described in the previous section. Our approach of calculating a reference solution and using this reference solution to estimate the error in other calculations is the same as the approach outlined in Section 2.1.8.5. We will consider two methods of solving the system of equations (3.7) and (3.8).

- Method 1 - Initially, solve (3.13) and (3.15) for  $u^{[n+1,1]}$  and solve (3.16) for  $w_j^{[n+1,1]}$ . Using these initial estimates, calculate  $u^{[n+1,2]}$  using (3.17) and (3.18) and then calculate  $w^{[n+1,2]}$  using (3.19).
- Method 2 - Solve (3.13) and (3.15) for  $u^{[n+1,1]}$  and solve (3.16) for  $w_j^{[n+1,1]}$ .

For each number of time steps chosen, and for each method, we compared  $u$  and  $w$  at the final time step with the reference solution (calculated using Method 1) at the final time step. The error in  $u$  is defined using (2.52), and the error in  $w$  is defined in the same way.

For the convergence tests the following dimensional model parameters were used:  $L = 100 \mu\text{m}$ ,  $[\text{O}_2]_0 = 0.062 \text{ mol m}^{-3}$ ,  $[\text{LMB}]_0 = 0.31 \text{ mol m}^{-3}$ ,  $D = 1.35 \times 10^{-11} \text{ m}^2\text{s}^{-1}$ ,  $k = 0.45 \text{ mol}^{-1}\text{s}^{-1}$ ,  $p = 1.2$  and  $m = 0.8$ . These were the parameters used in simulations carried out by Marek [46]. Note that the parameters were converted into dimensionless form using the scalings given in Section 3.3.2 before performing any convergence tests. For the convergence tests we used  $T = 300$  throughout.

Figures 3.12 and 3.13 show the temporal convergence results when we apply Method 1 with  $1.28 \times 10^5$  time steps for our most accurate reference solution. To test the accuracy of our scheme, a range of time steps were used varying from 1600 to  $1.28 \times 10^4$ . For all simulations in this test,  $N = 200$ . The results show that, for both  $u$  and  $w$ , Method 1 is second-order convergent where as Method 2 is only first-order.

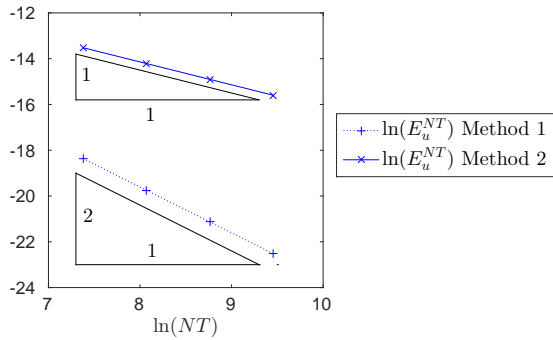


Figure 3.12: Temporal convergence results of  $u$  using Methods 1 and 2.

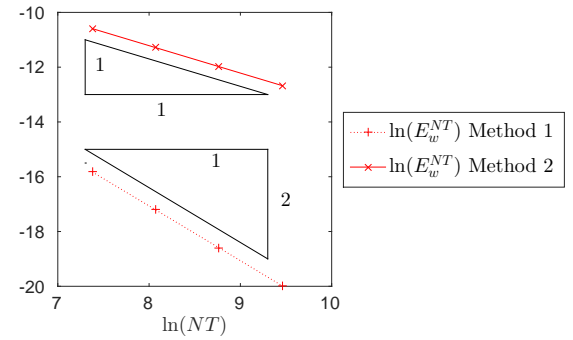


Figure 3.13: Temporal convergence results of  $w$  using Methods 1 and 2.

Figures 3.14 and 3.15 show the spatial convergence results when we apply Method 1 with  $N = 500$  to find our reference solution. To test the accuracy of our scheme,  $N$  was varied from  $N = 10$  to  $N = 80$ . For all simulations in this test,  $NT = 1.28 \times 10^5$ . The results show that, for both  $u$  and  $w$ , Method 1 and 2 are both second-order convergent in space.

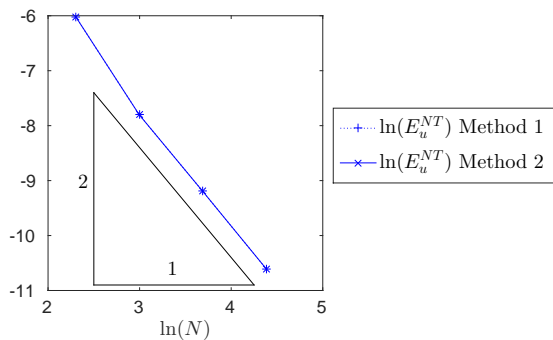


Figure 3.14: Spatial convergence results of  $u$  using Methods 1 and 2.

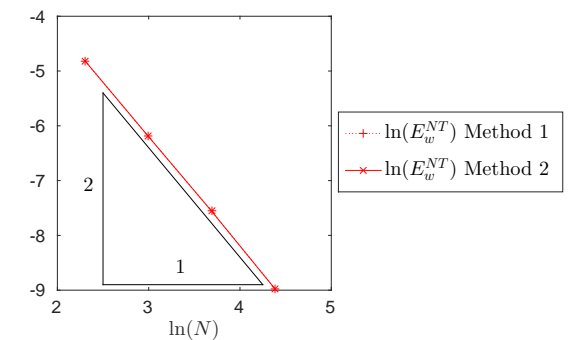


Figure 3.15: Spatial convergence results of  $w$  using Methods 1 and 2.

Similar to the QSSA system considered in the previous Chapter, we have to solve for both  $u$  and  $w$  at least twice at each time step. Ideally we would only be solving once each time step, however, by recalculating  $u$  and  $w$  once at each time step we have demonstrated that Method 1 is second-order convergent in time and space.

### 3.3.4 Numerical simulations

#### 3.3.4.1 Replicating existing results

To compare our predictions with those of Marek *et al.* [46] the model parameters used were as follows:  $L = 100 \mu\text{m}$ ,  $[\text{O}_2]_0 = 0.062 \text{ mol m}^{-3}$ ,  $[\text{LMB}]_0 = 0.31 \text{ mol m}^{-3}$ ,  $D = 1.35 \times 10^{-11} \text{ m}^2\text{s}^{-1}$ ,  $k = 0.45 \text{ mol}^{-1}\text{s}^{-1}$ ,  $p = 1.2$  and  $m = 0.8$ . These quantities were obtained from a combination of experiments and modelling. All further simulations, along with the convergence tests presented in the previous section, were performed using these parameters unless specifically stated otherwise. For all simulations, the scaling covered in Section 3.3.2 was used to convert dimensional parameters into a nondimensional form. As before, all results presented are in a dimensional form. For the simulation results presented in Sections 3.3.4 and 3.3.4.2 Method 1 was used with  $N = 100$  and  $NT = 1 \times 10^4$ .

Figure 3.16 shows concentrations of LMB and  $\text{O}_2$  at ten uniform positions (ranging from  $x = 10 \mu\text{m}$  to  $x = 100 \mu\text{m}$ ), where the arrow indicates the smallest  $x$  values ranging to the largest. Our numerical results are identical to those of Marek *et al.* [46] to plotting accuracy. It is evident that the concentration of LMB decreases far more quickly close to the film surface than in the middle of the film. Similarly, the concentration of  $\text{O}_2$  increases far more rapidly at the film surface than in the middle of the film. This is due to there being a constant supply of  $\text{O}_2$  at the surface. Hence, in the middle of the film the increase in  $\text{O}_2$  is slowed down by the need for molecules to diffuse across the film. Similarly, the decrease in LMB is caused by a reaction between LMB and  $\text{O}_2$ . Hence, as the supply of  $\text{O}_2$  is limited in the middle of the film, the decrease in concentration of LMB will also be limited. It is clear from the plots presented that the diffusion of  $\text{O}_2$  determines, at least to some extent, the overall rate of conversion of LMB to MB.

Marek *et al.* [46] have shown that their model can predict numerous experimental results very well. By showing that we can replicate the predictions made by Marek *et al.* we are in a position where the proposed model can be used to

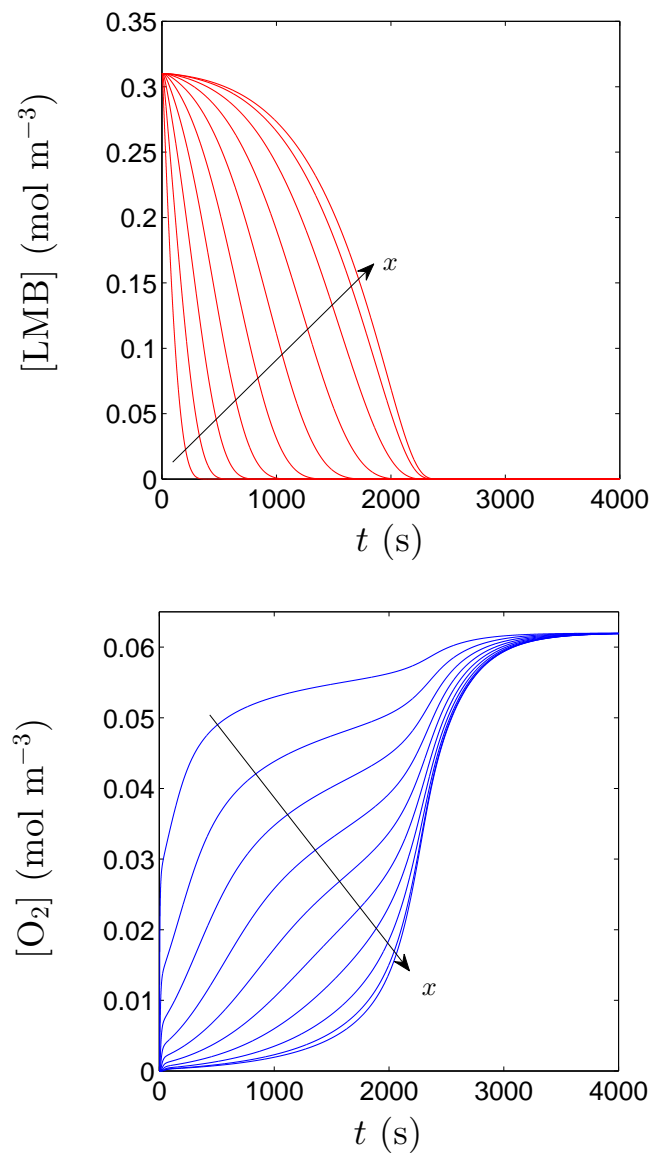


Figure 3.16: Concentration profiles of LMB and  $O_2$  plotted at ten uniform positions ranging from  $x = 10 \mu\text{m}$  to  $x = 100 \mu\text{m}$ .

make further predictions.

### 3.3.4.2 Further results

In addition to the plots shown in Figure 3.16, the following figures were produced using the same parameters. Figure 3.17 shows concentration profiles of  $O_2$ , LMB and MB at 20 different times ranging from  $t = 200$  s to  $t = 4000$  s. The arrows

indicate how the profiles change with time. It appears that the diffusion process limits the progress of the overall reaction, as the lack of oxygen able to transport through the layer causes the reaction to happen far more quickly at  $x = 0$  than at  $x = L$ .

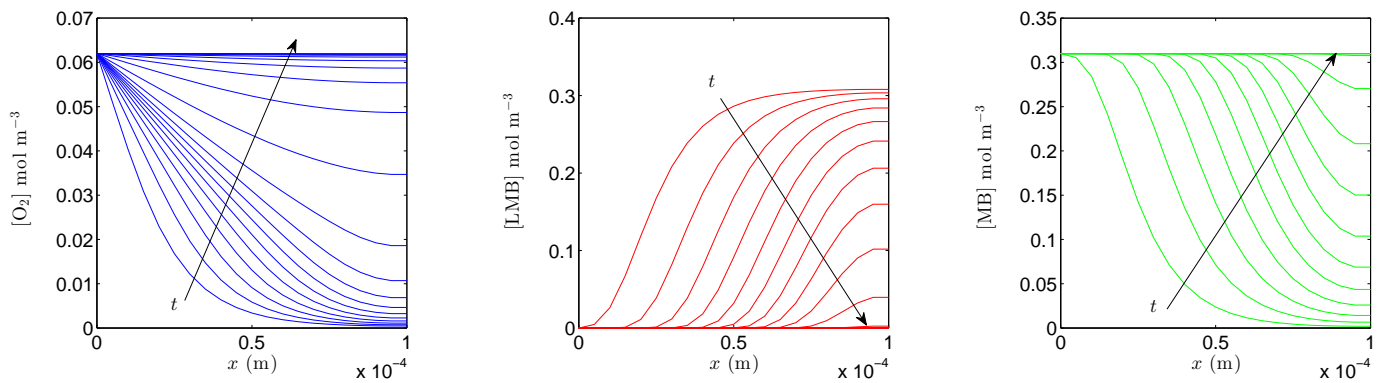


Figure 3.17: Evolution of concentration profiles of  $O_2$ , LMB and MB in equal time increments from  $t = 200$  s to  $t = 4000$  s.

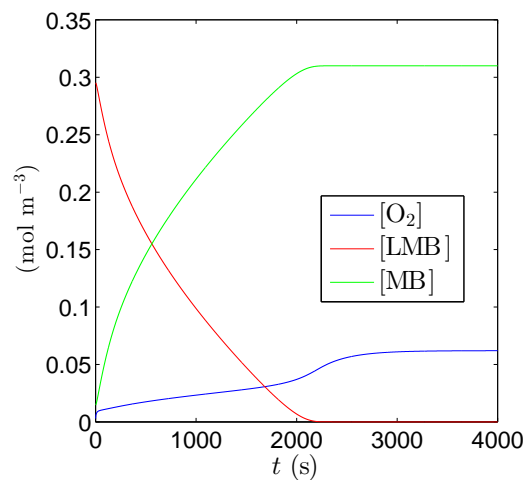


Figure 3.18: Average concentrations of  $O_2$ , LMB and MB against time produced using the same parameters as Figure 3.16.

Figure 3.18 shows the average concentrations of  $O_2$ , LMB and MB plotted against time. We can see that the reaction is almost complete just after  $t = 2000$  s once LMB has been completely converted into MB. There is a slight increase in  $O_2$

concentration after the conversion is complete which is due to oxygen continuing to diffuse into the film until it is completely saturated.

### 3.3.4.3 Experimenting with film thickness

One aspect of this system which was not investigated by Marek *et al.* [46] was the influence that film thickness has on the initial reaction rate. Like the previous model in Chapter 2, there are several different parameter regimes which will display typical behaviour. For example, if the rate of diffusion of oxygen throughout the domain is slow in comparison to the rate of the reaction between  $O_2$  and LMB we say the overall process is diffusion-limited. Alternatively, if the overall reaction is slowed down by the reaction between  $O_2$  and LMB we say the overall process is reaction-limited.

As before, we expect that in a diffusion-limited regime the initial reaction rate,  $R_i$  will be inversely proportional to the film thickness squared, i.e.,

$$R_i \propto \frac{1}{L^2},$$

where we define  $R_i$  to be the rate at which the average concentration of product is increasing, i.e.

$$R_i = \left. \frac{\partial [MB]_{ave}}{\partial t} \right|_{t=0},$$

where  $[MB]_{ave}(t) = \int_0^L [MB](x, t) dx$ . Similarly, within an entirely reaction-limited regime we expect the initial rate to be independent of film thickness.

During experiments carried out by Marek *et al.* [46] the film thickness used was  $200 \mu\text{m}$  (equivalent to  $L = 10^{-4}$  m when performing simulations). We carried out numerical simulations using  $L$  values ranging from  $10^{-6}$  m to  $10^{-3}$  m (corresponding to  $\ln(L)$  ranging from -13.8 to -6.5). We are mainly interested in the initial reaction rate  $R_i$  of the increase of the average concentration of MB. There are a number of ways of estimating  $R_i$  from simulation data. One common method is to fit a straight line through data points close to  $t = 0$  and measure the gradient of

the line. We expect the average concentration of MB to tend to a specific value,  $[\text{MB}]_{max}$ . This is due to there being a limited amount of LMB which can be converted into MB. We measure how long it takes for 10% of the final concentration of MB to be formed and fit a straight line through the data corresponding to this period of time. The gradient of this line gives an approximation to  $R_i$ . Note that we choose to use 10% in this case because the production of MB (or destruction of LMB) does not happen at a constant rate for the range of parameters which we are considering.

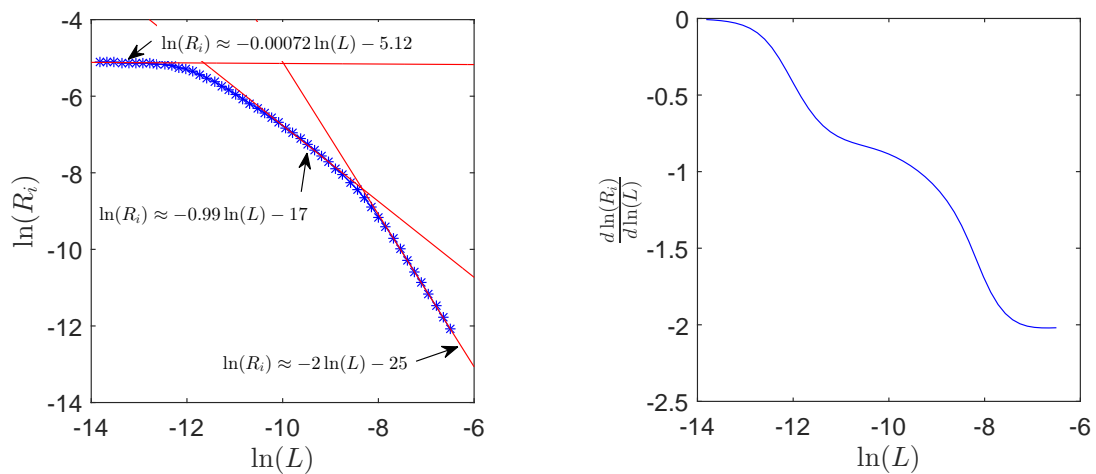


Figure 3.19: Plot of  $\ln(R_i)$  against  $\ln(L)$  with straight lines fitted through different sets of data (LHS) and a plot showing the derivative of  $\ln(R_i)$  with respect to  $\ln(L)$  (RHS) with  $L$  ranging from  $L = 10^{-6}$  m to  $L = 10^{-3}$  m.

Figure 3.19 shows simulation results when a wide range of  $L$  values are used. The left hand plot shows  $\ln(R_i)$  plotted against  $\ln(L)$ . For the three distinct regimes, a best fit straight line is fitted to selected data points. The gradients of the three lines show that there are three regimes where  $R_i \propto \frac{1}{L^a}$  and  $a = 0, 1$  and  $2$ . The second plot of Figure 3.19 shows the derivative of  $\ln(R_i)$  with respect to  $\ln(L)$  plotted against  $\ln(L)$ . From this plot we can see the two extreme cases very clearly, where minus the derivative of  $\ln(R_i)$  is approximately equal to zero for  $L$  small enough and equal to approximately two for  $L$  large enough. There also appears to be an intermediate regime where minus the derivative is approximately

equal to one, corresponding to an initial reaction rate inversely proportional to film thickness.

The left hand plot of Figure 3.19 shows that, for the extreme cases, we see the expected kinetics. For very small  $L$  we see that  $R_i$  is approximately constant. In this regime, we have that diffusion of oxygen will be very quick relative to the reactions taking place. Hence, throughout the regime, reactions will be occurring at the same rate throughout the domain. As  $L$  is further decreased, the rate at which reactions are taking place at each point in the domain will remain the same, however, as  $L$  is decreasing there will be less space available for reactions to take place at. Hence, we find that, the rate of production of MB is independent of  $L$ , assuming  $L$  is small enough. For large values of  $L$ ,  $R_i$  is approximately inversely proportional to  $L^2$ . This is typical of a diffusion-limited regime. Additionally, similar to the resazurin case considered in Section 2.3.2, there appears to be a region where  $R_i$  is inversely proportional to  $L$ .

To further investigate the intermediate region, where we have that  $R_i$  is approximately inversely proportional to  $L$ , we consider three films;  $L = 0.65 \times 10^{-4}$  m,  $L = 1.25 \times 10^{-4}$  m and  $L = 2.5 \times 10^{-4}$  m. The three films correspond to  $\ln(L)$  ranging from -9.68 to -8.29, which is part of the approximate region where  $R_i$  is inversely proportional to  $L$ . Figure 3.20 shows the average concentration of MB divided by the maximum average concentration against  $t$  for the three films considered. The figure shows that by increasing the film thickness it takes longer for the average concentration to decrease. Figure 3.21 shows the total amount of MB plotted against  $t$  for the same three films as Figure 3.20. This figure shows that, for the three films studied, the rate at which the total amount of MB is increasing is approximately independent of  $L$ . Recall that the rate at which MB is being produced is the same as the rate that LMB is being destroyed. Hence, similar to the resazurin case discussed in the previous chapter, the apparent  $\frac{1}{L}$  dependence is due to the fact that the rate at which the total amount of LMB is being destroyed remains constant, but by increasing  $L$  the total amount of LMB in the domain will

increase. We have a situation where there is a finite amount of LMB which can be converted into MB at any one time, so by increasing the total amount of LMB in the system the rate at which the average concentration of LMB is decreasing will have to decrease as  $L$  is increased.

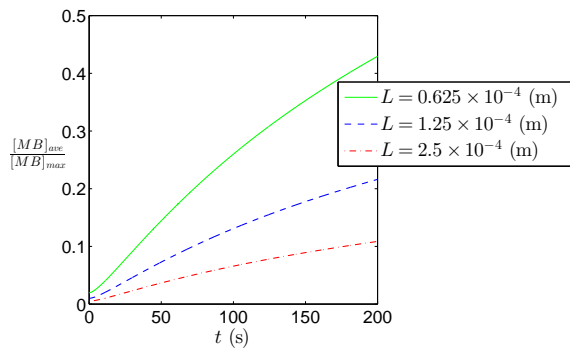


Figure 3.20: Simulations showing  $\frac{[MB]_{ave}}{[MB]_{max}}$  plotted against  $t$  for three different film thicknesses.

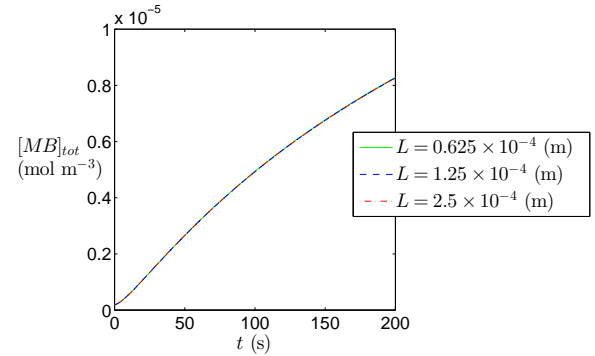


Figure 3.21: Simulations showing  $\frac{[MB]_{ave}}{[MB]_{max}}$  plotted against  $t$  for three different film thicknesses.

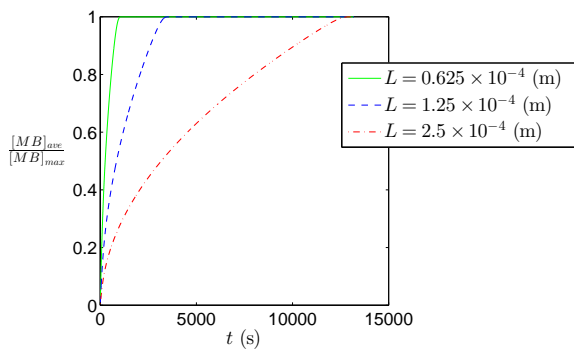


Figure 3.22: Simulations showing  $\frac{[MB]_{ave}}{[MB]_{max}}$  plotted against  $t$  for three different film thicknesses.

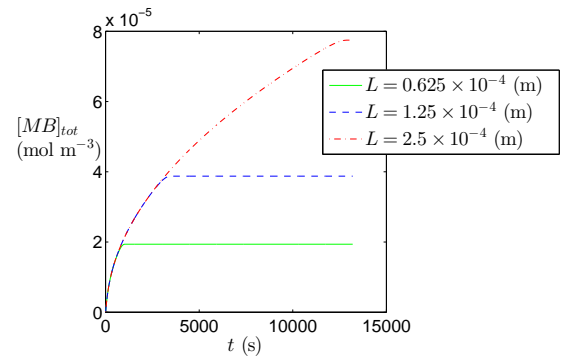


Figure 3.23: Simulations showing  $\frac{[MB]_{ave}}{[MB]_{max}}$  plotted against  $t$  for three different film thicknesses.

Figures 3.22 and 3.23 show the same results as Figure 3.20 and Figure 3.21 plotted on alternative axes with  $t$  ranging from 0 to 15,000 s. These plots demonstrate that by increasing the film thickness the total amount of MB produced will increase. Additionally, in terms of the total amount of MB being produced, all three films give very similar results until  $t$  equals approximately 550 s. At this

point, for the thinnest film the total amount of MB produced is approaching the maximum possible value. Between  $t = 0$  and  $t = 2500$  s we have the two thickest films give almost identical results until the second film reaches the maximum amount of MB which that particular system can produce.

Figures 3.24 - 3.26 show concentration profiles of  $O_2$ , LMB and MB for the three different films considered. The first three figures show profiles which were plotted at 20 uniform times ranging from  $t = 0$  to  $t = 200$  s. These figures demonstrate that, for all three films, the behaviour of  $O_2$ , LMB and MB is almost identical. This suggests that, over the period of time studied, the reaction kinetics are independent of film thickness in terms of total production of MB.

Figures 3.27 - 3.29 are similar to Figures 3.24 - 3.26, however in this case the profiles are plotted at 20 uniform times ranging from  $t = 0$  to  $t = 3,000$  s and the  $x$ -axes have been increased. These figures show that the kinetics for all three films are very similar until the LMB at  $x = L$  starts to react with  $O_2$ . The concentration profiles of MB and LMB for the three films considered show similar travelling wave type behaviour. It is this behaviour which causes the  $\frac{1}{L}$  dependence. We have that the waves of MB being produced are travelling at approximately the same rate for all three films. However, because we are using the average of MB to define the initial reaction rate, our results show that  $R_i$  is approximately inversely proportional to  $L$  for this regime.

After initially replicating the results produced by Marek *et al.* [46] we were able to use the proposed model and carry out further simulations. By performing simulations over a wide range of  $L$  values we were able to show that there are three distinct kinetic regimes and give reasons why the system is demonstrating this kind of behaviour.

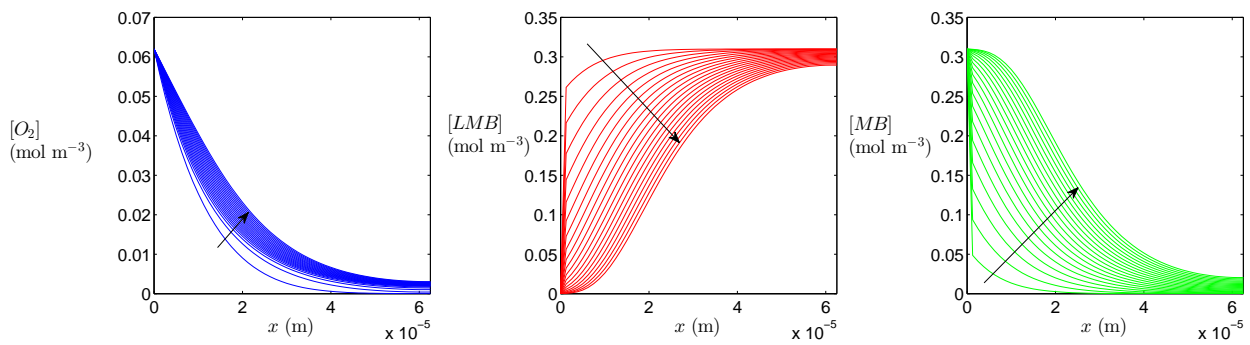


Figure 3.24: Concentration profiles at 20 uniform times ranging from  $t = 0$  to  $t = 200$  s with  $L = 0.65 \times 10^{-4}$  (m).

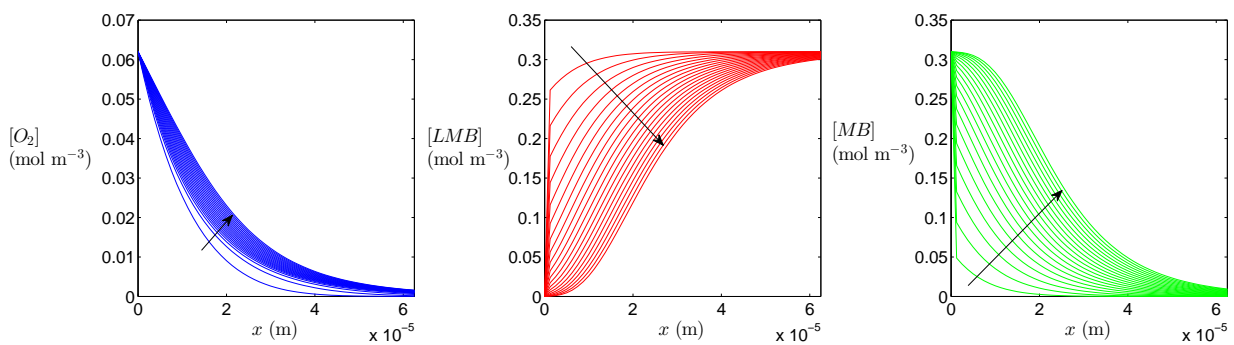


Figure 3.25: Concentration profiles at 20 uniform times ranging from  $t = 0$  to  $t = 200$  s with  $L = 1.25 \times 10^{-4}$  (m).

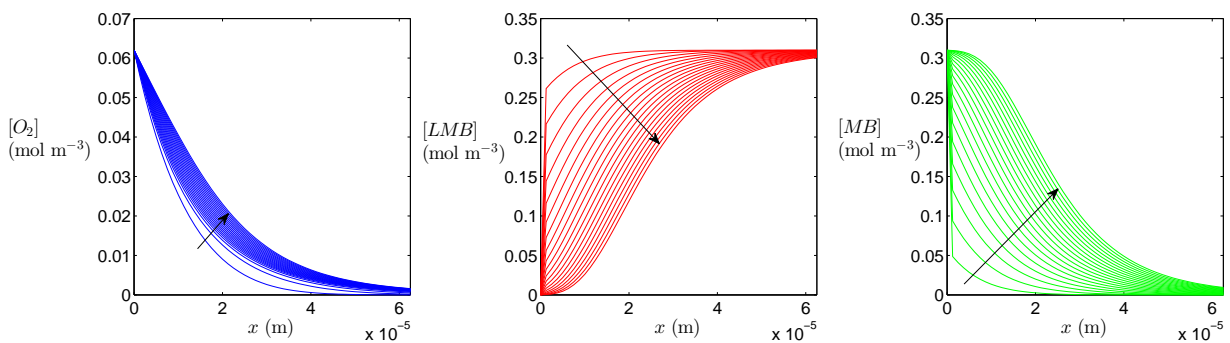


Figure 3.26: Concentration profiles at 20 uniform times ranging from  $t = 0$  to  $t = 200$  s with  $L = 2.5 \times 10^{-4}$  (m).

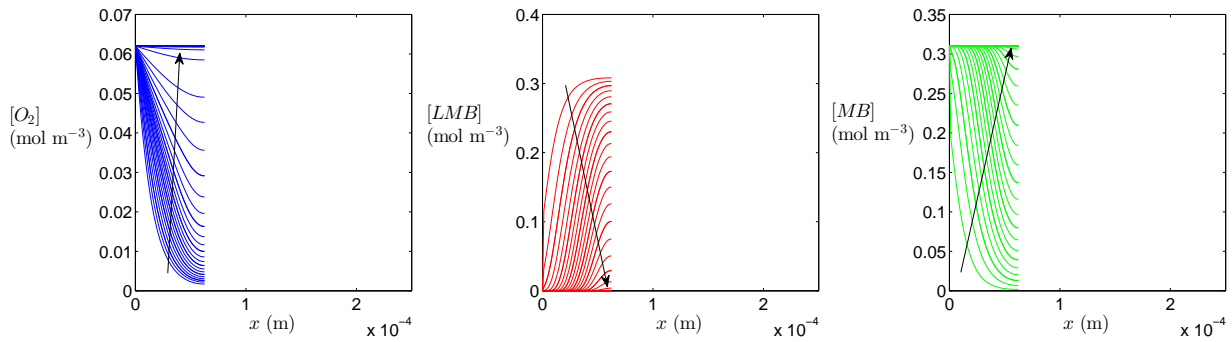


Figure 3.27: Concentration profiles at 20 uniform times ranging from  $t = 0$  to  $t = 3000$  s with  $L = 0.65 \times 10^{-4}$  (m).

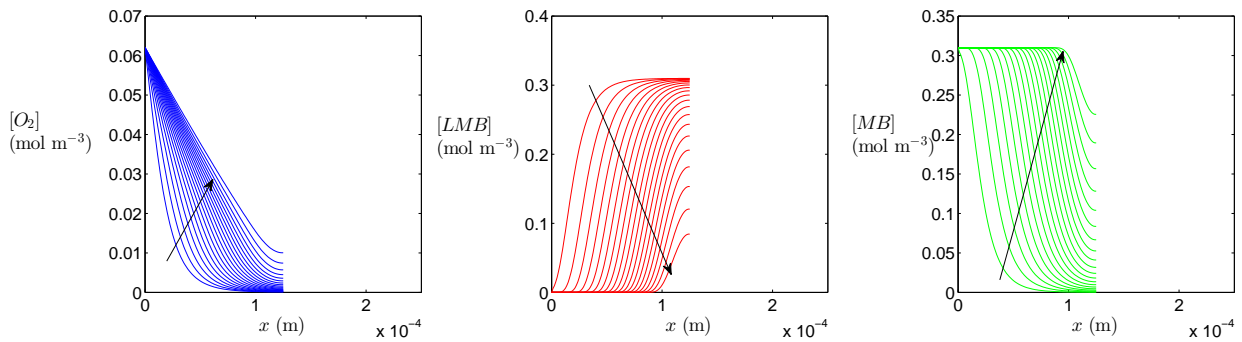


Figure 3.28: Concentration profiles at 20 uniform times ranging from  $t = 0$  to  $t = 3000$  s with  $L = 1.25 \times 10^{-4}$  (m).

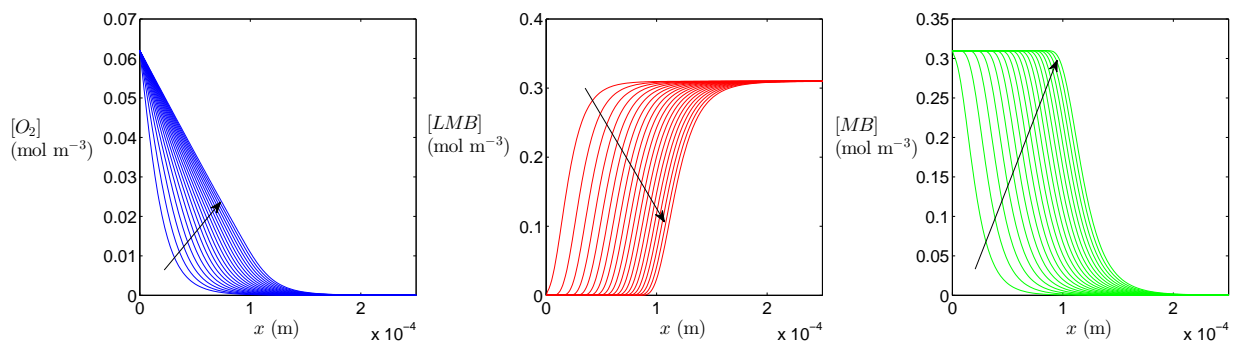


Figure 3.29: Concentration profiles at 20 uniform times ranging from  $t = 0$  to  $t = 3000$  s with  $L = 2.5 \times 10^{-4}$  (m).

### 3.4 Reactant activated by diffusion of gas

The work in this section is motivated by preliminary experimental results for a system where gas diffuses into a polymer film before reacting with a dye throughout the film. The experimental results show that the initial reaction rate is approximately inversely proportional to the film thickness. The general model we present in this chapter could be applied to such a system.

As shown in Figure 3.30, we consider a polymer film of thickness  $L$  lying on a glass support. Molecules of reactant are homogeneously distributed throughout the film. Molecules of gas continuously enter the film and diffuse throughout the domain, reacting with molecules of reactant. The reactant in this case could represent various substances, for example a dye.

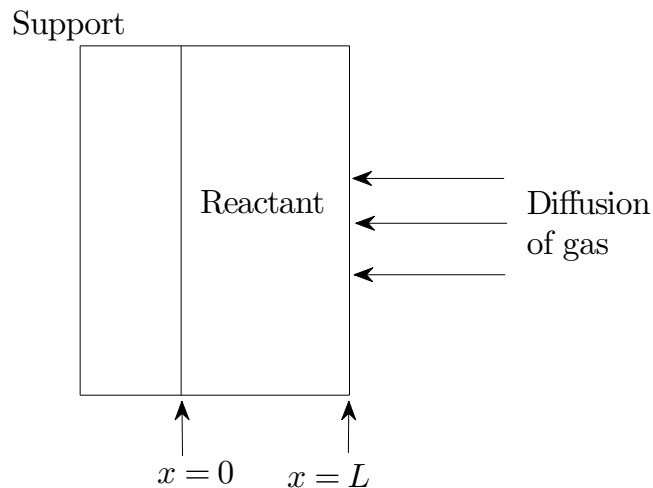


Figure 3.30: Diagram of the initial set-up showing how gas diffuses through a polymer film.

#### 3.4.1 Initial model

The model we propose in this section is similar to the model introduced in Section 3.2. In both cases we have an adsorption/desorption process taking place and have reactions occurring throughout the domain. However, in this case we have

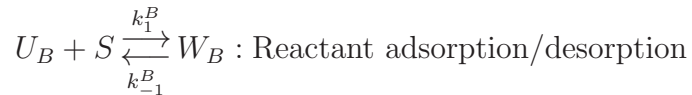
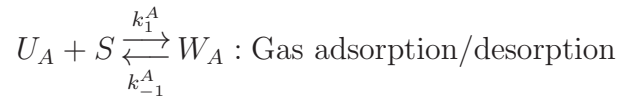
two reactants in the system which are both adsorbing/desorbing and reacting together. This makes the model more complicated than the model described in Section 3.2.

We assume that the gas molecules can be in two states. Molecules are either free to diffuse, denoted by  $U_A$ , or they have been adsorbed and are ready to react,  $W_A$ . Similarly, reactant molecules are either free to diffuse,  $U_B$ , or they have been adsorbed and are ready to react,  $W_B$ . We assume that the gas molecules are adsorbed at the rate  $k_1^A$  and desorbed at the rate  $k_{-1}^A$ . The reactant molecules can be adsorbed at the rate  $k_1^B$  and desorbed at the rate  $k_{-1}^B$ . We assume that

$$\theta_A + \theta_B + \theta_E = 1, \quad (3.20)$$

where  $\theta_A = \frac{w_A}{s_{tot}}$  represents the fraction of sites occupied by gas molecules,  $\theta_B = \frac{w_B}{s_{tot}}$  represents the fraction of sites occupied by reactant molecules,  $\theta_E$  represents the fraction of empty sites. Furthermore,  $w_A$  represents the concentration of  $W_A$ ,  $w_B$  represents the concentration of  $W_B$  and  $s_{tot}$  represents the concentration of the total number of adsorption sites. In this case, reactant and gas molecules share the same sites. If adsorbed gas molecules and adsorbed reactant molecules are present at any reaction site they will react irreversibly to produce a product at the rate  $k_2$ .

We assume the following reaction scheme





where  $S$  represents unoccupied adsorption sites.

Note that the proposed reaction mechanism is very similar to the mechanism proposed in Chapter 2. The adsorption/desorption process assumed for both gas and reactant molecules is identical to the previous process. However, in this case, we assume that there are adsorption sites throughout the domain as opposed to purely existing at the photocatalyst surface. Hence for this system we have an adsorption/desorption process going on throughout the domain for both gas and reactant. Additionally, for products to be created both gas and reactant have to be present at an adsorption site.

The mechanism is also similar to the model proposed by Marek *et al.* [46] which we discussed in Section 3.3. However, there are substantial differences. Firstly, in our proposed model we consider two diffusing reactants as opposed to one stationary reactant and one diffusing reactant. Secondly, we consider an adsorption/desorption Langmuir type mechanism throughout the domain whereas Marek *et al.* [46] considers a constant reaction rate and includes parameters which can define the order of the reaction with respect to the concentration of gas and reactant.

We will define  $u_A$ ,  $u_B$  and  $p$  as the concentrations of  $U_A$ ,  $U_B$  and  $P$ , respectively. For this particular model,  $u_A$ ,  $u_B$ ,  $w_A$ ,  $w_B$  and  $p$  will all be dependent on  $x$  and  $t$ . We will assume that molecules of  $U_A$  are transported through the polymer film via linear diffusion, hence, assuming the law of mass action kinetics we have

$$\frac{\partial u_A}{\partial t} = \overbrace{D_A \frac{\partial^2 u_A}{\partial x^2}}^{\text{Diffusion in polymer film}} - \overbrace{k_1^A \theta_E s_{tot} u_A}^{\text{Local adsorption}} + \overbrace{k_{-1}^A \theta_A s_{tot}}^{\text{Local desorption}},$$

$$\frac{\partial w_A}{\partial t} = \overbrace{-k_2 \theta_A \theta_B s_{tot}^2}^{\text{Molecules which are reacting}} + \overbrace{k_1^A \theta_E s_{tot} u_A}^{\text{Local adsorption}} - \overbrace{k_{-1}^A \theta_A s_{tot}}^{\text{Local desorption}},$$

where  $D_A$  is the diffusion coefficient of the gas.

Using (3.20) and the fact that  $\theta_A = \frac{w_A}{s_{tot}}$  and  $\theta_B = \frac{w_B}{s_{tot}}$  we have that

$$\frac{\partial u_A}{\partial t} = D_A \frac{\partial^2 u_A}{\partial x^2} - k_1^A u_A (s_{tot} - w_A - w_B) + k_{-1}^A w_A, \quad (3.21)$$

$$\frac{\partial w_A}{\partial t} = k_1^A u_A (s_{tot} - w_A - w_B) - k_{-1}^A w_A - k_2 w_A w_B. \quad (3.22)$$

Similarly, for free and adsorbed reactant molecules we have

$$\frac{\partial u_B}{\partial t} = D_B \frac{\partial^2 u_B}{\partial x^2} - k_1^B u_B (s_{tot} - w_A - w_B) + k_{-1}^B w_B, \quad (3.23)$$

$$\frac{\partial w_B}{\partial t} = k_1^B u_B (s_{tot} - w_A - w_B) - k_{-1}^B w_B - k_2 w_A w_B, \quad (3.24)$$

where  $D_B$  is the diffusion coefficient of the reactant.

Using the law of mass action kinetics we have the following equation for the concentration of products  $p$ ;

$$\frac{dp}{dt} = k_2 w_A w_B.$$

### 3.4.2 Boundary and initial conditions

We assume that at  $x = L$  there is a continuous supply of gas molecules able to diffuse through the polymer film. At  $x = 0$  we again have a zero flux boundary condition, hence the boundary conditions for  $u_A$  are given by

$$\left. \frac{\partial u_A}{\partial x} \right|_{x=0} = 0 \quad u_A(L, t) = u_A^{BC},$$

where  $u_A^{BC}$  is a constant concentration which will determine how much gas is able to enter into the system.

For the reactant we have zero flux boundary conditions at both ends of the film (i.e. at  $x = 0$  and  $x = L$ ) due to the symmetry in the system. Hence, our

boundary conditions are given by

$$\left. \frac{\partial u_B}{\partial x} \right|_{x=0} = \left. \frac{\partial u_B}{\partial x} \right|_{x=L} = 0.$$

Before the reaction has commenced, the concentration of free gas molecules will be zero everywhere, except at  $x = L$  where the concentration will equal  $u_A^{BC}$ . Initially we expect  $u_B = u_{B0}$  and  $w_B = 0$ , where  $u_{B0}$  represents the initial concentration of reactant which is evenly distributed throughout the domain. However, before any gas enters the system, we assume that reactant molecules are free to adsorb and desorb until equilibrium is reached. We will describe exactly how the equilibrium concentrations are calculated later in this chapter. Initially, we have that  $w_A(x, 0) = 0$  and  $p(x, 0) = 0$ .

### 3.4.3 Nondimensionalisation

We nondimensionalise (3.21)-(3.24) using the following scaling:

$$\hat{t} = \frac{t}{T}, \quad \hat{x} = \frac{x}{L}, \quad \hat{u}_A = \frac{u_A}{u_A^{BC}},$$

$$\hat{u}_B = \frac{u_B}{u_A^{BC}}, \quad \hat{w}_A = \frac{w_A}{u_A^{BC}}, \quad \hat{w}_B = \frac{w_B}{u_A^{BC}}, \quad \hat{p} = \frac{p}{u_A^{BC}},$$

and we let our characteristic time be  $T = \frac{L^2}{D_B}$ . Additionally, we have

$$\hat{k}_1^A = k_1^A u_A^{BC} \frac{L^2}{D_B}, \quad \hat{k}_{-1}^A = k_{-1}^A \frac{L^2}{D_B}, \quad \hat{k}_2 = k_2 u_A^{BC} \frac{L^2}{D_B},$$

$$\hat{k}_1^B = k_1^B u_A^{BC} \frac{L^2}{D_B}, \quad \hat{k}_{-1}^B = k_{-1}^B \frac{L^2}{D_B}, \quad \hat{s}_{tot} = \frac{s_{tot}}{u_A^{BC}}, \quad \hat{D}_A = \frac{D_A}{D_B}.$$

Once the hat notation has been dropped, the nondimensional versions of (3.21)-(3.24) are identical to the dimensional versions, however due to our choice of scaling we have eliminated the diffusion coefficient from (3.23). Note that all simulations performed in Section 3.4 are nondimensional.

### 3.4.4 Pre-reaction concentrations

We assume that  $u_B$  and  $w_B$  are in equilibrium before the reaction begins. Hence, before reactant and gas molecules can react together, adsorption and desorption of reactant molecules will take place until both concentrations tend to their equilibrium values. Before the initial adsorption/desorption takes place we assume that  $u_B(x, 0) = u_{B0}$  and  $w_B(x, 0) = 0$ . To calculate the equilibrium concentrations of  $u_B$  and  $w_B$ , which we define as  $u_{Bq}$  and  $w_{Bq}$ , we set both  $\frac{\partial u_B}{\partial t}$  and  $\frac{\partial w_B}{\partial t}$  equal to zero with  $k_2 = 0$  and  $w_A = 0$  (due to the reaction having not started at this point).

Hence we have

$$\frac{\partial^2 u_{Bq}}{\partial x^2} - k_1^B u_{Bq}(s_{tot} - w_{Bq}) + k_{-1}^B w_{Bq} = 0.$$

Initially all reactant molecules are evenly distributed throughout the domain, since the adsorption/desorption process will be the same throughout the domain we will have that  $\frac{\partial u_B}{\partial x} = 0$ , and hence

$$k_1^B u_{Bq}(s_{tot} - w_{Bq}) - k_{-1}^B w_{Bq} = 0. \quad (3.25)$$

As the reaction is yet to start, we must have that all dye molecules are either free or adsorbed, so that

$$u_{B0} = u_{Bq} + w_{Bq}. \quad (3.26)$$

Substituting (3.26) into (3.25) gives the following

$$u_{Bq} = \frac{-(k_1^B(s_{tot} - u_{B0}) + k_{-1}^B) + \sqrt{(k_1^B(s_{tot} - u_{B0}) + k_{-1}^B)^2 + 4k_1^B k_{-1}^B u_{B0}}}{2k_1^B},$$

where it can be shown that we must take the positive root otherwise we will have a negative solution. By substituting  $u_{Bq}$  into (3.26) we can find  $w_{Bq}$ . These equilibrium values become our initial conditions for  $u_B$  and  $w_B$ .

Hence we have the following system of equations

$$\left\{ \begin{array}{l} \frac{\partial u_A}{\partial t} = D_A \frac{\partial^2 u_A}{\partial x^2} - k_1^A u_A (s_{tot} - w_A - w_B) + k_{-1}^A w_A, \quad 0 \leq x \leq 1, \\ \frac{\partial u_A}{\partial x} \Big|_{x=0} = 0, \quad u_A(1, t) = 1, \quad \forall t \geq 0, \\ u_A(x, 0) = 0, \quad 0 \leq x < 1, \end{array} \right. \quad (3.27)$$

$$\left\{ \begin{array}{l} \frac{\partial w_A}{\partial t} = k_1^A u_A (s_{tot} - w_A - w_B) - k_{-1}^A w_A - k_2 w_A w_B, \quad 0 \leq x \leq 1, \\ w_A(x, 0) = 0, \quad 0 \leq x \leq 1, \end{array} \right. \quad (3.28)$$

$$\left\{ \begin{array}{l} \frac{\partial u_B}{\partial t} = \frac{\partial^2 u_B}{\partial x^2} - k_1^B u_B (s_{tot} - w_A - w_B) + k_{-1}^B w_B, \quad 0 \leq x \leq 1, \\ \frac{\partial u_B}{\partial x} \Big|_{x=0} = 0, \quad \frac{\partial u_B}{\partial x} \Big|_{x=1} = 0, \\ u_B(x, 0) = u_{Bq}, \quad 0 \leq x \leq 1, \end{array} \right. \quad (3.29)$$

$$\left\{ \begin{array}{l} \frac{\partial w_B}{\partial t} = k_1^B u_B (s_{tot} - w_A - w_B) - k_{-1}^B w_B - k_2 w_A w_B, \quad 0 \leq x \leq 1, \\ w_B(x, 0) = w_{Bq}, \quad 0 \leq x \leq 1. \end{array} \right. \quad (3.30)$$

$$\left\{ \begin{array}{l} \frac{\partial p}{\partial t} = k_2 w_A w_B, \quad 0 \leq x \leq 1, \\ p(x, 0) = 0, \quad 0 \leq x \leq 1. \end{array} \right. \quad (3.31)$$

### 3.4.5 Quasi-steady state assumption

As in the last model we can invoke the QSSA in an attempt to simplify our system. This would entail setting (3.28) and (3.30) equal to zero which gives

$$w_{AQ} = \frac{k_1^A u_A s_{tot} - k_1^A u_A w_{BQ}}{k_1^A u_A + k_{-1}^A + k_2 w_{BQ}}, \quad (3.32)$$

$$w_{BQ} = \frac{k_1^B u_B s_{tot} - k_1^B u_B w_{AQ}}{k_1^B u_B + k_{-1}^B + k_2 w_{AQ}}, \quad (3.33)$$

where  $w_{AQ}$  and  $w_{BQ}$  represent the QSSA concentrations of  $w_A$  and  $w_B$  respectively.

By solving (3.32) and (3.33) simultaneously we can find expressions for  $w_{AQ}$  and  $w_{BQ}$  in terms of  $u_A$ ,  $u_B$  and various parameters. Hence, we are effectively able to eliminate  $w_A$  and  $w_B$  from our system. However, unlike our previous model, the QSSA concentrations  $w_{AQ}$  and  $w_{BQ}$  come from solving a complicated quadratic equation and hence do not significantly simplify the overall system of equations. Hence, unless further assumptions are made, invoking the QSSA for this particular model does not significantly simplify our overall system or enable us to do any significant analysis which would not be possible to do otherwise. Hence, for this model we will focus on the full system of equations (3.27) - (3.30).

### 3.4.6 Measuring the initial reaction rate

We define the average concentration of product,  $p(t)$  as  $\bar{p}(t) = \int_0^1 p(x, t) dx$ . We are mainly interested in the initial rate of production of product. As in the previous model, we measure how long it takes for 10% of the final product to be formed and fit a straight line over this period of time. We define the gradient of this line as our approximation to  $R_i$ .

### 3.4.7 Numerical method

As for previous systems considered, we will use a finite difference method to find a numerical solution to the systems of equations (3.27) - (3.31). We again divide the spatial domain  $(0, 1)$  into  $N$  equal intervals, and the temporal domain  $(0, T)$  into  $NT$  equal intervals, with mesh spacings  $\Delta x$  and  $\Delta t$ , respectively. We will find approximations of  $u_A$ ,  $u_B$ ,  $w_A$ ,  $w_B$  and  $p$  at all grid points, denoted by  $u_{A_i}^n = u_A(i\Delta x, n\Delta t)$ ,  $u_{B_i}^n = u_B(i\Delta x, n\Delta t)$ ,  $w_{A_i}^n = w_A(i\Delta x, n\Delta t)$ ,  $w_{B_i}^n = w_B(i\Delta x, n\Delta t)$  and  $p_i^n = p(i\Delta x, n\Delta t)$ , respectively.

Our approach for solving this system is similar to the approach used to solve the full system in the resazurin case in Chapter 2. We initially approximate  $w_A$  and  $w_B$  at the forward time step using a forward Euler method. These approximations are used for a Crank-Nicolson discretisation of (3.27) and (3.29). Once an approximation of  $u_A$  and  $u_B$  have been found we can recalculate  $w_A$  and  $w_B$  using a Crank-Nicolson method. As in the previous model this process can be repeated a number of times until a sufficiently accurate solution is found.

We initially discretise (3.28) and (3.30) using a forward euler method. We refer to these initial approximations of  $w_A^{n+1}$  and  $w_B^{n+1}$  as  $w_A^{[n+1,1]}$  and  $w_B^{[n+1,1]}$ , respectively. Hence we have

$$\frac{w_{A_j}^{[n+1,1]} - w_{A_j}^n}{\Delta t} = k_1^A u_{A_j}^n (s_{tot} - w_{A_j}^n - w_{B_j}^n) - k_{-1}^A w_{A_j}^n - k_2 w_{A_j}^n w_{B_j}^n,$$

for  $j = 0, 1, 2, \dots, N$  and  $n = 0, 1, 2, \dots, NT - 1$ , which can be rearranged to give

$$w_{A_j}^{[n+1,1]} = w_{A_j}^n + \Delta t (k_1^A u_{A_j}^n (s_{tot} - w_{A_j}^n - w_{B_j}^n) - k_{-1}^A w_{A_j}^n - k_2 w_{A_j}^n w_{B_j}^n). \quad (3.34)$$

We find a similar expression for  $w_{B_j}^{[n+1,1]}$  given by

$$w_{B_j}^{[n+1,1]} = w_{B_j}^n + \Delta t (k_1^B u_{B_j}^n (s_{tot} - w_{A_j}^n - w_{B_j}^n) - k_{-1}^B w_{B_j}^n - k_2 w_{A_j}^n w_{B_j}^n). \quad (3.35)$$

Having found  $w_A^{[n+1,1]}$  and  $w_B^{[n+1,1]}$  we can now discretise (3.27) and (3.29) using a Crank-Nicolson method.

We have the following discretisation of (3.27) where  $u_A^{[n+1,1]}$  represents the initial approximation to  $u_A^{n+1}$ ;

$$\begin{aligned} \frac{u_{A_j}^{[n+1,1]} - u_{A_j}^n}{\Delta t} = & \frac{D_A}{2(\Delta x)^2} \left( (u_{A_{j+1}}^{[n+1,1]} - 2u_{A_j}^{[n+1,1]} + u_{A_{j-1}}^{[n+1,1]}) + (u_{A_{j+1}}^n - 2u_{A_j}^n + u_{A_{j-1}}^n) \right) \\ & - \frac{1}{2} \left( k_1^A u_{A_j}^{[n+1,1]} (s_{tot} - w_{A_j}^{[n+1,1]} - w_{B_j}^{[n+1,1]}) - k_{-1}^A w_{A_j}^{[n+1,1]} \right. \\ & \left. + k_1^A u_{A_j}^n (s_{tot} - w_{A_j}^n - w_{B_j}^n) - k_{-1}^A w_{A_j}^n \right), \end{aligned}$$

for  $j = 0, 1, 2, \dots, N-1$  and  $n = 0, 1, 2, \dots, NT-1$ . If we let  $V_A = \frac{D_A \Delta t}{2(\Delta x)^2}$  we have

$$\begin{aligned} -V_A u_{A_{j+1}}^{[n+1,1]} + (1 + 2V_A + \frac{\Delta t}{2} k_1^A (s_{tot} - w_{A_j}^{[n+1,1]} - w_{B_j}^{[n+1,1]})) u_{A_j}^{[n+1,1]} - V_A u_{A_{j-1}}^{[n+1,1]} \\ = V_A u_{A_{j+1}}^n + (1 - 2V_A - \frac{\Delta t}{2} k_1^A (s_{tot} - w_{A_j}^n - w_{B_j}^n)) u_{A_j}^n + V_A u_{A_{j-1}}^n \\ + \frac{\Delta t}{2} k_{-1}^A (w_{A_j}^{[n+1,1]} + w_{A_j}^n). \end{aligned} \quad (3.36)$$

At  $x = 0$  we have a zero-flux boundary condition. We again use a ghost node approach, hence with  $j = 0$  (3.36) gives

$$\begin{aligned} -2V_A u_{A_1}^{n+1} + (1 + 2V_A + \frac{\Delta t}{2} k_1^A (s_{tot} - w_{A_0}^{[n+1,1]} - w_{B_0}^{[n+1,1]})) u_{A_0}^{n+1} \\ = 2V_A u_{A_1}^n + (1 - 2V_A - \frac{\Delta t}{2} k_1^A (s_{tot} - w_{A_0}^n - w_{B_0}^n)) u_{A_0}^n \\ + \frac{\Delta t}{2} k_{-1}^A (w_{A_0}^{[n+1,1]} + w_{A_0}^n). \end{aligned} \quad (3.37)$$

At  $x = 1$  we have that  $u_A = 1$ , hence with  $j = N - 1$ , (3.36) gives

$$\begin{aligned}
& (1 + 2V_A + \frac{\Delta t}{2}k_1^A(s_{tot} - w_{A_{N-1}}^{[n+1,1]} - w_{B_{N-1}}^{[n+1,1]}))u_{A_{N-1}}^{[n+1,1]} - V_A u_{A_{N-2}}^{[n+1,1]} \\
&= (1 - 2V_A - \frac{\Delta t}{2}k_1^A(s_{tot} - w_{A_{N-1}}^n - w_{B_{N-1}}^n))u_{A_{N-1}}^n + V_A u_{A_{N-2}}^n \\
& \quad + \frac{\Delta t}{2}k_{-1}^A(w_{A_{N-1}}^{[n+1,1]} + w_{A_{N-1}}^n) + 2V_A.
\end{aligned} \tag{3.38}$$

Hence, we can now solve (3.36), (3.37) and (3.38) for  $u_A^{[n+1,1]}$ . By undertaking a similar approach for  $u_B$  we can find  $u_B^{[n+1,1]}$  using the following discretisations

$$\begin{aligned}
& -V_B u_{B_{j+1}}^{[n+1,1]} + (1 + 2V_B + \frac{\Delta t}{2}k_1^B(s_{tot} - w_{A_j}^{[n+1,1]} - w_{B_j}^{[n+1,1]}))u_{B_j}^{[n+1,1]} - V_B u_{B_{j-1}}^{[n+1,1]} \\
&= V_B u_{B_{j+1}}^n + (1 - 2V_B - \frac{\Delta t}{2}k_1^B(s_{tot} - w_{A_j}^n - w_{B_j}^n))u_{B_j}^n + V_B u_{B_{j-1}}^n \\
& \quad + \frac{\Delta t}{2}k_{-1}^B(w_{B_j}^{[n+1,1]} + w_{B_j}^n),
\end{aligned} \tag{3.39}$$

where  $V_B = \frac{\Delta t}{2(\Delta x)^2}$ , for  $j = 0, 1, 2, \dots, N$  and  $n = 0, 1, 2, \dots, NT - 1$ . At  $x = 0$  we have a zero-flux boundary condition. We again use a ghost node approach, hence with  $j = 0$  (3.39) gives

$$\begin{aligned}
& -2V_B u_{B_1}^{n+1} + (1 + 2V_B + \frac{\Delta t}{2}k_1^B(s_{tot} - w_{A_0}^{[n+1,1]} - w_{B_0}^{[n+1,1]}))u_{B_0}^{n+1} \\
&= 2V_B u_{B_1}^n + (1 - 2V_B - \frac{\Delta t}{2}k_1^B(s_{tot} - w_{A_0}^n - w_{B_0}^n))u_{B_0}^n + \frac{\Delta t}{2}k_{-1}^B(w_{B_0}^{[n+1,1]} + w_{B_0}^n).
\end{aligned} \tag{3.40}$$

At  $x = 1$  we have a zero-flux boundary condition. We again use a ghost node approach, hence with  $j = N$  (3.39) gives

$$\begin{aligned}
& (1 + 2V_B + \frac{\Delta t}{2}k_1^B(s_{tot} - w_{A_N}^{[n+1,1]} - w_{B_N}^{[n+1,1]}))u_{B_N}^{[n+1,1]} - 2V_B u_{B_{N-1}}^{[n+1,1]} \\
&= (1 - 2V_B - \frac{\Delta t}{2}k_1^B(s_{tot} - w_{A_N}^n - w_{B_N}^n))u_{B_N}^n + 2V_B u_{B_{N-1}}^n + \frac{\Delta t}{2}k_{-1}^B(w_{B_N}^{[n+1,1]} + w_{B_N}^n).
\end{aligned} \tag{3.41}$$

Hence, we can now solve (3.39), (3.40) and (3.41) for  $u_B^{[n+1,1]}$ .

We can now improve our initial approximations of  $w_A^{n+1}$  and  $w_B^{n+1}$  which we will refer to as  $w_A^{[n+1,2]}$  and  $w_B^{[n+1,2]}$ . We discretise (3.28) and (3.30) using a Crank-Nicolson method where  $u_A^{[n+1,1]}$ ,  $u_B^{[n+1,1]}$ ,  $w_A^{[n+1,1]}$  and  $w_B^{[n+1,1]}$  are used as approximations to  $u_A^{n+1}$ ,  $u_B^{n+1}$ ,  $w_A^{n+1}$  and  $w_B^{n+1}$ , respectively. Hence, we have that

$$\begin{aligned} \frac{w_{A_j}^{[n+1,2]} - w_{A_j}^n}{\Delta t} = & \frac{1}{2} \left( k_1^A u_{A_j}^{[n+1,1]} (s_{tot} - w_{A_j}^{[n+1,2]} - w_{B_j}^{[n+1,1]}) \right. \\ & - k_{-1}^A w_{A_j}^{[n+1,2]} - k_2 w_{A_j}^{[n+1,2]} w_{B_j}^{[n+1,1]} \\ & \left. + k_1^A u_{A_j}^n (s_{tot} - w_{A_j}^n - w_{B_j}^n) - k_{-1}^A w_{A_j}^n - k_2 w_{A_j}^n w_{B_j}^n \right), \end{aligned}$$

which can be rearranged to give

$$w_{A_j}^{[n+1,2]} = \frac{f_1}{f_2}, \quad (3.42)$$

where

$$\begin{aligned} f_1 = & w_{A_j}^n + \frac{\Delta t}{2} \left( k_1^A u_{A_j}^{[n+1,1]} (s_{tot} - w_{B_j}^{[n+1,1]}) \right. \\ & \left. + k_1^A u_{A_j}^n (s_{tot} - w_{A_j}^n - w_{B_j}^n) - k_{-1}^A w_{A_j}^n - k_2 w_{A_j}^n w_{B_j}^n \right), \end{aligned}$$

and

$$f_2 = 1 + \frac{\Delta t}{2} \left( k_1^A u_{A_j}^{[n+1,1]} + k_{-1}^A + k_2 w_{B_j}^{[n+1,1]} \right).$$

Hence, we now have an improved approximation for  $w_A^{n+1}$ . A similar approximation of  $w_B^{n+1}$  can be found from

$$w_{B_j}^{[n+1,2]} = \frac{g_1}{g_2}, \quad (3.43)$$

where

$$g_1 = w_{B_j}^n + \frac{\Delta t}{2} \left( k_1^B u_{B_j}^{[n+1,1]} (s_{tot} - w_{A_j}^{[n+1,2]}) + k_1^B u_{B_j}^n (s_{tot} - w_{A_j}^n - w_{B_j}^n) - k_{-1}^B w_{B_j}^n - k_2 w_{A_j}^n w_{B_j}^n \right),$$

and

$$g_2 = 1 + \frac{\Delta t}{2} \left( k_1^B u_{B_j}^{[n+1,1]} + k_{-1}^B + k_2 w_{A_j}^{[n+1,2]} \right).$$

Once  $u_A$ ,  $u_B$ ,  $w_A$  and  $w_B$  have been approximated at the forward time step, (3.31) can be discretised using a Crank-Nicolson method, and rearranged, to give

$$p_j^{[n+1,1]} = p_j^n + \frac{\Delta t k_2}{2} \left( w_{A_j}^{[n+1,2]} w_{B_j}^{[n+1,2]} + w_{A_j}^n w_{B_j}^n \right), \quad (3.44)$$

for  $j = 0, 1, 2, \dots, N$  and  $n = 0, 1, 2, \dots, NT - 1$ . Note that  $p$  could have been approximated at the forward time step earlier in the process using earlier approximations of  $w_A^{n+1}$  and  $w_B^{n+1}$ . However, using the updated approximations of  $w_A^{n+1}$  and  $w_B^{n+1}$  will give a more accurate approximation of  $p^{n+1}$ .

Hence, at this stage we set  $w_A^{n+1} = w_A^{[n+1,2]}$ ,  $w_B^{n+1} = w_B^{[n+1,2]}$ ,  $u_A^{n+1} = u_A^{[n+1,1]}$ ,  $u_B^{n+1} = w_B^{[n+1,1]}$  and  $p^{n+1} = p^{[n+1,1]}$  and proceed to the following time step. In summary, we can use the following scheme to solve for  $u_A^{n+1}$ ,  $w_A^{n+1}$ ,  $u_B^{n+1}$ ,  $w_B^{n+1}$  and  $p^{n+1}$  at each time step:

1. Calculate  $w_A^{[n+1,1]}$  and  $w_B^{[n+1,1]}$  using (3.34) and (3.35);
2. Calculate  $u_A^{[n+1,1]}$  and  $u_B^{[n+1,1]}$  using a Crank-Nicolson scheme by solving the system of equations given by (3.36), (3.37) and (3.38) and (3.39), (3.40) and (3.41);
3. Calculate  $w_A^{[n+1,2]}$  and  $w_B^{[n+1,2]}$  using (3.42) and (3.43);

4. Calculate an approximation to  $p^{n+1}$  using (3.44) using the most recent approximations to  $w_A^{n+1}$  and  $w_B^{n+1}$ , and proceed to the following time step.

### 3.4.8 Accuracy of numerical scheme

We will define the error in the approximation of  $u_A$ ,  $u_B$ ,  $w_A$ ,  $w_B$  and  $p$  as follows;

$$E_{u_A}^n = \max\{|u_{A_j}^n - u_A(x_j, t^n)|, j = 0, 1, \dots, N\},$$

$$E_{u_B}^n = \max\{|u_{B_j}^n - u_B(x_j, t^n)|, j = 0, 1, \dots, N\},$$

$$E_{w_A}^n = \max\{|w_{A_j}^n - w_A(x_j, t^n)|, j = 0, 1, \dots, N\},$$

$$E_{w_B}^n = \max\{|w_{B_j}^n - w_B(x_j, t^n)|, j = 0, 1, \dots, N\}.$$

$$E_p^n = \max\{|p_j^n - p(x_j, t^n)|, j = 0, 1, \dots, N\}.$$

We will consider two methods

- Method 1 - Carry out one iteration of our algorithm at each time step. This involves solving for  $u_A^{n+1}$  and  $u_B^{n+1}$  only once and solving for  $w_A^{n+1}$  and  $w_B^{n+1}$  twice, i.e. perform steps 1 to 3 of the algorithm at each time step.
- Method 2 - Solve once for  $w_A^{n+1}$  and  $w_B^{n+1}$  and solve for  $u_A^{n+1}$  and  $u_B^{n+1}$  only once before proceeding to the next time step, i.e. perform steps 1 and 2 of the algorithm at every time step.

Our approach to testing the accuracy of the proposed numerical scheme is very similar to the approach outlined in Section 2.1.8.5. To test temporal convergence we will calculate a reference solution using Method 1 with a large number of time steps. We will then vary the number of time steps used and compare our solution to the reference solution. For all simulations the number of grid points used will remain constant.

We considered an intermediate regime and performed a similar temporal convergence test to those performed previously. The results presented are very similar to results presented in the previous chapter. The following parameters were used;  $k_1^A = k_{-1}^A = k_1^B = k_{-1}^B = 1$ ,  $k_2 = 20$ ,  $s_{tot} = 0.5$ ,  $u_{B0} = 1$ ,  $D_A = 0.1$ ,  $T = 5$ ,  $N = 400$ .

For our most accurate solution  $1.6 \times 10^6$  time steps were used. To test the accuracy of our scheme, a range of time steps from  $NT = 2 \times 10^3$  to  $NT = 1.6 \times 10^4$  were used.

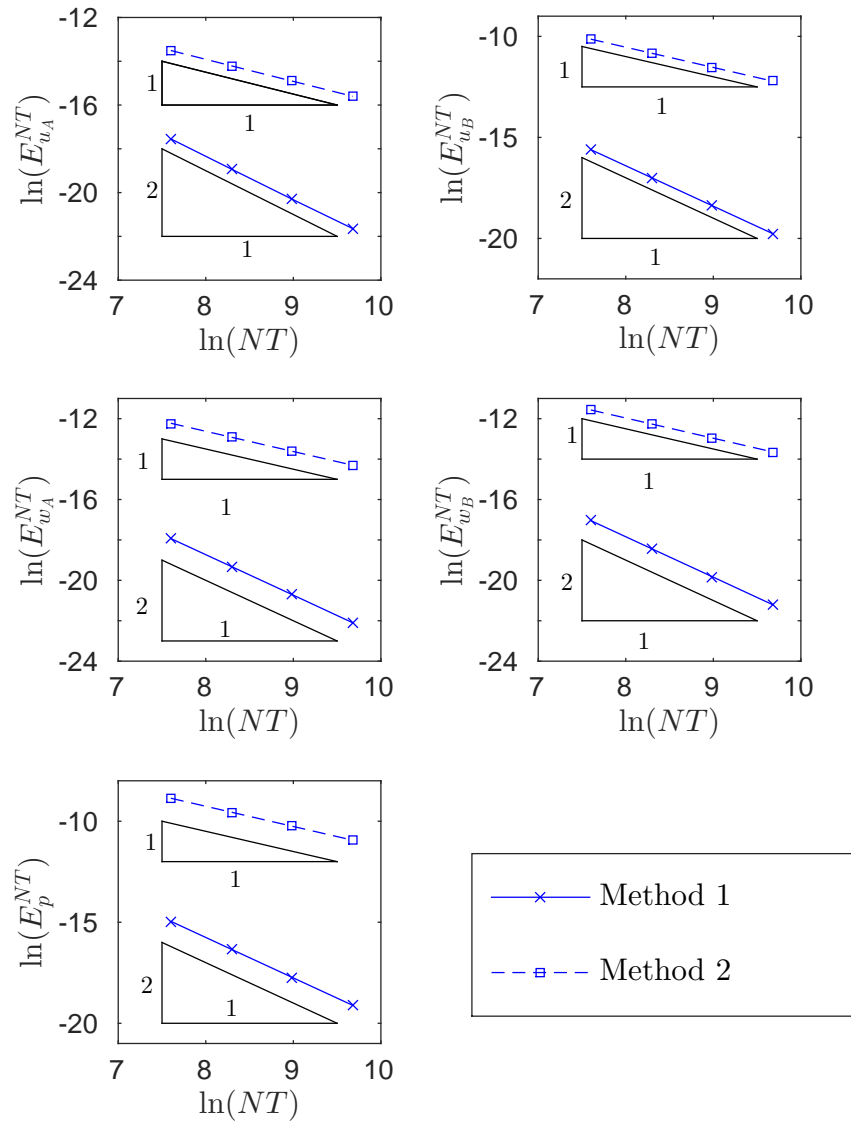


Figure 3.31: Temporal convergence results for  $u_A$ ,  $u_B$ ,  $w_A$ ,  $w_B$  and  $p$  when the kinetic parameters are chosen such that we are in an intermediate regime. All plots show that Method 1 is second-order convergent in time.

A spatial convergence test was also carried out. The following parameters were used;  $k_1^A = k_{-1}^A = k_1^B = k_{-1}^B = 1, k_2 = 20, s_{tot} = 0.5, u_{B0} = 1, D_A = 0.1, T = 5, NT = 9.6 \times 10^4$ . For our most accurate solution we have  $N = 800$ . To test the accuracy of our scheme a range of grid points from 10 to 80 were used.

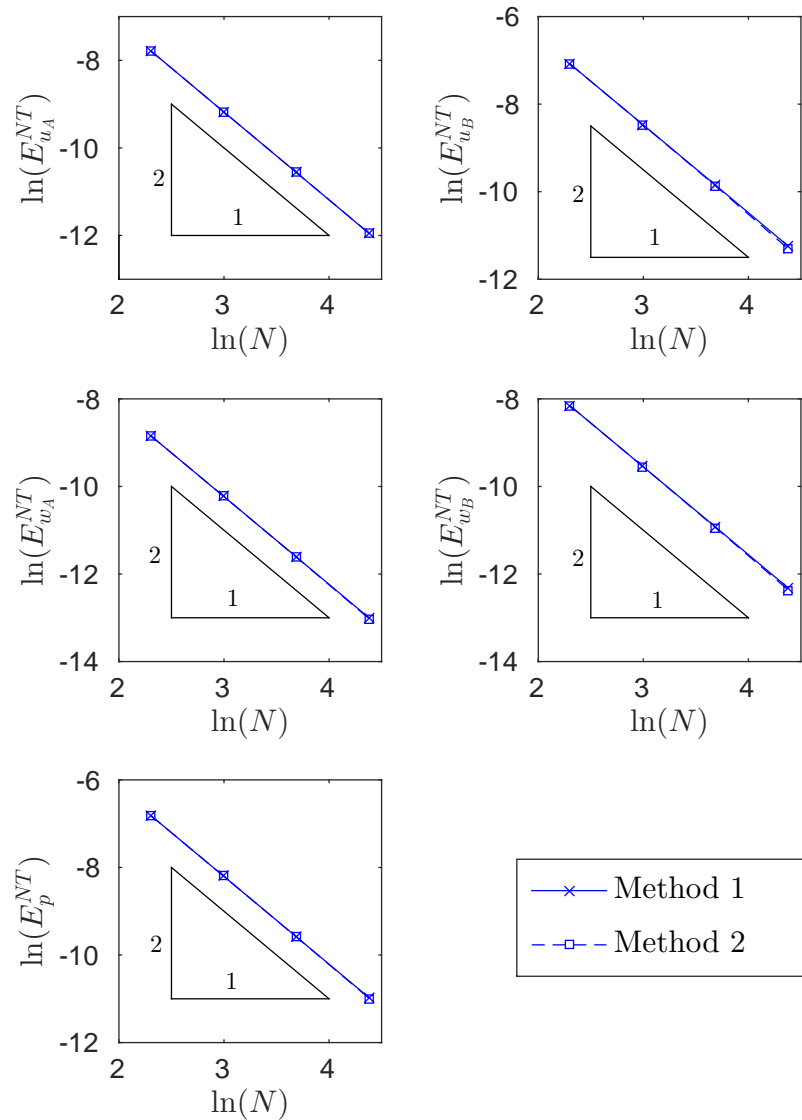


Figure 3.32: Spatial convergence results for  $u_A$ ,  $u_B$ ,  $w_A$  and  $w_B$  when the kinetic parameters are chosen such that we are in an intermediate regime. All plots show that Method 1 is second-order convergent in space.

The results presented in Figures 3.31 and 3.32 clearly demonstrate that by using Method 1 we are able to maintain second-order temporal and spatial convergence when solving this system. The improved performance of Method 1, in comparison to Method 2, justifies the slight extra cost which is required to perform this method.

### 3.4.9 Typical concentration profiles

As in previous models there are a number of different parameter regimes. In this case there will be a wider range of regimes due to the overall reaction rate being dependent on the concentration of both reactant and gas. For example we now have to consider the adsorption process of both gas and reactant. However, the overall kinetics are similar to those presented in the previous chapter.

For this model we will present various plots when we choose parameters such that we are in an intermediate parameter regime. That is, no single process will be completely rate limiting. The following parameters were used throughout our simulations;  $k_1^A = k_{-1}^A = k_1^B = k_{-1}^B = 1$ ,  $k_2 = 20$ ,  $s_{tot} = 0.5$ ,  $u_{B0} = 1$ ,  $D_A = 0.1$ ,  $T = 25$ . In this case we have chosen  $D_A$  to be relatively small to ensure we are in a regime where diffusion of gas influences the overall reaction kinetics. However, the rest of the parameters chosen are not large enough to ensure that the system is entirely limited by the diffusion of gas. The results presented in this section are not sensitive to small changes in the parameter values used. Note that, there are several other regimes which will give substantially different results. As we are now considering two different reactants in the one system, there are a wider range of possible regimes. When solving the numerical system Method 1 was used with  $N = 50$  and  $NT = 8.6 \times 10^4$ .

Figure 3.33 shows concentration profiles of  $u_A$ ,  $u_B$ ,  $w_A$ ,  $w_B$  and  $p$  plotted at 10 uniform times ranging from  $t = 0$  to  $t = 25$ . The first plot shows that gas molecules are diffusing from  $x = 1$  throughout the domain, and the concentration is tending to 1 throughout. The second plot demonstrates that close to  $x = 1$  there is more gas being adsorbed than at  $x = 0$ . Due to the fact that gas molecules have to travel across the domain, at  $x = 0$  the adsorbed concentration of gas is less. Similar to  $u_A$ ,  $w_A$  tends to 1. The third plot shows that  $u_B$  profiles remain fairly flat throughout the reaction. This is not surprising considering that the initial profile is completely flat, and we expect molecules to be adsorbed/desorbed at

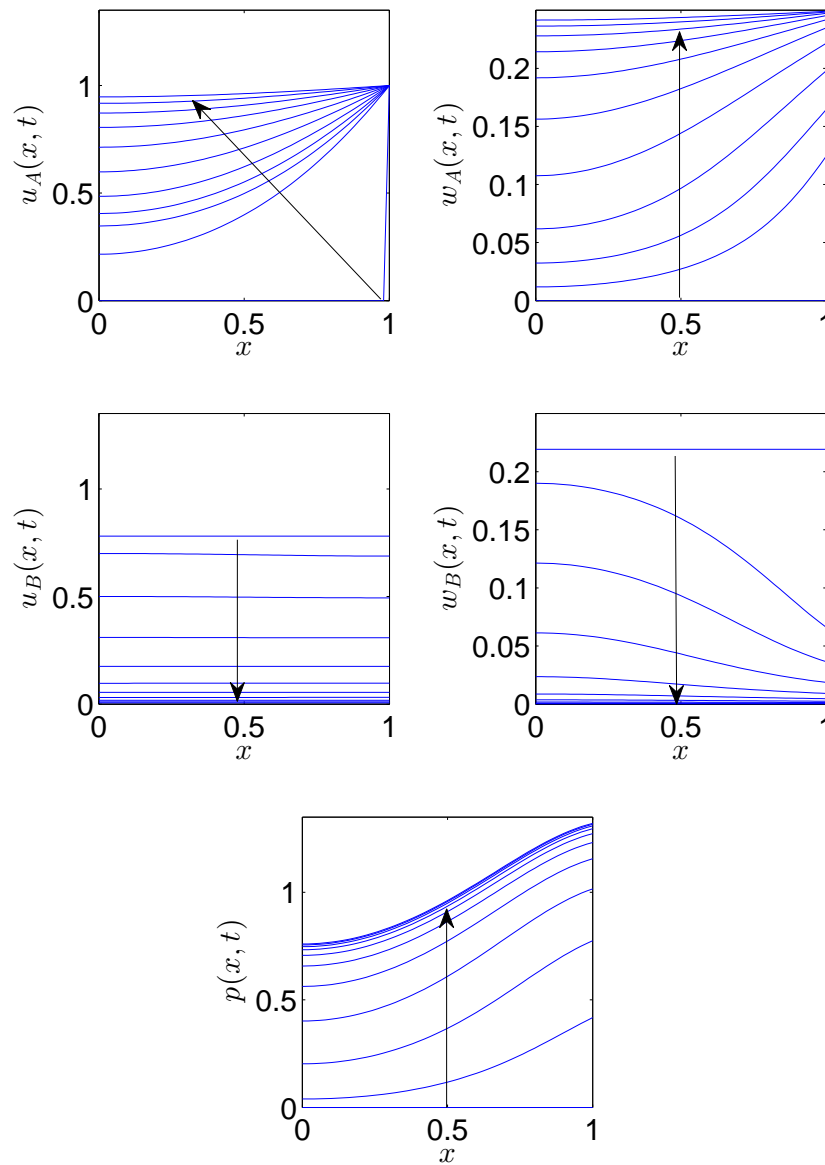


Figure 3.33: Concentration profiles of  $u_A$ ,  $u_B$ ,  $w_A$ ,  $w_B$  and  $p$  at 10 uniform times ranging from  $t = 0$  to 25 when parameters are chosen such that we are in an intermediate regime.

roughly the same rate throughout the domain. From the fourth plot we can see that the adsorbed concentration of reactant decreases more quickly at  $x = 1$  than

$x = 0$ . This is due to the increased concentration of  $w_A$  being able to react with  $w_B$  close to  $x = 1$ . The final plot shows that the product forms more quickly at  $x = 1$  than  $x = 0$  and that the final concentration of  $p$  is significantly larger at  $x = 1$  than  $x = 0$ .

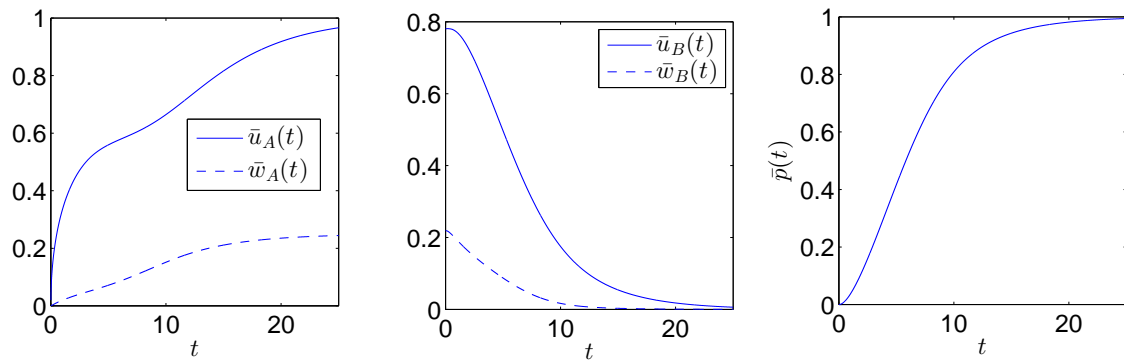


Figure 3.34: Average concentrations of  $u_A$ ,  $u_B$ ,  $w_A$ ,  $w_B$  and  $p$  plotted against time when parameters are chosen such that we are in an intermediate regime.

Figure 3.34 shows average concentrations of  $u_A$ ,  $u_B$ ,  $w_A$ ,  $w_B$  and  $p$  plotted against time. From these plots we can see that, although the increase in  $u_A$  and  $w_A$  is slightly different, the decrease in  $u_B$  and  $w_B$  does not look unlike the plots presented in the previous chapter. Similarly, the production of product look fairly similar to previous systems.

### 3.4.10 Experimenting with film thickness

As in previous models, we are interested in how  $R_i$  varies with  $L$ , where  $R_i$  is defined in Section 3.4.6. Using the nondimensional scalings given in Section 3.4.3, we are able to redefine our parameters such that we are always solving over an  $x$  region ranging from 0 to 1. This simply means that we rescale our parameters appropriately before numerically solving the system. To present our results we scale all parameters back to their original form. For each simulation, Method 1 was used with 20 grid points and  $2.5 \times 10^6$  time steps.

Both plots of Figure 3.35 show the results when  $\ln(L)$  is varied from approxi-

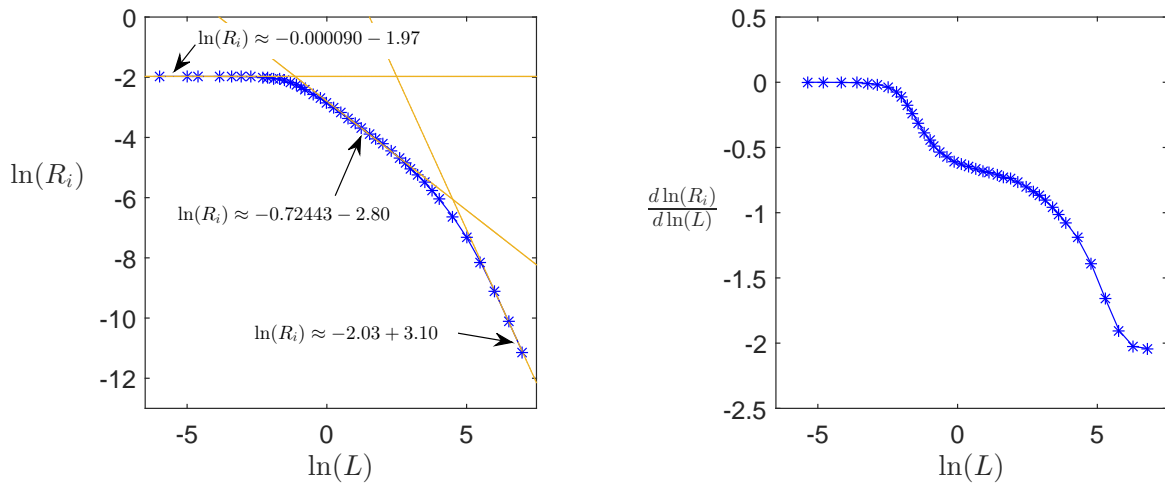


Figure 3.35: The left hand plot shows how  $\ln(R_i)$  varies with  $\ln(L)$  and the right hand plot shows how  $\frac{d \ln(R_i)}{d \ln(L)}$  varies with  $\ln(L)$ . Both plots show that there are three distinct regions.

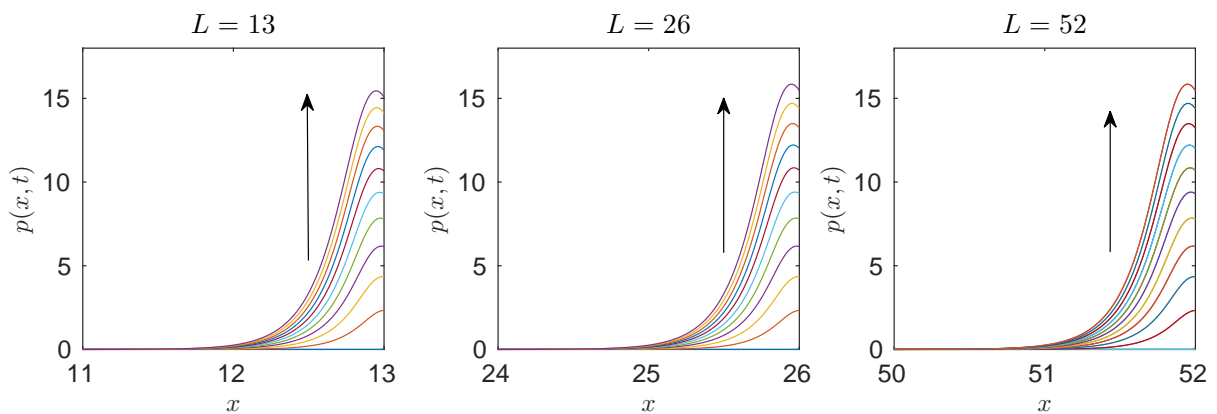


Figure 3.36: The three plots show simulation results when we have  $L = 13$ ,  $L = 26$  and  $L = 52$ . All three plots show profiles of  $p(x, t)$  plotted at 10 uniform times ranging from  $t = 0$  to  $t = 150$ . The  $x$ -axis in each plot corresponds to  $x = L - 2$  to  $x = L$ .

mately -6 to 7. The first plot shows  $\ln(R_i)$  plotted against  $\ln(L)$ . For the smallest  $L$  values considered, Figure 3.35 shows that the initial reaction rate is approximately constant, whereas for the largest values of  $L$  considered, the initial reaction rate is approximately proportional to  $\frac{1}{L^2}$ . These extreme parameter regimes are similar

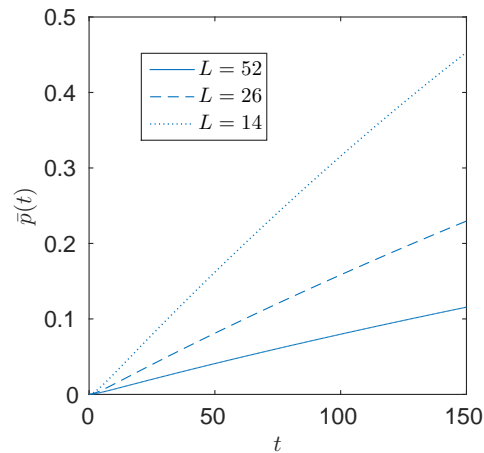


Figure 3.37: Plot of  $\bar{p}(t)$  against  $t$  for  $L = 13$ ,  $L = 26$  and  $L = 52$ . The plot demonstrates that as  $L$  is increased, it takes longer for  $\bar{p}(t)$  to reach 0.1.

to the Marek case discussed in Section 3.3.4.3. There is an intermediate regime where we have that  $R_i$  is approximately proportional to  $L^{-0.72}$ . Note that this is different to previous models where we found distinct regimes where  $R_i$  is approximately proportional to  $L^{-1}$ . The second plot of Figure 3.35 reinforces the fact that there are three distinct regions for the range of  $L$  values we have considered.

Although in this case we do not have a clear  $\frac{1}{L}$  dependence on the initial reaction rate, from the second plot of 3.35 we can see that there is a small region where we would expect the initial reaction rate to be inversely proportional to  $L$ . We consider three different films where  $L = 13, 26$  and  $52$  (corresponding to  $\ln(L)$  values of approximately 2.6, 3.3 and 4.0, respectively). Figure 3.36 shows profiles of  $p(x, t)$  plotted at 10 uniform times ranging from  $t = 0$  to  $t = 150$  for the three different films considered. For each film, the plots presented focus on the increase in  $p(x, t)$  close to the right hand boundary. The plots show that, the production of  $p$  is very similar across the three films. Hence, the rate that the total amount of product is being produced is constant for this regime; however, as we are considering the average of  $p$  when calculating  $R_i$ , we have that  $R_i$  is inversely proportional to  $L$ . This is illustrated in Figure 3.37, which shows that the average concentration of product increases less quickly for larger values of  $L$ . However, this

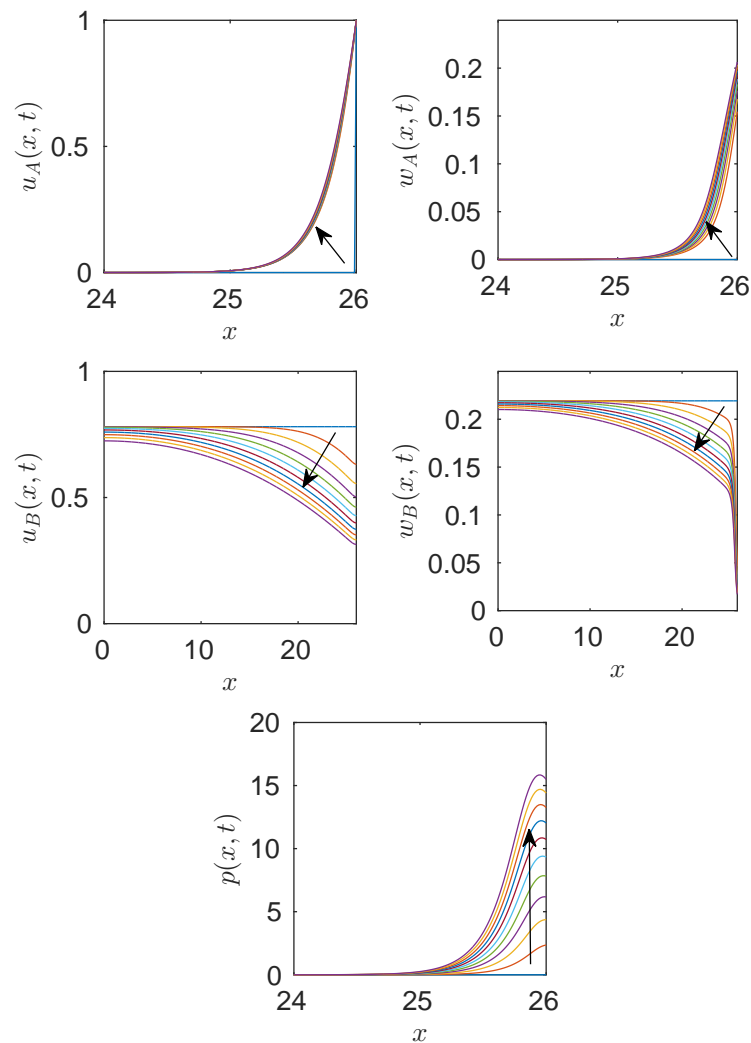


Figure 3.38: Concentration profiles of  $u_A$ ,  $u_B$ ,  $w_A$ ,  $w_B$  and  $p$  at 10 uniform times ranging from  $t = 0$  to  $t = 25$  when parameters are chosen such that we are in an intermediate regime with  $L = 26$ .

behaviour is only observed for a very small range of  $L$  values. When we decrease  $L$  below 13, the film is not thick enough to ensure that diffusion of reactant is slow enough to ensure that what happens at the boundary is independent of film thickness. Hence, we do not see a wider range of  $L$  values where  $R_i$  is inversely proportional to  $L$ . The reason behind the distinct region where  $R_i$  is approximately

proportional to -0.72 is not clear.

Figure 3.38 shows concentration profiles of  $u_A$ ,  $u_B$ ,  $w_A$ ,  $w_B$  and  $p$  plotted at 10 uniform times ranging from  $t = 0$  to  $t = 150$  with  $L = 26$ . For this particular regime, we have that the constant supply of  $U_A$  is allowing a continual supply of  $W_A$  at  $x = L$ . Due to the relatively fast rate of diffusion of  $U_B$ , relative to  $U_A$ , the amount of  $W_B$  at the boundary is continually replenished to allow the reaction to continue close to  $x = L$ . As the reaction is happening close to  $x = L$ , varying  $L$  does not have an influence on the rate at which the total amount of  $P$  is increasing, which is why we have the result of  $R_i$  being approximately inversely proportional to  $L$  for a small region of  $L$  values.

### 3.5 Conclusions

In this chapter we have considered a number of systems where reactions take place throughout the domain. We devised a general model which we initially applied to a simple model proposed by Ollis [67]. We were able to replicate the results presented by Ollis. Additionally, we were able to show that there is a parameter regime outwith the case considered by Ollis where the same qualitative results can be observed. We also considered the applicability of the QSSA for this system and were able to show that, although for two cases the QSSA gave very similar results to the full system, the QSSA is not valid universally for this system.

In Section 3.2.3 we were able to replicate results presented by Ollis, which partially validated the general model we proposed. Further experimental data would be useful to validate our model in a range of different parameter regimes. For example, we considered a regime where the adsorption process was significantly quicker than the surface reaction rate. This was a regime that the simple Ollis model could not replicate. This scenario could be explored experimentally by creating a system where the intensity of light at the photocatalyst surface is very low. This would lead to a slow surface reaction rate, relative to adsorption/desorption

process, and our model could potentially be used to model this system. Alternative systems which are known to have a quicker adsorption rate than surface reaction rate could be explored to further probe our proposed model.

By replicating the numerical results presented by Marek *et al.* [46] we were able to use this previously proposed model to experiment with film thickness. We were able to demonstrate that there is range of  $L$  values where the initial reaction rate was approximately proportional to  $\frac{1}{L}$ . As in the previous chapter, we gave a suggestion as to why this may be the case. Our results could be further validated by experiments examining how varying the film thickness influences the reaction rate. In particular, if experiments focused on films ranging from extremely thin to extremely thick films we may be able to validate our identification of three distinct regimes.

Finally we presented a general model which was motivated by informal experimental results for a system where gas diffuses into a polymer film before reacting with a dye throughout the film. For one particular set of parameters, like previous systems, we explored how the initial reaction rate varied with the film thickness. Although, unlike previous systems, there was not a distinct region where the initial rate was inversely proportional to the film thickness, there was a small region of  $L$  values where this behaviour was demonstrated. Interestingly, there was a regime where the initial reaction rate was inversely proportional to the film thickness raised to the power of 0.72. The reason for this was not clear.

Future work could further explore the reason behind this dependence. Additionally, a good set of experimental data would allow us to fit realistic parameters to our proposed model. Performing experimental results over a range of films varying in thickness, as was done in chapter 2, would be extremely useful in validating our proposed model.

# Chapter 4

## A kinetic model for the photocatalysed removal of organic pollutants

### 4.1 Introduction

Photocatalyzed films are self-cleaning in that the majority of organic pollutants deposited onto a surface are readily mineralized by oxygen via the photocatalytic process [58]. Ollis [67] has developed four simple reaction kinetics models for photocatalyzed removal of carbonaceous and sulfur films on self-cleaning surfaces. We consider three of these within this chapter; the other case considered by Ollis was discussed in Section 3.1:

**Case 1.** Non-porous photocatalyst, non-porous transparent organic overlayer (e.g. stearic, palmitic acids).

**Case 2.** Non-porous photocatalyst, non-transparent porous overlayer (e.g. sulfur).

**Case 3.** Non-porous photocatalyst, adjacent organic layer (e.g. soot).

Ollis shows that his proposed models provide a good fit to published data available for each system.

The systems considered in this chapter are similar to the resazurin case considered in Chapter 2. However, within this chapter, all systems considered involve domains which either increase or decrease in size as a function of time. We develop general models and apply them to three cases considered by Ollis. We will investigate the accuracy of the QSSA as we did in previous chapters. As we are proposing more general models, which make fewer assumptions than the models proposed by Ollis, there is potential to apply our models to a far wider range of systems than the simple models presented by Ollis.

## 4.2 Case 1: Non-absorbing film overlayer on a photocatalyst

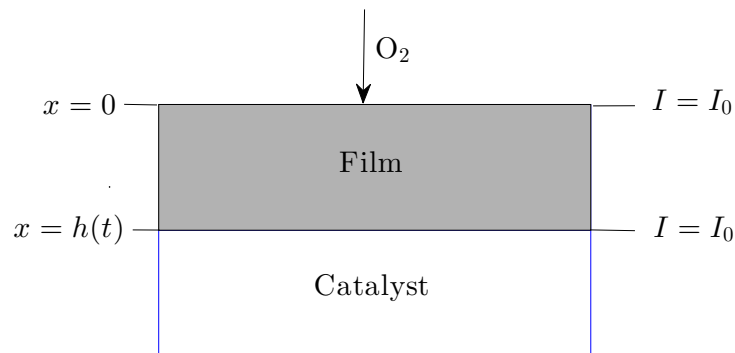


Figure 4.1: Diagram of the initial set-up of Case 1 (Ollis [67]) where a continuous supply of oxygen enters a non-absorbing film layer on a photocatalyst support.

Ollis considers a non-absorbing film overlayer on a non-porous photocatalyst support as shown in Figure 4.1. At one end of the film it is assumed that there is an unlimited supply of oxygen, meaning that the concentration of oxygen at one end

of the film remains constant throughout. Oxygen is free to diffuse throughout the film layer. At the photocatalyst surface it is assumed that oxygen is adsorbed and reacts with electron-hole pairs to form OH radicals. As the film is non-absorbing, the intensity of light reaching the catalyst is assumed to be constant. Hence, it is assumed that the rate at which bound oxygen molecules are converted to OH radicals is constant. The OH radicals are then assumed to react with organic molecules at the photocatalyst surface which results in the thinning of the film overlayer and the release of CO<sub>2</sub>. We therefore assume the following reaction mechanism at the photocatalyst surface



where the notation used is similar to previous chapters and  $S$  represents surface binding sites. This reaction is followed by the subsequent reaction between OH radicals and organics



where  $k$  represents the rate at which CO<sub>2</sub> and products are produced. Assuming simple mass action kinetics the rate equation for (4.2) is given by

$$\frac{d[\text{CO}_2 + \text{Products}]}{dt} = k[\text{OH}][\text{Organic}]_S,$$

where  $t$  represents time,  $k$  is a reaction rate constant, square brackets denote concentrations and  $[\text{Organic}]_S$ , specifically refers to the concentration of organic directly at the photocatalyst surface. We assume that this concentration remains constant. This is due to the fact that as soon as any organic substance reacts at the photocatalyst surface, any remaining organic substance will instantly fill the gap left by the organic which was involved in the reaction. This is what we assume

causes the film thickness to decrease. Hence, we assume the following reaction

$$\frac{d[\text{Organic}]_T}{dt} = -k[\text{OH}][\text{Organic}]_S,$$

where  $[\text{Organic}]_T$  represents the total amount of organic substance in the system. Hence, as we assume that the concentration of the organic at the photocatalyst surface remains constant throughout the reaction, then we have that

$$\frac{d[\text{Organic}]_T}{dt} = -\hat{k}[\text{OH}],$$

where  $\hat{k}$  is an effective rate constant. As it is assumed that the density  $\rho$  of the organic substance within the film is constant, we have that  $\rho h(t) = m[\text{Organic}]_T$  (where  $m$  is the molar mass of the organic substance), hence

$$\rho \frac{dh(t)}{dt} = -\bar{k}[\text{OH}], \quad (4.3)$$

where  $\bar{k}$  is an effective rate constant.

Ollis assumes that mass transfer of oxygen is not the rate limiting step in the reaction. For thin films it is therefore assumed that the rate of oxygen diffusion is rapid in relation to the rate of reaction at the photocatalyst surface. Hence, the concentration of reactant (OH radicals) at the surface is assumed constant until the film has disappeared completely. This assumption allows Ollis to simplify (4.3) to give

$$\rho \frac{dh(t)}{dt} = -k_0, \quad (4.4)$$

where  $k_0$  is an effective rate constant and the film mass per unit surface area is given by  $\rho$  times  $h(t)$ . Integrating (4.4) with respect to  $t$  gives

$$h(t) = h(0) - \frac{k_0 t}{\rho}.$$

Multiplying by the total film area  $A$  and  $\rho$  gives

$$M(t) = M(0) - Ak_0t,$$

where  $M(t)$  is the total mass of the film. Hence, Ollis predicts a zeroth-order reduction in film thickness with respect to concentration of reactant. It follows that the total film mass loss rate is also zeroth-order.

### 4.2.1 Experimental results

Two studies of multilayer carboxylic acid films (which appear to be non-porous) show zeroth-order reduction of film thickness. Paz *et al.* [71] have published data showing the integrated infra-red absorbance of stearic acid on  $\text{TiO}_2$ /fused quartz slides as a function of exposure to 365 nm light. It follows from the Beer-Lambert law that absorbance is proportional to film thickness [83]. Hence, as the absorbance is decreasing at an apparently constant rate, so is the thickness of the film. Hence, the rate at which the film thickness is decreasing is zeroth-order. Roméas *et al.* [75] have shown how the total concentration of palmitic acid decreases with time. Ollis has shown that this data is approximately zeroth-order, and hence agrees with the predictions obtained from the model.

## 4.3 Proposed model

We now present a general model which can be applied to the system discussed in the previous section. Our model will make less assumptions than the model presented by Ollis. Specifically, we will not assume that the transport of reactant (oxygen in the previous example) is rapid in relation to the reaction at the photocatalyst surface. We will also consider a reaction mechanism at the photocatalyst surface similar to the mechanism introduced in Section 2.1.1 to model the adsorption/desorption and subsequent conversion of reactant into product (equivalent to

the conversion of oxygen into OH radicals from the previous example). Finally, we will consider the reaction between the product at the surface and the organics within the film. This reaction results in a reduction in film thickness.

Hence we present a generalisation of (4.1) and (4.2), given by



where  $U$  represents a reactant, which once transported across the domain, can be adsorbed at the rate  $k_1$  onto a vacant surface reaction sites  $S$  to form a bound species  $W$ . The bound species can then either desorb at the rate  $k_{-1}$ , or alternatively, if illuminated with sufficient photons, be converted into a product  $P$  at the rate  $k_2$ . This product  $P$  reacts with organics at the rate  $k_3$  to produce additional products. This final reaction results in the film thickness reducing. This reaction scheme is similar to those presented in the previous two chapters; however, in this case there is an intermediate formed which goes on to form another product.

We let the film thickness be of length  $h(t)$  (as shown in Figure 4.1) and assume that the concentration of reactant  $U$  (this would represent oxygen in the previous section) is given by  $u(x, t)$ . We will assume that molecules of  $U$  are transported through the reactant layer via linear diffusion;

$$\frac{\partial u}{\partial t} = D \frac{\partial^2 u}{\partial x^2}, \quad 0 < x < h(t),
 \tag{4.6}$$

where  $D$  is a diffusion coefficient.

At  $x = 0$  we will assume that there is a constant supply of reactant, which is represented by  $u(0, t) = u_0$ . At  $x = h(t)$  we assume the reaction mechanism

described in (4.5), and hence

$$\left. \frac{\partial u}{\partial x} \right|_{x=h(t)} = \frac{1}{D} \left( -k_1 u(h(t), t) s_{tot} + (k_1 u(h(t), t) + k_{-1}) w(t) \right), \quad (4.7)$$

where  $w(t)$  represents the concentration of adsorbed reactant, and (2.2) defines how  $w(t)$  varies with time.

We will assume that prior to our system being illuminated, the reactant is free to enter the system and adsorb/desorb from the photocatalyst surface before a surface reaction occurs. As in Section 2.1.4, we can find pre-illumination concentrations  $u_q$  and  $w_q$  which we will make use of when defining our initial conditions for  $u$  and  $w$ , respectively.

When finding the pre-illumination equilibrium concentrations we assume that  $u$  and  $w$  are constant in time. Hence, by integrating the right hand side of (4.6) we have that  $u(x, t) = ax + b$ , where  $a$  and  $b$  are constants. At  $x = 0$  we have that  $u = u_0$  at all times. At  $x = h(0)$  we assume that  $u = u_q$ . Hence, pre-illumination (with  $k_2 = 0$ ) we have that

$$u(x, t) = \left( \frac{u_q - u_0}{h(0)} \right) x + u_0. \quad (4.8)$$

We differentiate (4.8) with respect to  $x$  and equate to the boundary condition (4.7) where, assuming we are in equilibrium,  $u(h(0), t) = u_q$ , hence

$$\frac{u_q - u_0}{h(0)} = -\frac{1}{D} (k_1 u_q s_{tot} - (k_1 u_q + k_{-1}) w_q). \quad (4.9)$$

Assuming the system is in equilibrium we can find an expression for the equilibrium concentration  $w_q$  by setting our equation for  $\frac{dw}{dt}$  (given by (2.2) in Section 2.1.1) equal to zero (with  $k_2 = 0$ ), which gives

$$w_q = \frac{k_1 u_q s_{tot}}{k_1 u_q + k_{-1}}. \quad (4.10)$$

We can now solve (4.9) and (4.10) simultaneously for  $u_q$  and  $w_q$ . The process is similar to our approach in Section 2.1.4. From this point forward we will assume that  $t = 0$  refers to a time where our system is already in pre-illumination equilibrium.

In previous chapters we assumed that the rate of change of the concentration of products  $p$  (equivalent to OH radicals from Section 4.2) at the photocatalyst surface is directly proportional to  $w$  (as in (2.3)). However, in this case the product  $P$  reacts with organics within the film. Therefore, by mass action kinetics we have

$$\frac{dp(t)}{dt} = k_2w(t) - k_3p(t), \quad (4.11)$$

where  $k_3$  is the reaction rate constant which dictates the rate at which the surface product is reacting with organics. Following a similar argument to that presented in the previous section we have the equivalent of (4.3) is given by

$$\rho \frac{dh(t)}{dt} = -k_3p(t). \quad (4.12)$$

As in the previous models we have considered, we can assume that the bound surface species are in a quasi-steady state. This will lead to an alternative boundary condition for  $u$  given by

$$\left. \frac{\partial u}{\partial x} \right|_{x=h(t)} = \frac{1}{D} \left( - \frac{k_1 k_2 s_{tot} u(h(t), t)}{k_1 u(h(t), t) + k_{-1} + k_2} \right). \quad (4.13)$$

By setting  $\frac{dw}{dt} = 0$  we can solve (2.2) for the steady state concentration of  $w(t)$ . In this case we have that  $w$  and  $p$  are both intermediate concentrations, hence if we apply the QSSA to both concentrations, we set (4.11) equal to zero and have

$$k_2w(t) = k_3p(t).$$

Hence, substituting the steady state concentration of  $w(t)$  into (4.12) gives the

following

$$\rho \frac{dh(t)}{dt} = -\frac{k_1 k_2 s_{tot} u(h(t), t)}{k_1 u(h(t), t) + k_{-1} + k_2}.$$

The nondimensionalisation in this case is similar to the process outlined in Section 2.1.2. However, in this case  $h_0$  will replace  $L$  in all scalings and we will have to nondimensionalise  $\rho$  and  $k_3$  in the following way

$$\hat{\rho} = \frac{\rho}{\rho_0}, \quad \hat{k}_3 = \frac{k_3 h_0^2}{D},$$

where  $\rho_0$  represents the density of any film being considered. Otherwise, there is no difference to the previous nondimensionalisation. Unless stated otherwise, all equations are nondimensional. As before, we will drop the hat notation for convenience.

The full system therefore evolves according to the equations

$$\left\{ \begin{array}{l} \frac{\partial u}{\partial t} = \frac{\partial^2 u}{\partial x^2}, \\ u(0, t) = 1, \\ \frac{\partial u}{\partial x}(h(t), t) = -k_1 u(h(t), t) s_{tot} + (k_1 u(h(t), t) + k_{-1}) w(t), \\ u(x, 0) = (1 - u_q)x + u_q, \\ \frac{dw}{dt} = k_1 u(0, t) s_{tot} - (k_1 u(0, t) + k_{-1} + k_2) w(t), \\ \frac{dp}{dt} = k_2 w(t) - k_3 p(t), \end{array} \right. \quad \begin{array}{l} 0 < x < h(t), \\ \\ \\ 0 \leq x \leq h(0), \\ w(0) = w_q, \\ p(0) = 0, \end{array} \quad (4.14)$$

$$\left\{ \begin{array}{l} \rho \frac{dh}{dt} = -k_3 p(t), \\ h(0) = 1. \end{array} \right. \quad (4.15)$$

Similarly, when the QSSA is invoked we have

$$\left\{ \begin{array}{l} \frac{\partial u}{\partial t} = \frac{\partial^2 u}{\partial x^2}, \quad 0 < x < h(t), \\ u(0, t) = 1, \\ \frac{\partial u}{\partial x}(h(t), t) = -\frac{k_1 k_2 s_{tot} u(h(t), t)}{k_1 u(h(t), t) + k_{-1} + k_2}, \\ u(x, 0) = (1 - u_q)x + u_q, \quad 0 \leq x \leq h(0), \end{array} \right. \quad (4.16)$$

$$\left\{ \begin{array}{l} \frac{dh}{dt} = -\frac{k_1 k_2 s_{tot} u(h(t), t)}{k_1 u(h(t), t) + k_{-1} + k_2}, \quad h(0) = 1. \end{array} \right. \quad (4.17)$$

## 4.4 Numerical method

The numerical method we propose is very similar to the method used to solve the system presented in Section 2.1.8. Note that, although we initially consider a contracting domain, the method of solving our systems is easily applied to an expanding domain.

We will use a similar method to that outlined by Mackenzie and Mekwi [44]. We will present the following analysis assuming we are solving the full system of equations; however, the method will be similar if the QSSA is invoked.

Let  $T > 0$  and for each  $t \in [0, T]$ ,  $\Omega_t$  be a time dependent domain in  $\mathbb{R}$ . We shall use the notation

$$Q_T = \{(x, t) \in \mathbb{R}^2 : x \in \Omega_t, t \in (0, T)\}.$$

We consider the linear diffusion equation

$$\left. \begin{aligned} \frac{\partial u}{\partial t} - \frac{\partial^2 u}{\partial x^2} &= 0, & (x, t) \in Q_T \\ u &= (1 - u_q)x + u_q, & x \in [0, h(0)], t = 0 \\ u(0, t) &= 1, & t \geq 0 \\ \frac{\partial u}{\partial x}(h(t), t) &= -k_1 u(h(t), t) s_{tot} + (k_1 u(h(t), t) + k_{-1})w(t), & t > 0. \end{aligned} \right\} \quad (4.18)$$

Let  $\mathcal{A}_t$  be a family of mappings, which at each  $t \in [0, T]$  maps the point  $\xi$  of a reference or computational domain  $\Omega_c$ , into the points of the domain  $\Omega_t$  at time  $t$ . Then, for each  $t \in [0, T]$

$$\mathcal{A}_t : \Omega_c \rightarrow \Omega_t, \quad x(\xi, t) = \mathcal{A}_t(\xi).$$

We assume that  $\mathcal{A}_t$  is bijective and  $\Omega_t = \mathcal{A}_t(\Omega_c)$  is bounded. For a function  $g : Q_T \rightarrow \mathbb{R}$  defined on the physical domain, the time derivative in the reference domain is

$$\dot{g} \equiv \left. \frac{\partial g}{\partial t} \right|_{\xi} : Q_T \rightarrow \mathbb{R}.$$

If  $u : Q_T \rightarrow \mathbb{R}$  is regular enough, then by the chain rule

$$\dot{u} = \left. \frac{\partial u}{\partial t} \right|_x + \dot{x} \left. \frac{\partial u}{\partial x} \right|_x,$$

where  $\dot{x}$  represents the ALE velocity. The diffusion equation of (4.18) in the physical domain therefore takes the form

$$\dot{u} - \frac{\partial^2 u}{\partial x^2} - \dot{x} \frac{\partial u}{\partial x} = 0, \quad (x, t) \in Q_T. \quad (4.19)$$

By the chain rule,

$$u_\xi = \frac{\partial u}{\partial x} x_\xi,$$

which can be rearranged to give

$$\frac{\partial u}{\partial x} = \frac{u_\xi}{x_\xi}. \quad (4.20)$$

By the chain rule, differentiating (4.20) with respect to  $x$  gives

$$\frac{\partial^2 u}{\partial x^2} = \left( \frac{u_\xi}{x_\xi} \right)_\xi \frac{1}{x_\xi}. \quad (4.21)$$

Hence, by substituting (4.20) and (4.21) into (4.19) and multiplying by  $x_\xi$ , we can rewrite the spatial derivatives in terms of the computational coordinate to get

$$x_\xi \dot{u} - \left( \frac{u_\xi}{x_\xi} \right)_\xi - \dot{x} u_\xi = 0, \quad (\xi, t) \in Q_C,$$

where

$$Q_C = \{(x, t) \in \mathbb{R}^2 : x \in \Omega_C, t \in (0, T)\}.$$

This is a non-conservative formulation and is the form that we will use when proceeding with our numerical method.

Instead of solving the diffusion equations given in (4.14) and (4.16) we now have to solve (4.19). Both  $\dot{u}$  and  $\dot{x}$  must be included in our numerical scheme to account for the time dependent domain. Throughout each simulation we will use a constant number of grid points, hence as  $h(t)$  decreases,  $\Delta x$  will decrease (as shown in Figure 4.2).

We will again use a finite difference method to find a numerical solution to the systems of equations (4.14) (full system) and (4.16) (QSSA system). We divide the spatial domain  $(0, h(t))$  into  $N$  equal intervals, and the temporal domain  $(0, T)$  into  $NT$  equal intervals with mesh spacings  $\Delta x(t)$  and  $\Delta t$ , respectively. We will find approximations of  $u$  at grid points, denoted by  $u_i^n = u(i\Delta x(t), n\Delta t)$ . When

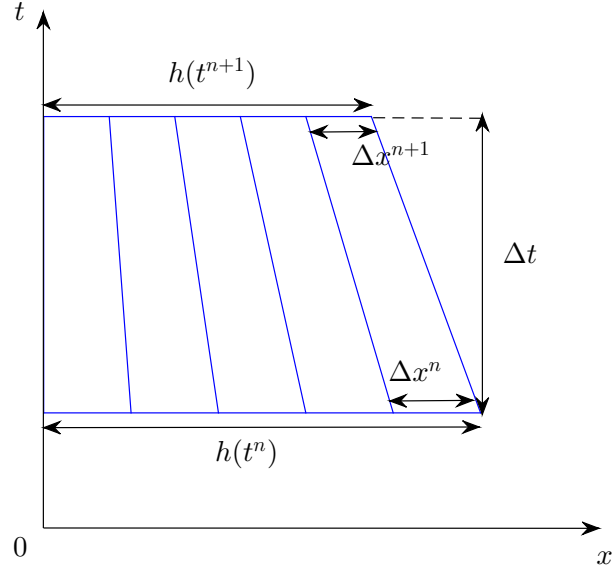


Figure 4.2: An example of how  $h(t)$  changes at each time step and how the grid changes to accommodate a contracting domain.

the QSSA is not invoked we will also approximate  $w$  at each time step, denoted by  $w^n = w(n\Delta t)$ . Additionally, for both systems we will approximate  $p$  and  $h$  at each time step, which will be denoted by  $p^n = p(n\Delta t)$  and  $h^n = h(n\Delta t)$ , respectively.

To solve the full system (4.14) and the QSSA system (4.16), a Crank-Nicolson scheme is proposed. A discretisation of (4.19) is given by

$$\begin{aligned} \frac{u_j^{n+1} - u_j^n}{\Delta t} - \left( \frac{x_j^{n+1} - x_j^n}{\Delta t} \right) \frac{1}{2} \left( \frac{u_{j+1}^{n+1} - u_{j-1}^{n+1}}{2\Delta x^{n+1}} + \frac{u_{j+1}^n - u_{j-1}^n}{2\Delta x^n} \right) \\ = \frac{1}{2} \left( \frac{u_{j+1}^{n+1} - 2u_j^{n+1} + u_{j-1}^{n+1}}{(\Delta x^{n+1})^2} + \frac{u_{j+1}^n - 2u_j^n + u_{j-1}^n}{(\Delta x^n)^2} \right), \end{aligned}$$

for  $j = 0, 1, 2, \dots, N$  and  $n = 0, 1, 2, \dots, NT - 1$ . If we let  $V^n = \frac{\Delta t}{2(\Delta x^n)^2}$  we have

$$\begin{aligned} & u_{j+1}^{n+1} \left( -\frac{x_j^{n+1} - x_j^n}{4\Delta x^{n+1}} - V^{n+1} \right) + u_j^{n+1} \left( 1 + 2V^{n+1} \right) + u_{j-1}^{n+1} \left( \frac{x_j^{n+1} - x_j^n}{4\Delta x^{n+1}} - V^{n+1} \right) \\ &= u_{j+1}^n \left( \frac{x_j^{n+1} - x_j^n}{4\Delta x^n} + V^n \right) + u_j^n \left( 1 - 2V^n \right) + u_{j-1}^n \left( -\frac{x_j^{n+1} - x_j^n}{4\Delta x^n} + V^n \right). \end{aligned} \quad (4.22)$$

At  $x = 0$  we have that  $u$  remains constant, where  $u_0^n = 1$  for all  $n$ . Evaluating (4.22) at  $j = 1$  and simplifying gives

$$\begin{aligned} & u_2^{n+1} \left( -\frac{x_1^{n+1} - x_1^n}{4\Delta x^{n+1}} - V^{n+1} \right) + u_1^{n+1} \left( 1 + 2V^{n+1} \right) \\ &= u_2^n \left( \frac{x_1^{n+1} - x_1^n}{4\Delta x^n} - V^n \right) + u_1^n \left( 1 - 2V^n \right) - \frac{x_1^{n+1} - x_1^n}{4\Delta x^{n+1}} - \frac{x_1^{n+1} - x_1^n}{4\Delta x^n} + V^n + V^{n+1}. \end{aligned} \quad (4.23)$$

How we proceed at this point depends on the system we are solving.

#### 4.4.1 Solving the full system

At  $x = h(t)$  we have the boundary condition defined in (4.14), which we discretise using a central finite difference approximation to give

$$\frac{u_{N+1}^n - u_{N-1}^n}{2\Delta x^n} = -k_1 u_N^n s_{tot} + (k_1 u_N^n + k_{-1}) w^n, \quad (4.24)$$

where  $u_{N+1}^n$  is a ghost node which does not appear explicitly in our numerical scheme. Rearranging (4.24) gives

$$u_{N+1}^n = u_{N-1}^n + c^n u_N^n + d^n,$$

where  $c^n = 2\Delta x^n k_1(w^n - s_{tot})$  and  $d^n = 2\Delta x^n k_{-1}w^n$ . Hence, evaluating (4.22) at  $j = N$  and simplifying gives

$$\begin{aligned} & u_N^{n+1} \left( 1 + 2V^{n+1} - c^{n+1} \left( -\frac{x_N^{n+1} - x_N^n}{4\Delta x^{n+1}} - V^{n+1} \right) \right) + u_{N-1}^{n+1} \left( -2V^{n+1} \right) \\ &= u_N^n \left( 1 - 2V^n - c^n \left( -\frac{x_N^{n+1} - x_N^n}{4\Delta x^n} + V^n \right) \right) + u_{N-1}^n \left( 2V^n \right) \\ &+ d^n \left( \frac{x_N^{n+1} - x_N^n}{4\Delta x^n} + V^n \right) - d^{n+1} \left( -\frac{x_N^{n+1} - x_N^{n+1}}{4\Delta x^{n+1}} + V^{n+1} \right). \end{aligned} \quad (4.25)$$

Our approach involves finding an initial estimate of  $w^{n+1}$  and using this estimate to approximate  $p^{n+1}$ , and ultimately to define how the boundary moves at each time step. We will refer to this initial estimate of  $w^{n+1}$  as  $w^{[n+1,1]}$ . We obtain this estimate by discretising the differential equation defining  $\frac{dw}{dt}$  from (4.14) using a forward Euler method to give

$$w^{[n+1,1]} = w^n + \Delta t(k_1 u_N^n s_{tot} - (k_1 u_N^n + k_{-1} + k_2)w^n). \quad (4.26)$$

A Crank-Nicolson discretisation of the differential equation defining  $\frac{dp}{dt}$  from (4.14) gives

$$p^{[n+1,1]} = \frac{p^n + \frac{\Delta t}{2}(k_2(w^{[n+1,1]} + w^n) - k_3 p^n)}{1 + \frac{\Delta t k_3}{2}}. \quad (4.27)$$

Discretising (4.15) using a Crank-Nicolson method gives

$$h^{[n+1,1]} = h^n + \frac{\Delta t k_3}{2}(p^{[n+1,1]} + p^n). \quad (4.28)$$

At this stage we can solve (4.22), (4.23) and (4.25) for an approximation of  $u^{n+1}$  which we will refer to as  $u^{[n+1,1]}$ . Using this approximation we can correct our approximation  $w^{[n+1,1]}$ , which we will refer to as  $w^{[n+1,2]}$ . Discretising the differential equation defining  $\frac{dw}{dt}$  from (4.14) using a Crank-Nicolson method we

have

$$w^{[n+1,2]} = w^n + \frac{\Delta t}{2} \left( k_1 u_N^n s_{tot} - (k_1 u_N^n + k_{-1} + k_2) w^n + k_1 u_N^{[n+1,1]} s_{tot} - (k_1 u_N^{[n+1,1]} + k_{-1} + k_2) w^{[n+1,1]} \right). \quad (4.29)$$

We can now recalculate an approximation of  $p^{n+1}$  from (4.27) by replacing  $w^{[n+1,1]}$  with  $w^{[n+1,2]}$ .

In summary, we use the following scheme to solve our full system:

1. Approximate  $w^{[n+1,1]}$  using a forward Euler method from (4.26);
2. Approximate  $p^{[n+1,1]}$  using a Crank-Nicolson method from (4.27);
3. Calculate  $h^{[n+1,1]}$  using a Crank-Nicolson method from (4.28) and create a uniform grid over the new domain  $[0, h^{[n+1,1]}]$ ;
4. Calculate  $u^{[n+1,1]}$  using a Crank-Nicolson method by solving (4.22), (4.23) and (4.25);
5. Calculate  $w^{[n+1,2]}$  using a Crank-Nicolson method from (4.29) using the approximation  $u^{[n+1,1]}$ ;
6. Calculate  $p^{[n+1,2]}$  using a Crank-Nicolson method from (4.27) replacing  $w^{[n+1,1]}$  with  $w^{[n+1,2]}$ .

As in previous cases, we can perform an iterative process at each time step by repeating Steps 4 to 6 as many times as required. However, we will demonstrate that the above algorithm is sufficient to maintain second-order temporal convergence.

### 4.4.2 Solving the QSSA system

If the QSSA is invoked, at  $x = h(t)$  we have the boundary condition defined in (4.13), which we discretise using a central finite difference approximation to give

$$\frac{u_{N+1}^n - u_{N-1}^n}{2\Delta x^n} = -\frac{k_1 k_2 u_N^n s_{tot}}{k_1 u_N^n + k_{-1} + k_2}. \quad (4.30)$$

Note that  $u_{N+1}^n$  is a ghost node which does not appear explicitly in our numerical scheme. Rearranging (4.30) gives

$$u_{N+1}^n = u_{N-1}^n - 2\Delta x^n \left( \frac{k_1 k_2 u_N^n s_{tot}}{k_1 u_N^n + k_{-1} + k_2} \right).$$

Hence, evaluating (4.22) at  $j = N$  and simplifying gives

$$\begin{aligned} & \left( u_{N-1}^{n+1} - 2\Delta x^{n+1} \left( \frac{k_1 k_2 u_N^{n+1} s_{tot}}{k_1 u_N^{n+1} + k_{-1} + k_2} \right) \right) \left( -\frac{x_N^{n+1} - x_N^n}{4\Delta x^{n+1}} - V^{n+1} \right) \\ & \quad + u_N^{n+1} \left( 1 + 2V^{n+1} \right) + u_{N-1}^{n+1} \left( \frac{x_N^{n+1} - x_N^n}{4\Delta x^{n+1}} - V^{n+1} \right) \\ & = \left( u_{N-1}^n - 2\Delta x^n \left( \frac{k_1 k_2 u_N^n s_{tot}}{k_1 u_N^n + k_{-1} + k_2} \right) \right) \left( \frac{x_N^{n+1} - x_N^n}{4\Delta x^n} + V^n \right) \\ & \quad + u_N^n \left( 1 - 2V^n \right) + u_{N-1}^n \left( -\frac{x_N^{n+1} - x_N^n}{4\Delta x^n} + V^n \right). \end{aligned} \quad (4.31)$$

We linearise (4.31) by using  $u_N^n$  as an approximation for  $u_N^{n+1}$  in the denominator from the first line and hence we replace

$$\frac{k_1 k_2 u_N^{n+1} s_{tot}}{k_1 u_N^{n+1} + k_{-1} + k_2} \quad \text{with} \quad \frac{k_1 k_2 u_N^{n+1} s_{tot}}{k_1 u_N^n + k_{-1} + k_2}.$$

This allows us to simplify (4.31) giving

$$\begin{aligned}
& u_N^{n+1} \left( 1 + 2V^{n+1} - 2\Delta x^{n+1} \left( \frac{k_1 k_2 s_{tot}}{k_1 u_N^n + k_{-1} + k_2} \right) \left( -\frac{x_N^{n+1} - x_N^n}{4\Delta x^{n+1}} - V^{n+1} \right) \right) \\
& \quad + u_{N-1}^{n+1} \left( -2V^{n+1} \right) \\
= & -2\Delta x^n \left( \frac{k_1 k_2 u_N^n s_{tot}}{k_1 u_N^n + k_{-1} + k_2} \right) \left( \frac{x_N^{n+1} - x_N^n}{4\Delta x^n} + V^n \right) + u_N^n \left( 1 - 2V^n \right) + u_{N-1}^n \left( 2V^n \right).
\end{aligned} \tag{4.32}$$

A forward Euler discretisation of the equation defining the evolution of  $h(t)$  from (4.16) gives

$$h^{[n+1,1]} = h^n - \Delta t \left( \frac{k_1 k_2 u_N^n s_{tot}}{k_1 u_N^n + k_{-1} + k_2} \right). \tag{4.33}$$

We next produce a uniform grid covering the interval  $[0, h^{[n+1,1]}]$  and solve (4.22), (4.23) and (4.32) for an estimate of  $u^{n+1}$  which we will refer to as  $u^{[n+1,1]}$ .

Having an estimate of  $u$  at the forward time step allows us to improve the approximation of  $h^{n+1}$  using the following discretisation

$$h^{[n+1,2]} = h^n - \frac{\Delta t}{2} \left( \frac{k_1 k_2 u_N^n s_{tot}}{k_1 u_N^n + k_{-1} + k_2} + \frac{k_1 k_2 u_N^{[n+1,1]} s_{tot}}{k_1 u_N^{[n+1,1]} + k_{-1} + k_2} \right). \tag{4.34}$$

After updating  $h^{n+1}$  using (4.34) we use  $u_N^{[n+1,1]}$  to replace  $\frac{k_1 k_2 s_{tot}}{k_1 u_N^n + k_{-1} + k_2}$  with  $\frac{k_1 k_2 s_{tot}}{k_1 u_N^{[n+1,1]} + k_{-1} + k_2}$  in (4.31) and solve for an improved approximation  $u^{[n+1,2]}$ . As previously, this routine can be repeated as many times as required.

In summary, we can use the following scheme to solve our QSSA system

- 1<sub>Q</sub>. Approximate  $h^{n+1}$  using a forward Euler method given in (4.33) and create a new grid;
- 2<sub>Q</sub>. Calculate  $u^{[n+1,1]}$  using a Crank-Nicolson method by solving (4.22), (4.23) and (4.32);
- 3<sub>Q</sub>. Calculate  $h^{[n+1,2]}$  using a Crank-Nicolson method given in (4.34) and create a

new grid;

- 4<sub>Q</sub>. Calculate  $u^{[n+1,2]}$  using a Crank-Nicolson method by solving (4.22), (4.23) and (4.32) using  $u_N^{[n+1,1]}$ .

### 4.4.3 Accuracy of the numerical scheme

We define the errors in the approximations as we did in (2.52) and (2.53) in Section 2.1.8.5. Our approach to testing temporal convergence will be very similar to the previous method. However, in this case, as the size of the domain is dependent on the solution at each time step, we have that the size of the domain possibly differs depending on the size of time step used. For example, by taking fewer time steps the solution will be less accurate, hence the approximation of how the domain is changing will be less accurate.

Recall that when we previously tested for temporal convergence we would calculate a solution using a large number of time steps and use this as our most accurate solution. This allowed us to approximate the rate of convergence. We will use the same approach in this case. From our most accurate solution we can determine how the domain size  $h(t)$  changes with time. When testing the convergence rates of  $u$ ,  $w$  and  $p$  we will simply ensure that the domain is changing at the same rate as the most accurate solution by using linear interpolation to determine the size of domain at each time step. Hence, although we will solve for  $u$ ,  $w$  and  $p$  at each time step, we will not use these approximations to determine how the domain is changing.

To approximate the convergence rate of  $h$  we perform a similar test to the one described above. For this test we calculate  $h(t)$  in each simulation as opposed to interpolating from the most accurate solution. Using the most accurate approximation of  $h(T)$ , we simply vary the number of time steps and compare  $h(T)$  with our most accurate solution in each case.

When solving the full system, Method 1 involves performing steps 1-6 of the

algorithm whereas Method 2 involves performing steps 1-4 only. When solving the QSSA system, Method  $1_Q$  involves performing steps  $1_Q$  to  $4_Q$  before repeating steps  $3_Q$  and  $4_Q$  to calculate  $h^{[n+1,3]}$  and  $u^{[n+1,3]}$ . Method  $2_Q$  involves performing steps  $1_Q$  to  $4_Q$ , and Method  $3_Q$  involves performing steps  $1_Q$  to  $2_Q$ .

We will choose parameters such that we are in an intermediate regime. The following parameters were used during simulations to test temporal and spatial convergence;  $s_{tot} = 1$ ,  $k_1 = 1$ ,  $k_{-1} = 1$ ,  $k_2 = 1$ ,  $k_3 = 1$ ,  $\rho = 1$  and  $T = 3$ .

We initially test the temporal convergence rates when solving our full system. For these simulations we have  $N = 200$ . For our most accurate solution we have  $NT = 1.24 \times 10^5$ . We compare this solution with solutions obtained when we vary  $NT$  from 800 to  $1.28 \times 10^4$ . The results in Figures 4.3 - 4.6 show that Method 1 gives second-order temporal convergence when the full system is solved using this particular set of parameters and Method 2 is only first-order convergent.

The results in Figures 4.7 - 4.10 show that we have second-order spatial convergence when the full system is solved using Method 1 and Method 2. For all simulations  $NT = 1.28 \times 10^5$ . For our approximation to the exact solution  $N = 400$  grid points were used. We compared this exact solution with the solution when we varied  $N$  from 5 to 40. Note that we have chosen  $NT$  large enough to ensure that there is little to no benefit of solving for  $u^{n+1}$  more than once per time step. This is true for both the full system and QSSA system.

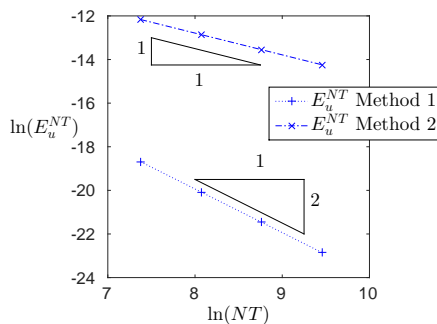


Figure 4.3: Temporal convergence results for  $u$  using Methods 1 and 2.

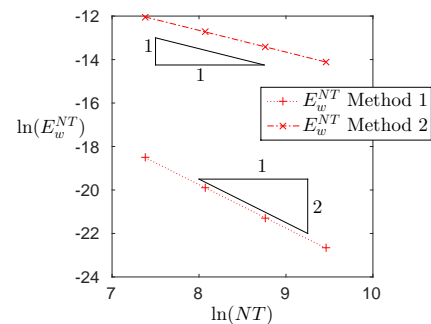


Figure 4.4: Temporal convergence results for  $w$  using Methods 1 and 2.

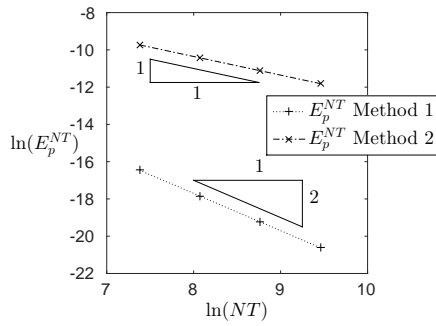


Figure 4.5: Temporal convergence results for  $p$  using Methods 1 and 2.

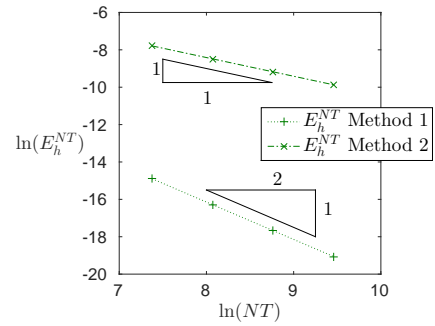


Figure 4.6: Temporal convergence results for  $h$  using Methods 1 and 2.

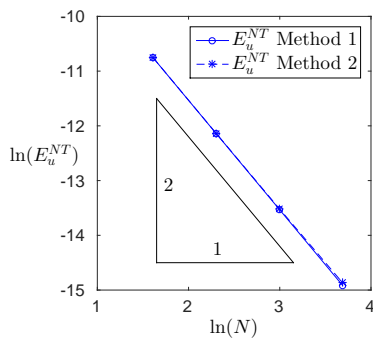


Figure 4.7: Spatial convergence results for  $u$  using Methods 1 and 2.

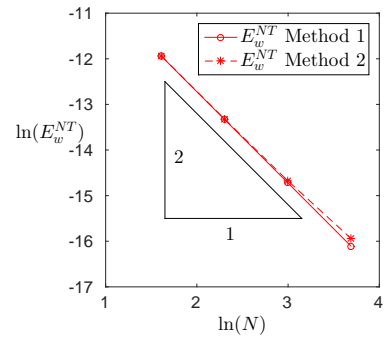


Figure 4.8: Spatial convergence results for  $w$  using Methods 1 and 2.

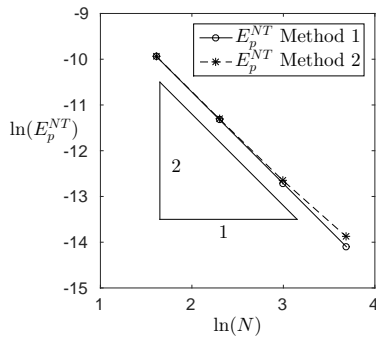


Figure 4.9: Spatial convergence results for  $p$  using Methods 1 and 2.

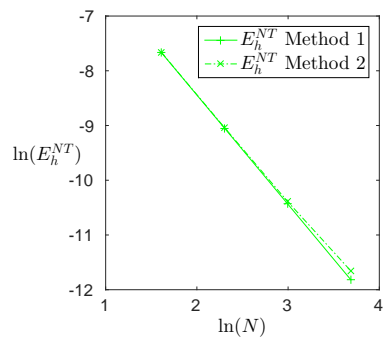


Figure 4.10: Spatial convergence results for  $h$  using Methods 1 and 2.

The same convergence test was carried out when we solve the QSSA system using the same parameters. For the spatial convergence tests we vary  $NT$  from 3,200 to  $5.1 \times 10^4$  and use  $NT = 5.5 \times 10^5$  to calculate the reference solution. Throughout the simulation  $N = 400$  grid points were used. The results presented

in Figures 4.11 and 4.12 are less convincing than when the full system is solved. Both figures shows that for second-order convergence Method  $1_Q$  has to be used. This method involves solving a linear system for  $u^{n+1}$  three times at each time step which is expensive.

We also performed spatial convergence tests using the same set of parameters. Convergence results for  $u$  and  $h$  are shown in Figures 4.13 and 4.14, respectively. For these simulations  $NT = 5.5 \times 10^5$  throughout. For the reference solution we use  $N = 400$  and compare the solution when we vary  $N$  from 5 to 40. Both plots show that we have second-order spatial convergence.

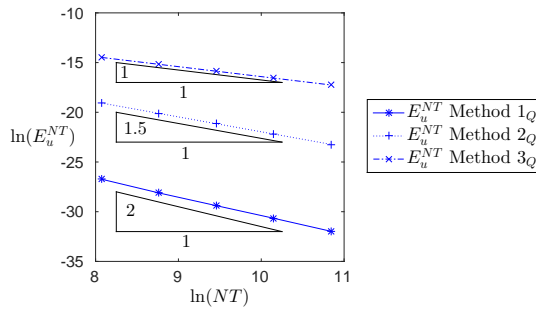


Figure 4.11: Temporal convergence results for  $u$  when the QSSA is invoked.

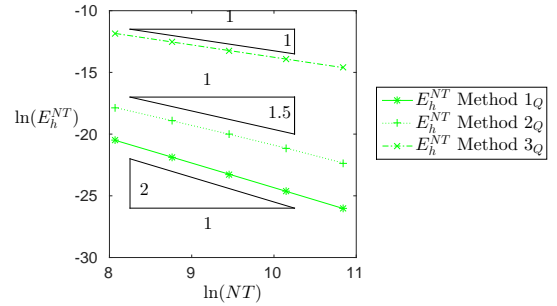


Figure 4.12: Temporal convergence results for  $h$  when the QSSA is invoked.

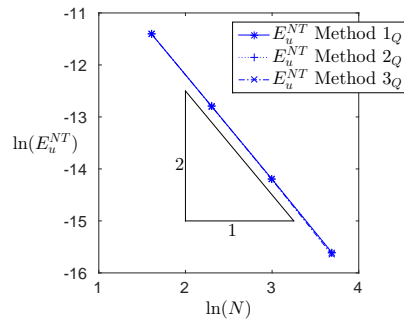


Figure 4.13: Spatial convergence results for  $u$  when the QSSA is invoked.

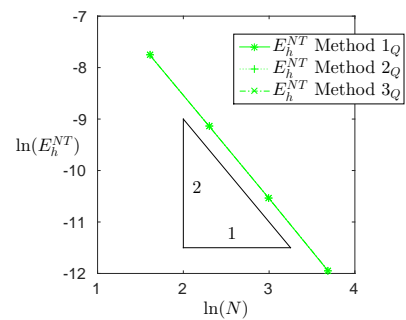


Figure 4.14: Spatial convergence results for  $h$  when the QSSA is invoked.

The temporal convergence results presented above are very similar to those presented earlier when solving on a stationary domain (Sections 2.1.8.5 and 2.1.8.6). When we are solving the full system our method gives second-order temporal

convergence by calculating  $u$  and  $h$  only once at each time step (followed by recalculating  $w$  and  $p$  at each time step). However, when solving the QSSA system, for this particular set of parameters, we must solve for  $u$  and  $h$  three times at each time step to maintain second-order temporal convergence. Hence, it is more efficient to solve the full system as fewer assumptions are made and it is less expensive to maintain second-order temporal convergence. However, we will continue to use our numerical method to investigate the applicability of the QSSA.

#### 4.4.4 General model

We can apply the model presented in Section 4.3 to the problem described in Section 4.2. In this case  $u(x, t)$  represents the concentration of oxygen throughout the domain and  $w(t)$  represents the adsorbed concentration of oxygen at the photocatalyst surface. The reaction occurring at the surface causes the thickness of the film to decrease.

Ollis [67] assumes that diffusion does not play a major role in the overall kinetics, i.e. that diffusion is not the rate limiting step, and has assumed that the surface reaction rate is zeroth-order; our model does not make either of these assumptions.

We initially assume that diffusion is fast in comparison to the reaction kinetics at the boundary. We came to the conclusion in Section 2.1.5 that if this was the case the QSSA will only hold for certain parameter regimes. However, our previous model did not consider a moving domain or a constant supply of reactant. Recall that we previously calculated  $\epsilon$  using (2.18) from Section 2.1.5. However, this was assuming that we were solving over a stationary domain (which we nondimensionalised) and assumed that there was a finite amount of reactant in the system. Previously, due to our choice of scaling when nondimensionalising we had that  $L$  was effectively one. However, in this case, as  $h(t)$  varies with time, we would have to include  $h(t)$  in our expression for  $\epsilon$  (which would also be time dependent). Hence, due to the substantial differences between this current system

and the previous system considered we will not use  $\epsilon$  to estimate the applicability of the QSSA.

Table 4.1 shows the parameters used for two different simulations. The parameters used in case (a) were chosen to replicate the results presented by Ollis [67]. As Ollis has assumed that the mass transfer of oxygen is not the rate-limiting step, we have chosen  $k_1$ ,  $k_{-1}$ ,  $k_2$  and  $k_3$  to be small relative the diffusion coefficient, which is effectively one. Ollis also assumed a constant supply of hydroxyl radicals at the photocatalyst surface. In our model this is equivalent to  $p(t)$  remaining constant. One way of ensuring that  $p(t)$  remains approximately constant is choosing parameters to ensure that  $p(t)$  remains close to zero. By choosing  $k_3$  to be large relative to  $k_2$ , any product  $p$  at the photocatalyst surface will react very quickly, relative to how quickly  $p(t)$  is produced. Hence, as  $p(t)$  is being used up more quickly than it is being formed,  $p(t)$  remains close to zero for the whole of the simulation. Hence,  $p(t)$  remains relatively constant. A range of parameter regimes were considered, and our simulations showed that, in all cases where diffusion was not the rate limiting step, and  $k_3$  was large relative to  $k_2$ , the results were qualitatively similar to the results we present in this chapter. Hence, case (a) is representative of a wide range of parameter regimes. Additionally, the results presented are not sensitive to small changes in the parameters chosen.

Figures 4.15 and 4.16 show a comparison between using the full system, the QSSA system, and an analytic approximation with the same set of parameters. For each set of parameters we compare how  $h(t)$  varies with  $t$  for all three methods. We also plot  $u(h(t), t)$ ,  $w(t)$  and  $p(t)$  against  $t$ , obtained from solving the full system, and  $u(h(t), t)$  when the QSSA system was solved, which we refer to as  $u_Q(h(t), t)$ .

	$k_1$	$k_{-1}$	$k_2$	$k_3$	$\rho$	$s_{tot}$	$T$
(a)	0.01	0.1	0.01	0.1	1	1	1200
(b)	0.1	0.01	0.1	0.1	1	1	30

Table 4.1: Table showing the parameters used for the two different regimes considered.

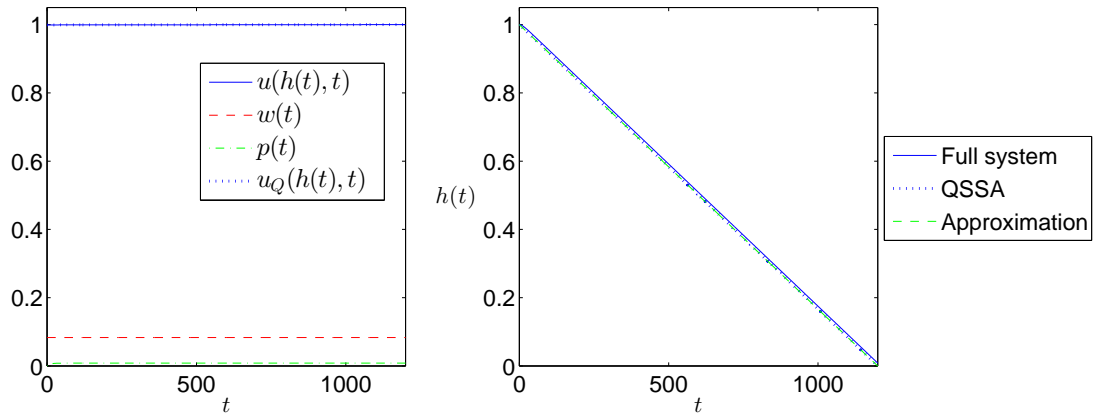


Figure 4.15: Case (a) simulation results demonstrating that the QSSA is a good approximation to the full system with this set of parameters.

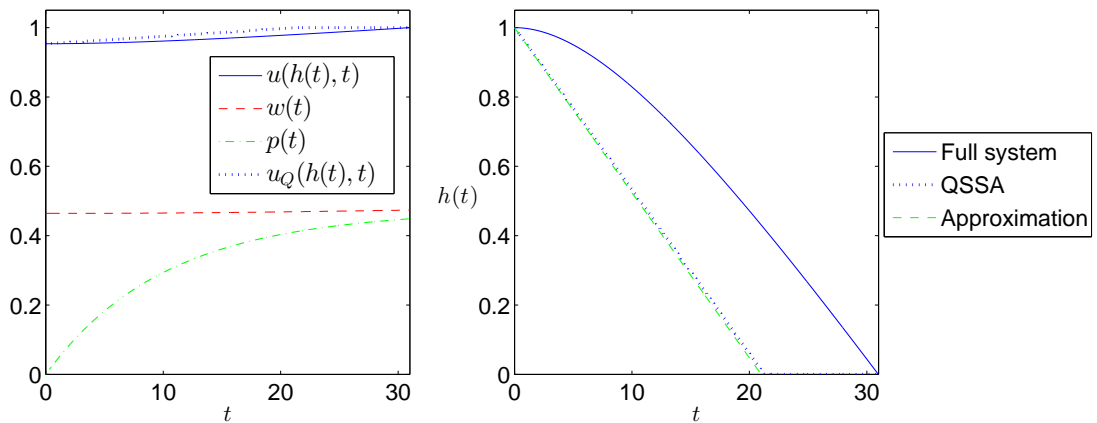


Figure 4.16: Case (b) simulation results demonstrating that the QSSA system and the full system give significantly different results.

Figure 4.15 gives an example of a regime where the QSSA system and the full system give almost identical results (in terms of  $u(h(t), t)$  and  $h(t)$ ). Due to the choice of parameters we are in a regime where very little product is formed at the boundary and  $w(t)$  remains constant throughout. Hence, it is unsurprising that

the QSSA holds in this case. The results also agree with the findings from the Ollis model, that  $h(t)$  decreases at a constant rate.

If we apply the assumptions made by Ollis to our model we have that the QSSA is valid, hence  $h(t)$  decreases according to (4.17). If we further assume, like Ollis, that the concentration of oxygen at the photocatalyst surface,  $u(h(t), t)$  in our model, remains constant throughout the reaction, we have that

$$\frac{dh}{dt} = -K_0, \quad (4.35)$$

where  $K_0 = \frac{1}{\rho} \left( \frac{k_1 k_2 s_{tot} u(h(t), t)}{k_1 u(h(t), t) + k_{-1} + k_2} \right)$ . This approximation of how  $h(t)$  varies with time is almost identical to the results obtained when the QSSA has been invoked, as demonstrated in Figure 4.15.

Although our model can replicate the results presented by Ollis, we are also able to simulate a far wider range of systems. For example, Figure 4.16 shows a parameter regime where the QSSA is not valid. The parameters chosen for case (b) were deliberately chosen such that  $k_2$  was of a similar size to  $k_3$ . This means that  $k_3$  is not large enough to ensure that any product formed is reacting much more quickly than it is being formed. Hence, unlike the previous case, we would not expect  $p(t)$  to remain approximately equal to zero throughout the simulation. Furthermore,  $k_1$  and  $k_{-1}$  were chosen to ensure that the adsorption process is not the rate-limiting step. If the adsorption was rate-limiting, we would expect  $w(t)$  to remain approximately equal to zero, leading to a regime where the QSSA is valid. Note that there are numerous other regimes where the QSSA will not be a valid assumption to make for this model. As in previous cases, the results presented in this section are not sensitive to small changes in parameter values.

The left hand plot of Figure 4.16 shows that, although  $w(t)$  remains approximately constant throughout the simulation,  $p(t)$  varies significantly. This example demonstrates that our model is able to predict significantly different behaviour than the simple model proposed by Ollis.

If we again apply the assumptions made by Ollis to this regime, we find that the approximation (4.35) is not particularly accurate, as is shown in Figure 4.16. Again, the approximation is very similar to the results obtained when the QSSA is assumed. This demonstrates that the assumptions made by Ollis do not hold for this particular parameter regime.

## 4.5 Case 2: Absorbing film overlayer on a photocatalyst

### 4.5.1 Ollis model

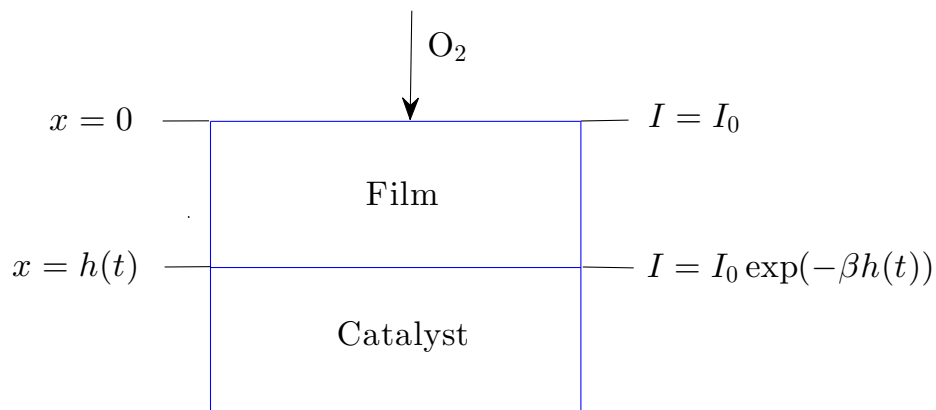


Figure 4.17: Diagram of the initial set-up of Case 2 (Ollis [67]).

Ollis considers an absorbing film overlayer on a photocatalyst surface. Like Case 1 discussed in Section 4.2,  $h(t)$  will decrease with time. As the film overlayer absorbs light, the intensity reaching the surface depends on the film thickness.

Ollis assumes a Beer's law decline of intensity in the film layer and assumes that diffusion does not influence the reduction of  $h(t)$ . As before, Ollis assumes that the concentration of reactant at the photocatalyst surface remains constant

throughout. The rate of change of the film thickness is given by

$$\frac{dh(t)}{dt} = -r = -k_0 \exp(-\beta h(t)), \quad (4.36)$$

where  $k_0$  is a zero order rate constant and  $\beta$  is the absorbance coefficient. Integrating (4.36) with respect to  $t$  gives

$$h(t) = \frac{1}{\beta} \ln(\exp(\beta h_0) - \beta k_0 t). \quad (4.37)$$

Note that this is very similar to the model proposed by Ollis which we presented in Section 4.2, however in this case  $k_0$  is replaced with  $k_0 \exp(-\beta h(t))$  to represent the fact that light is being absorbed by the film.

### 4.5.2 Experimental results

Mills *et al.* [49] have published a study on the disappearance of a sulfur layer on a typical thick titania film in air by semiconductor photocatalysis. Mills *et al.* plot the change in absorbance (at a wavelength of 600nm) due to sulfur on a typical titania film against irradiation time. It appears that the kinetics are initially zeroth-order before becoming first-order. As absorbance is proportional to concentration, and in this case film thickness, it is possible to compare these results with the prediction made by Ollis given in (4.37). The model proposed by Ollis is a fairly good fit for the experimental data [67].

### 4.5.3 Generalised model

We will apply the model proposed in Section 4.3 to the problem described in this section. In this case sulphur replaces the organic in reaction (4.2). In this case we

have that  $k_2$  varies with  $h(t)$ , hence we will define  $k_2$  as

$$k_2(t) = k'_2 I(h(t)) = k'_2 I_0 \exp(-\beta h(t)).$$

The numerical method used to solve both the full system and the QSSA system is as described in Section 4.2. However, since  $k_2$  is time dependent, we update  $k_2$  at each time step. The numerical method used to solve the system is very similar to the methods presented in Sections 4.4.1 and 4.4.2.

#### 4.5.4 Simulations

We use the same parameters as those shown in Table 4.1, however, we reduce the  $k_2$  value from case (a) by a factor of 10 for this simulation to replicate the results presented by Ollis. Note that, were we to use the original  $k_2$  value, i.e. without reducing by a factor of 10, the observed kinetics would be qualitatively very similar to those presented in this section. This is due to  $k_3$  being substantially larger than  $k_2$  in both cases. We compare results when the full system is solved and the QSSA system is solved. For both simulations we set  $I_0 = 1$  and  $\beta = 1$ . The results presented in this section are not sensitive to small changes in parameter values. The first set of parameters relate to a regime, when  $k_2$  was constant, where the QSSA was a good approximation. Figure 4.18 shows that, even with a time dependent  $k_2$ , the QSSA is a fairly good approximation.

Similar to the previous model, if we make similar assumptions to Ollis, we assume the QSSA is valid and we have that the equivalent of (4.35) would be given by

$$\frac{dh}{dt} = -\frac{1}{\rho} \left( \frac{k_1 k'_2 I_0 \exp(\beta h(t)) s_{tot} u(h(t), y)}{k_1 u(h(t), t) + k_1 + k'_2 I_0 \exp(\beta(h(t)))} \right).$$

If we assume that  $k'_2 I_0 \exp(\beta(h(t)))$  is small in comparison to  $k_1 u(g(t), t)$  and  $k_{-1}$  (which is the case for the parameters we have chosen), we have that

$$\frac{dh}{dt} \approx -K_0 \exp(\beta h(t)),$$

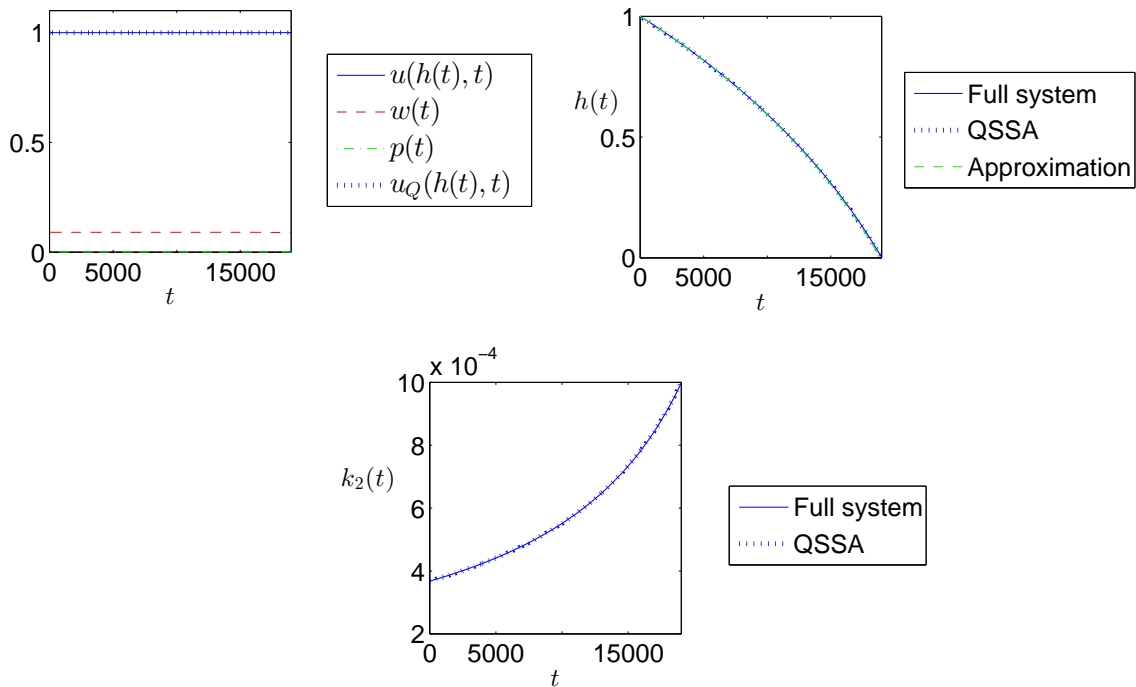


Figure 4.18: Case (a) simulation results demonstrating that the QSSA is a good approximation to the full system for this set of parameters.

where  $K_0 = \frac{1}{\rho} \left( \frac{k_1 k_2' I_0 s_{tot} u(h(t), t)}{k_1 u(h(t), t) + k_{-1}} \right)$ . This is similar to the expression which arose from the Ollis model. Figure 4.18 shows that this approximation is similar to the QSSA results and the full system results. However, it should be noted that this finding is dependent on an extra assumption regarding the size of  $k_2$  in comparison to other parameters and concentrations. Hence, we have shown with this particular set of parameters, that we can qualitatively replicate the results presented by Ollis, i.e. the reduction of  $h(t)$  predicted in Figure 4.18 is very similar to the reduction predicted by the simple model proposed by Ollis.

Figure 4.19 shows an example of a parameter regime where the full system, QSSA system and analytical approximation all give different results. We use the same case (b) parameters as those shown in Table 4.1. Note that the full system and QSSA results are similar to the results presented in Figure 4.16. Note that

the results presented in this section are not sensitive to small changes in parameter values. In this case the QSSA and the approximation are substantially different as the approximation (4.38) contains  $h(t)$  which is not updated to allow for the reduction of  $h(t)$ . This was not an issue in the previous example as  $k_2' I_0 \exp(\beta h(t))$  was small in comparison to  $k_1 u(g(t), t)$ , as previously discussed.

This demonstrates that the model proposed by Ollis is only applicable to a specific parameter regime. For this particular parameter regime, solving the full system is the only way of accurately approximating the solution of this system. Hence, we have shown that our model can replicate results presented by Ollis when parameters are chosen appropriately. Additionally, we have shown that our model has the potential to solve a far wider range of problems than the model proposed by Ollis.

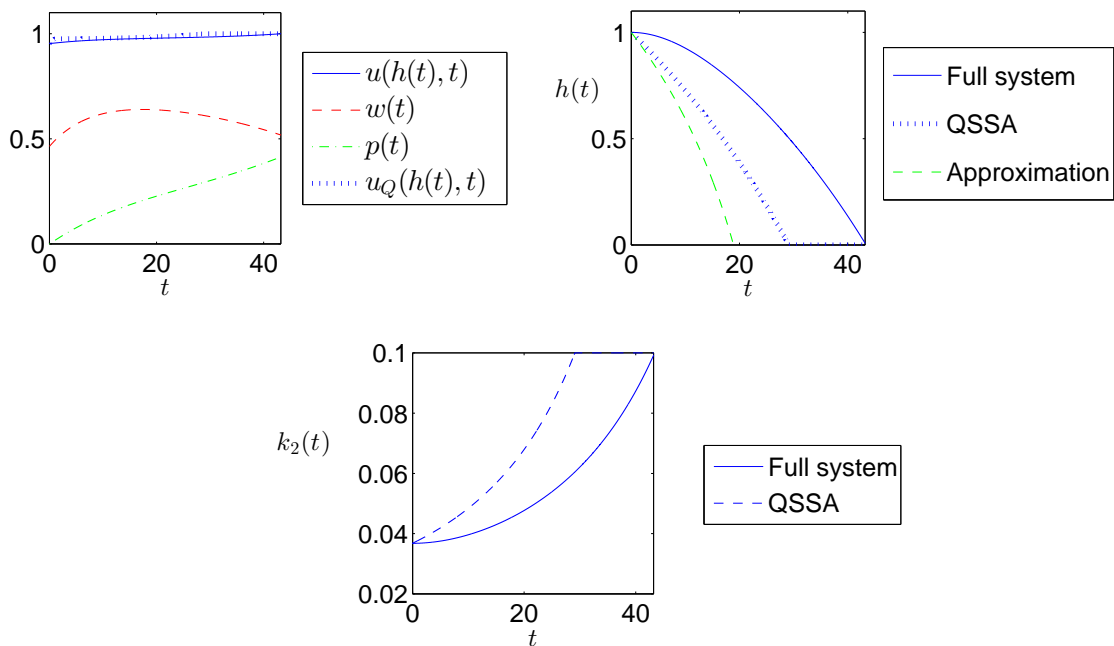


Figure 4.19: Case (b) simulation results demonstrating that the QSSA system and the full system give significantly different results.

## 4.6 Case 3: Film adjacent to a photocatalyst layer

### 4.6.1 Ollis model

In this case Ollis considers a lateral oxidation example. The initial setup is shown in Figures 4.20 and 4.21. As shown in Figure 4.21, there is an initial soot layer uniformly deposited on exposed titania and glass surfaces. The overlayer of soot on the titania is directly oxidized over a relatively short time scale. Once the overlayer, which is in direct contact with the titania, is completely oxidized (as shown in the second diagram of Figure 4.21), lateral oxidation of the adjacent soot layer begins. As shown in the third diagram of Figure 4.21, a growing gap  $g(t)$  is created between the edge of the photocatalyst and the soot layer, which is receding. Mobile oxidants, in this case OH radicals, react at the edge of the soot, causing the soot edge to move. Ollis models the period of time after the initial soot layer on exposed titania is completely oxidized.

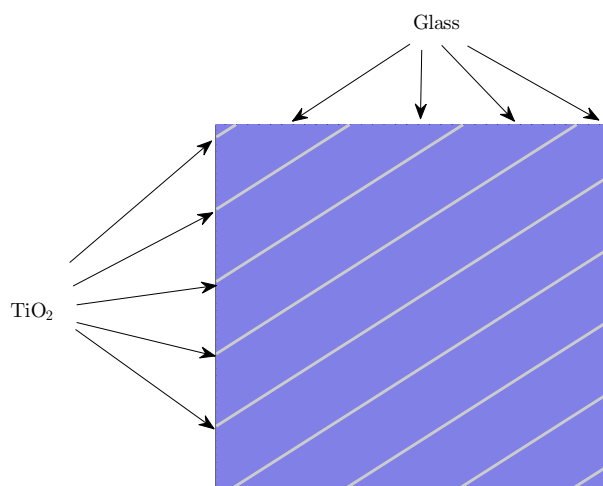


Figure 4.20: Aerial view of how a semiconductor photocatalyst could be applied to a piece of glass in a striped pattern.

Ollis assumes a constant concentration  $[\text{OH}]_0$  of OH radicals on the photocatalyst surface. The OH radicals at the surface are free to diffuse to the soot edge,

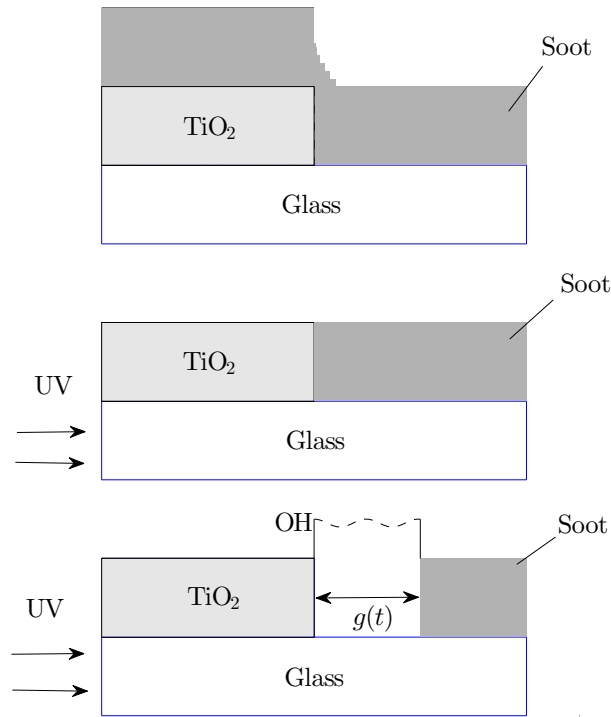


Figure 4.21: Initial set-up of Case 3. This diagram shows a side-on view of one particular strip of  $\text{TiO}_2$  applied to a glass structure.

where they react with the soot to produce  $\text{CO}_2$  and increase the gap  $g(t)$ . Assuming the reaction is in a pseudo-steady state, the rate at which the OH radicals diffuse must equal the edge reaction rate which is dependent on the concentration of OH radicals at the soot layer  $[\text{OH}]_S$ . Ollis assumes a first-order reaction rate at the soot edge with respect to  $[\text{OH}]$ , i.e.  $r = k_{cat}[\text{OH}]_S$ , where  $k_{cat}$  is a reaction constant. This simply means that the rate at which hydroxyl radicals are being transported to the soot edge is equal to the rate at which the radicals are reacting at the soot edge. Hence,

$$\frac{D([\text{OH}]_0 - [\text{OH}]_S)}{g(t)} = k_{cat}[\text{OH}]_S, \quad (4.38)$$

where  $D$  is the diffusion coefficient. To arrive at (4.38) Ollis assumes that the change in concentration from  $[\text{OH}]_0 - [\text{OH}]_S$  is linear. The reaction rate at the

soot edge is directly proportional to the velocity of the soot edge. Hence,

$$\frac{dg(t)}{dt} = k_{cat}[\text{OH}]_S. \quad (4.39)$$

Solving (4.38) for  $[\text{OH}]_S$  and substituting into (4.39) gives

$$\frac{dg(t)}{dt} = \frac{k_{cat}[\text{OH}]_0}{1 + g(t)\frac{k_{cat}}{D}}. \quad (4.40)$$

Solving (4.40) and taking the positive root gives

$$g(t) = \frac{-1 + \sqrt{1 + 2\frac{k_{cat}}{D}k_{cat}[\text{OH}]_0t}}{\frac{k_{cat}}{D}}.$$

With  $a = \frac{k_{cat}}{D}$  and  $b = k_{cat}[\text{OH}]_0$ ,  $g(t)$  is given by

$$g(t) = \frac{-1 + \sqrt{1 + 2abt}}{a}. \quad (4.41)$$

Two extreme cases are considered by Ollis. Firstly, for a fast reaction, relative to diffusion, it is assumed that  $abt \gg 1$ , hence, (4.41) simplifies to give

$$g(t) \approx \sqrt{\frac{2bt}{a}}. \quad (4.42)$$

This expression for  $g(t)$  corresponds to a diffusion-limited regime. For a slow reaction, relative to diffusion, it is assumed that  $abt \ll 1$ . If  $\tau = 2abt$ ,  $f(\tau) = \sqrt{1 + \tau}$  and expanding  $f(\tau)$  about  $\tau = 0$  gives

$$\begin{aligned} f(\tau) &\approx f(0) + f'(0)(\tau - 0) + \frac{f''(0)}{2!}(\tau - 0)^2 + \frac{f'''(0)}{3!}(\tau - 0)^3 + \dots \\ &= 1 + \frac{1}{2}\tau - \frac{1}{8}\tau^2 + \frac{1}{16}\tau^3 + \dots \end{aligned}$$

Substituting  $f(\tau) = \sqrt{1 + 2abt}$  expanded about  $2abt = 0$  into (4.41) gives

$$\begin{aligned} g(t) &\approx \frac{-1 + 1 + \frac{1}{2}\tau - \frac{1}{8}\tau^2 + \frac{1}{16}\tau^3 + \dots}{a} \\ &= bt - \frac{1}{8} \frac{(2abt)^2}{a} + \frac{1}{16} \frac{(2abt)^3}{a} + \dots \end{aligned}$$

Ignoring all terms of  $2abt$  of power 2 or larger, we have

$$g(t) \approx bt. \quad (4.43)$$

This expression corresponds to a reaction-limited regime.

## 4.6.2 Experimental data

Ollis compared results obtained from the model outlined above with experimental data produced by Lee and Choi [39]. Ollis identifies a time delay of approximately 5 hours in the experimental data before any significant diffusion takes place. With the time shift, Ollis fits the two parameter model to two points of the experimental data and obtains  $a = 0.0156$  and  $b = 1.063$ .

Figure 4.22 shows plots of gap length  $g(t)$  against time  $t$  for the three cases Ollis considered. The reaction-limited case (4.43) (red dash-dot line), the diffusion-limited case (4.42) (green dashed line) and the full rate form (4.41) (blue solid line) for chosen  $a$  and  $b$  values are plotted in Figure 4.22. Ollis demonstrates that the full rate form plot fits the experimental data well and concludes that the experimental data is influenced by both surface reaction and diffusion, hence the data appears to be a combination of both cases.

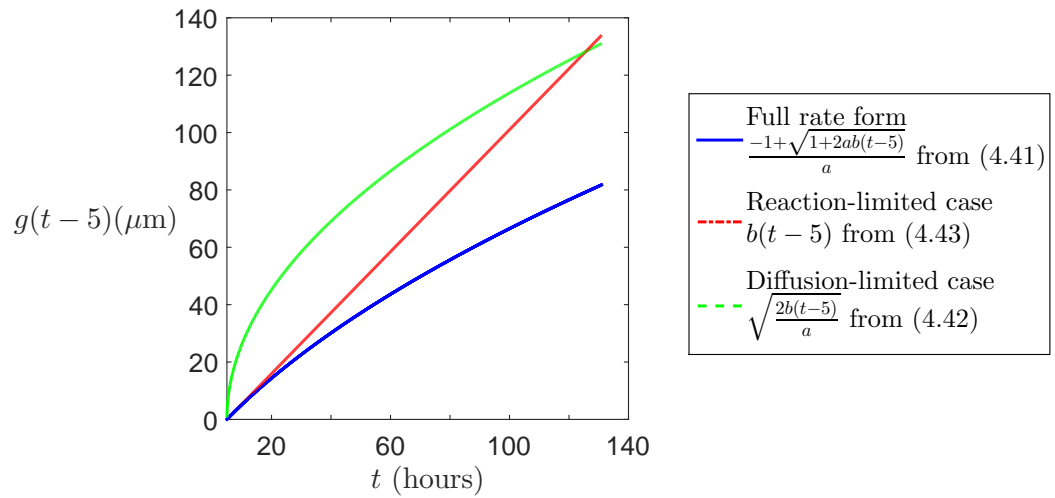


Figure 4.22: Replication of the predictions made by the Ollis model showing how  $g(t)$  varies with time for a reaction-limited case (red dash dot line), a diffusion-limited case (green dashed line) and the full rate form (blue solid line).

### 4.6.3 Generalised model

We apply a model similar to the one introduced in Section 4.3 to the problem described above. The main difference in this case is that there is only one reaction taking place. We assume that a constant supply of hydroxyl radicals are produced at  $x = 0$ , which diffuse through the domain and, after an adsorption/desorption process, react with organics at the photocatalyst surface causing the gap to widen. In this case there is no subsequent reaction which takes place after the adsorption/desorption/surface reaction process. Additionally, the domain expands rather than contracts. However, our model, and indeed the numerical method, are similar to those previously described.

### 4.6.4 Simulations

Parameters are chosen to illustrate how the increase in the gap length (which we refer to as  $h(t)$  in our plots) varies depending on the parameter regime. Throughout all simulations, we have that  $k_1 = 1$ ,  $k_{-1} = 1$ ,  $h_0 = 0.1$ ,  $s_{tot} = 1$ . Note that the

parameters chosen are representative of a wide range of parameter regimes. A number of regimes were tested. In all cases the results were qualitatively similar to the results presented in this section. Additionally, the results presented in this section are not sensitive to small changes in any of the parameters used. By varying  $k_2$  and keeping all other parameters constant we can demonstrate two extreme regimes (i.e. surface reaction-limited and diffusion-limited) and also investigate intermediate regimes. Note that we effectively have a diffusion coefficient of one due to our nondimensionalisation.

Figure 4.23 shows how  $h(t)$  increases with time for six different choices of  $k_2$ . In each plot we have also plotted a straight line from the origin to  $(T, h(t))$  to illustrate how each plot is qualitatively changing as  $k_2$  is increased.

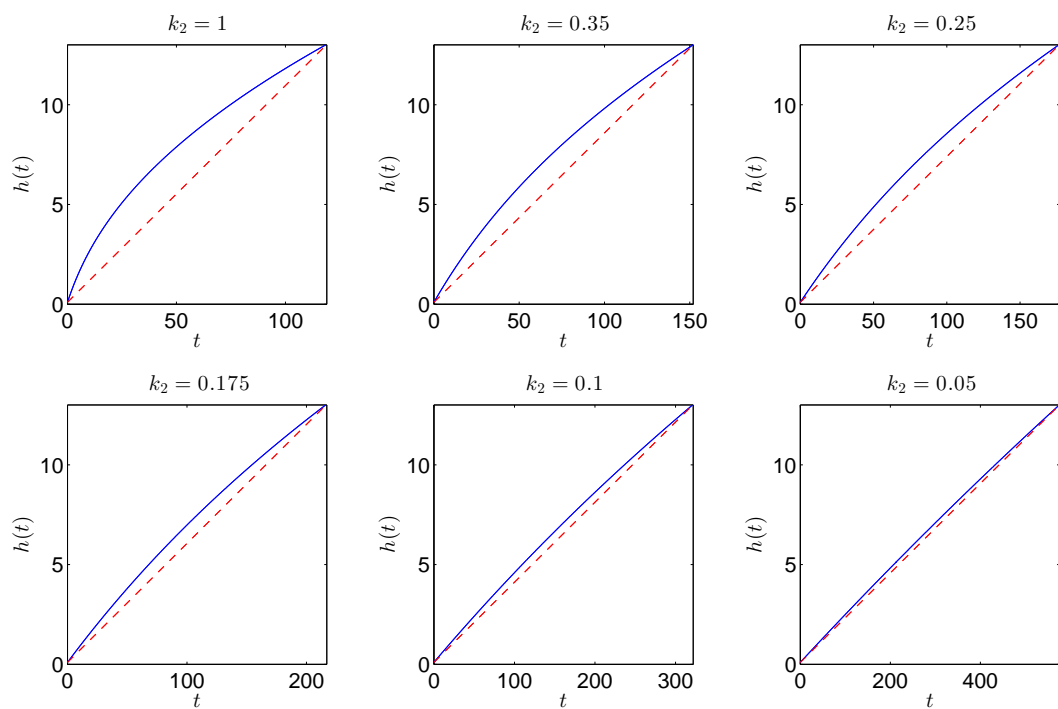


Figure 4.23: Plots of  $h(t)$  versus  $t$  with  $k_1 = 1, k_{-1} = 1, h_0 = 0.1$  and  $s_{tot} = 1$  with various different  $k_2$  values. The dashed red line shows a straight line plotted from  $(0, h(0))$  to  $(T, h(T))$ .

From the first plot of Figure 4.23 we can see that the increase in  $h(t)$  looks

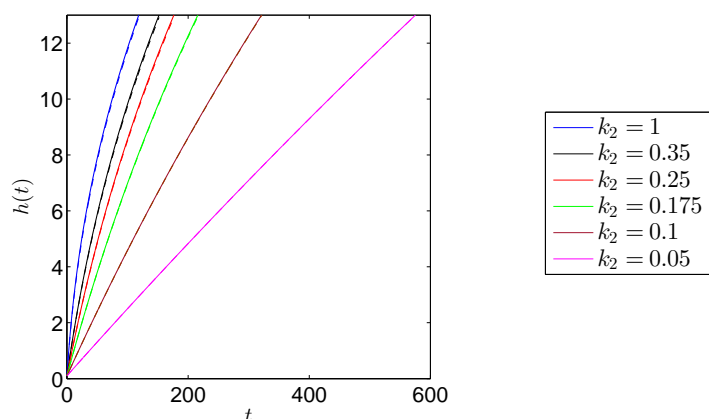


Figure 4.24: Plot of  $h(t)$  with  $k_1 = 1, k_{-1} = 1, h_0 = 0.1, s_{tot} = 1$  and various different  $k_2$  values.

very similar to the diffusion-limited case presented in Figure 4.22. Although we are using fairly conservative parameter values ( $k_1 = 1, k_{-1} = 1$  and  $k_2 = 1$ ), the domain is increasing quite quickly which causes diffusion to be the limiting step at an early stage in the simulation. From the plot we can see a clear decrease in the rate at which  $h(t)$  increases as the domain grows larger.

The final plot of Figure 4.23 shows very similar results to the reaction-limited case presented in Figure 4.22. This is unsurprising considering we have set  $k_2 = 0.05$ . This means that even with  $h(t)$  larger than 12, we have that the rate of diffusion is still quick enough to ensure it is the surface reaction which is limiting the overall rate. For this set of parameters we have that  $h(t)$  is increasing at an approximately constant rate.

From the four intermediate plots of Figure 4.23 we can see a gradual change from diffusion-limited behaviour to reaction-limited behaviour. This would reinforce the conclusion reached by Ollis that the experimental results are due to being in a regime where both diffusion and the surface reaction play a role in determining the overall reaction rate.

Figure 4.24 shows all six cases plotted on the same axis. This demonstrates that, unsurprisingly, by decreasing  $k_2$  the time it takes for  $h(t)$  to reach a specific

value will increase. For each of the six cases we also plotted the results obtained from the QSSA in dashed lines. For all six cases, the results from the QSSA and the full system are almost identical to plotting accuracy.

Figure 4.25 shows a situation where the QSSA is not a valid assumption to make. The following parameters were used:  $s_{tot} = 10$ ,  $k_1 = 1$ ,  $k_2 = 0.1$ ,  $k_{-1} = 0.1$  and  $T = 200$ . Note that the following results are not sensitive to small changes in the parameters used. In this regime, by choosing a large  $s_{tot}$  value and setting  $k_1$  to be large relative to  $k_{-1}$ , we allow a large amount of reactant to bind to the surface sites initially. However, as the domain increases it takes longer for the reactant to diffuse to the boundary and replace any molecules which have reacted. This causes  $w(t)$  to decrease significantly as the boundary increases. Figure 4.26 illustrates this point and helps to explain why the QSSA is invalid for this particular regime. This particular regime has demonstrated that the QSSA is not always valid when considering this system.

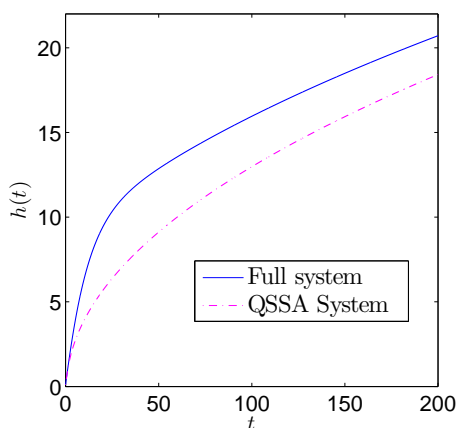


Figure 4.25: Comparison between solving the full system and assuming the QSSA with the following parameters:  $s_{tot} = 10$ ,  $k_1 = 1$ ,  $k_2 = 0.1$ ,  $k_{-1} = 0.1$  and  $T = 200$ .

## 4.7 Conclusions

In this chapter we have considered three photocatalyst systems where the domain considered varied with time. General models were presented and applied to three

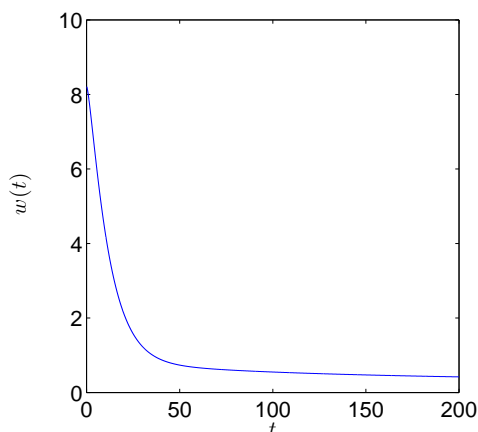


Figure 4.26: Plot showing how  $w(t)$  varies with time.

different cases considered by Ollis [67]. For the first case, where we considered a non-absorbing film overlayer on a photocatalyst, we were able to replicate the results obtained from the simple model proposed by Ollis for a particular set of parameters. In this instance we were able to show that the results obtained when solving the full system were very similar to results obtained from the QSSA system. Additionally, for an alternative set of parameters we were able to show that our model predicts a reduction in film thickness significantly different to the reduction predicted by the Ollis model. For this set of parameters our results suggested that the QSSA was not valid.

Additional experimental data would be useful to validate the proposed general model. Unlike the simple model proposed by Ollis, our model considers the transport of reactant throughout the domain. Ollis made the assumption that diffusion was quick enough to not limit the overall reaction rate. By considering a thicker film, diffusion would potentially start to play a role in limiting the overall reaction rate. Such a system could be used to test the applicability of our proposed model.

For the second system considered, absorbing film overlayer on a photocatalyst, with our general model we were again able to replicate the results obtained from the simple model proposed by Ollis. For this set of parameters the QSSA was a valid assumption to make. We demonstrated that for another set of parameters

the QSSA gave significantly different results to the results obtained from the full system. As the QSSA was assumed by Ollis, this particular set of parameters demonstrated that the simple model proposed by Ollis would be applicable for all parameter regimes.

Similar to the first system discussed above, further experimental data would be useful to further validate our proposed model. As this system involved an intensity dependence, experiments where the initial intensity applied to the system is varied, with all other parameters remaining constant, would be useful to test our proposed model. By varying the intensity from very low values to very high values, we would expect to see a range of kinetic regimes.

For the final system considered, film adjacent to a photocatalyst layer, the general model we proposed was able to replicate predictions made by Ollis for three different regimes. However, we were also able to give an example, using our proposed model, where the QSSA was not valid. Similar to the previous case, as Ollis invoked the QSSA, the simple model proposed by Ollis would not be applicable for all parameter regimes.

To further validate both the simple model proposed by Ollis, and our more general model, it would be useful if the two extreme parameter regimes, i.e. reaction-limited and diffusion-limited, could be tested experimentally. For the diffusion-limited case this could involve using thicker films to ensure that diffusion starts to play a role in the overall reaction rate. For the reaction-limited case, this could involve using a very low intensity of light and as thin a film as possible to ensure that the surface reaction is rate-limiting. We presented an example of a regime where the QSSA was not valid. This regime involved setting  $s_{tot}$  to be large. If experiments could be performed where the concentration of surface reaction sites is very large relative to the initial concentration of reactant, we could test the applicability of our proposed model for a regime which the simple Ollis model could not be applied to.

For all three models we have presented, we have been able to replicate the

predictions made by Ollis when appropriate parameters are used. Additionally, we have been able to give, in all three cases, examples of situations which, using the simple models proposed, Ollis would not be able to accurately simulate.

## Chapter 5

# A moving mesh finite element method for surface catalysed reactions in two-dimensional time-dependant domains

In this chapter we consider two-dimensional systems based on the semiconductor photocatalysis process studied in previous chapters. We will initially present a general computational method which can solve coupled differential equations in two dimensions before applying the method to problems motivated by semiconductor photocatalysis.

As before, the main focus is on the coupling between a diffusing bulk species and a surface species. Computational modelling in two dimensions is considerably more challenging than the one-dimensional case. In two dimensions the boundary is an infinite collection of points and we have the additional potential geometric complexity of the boundary and the bulk domain to deal with.

We will initially consider circular domains, before moving onto more challenging geometries. In previous chapters we exclusively used a finite difference method;

however, as we now consider more complex geometries, a finite element method will be used. The first problem considered is a simple coupled system on a stationary circular domain. In this particular instance we are able to find an analytical solution which is used to validate our numerical approximations. We then consider a situation where we have the reaction mechanism introduced in Section 2.1.1 taking place at the boundary on a stationary domain. Using this example we will demonstrate that the developed numerical method has the desirable property of predicting the global conservation of reactants and products.

We then consider cases where the boundary of the domain is expanding. Initially, we assume a constant rate of expansion before considering systems where the reaction taking place at the surface is causing the boundary to expand. We initially consider a simple circular geometry before giving an example of a more complex geometry. The final situation considered will involve an internal source of reactant where the boundary will expand due to the reaction taking place at the surface.

## 5.1 Model system equations

We consider a general system where the bulk concentration is coupled to a surface concentration through a flux boundary condition. For each  $t \in [0, T]$ ,  $T > 0$ , let  $\Omega(t) \subset \mathbb{R}^2$  be a smooth bounded time-dependent domain with boundary  $\Gamma(t)$ . Let  $\mathbf{n} = (n_1, n_2)$  denote the unit outward normal to  $\Gamma(t)$  and let  $\mathcal{N}(t)$  be any open subset of  $\mathbb{R}^2$  containing  $\Gamma(t)$ . For any function  $\zeta$ , which is differentiable in  $\mathcal{N}(t)$ , we define the tangential gradient on  $\Gamma(t)$  by  $\nabla_{\Gamma}\zeta = \nabla\zeta - (\nabla\zeta \cdot \mathbf{n})\mathbf{n}$ , where  $\cdot$  denotes the usual scalar product and  $\nabla\zeta$  denotes the usual gradient on  $\mathbb{R}^2$ . For a vector function  $\boldsymbol{\zeta} = (\zeta_1, \zeta_2) \in \mathbb{R}^2$ , the tangential divergence is defined by

$$\nabla_{\Gamma} \cdot \boldsymbol{\zeta} = \nabla \cdot \boldsymbol{\zeta} - \sum_{i=1}^2 (\nabla \zeta_i \cdot \mathbf{n}) n_i.$$

The Laplace-Beltrami operator on  $\Gamma(t)$  is defined as the tangential divergence of the tangential gradient  $\Delta_\Gamma \zeta = \nabla_\Gamma \cdot (\nabla_\Gamma \zeta)$ .

We consider the behaviour of a single chemical species with a straightforward generalization to a system of interacting chemicals. Let us define

$$Q_T = \{(\mathbf{x}, t) \in \mathbb{R}^3 : \mathbf{x} \in \Omega(t), t \in (0, T)\}.$$

The equation for mass conservation for a chemical  $C$ , which diffuses with constant  $D$ , is given by

$$\frac{\partial c}{\partial t} = D\Delta c, \quad (\mathbf{x}, t) \in Q_T, \quad (5.1)$$

where  $c(\mathbf{x}, t)$  is the concentration at position  $\mathbf{x} \in \Omega(t)$  at time  $t$ .

Simultaneously, we consider the evolution of a chemical species  $C_s$  that resides on the boundary  $\Gamma(t)$ . The bulk species  $C$  will be coupled to  $C_s$  through the generally nonlinear flux boundary condition

$$\overbrace{-D \frac{\partial c}{\partial \mathbf{n}} \Big|_{\Gamma(t)}}^{\text{Diffusive flux}} = \overbrace{g(c|_{\Gamma(t)}, c_s)}^{\text{Rate of surface reaction}}, \quad (5.2)$$

where  $c_s(\mathbf{x}, t)$  denotes the concentration of  $C_s$  at the point  $\mathbf{x} \in \Gamma(t)$ ,  $\mathbf{n}$  is the outward unit normal to  $\Gamma(t)$ , and  $g(c|_{\Gamma(t)}, c_s)$  is a reaction term which couples  $c$  and  $c_s$ .

We will assume that the boundary species evolves such that

$$\frac{\partial c_s}{\partial t} = D_s \Delta_\Gamma c_s + g(c|_{\Gamma(t)}, c_s) + h(c_s), \quad (\mathbf{x}, t) \in \Gamma(t) \times (0, T), \quad (5.3)$$

where  $D_s$  is the boundary diffusion coefficient,  $h(c_s)$  is an additional surface reaction term. We can use this approach to implement a Langmuir-Hinshelwood surface adsorption and reaction mechanism by choosing  $g(c|_{\Gamma(t)}, c_s)$  and  $h(c_s)$  appropriately, which we will demonstrate later in the chapter.

### 5.1.1 ALE reformulation

When the domain is time-dependent, a common frame of reference adopted for computational purposes is the Arbitrary Lagrangian Eulerian (ALE) frame [20, 35]. Let  $\mathcal{A}_t$  be a family of bijective mappings, which at each  $t \in I = [0, T]$ , map points in a reference or computational configuration  $\Omega_c$  with coordinates  $\boldsymbol{\xi} = (\xi, \eta)$ , to points in the current physical configuration  $\Omega(t)$  with coordinates  $\boldsymbol{x} = (x, y)$ , so that

$$\mathcal{A}_t : \Omega_c \subset \mathbb{R}^2 \rightarrow \Omega(t) \subset \mathbb{R}^2, \quad \boldsymbol{x}(\boldsymbol{\xi}, t) = \mathcal{A}_t(\boldsymbol{\xi}).$$

The computational configuration could simply be the initial physical configuration  $\Omega(0)$ . We leave the discussion on how to construct the mapping  $\mathcal{A}_t$  to Section 5.3.

For an arbitrary function  $g : Q_T \rightarrow \mathbb{R}$ , defined on the fixed Eulerian frame, its temporal derivative in the ALE frame is defined as

$$\left. \frac{\partial g}{\partial t} \right|_{\boldsymbol{\xi}} : Q_T \rightarrow \mathbb{R}, \quad \left. \frac{\partial g}{\partial t} \right|_{\boldsymbol{\xi}}(\boldsymbol{x}, t) = \frac{\partial \hat{g}}{\partial t}(\boldsymbol{\xi}, t), \quad \boldsymbol{\xi} = \mathcal{A}_t^{-1}(\boldsymbol{x}),$$

where  $\hat{g} : \Omega_c \times I \rightarrow \mathbb{R}$  is the corresponding function in the ALE frame; that is  $\hat{g}(\boldsymbol{\xi}, t) = g(\boldsymbol{x}(t), t) = g(\mathcal{A}_t(\boldsymbol{\xi}, t))$ . Taking the time derivative of the ALE mapping defines the ALE velocity  $\boldsymbol{w}$  as

$$\boldsymbol{w}(\boldsymbol{x}, t) = \left. \frac{\partial \boldsymbol{x}}{\partial t} \right|_{\boldsymbol{\xi}}(\mathcal{A}_t^{-1}(\boldsymbol{x}), t).$$

To relate the time derivatives with respect to the ALE transformation to the material derivative, a standard application of the chain rule gives

$$\left. \frac{\partial c}{\partial t} \right|_{\boldsymbol{\xi}} = \left. \frac{\partial c}{\partial t} \right|_{\boldsymbol{x}} + \boldsymbol{w} \cdot \nabla c. \quad (5.4)$$

The reformulation of (5.1) in terms of the ALE reference frame therefore takes the

form

$$\left. \frac{\partial c}{\partial t} \right|_{\boldsymbol{\xi}} - \mathbf{w} \cdot \nabla c = D \Delta c, \quad \boldsymbol{\xi} \in \Omega_c. \quad (5.5)$$

On the boundary, the equivalent of (5.4) is

$$\left. \frac{\partial c_s}{\partial t} \right|_{\boldsymbol{\xi}} = \left. \frac{\partial c_s}{\partial t} \right|_{\mathbf{x}} + \mathbf{w} \cdot \nabla_{\Gamma} c.$$

Hence, the ALE formulation of (5.3) takes the form

$$\left. \frac{\partial c_s}{\partial t} \right|_{\boldsymbol{\xi}} - \mathbf{w} \cdot \nabla_{\Gamma} c = D_s \Delta_{\Gamma} c + g(c|_{\Gamma(t)}, c_s) + h(c_s), \quad \boldsymbol{\xi} \in \partial\Omega_c. \quad (5.6)$$

The ALE reformulated equations (5.5) and (5.6) remain coupled through the flux boundary condition (5.2).

### 5.1.2 A conservative weak ALE formulation

To construct a weak formulation of (5.5), we consider a space of admissible test functions defined on the reference domain made of function  $\hat{v} \in H^1(\Omega_c)$ . The ALE mapping then defines a set  $\mathcal{H}(\Omega(t))$  of test functions on the domain  $\Omega(t)$ , as follows:

$$\mathcal{H}(\Omega(t)) = \{v : \Omega(t) \rightarrow \mathbb{R} : v = \hat{v} \circ \mathcal{A}_t^{-1}, \hat{v} \in H^1(\Omega_c)\}, \quad t \in I.$$

A weak formulation of (5.5) can be obtained using Reynolds transport formula which states that if  $\psi(\mathbf{x}, t)$  is a function defined on  $\Omega(t)$ , and  $V_t \subseteq \Omega(t)$  such that  $V_t = \mathcal{A}_t(V_c)$  with  $V_c \subseteq \Omega_c$ , then

$$\frac{d}{dt} \int_{V_t} \psi(\mathbf{x}, t) \, d\mathbf{x} = \int_{V_t} \left( \left. \frac{\partial \psi}{\partial t} \right|_{\boldsymbol{\xi}} + \psi \nabla \cdot \mathbf{w} \right) \, d\mathbf{x} = \int_{V_t} \left( \left. \frac{\partial \psi}{\partial t} \right|_{\mathbf{x}} + \nabla \psi \cdot \mathbf{w} + \psi \nabla \cdot \mathbf{w} \right) \, d\mathbf{x}. \quad (5.7)$$

As functions  $\hat{v} \in H^1(\Omega_c)$  do not depend on time, then for any  $v \in \mathcal{H}(\Omega(t))$  we can establish from (5.7) that

$$\frac{d}{dt} \int_{\Omega(t)} v \, d\mathbf{x} = \int_{\Omega(t)} v \nabla \cdot \mathbf{w} \, d\mathbf{x} \quad (5.8)$$

and

$$\frac{d}{dt} \int_{\Omega(t)} v \psi \, d\mathbf{x} = \int_{\Omega(t)} v \left( \frac{\partial \psi}{\partial t} \Big|_{\boldsymbol{\xi}} + \psi \nabla \cdot \mathbf{w} \right) \, d\mathbf{x}. \quad (5.9)$$

Multiplying (5.5) by a test function  $v \in \mathcal{H}(\Omega(t))$ , integrating over  $\Omega(t)$  and the use of (5.2), (5.8) and (5.9) gives the conservative weak form: find  $c$  such that

$$\frac{d}{dt} \int_{\Omega(t)} cv \, d\mathbf{x} - \int_{\Omega(t)} (\nabla \cdot (\mathbf{w}c)) v \, d\mathbf{x} + D \int_{\Omega(t)} \nabla c \cdot \nabla v \, d\mathbf{x} \quad (5.10)$$

$$+ \int_{\Gamma(t)} gv \, ds = 0, \quad \forall v \in \mathcal{H}(\Omega(t)). \quad (5.11)$$

Similarly, on the boundary we have the weak formulation: find  $c_s$  such that

$$\begin{aligned} \frac{d}{dt} \int_{\Gamma(t)} c_s v_s \, ds - \int_{\Gamma(t)} (\nabla_{\Gamma} \cdot (\mathbf{w}c_s)) v_s \, ds + D_s \int_{\Gamma(t)} \nabla_{\Gamma} c_s \cdot \nabla_{\Gamma} v_s \, ds \\ = \int_{\Gamma(t)} (g + h) v_s \, ds, \quad \forall v_s \in \mathcal{H}_s(\Gamma(t)), \end{aligned} \quad (5.12)$$

where

$$\mathcal{H}_s(\Gamma(t)) = \{v_s : \Gamma(t) \rightarrow \mathbb{R} : v_s = \hat{v}_s \circ \mathcal{A}_t^{-1}, \hat{v}_s \in H^1(\Gamma_c)\}, \quad t \in I,$$

is the space of test functions on  $\Gamma(t)$ .

## 5.2 Moving finite element discretisation

### 5.2.1 Spatial semi-discretisation

We will assume that for each  $t \in [0, T]$ , the physical and reference domains  $\Omega(t)$  and  $\Omega_c$  are approximated by polygonal domains  $\Omega_h(t)$  and  $\Omega_{c,h}$ , respectively. We will assume that  $\Omega_{c,h}$  is covered by a fixed triangulation  $\mathcal{T}_{h,c}$  with straight edges, so that  $\Omega_{c,h} = \cup_{K \in \mathcal{T}_{h,c}} K$ . The approximation of the boundary domain  $\Gamma_h(t)$  is chosen to be simply the boundary of  $\Omega_h(t)$ . The total number of elements of  $\mathcal{T}_{h,c}$  will be denoted by  $N$ . The total number of vertices of  $\mathcal{T}_{h,c}$  will be denoted by  $\mathcal{N}$  and the number of vertices on the boundary as  $\mathcal{N}_s$ . We define the Lagrangian finite element space on  $\mathcal{T}_{h,c}$  as

$$\begin{aligned} \mathcal{L}^1(\Omega_{c,h}) &= \{\hat{v}_h \in H^1(\Omega_{c,h}) : \hat{v}_h|_K \in \mathbb{P}_1(K), \forall K \in \mathcal{T}_{h,c}\}, \\ \mathcal{L}_0^1(\Omega_{c,h}) &= \{\hat{v}_h \in H^1(\Omega_{c,h}) : \hat{v}_h|_K \in \mathcal{L}^1(\Omega_{c,h}) : \hat{v}_h = 0, \boldsymbol{\xi} \in \Gamma_{c,h}\}, \end{aligned}$$

where  $\mathbb{P}_1(K)$  is the space of linear polynomials on  $K$ .

In Section 5.3 we will describe a procedure for evolving the nodal positions of the triangulation covering  $\Omega_h(t)$ . Given the location of the mesh nodes, the ALE mapping will be interpolated using piecewise linear elements giving rise to a discrete mapping  $\mathcal{A}_{h,t} \in \mathcal{L}^1(\Omega_{c,h})^2$  of the form

$$\mathbf{x}_h(\boldsymbol{\xi}, t) = \mathcal{A}_{h,t}(\boldsymbol{\xi}) = \sum_{i=1}^{\mathcal{N}} \mathbf{x}_i(t) \hat{\phi}_i(\boldsymbol{\xi}),$$

where  $\mathbf{x}_i(t) = \mathcal{A}_{h,t}(\boldsymbol{\xi}_i)$  denotes the position of node  $i$  at time  $t$ , and  $\hat{\phi}_i$  is the associated nodal basis function in  $\mathcal{L}^1(\Omega_{c,h})$ . The discretised ALE velocity therefore takes the form

$$\mathbf{w}_h(\boldsymbol{\xi}, t) = \sum_{i=1}^{\mathcal{N}} \dot{\mathbf{x}}_i(t) \hat{\phi}_i(\boldsymbol{\xi}).$$

Let  $\mathcal{T}_{h,t}$  be the image of the reference triangulation  $\mathcal{T}_{h,c}$  under the discrete ALE

mapping  $\mathcal{A}_{h,t}$ . Since the mapping is linear, each  $K_t$ , which is the image of a triangle  $K \in \mathcal{T}_{h,c}$ , is also a triangle with straight edges. Using the ALE mapping, the finite element test space on  $\Omega_h(t)$  is therefore defined as

$$\mathcal{H}_h(\Omega_h(t)) = \{v_h : \Omega_h(t) \rightarrow \mathbb{R} : v_h = \hat{v}_h \circ \mathcal{A}_{h,t}^{-1}, \hat{v}_h \in \mathcal{L}^1(\Omega_{c,h})\}.$$

The finite element spatial discretisation of the conservative ALE formulation (5.11) then takes the form: find  $c_h(t) \in \mathcal{H}_h(\Omega_h(t))$  such that

$$\begin{aligned} \frac{d}{dt} \int_{\Omega_h(t)} c_h v_h \, d\mathbf{x} - \int_{\Omega_h(t)} (\nabla \cdot (\mathbf{w}_h c_h)) v_h \, d\mathbf{x} + D \int_{\Omega_h(t)} \nabla c_h \cdot \nabla v_h \, d\mathbf{x} \\ + \int_{\Gamma_h(t)} g v_h \, ds = 0, \quad \forall v_h \in \mathcal{H}_h(\Omega_h(t)). \end{aligned} \quad (5.13)$$

Similarly, on the boundary we have the weak formulation: find  $c_{s,h} \in \mathcal{H}_{s,h}(\Gamma_h(t))$  such that

$$\begin{aligned} \frac{d}{dt} \int_{\Gamma_h(t)} c_{s,h} v_{s,h} \, ds - \int_{\Gamma_h(t)} (\nabla_{\Gamma} \cdot (\mathbf{w}_h c_{s,h})) v_{s,h} \, ds + D_s \int_{\Gamma_h(t)} \nabla_{\Gamma} c_{s,h} \cdot \nabla_{\Gamma} v_{s,h} \, ds \\ = \int_{\Gamma_h(t)} (g + h) v_{s,h} \, ds, \quad \forall v_{s,h} \in \mathcal{H}_{s,h}(\Gamma_h(t)). \end{aligned} \quad (5.14)$$

The finite element approximation of the bulk and surface species can be expressed as

$$c_h(\mathbf{x}, t) = \sum_{j=1}^{\mathcal{N}} c_j(t) \phi_j(\mathbf{x}, t), \quad \text{and} \quad c_{s,h}(\mathbf{x}, t) = \sum_{j=1}^{\mathcal{N}_s} c_{s,j}(t) \phi_{s,j}(\mathbf{x}, t),$$

where  $\{\phi_j(\mathbf{x}, t)\}_{j=1}^{\mathcal{N}}$  and  $\{\phi_{s,j}(\mathbf{x}, t)\}_{j=1}^{\mathcal{N}_s}$  are the time-dependent bulk and surface nodal basis functions. If  $\mathbf{C}(t) = \{c_i(t)\}_{i=1}^{\mathcal{N}}$  and  $\mathbf{C}_s(t) = \{c_{s,i}(t)\}_{i=1}^{\mathcal{N}_s}$ , we can express

(5.13) as the system of ordinary differential equations

$$\frac{d}{dt}(M(t)\mathbf{C}(t)) + [K(t) - A(t, \mathbf{w}_h(t)) + B(t, \mathbf{w}_h(t))]\mathbf{C}(t) + \mathbf{D}(\mathbf{C}(t), \mathbf{C}_s(t)) = 0, \quad (5.15)$$

where

$$[M(t)]_{ij} = \int_{\Omega_h(t)} \phi_i(t)\phi_j(t) \, d\mathbf{x}$$

is the (time-dependent) mass matrix, while

$$[K(t)]_{ij} = D \int_{\Omega_h(t)} (\nabla\phi_j(t) \cdot \nabla\phi_i(t)) \, d\mathbf{x},$$

$$[A(t, \mathbf{w}_h(t))]_{ij} = \int_{\Gamma_h(t)} [\mathbf{w}_h \cdot \mathbf{n}] \phi_i(t)\phi_j(t) \, ds,$$

$$[B(t, \mathbf{w}_h(t))]_{ij} = \int_{\Omega_h(t)} [\mathbf{w}_h \cdot \nabla\phi_i(t)] \phi_j(t) \, d\mathbf{x},$$

$$[\mathbf{D}(\mathbf{C}(t), \mathbf{C}_s(t))]_i = \int_{\Gamma_h(t)} g(c_h(t), c_{s,h}(t)) \phi_i(t) \, ds.$$

Note that the vector  $\mathbf{D}$  will be sparse as only those values of  $i$  corresponding to boundary vertices will be non-zero. The spatial discretisation of the boundary equation (5.14) also results in a system of ODEs

$$\frac{d}{dt}(M_s(t)\mathbf{C}_s(t)) + [K_s(t) - A_s(t, \mathbf{w}_h(t))]\mathbf{C}_s(t) = \mathbf{D}_s(\mathbf{C}(t), \mathbf{C}_s(t)) + \mathbf{H}(\mathbf{C}_s(t)), \quad (5.16)$$

where

$$[M_s(t)]_{ij} = \int_{\Gamma_h(t)} \phi_{s,i}(t)\phi_{s,j}(t) \, ds,$$

$$[K_s(t)]_{ij} = D_s \int_{\Gamma(t)} (\nabla_{\Gamma}\phi_{s,j}(t) \cdot \nabla_{\Gamma}\phi_{s,i}(t)) \, ds,$$

$$[A_s(t, \mathbf{w}_h(t))]_{ij} = \int_{\Gamma_h(t)} ((\nabla_{\Gamma} \cdot \mathbf{w}_h) \phi_{s,i} \phi_{s,j} + [\mathbf{w}_h \cdot \nabla_{\Gamma}\phi_{s,j}(t)] \phi_{s,i}(t)) \, ds,$$

$$[\mathbf{H}(\mathbf{C}_s(t))]_i = \int_{\Gamma_h(t)} h(c_{s,h}(t)) \phi_{s,i}(t) \, ds.$$

and  $\mathbf{D}_s$  are the appropriately reordered non-zero elements of  $\mathbf{D}$ .

### 5.2.2 Temporal integration

To obtain a temporal discretisation of (5.15) and (5.16) we subdivide  $[0, T]$  into  $NT$  equal time intervals of size  $\Delta t = T/NT$  and denote  $t^n = n\Delta t$ ,  $n = 0, 1, \dots, NT$ . We will discretise the ALE mapping using linear interpolation between time levels. That is we will define

$$\mathcal{A}_{h,\Delta t}(\boldsymbol{\xi}, t) = \frac{t - t^n}{\Delta t} \mathcal{A}_{h,t^{n+1}}(\boldsymbol{\xi}) + \frac{t^{n+1} - t}{\Delta t} \mathcal{A}_{h,t^n}(\boldsymbol{\xi}), \quad t \in [t_n, t_{n+1}),$$

where  $\mathcal{A}_{h,t}$  is the piecewise linear map at time  $t$ . The mesh velocity is therefore piecewise constant in time and is given by

$$\begin{aligned} \mathbf{w}_{h,\Delta t}^{n+1}(\boldsymbol{\xi}) &= \frac{\mathcal{A}_{h,t^{n+1}} - \mathcal{A}_{h,t^n}}{\Delta t}, \quad t \in [t^n, t^{n+1}), \\ \mathbf{w}_{h,\Delta t}^{n+1}(\mathbf{x}, t) &= \mathbf{w}_{h,\Delta t}^{n+1}(\boldsymbol{\xi}) \circ \mathcal{A}_{h,\Delta t}^{-1}(\mathbf{x}). \end{aligned}$$

The temporal discretisation of the coupled systems (5.15) and (5.16) is obtained using a modified Crank-Nicolson semi-implicit approach. We begin by predicting the boundary solution  $\tilde{\mathbf{C}}_s^{n+1}$  using a semi-implicit backward Euler method where the linear diffusion and mesh movement terms are treated implicitly and the non-linear reaction and coupling terms are treated explicitly. The predicted boundary solution therefore satisfies the linear system

$$[M_s^{n+1} + \Delta t(K_s^{n+1} - A_s^{n+1})] \tilde{\mathbf{C}}_s^{n+1} = M_s^n \mathbf{C}_s^n + \Delta t[\mathbf{D}_s(\mathbf{C}^n, \mathbf{C}_s^n) + \mathbf{H}(\mathbf{C}_s^n)]. \quad (5.17)$$

The bulk approximation is then updated using a Crank-Nicolson step

$$\begin{aligned} [M^{n+1} + \frac{1}{2}\Delta t(K^{n+1} - A^{n+1} + B^{n+1})] \mathbf{C}^{n+1} &= [M^n - \frac{1}{2}\Delta t(K^n - A^n + B^n)] \mathbf{C}^{n+1} \\ &+ \frac{1}{2}\Delta t[\mathbf{F}(\mathbf{C}^{n+1}) + \mathbf{F}(\mathbf{C}^n) - \mathbf{D}(\mathbf{C}^{n+1}, \tilde{\mathbf{C}}_s^{n+1}) - \mathbf{D}(\mathbf{C}^n, \mathbf{C}_s^n)]. \end{aligned} \quad (5.18)$$

Finally, to ensure that the boundary solution is second-order in time, we perform a Crank-Nicolson correction step

$$\begin{aligned} [M_s^{n+1} + \frac{1}{2}\Delta t(K_s^{n+1} - A_s^{n+1})]\mathbf{C}_s^{n+1} &= [M_s^n - \frac{1}{2}\Delta t(K_s^n - A_s^n)]\mathbf{C}_s^n \\ &+ \frac{1}{2}\Delta t[\mathbf{D}_s(\mathbf{C}^{n+1}, \tilde{\mathbf{C}}_s^{n+1}) + \mathbf{D}_s(\mathbf{C}^n, \mathbf{C}_s^n) + \mathbf{H}(\tilde{\mathbf{C}}_s^{n+1}) + \mathbf{H}(\mathbf{C}_s^n)]. \end{aligned} \quad (5.19)$$

A direct solver is used to solve the linear systems (5.17)-(5.19). Note that this predictor-corrector method for solving the discretised coupled system is similar to the method used in one dimension.

### 5.2.3 A model bulk-surface problem in a stationary domain

To get an indication of the spatial and temporal convergence rate of the coupled bulk-surface finite element discretisation, we apply it to the solution of the following model problem:

$$\frac{\partial c}{\partial t} = \Delta c, \quad \mathbf{x} \in \Omega \quad (5.20)$$

$$\frac{\partial c_s}{\partial t} = \Delta_\Gamma c_s + c - c_s, \quad \mathbf{x} \in \Gamma, \quad (5.21)$$

$$-\frac{\partial c}{\partial n} = c - c_s, \quad \mathbf{x} \in \Gamma. \quad (5.22)$$

where  $\Omega$  is the unit circle.

This problem can be tackled analytically using polar coordinates  $x = r \cos \theta$ ,  $y = r \sin \theta$  so that

$$\frac{\partial c}{\partial t} = \frac{\partial^2 c}{\partial r^2} + \frac{1}{r} \frac{\partial c}{\partial r} + \frac{1}{r^2} \frac{\partial^2 c}{\partial \theta^2}, \quad \mathbf{x} \in \Omega$$

$$\frac{\partial c_s}{\partial t} = \frac{\partial^2 c_s}{\partial \theta^2} + c|_{r=1} - c_s, \quad \mathbf{x} \in \Gamma,$$

and

$$-\frac{\partial c}{\partial r}\Big|_{r=1} = c|_{r=1} - c_s.$$

Similar to Novak *et al* [65], we look for a solution in the form

$$c_s(\theta, t) = Ae^{-k^2t} \cos \theta,$$

and

$$c(r, \theta, t) = \rho(r)c_s(\theta, t).$$

The following exact solution has been used in this test:

$$c(r, \theta, t) = J_1(rk)e^{-k^2t} \cos \theta$$

and

$$c_s(\theta, t) = \frac{J_1(k)}{2 - k^2}e^{-k^2t} \cos \theta,$$

where  $J_1$  is the first-order Bessel function of the first kind and  $k = 1.177706027$ .

Figure 5.1 shows the computed approximate solutions in the bulk domain and on the domain boundary using an isotropic mesh with maximal cell diameter  $h = 0.1$  and a time step  $\Delta t = 2 \times 10^{-4}$ . We can see that the method performs well for these values of the discretisation parameters. To test the spatial rate of convergence of the algorithm, simulations were performed on a sequence of increasingly refined isotropic meshes. To ensure that the error was dominated by its spatial component, a sufficiently small time step of  $\Delta t = 10^{-3}$  was used. Figure 5.2 (a) shows the maximum error, over all grid nodes, for both the bulk and surface numerical solutions. We can see that both solution components converge at the rate of  $O(h^2)$ , as expected. To investigate the temporal rate of convergence, simulations were performed using a fine mesh with  $N = 150,000$  elements and various time steps. We can see from Fig. 5.2 (b) that the decoupled solution procedure results in approximations which are second-order accurate in time.

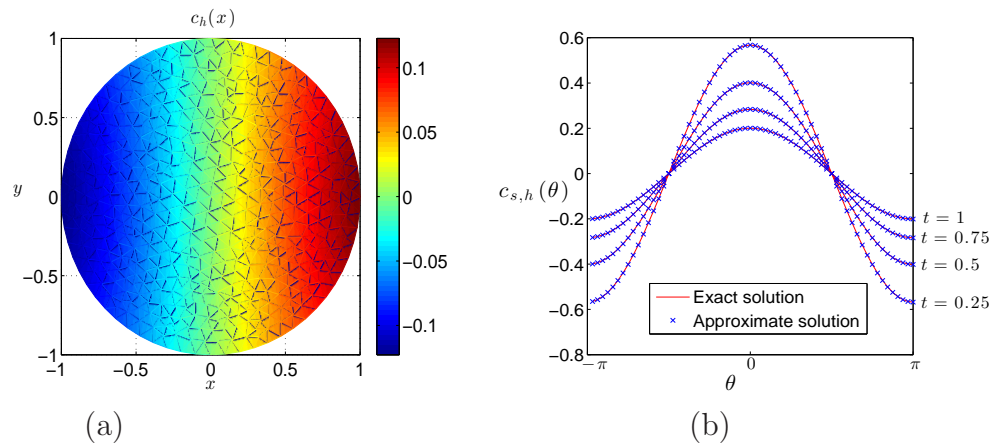


Figure 5.1: Numerical solution of coupled model problem (5.20)-(5.22) on a stationary unit circle. (a) Approximate bulk solution  $c_h(\mathbf{x})$  at  $t = 1$ . (b) Approximate solution  $c_{s,h}(\theta)$  on the boundary compared to the exact solution.

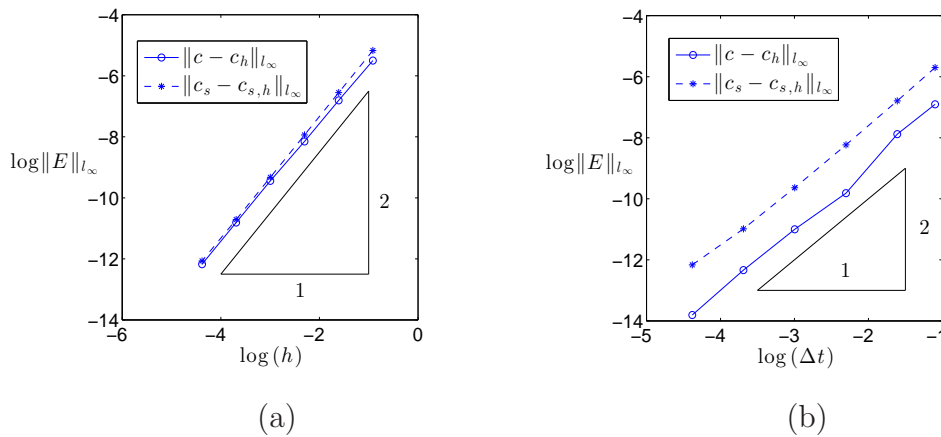


Figure 5.2: Second-order convergence of the maximum nodal error as (a)  $h \rightarrow 0$  and (b)  $\Delta t \rightarrow 0$  for a coupled model problem on a unit circle.

### 5.3 Practical evaluation of ALE mapping

For the ALE mapping to be useful, it must satisfy a number of properties. First, it must be inexpensive to construct, relative to the cost of solving the physical problem. Second, the meshes must evolve smoothly in time to avoid the need to use small time steps to maintain numerical stability.

### 5.3.1 Bulk domain mesh generation

To avoid potential mesh crossings or foldings, we derive a suitable evolution equation for the inverse ALE mapping  $\mathcal{A}_t^{-1}(x) = \boldsymbol{\xi}(\mathbf{x}, t)$  rather than  $\mathcal{A}_t(\boldsymbol{\xi}) = \mathbf{x}(\boldsymbol{\xi}, t)$  (see, for example, the discussion in [22]). As shown in Fig 5.3, a mesh  $\mathcal{T}_{h,t}$  on  $\Omega_h(t)$  can then be generated as the preimage of a fixed mesh  $\mathcal{T}_{h,c}$  on  $\Omega_{c,h}$ . As introduced in [34], we choose the mapping  $\boldsymbol{\xi}(\mathbf{x})$  corresponding to a fixed value of  $t$  in order to minimise the functional

$$I[\boldsymbol{\xi}] = \frac{1}{2} \int_{\Omega_t} [(\nabla \xi)^T (\nabla \xi) + (\nabla \eta)^T (\nabla \eta)] \, d\mathbf{x}, \quad (5.23)$$

where  $\nabla$  is the gradient operator with respect to  $\mathbf{x}$ . Rather than directly attempt to minimise (5.23), a more robust procedure is to evolve the mapping according to the modified gradient flow equations

$$\frac{\partial \xi}{\partial t} = \frac{P}{\tau} \nabla \cdot (\nabla \xi), \quad \text{and} \quad \frac{\partial \eta}{\partial t} = \frac{P}{\tau} \nabla \cdot (\nabla \eta). \quad (5.24)$$

Here,  $\tau > 0$  is a user-specified temporal smoothing parameter, which affects the temporal scale over which the mesh moves to minimise (5.23), and  $P$  is a positive function of  $(\mathbf{x}, t)$ , chosen such that the mesh movement has a spatially uniform time scale [33].

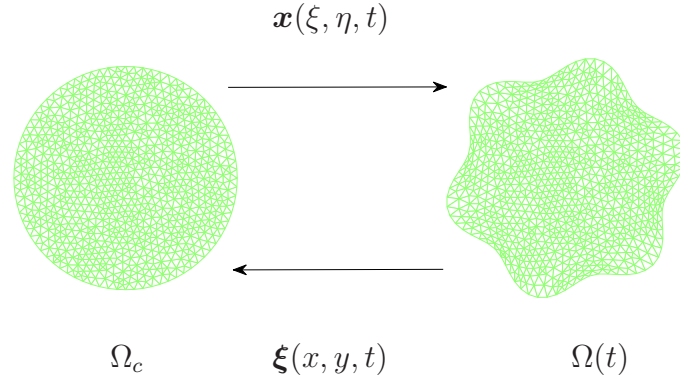


Figure 5.3: A moving mesh covering  $\Omega(t)$  is the image of a fixed mesh on a reference domain  $\Omega_c$  through a time-dependent ALE mapping  $\mathcal{A}_t(\boldsymbol{\xi}) = \mathbf{x}(\boldsymbol{\xi}, t)$ .

In practice, we interchange the roles of the dependent and independent variables in (5.24) since it's the location of the physical mesh points  $\{\mathbf{x}_i(t)\}_{i=1}^{\mathcal{N}}$  that defines the ALE map. The resulting moving mesh partial differential equations (MMPDEs) take the form

$$\tau \frac{\partial \mathbf{x}}{\partial t} = P(a\mathbf{x}_{\xi\xi} + b\mathbf{x}_{\xi\eta} + c\mathbf{x}_{\eta\eta}), \quad (\xi, \eta) \in \Omega_c, \quad (5.25)$$

where

$$a = \frac{x_\eta^2 + y_\eta^2}{J^2}, \quad b = -2\frac{(x_\xi x_\eta + y_\xi y_\eta)}{J^2}, \quad c = \frac{x_\xi^2 + y_\xi^2}{J^2},$$

and  $J = x_\xi y_\eta - x_\eta y_\xi$  is the Jacobian of the ALE mapping. To complete the specification of the coordinate transformation, the MMPDE (5.25) must be supplemented by suitable boundary conditions  $\mathbf{g}(\boldsymbol{\xi}, t), \boldsymbol{\xi} \in \partial\Omega_c$ ; these are obtained using a one-dimensional moving mesh approach outlined in Section 5.3.2.

The numerical solution of (5.25) requires both spatial and temporal discretisation. In space, we discretise using standard linear Galerkin finite elements. In the time direction, we use a backward Euler integration scheme to update the solution at  $t = t^{n+1}$ , and to avoid solving nonlinear algebraic systems, we evaluate the coefficients  $a, b, c$  at time  $t = t^n$ . We therefore seek  $\mathbf{x}_h^{n+1}(\boldsymbol{\xi}, t) \in (\mathcal{L}^1(\Omega_{c,h}))^2$  such

that

$$\begin{aligned} \tau \int_{\Omega_{c,h}} \left( \frac{\mathbf{x}_h^{n+1} - \mathbf{x}_h^n}{\Delta t} \right) \hat{\mathbf{v}}_h \, d\xi + \int_{\Omega_{c,h}} [(\mathbf{x}_h^{n+1})_\xi \cdot (a^n \hat{\mathbf{v}}_h)_\xi + (\mathbf{x}_h^{n+1})_\eta \cdot (c^n \hat{\mathbf{v}}_h)_\eta + \\ \frac{1}{2} [(\mathbf{x}_h^{n+1})_\xi \cdot (b^n \hat{\mathbf{v}}_h)_\eta + (\mathbf{x}_h^{n+1})_\eta \cdot (b^n \hat{\mathbf{v}}_h)_\xi]] \, d\xi = 0, \end{aligned} \quad (5.26)$$

for all  $\hat{\mathbf{v}}_h \in (\mathcal{L}_0^1(\Omega_{c,h}))^2$ . The resulting linear systems are solved using the iterative method BiCGSTAB and an incomplete LU (ILU) factorization as a preconditioner. An analysis of the performance of this iterative solver for the discretised MMPDE equations can be found in [10].

### 5.3.2 Boundary mesh generation

We use the method described in [42] to determine how the mesh points at the domain boundary move. Given a rate at which the boundary is expanding in the normal direction, the method will not only define a new set of boundary points at the appropriate locations, but will also equidistribute the points in the tangential direction while maintaining the shape of the boundary. This helps to ensure that boundary points do not cross and cause a tangled mesh in areas where the boundary has a high degree of curvature.

## 5.4 The complete algorithm

At the start of the time step  $t = t^n$  we have a mesh  $\mathcal{T}_{h,t^n}$  and finite element approximations  $c_h^n$  and  $c_{s,h}^n$  of the bulk and surface bound species, respectively. The following steps are then carried out to advance the mesh and approximation solutions forward in time.

1. *Update the physical mesh*
  - (a) Define the normal velocity of the boundary points (this will be discussed in Section 5.5).

- (b) Use the method described in Section 5.3.2 to update the boundary points.
  - (c) Using the updated boundary points as fixed Dirichlet data, update the interior mesh points by solving the linear systems arising from (5.26).
2. *Update the finite element solution in the bulk and the surface*
- (a) Use the meshes  $\mathcal{T}_{h,t^{n+1}}$  and  $\mathcal{T}_{h,t^n}$  to define the discrete ALE velocity  $\mathbf{w}_h$ .
  - (b) Predict the solution on the boundary  $c_{s,h}^{n+1}$  by solving (5.17).
  - (c) Update the solution in the bulk  $c_h^{n+1}$  by solving (5.18).
  - (d) Correct the solution on the boundary  $c_{s,h}^{n+1}$  by solving (5.19).

## 5.5 Application to Langmuir-Hinshelwood surface reaction mechanism

We now apply the computational method described above to solve two-dimensional models where we assume the same Langmuir-Hinshelwood adsorption kinetics as described earlier. The flux boundary condition and surface concentration equation take the form

$$-D \frac{\partial c}{\partial \mathbf{n}} \Big|_{\Gamma(t)} = k_1(s_{tot} - c_s)c|_{x \in \Gamma(t)} - k_{-1}c_s, \quad (\mathbf{x}, t) \in \Gamma(t) \times (0, T),$$

and

$$\frac{\partial c_s}{\partial t} = D_s \Delta_{\Gamma} c_s + k_1(s_{tot} - c_s)c|_{x \in \Gamma(t)} - k_{-1}c_s - k_2 c_s, \quad (\mathbf{x}, t) \in \Gamma(t) \times (0, T).$$

This is equivalent to setting  $g(c|_{\Gamma(t)}, c_s) = k_1(s_{tot} - c_s)c|_{x \in \Gamma(t)} - k_{-1}c_s$  and  $h(c_s) = -k_2 c_s$ , where all parameters are as previously described (note that  $s_{tot}, c|_{\Gamma(t)}$  and  $c_s$  are defined at all points on the boundary).

As before, we will define  $p$  as the concentration of product formed at the boundary and assume it evolves so that

$$\frac{\partial p}{\partial t} = k_2 c_s, \quad (\mathbf{x}, t) \in \Gamma(t) \times (0, T). \quad (5.27)$$

In this model we assume that product molecules instantaneously desorb from the surface and that the active site becomes available to bind molecules of the bulk species.

At each time step, the algorithm presented in Section 5.4 is used to update  $c_h$  and  $c_{s,h}$  at the following time step. By discretising (5.27) using a Crank-Nicolson method, we define the approximation of  $p$  at the forward time step as

$$p_h^{n+1} = p_h^n + \frac{\Delta t k_2}{2} (c_{s,h}^{n+1} + c_{s,h}^n).$$

When considering an expanding boundary we will assume that the rate at which the boundary is expanding is equal to the rate at which the bound species is being converted into product. Hence, we have that the outer boundary is expanding in the normal direction at a rate of  $k_2 c_s$ . Note that this is the two-dimensional equivalent to (4.3), where we have the boundary expanding in the direction of the outward facing normal.

## 5.5.1 Stationary domains

### 5.5.1.1 Circular domain

We will initially consider a stationary unit circle domain. The following results were produced with  $k_1 = k_{-1} = k_2 = 1$ ,  $s_{tot} = 1$ ,  $D = 1$ ,  $D_s = 1$  and  $T = 10$ . These parameters were chosen such that no one process (adsorption of reactant, surface reaction, or transport of reactant to the boundary) are completely rate-limiting. The results presented in this section are not sensitive to small changes in parameters. For the simulations we used  $NT = 10^3$  time steps and an isotropic

mesh with  $N = 888$  elements, which gives a maximum edge length of  $h = 0.08$ . The initial conditions for the bulk, the surface species, and the product are  $c_h(\mathbf{x}, 0) = 1$ ,  $c_{s,h} = 0$ , and  $p_h = 0$ .

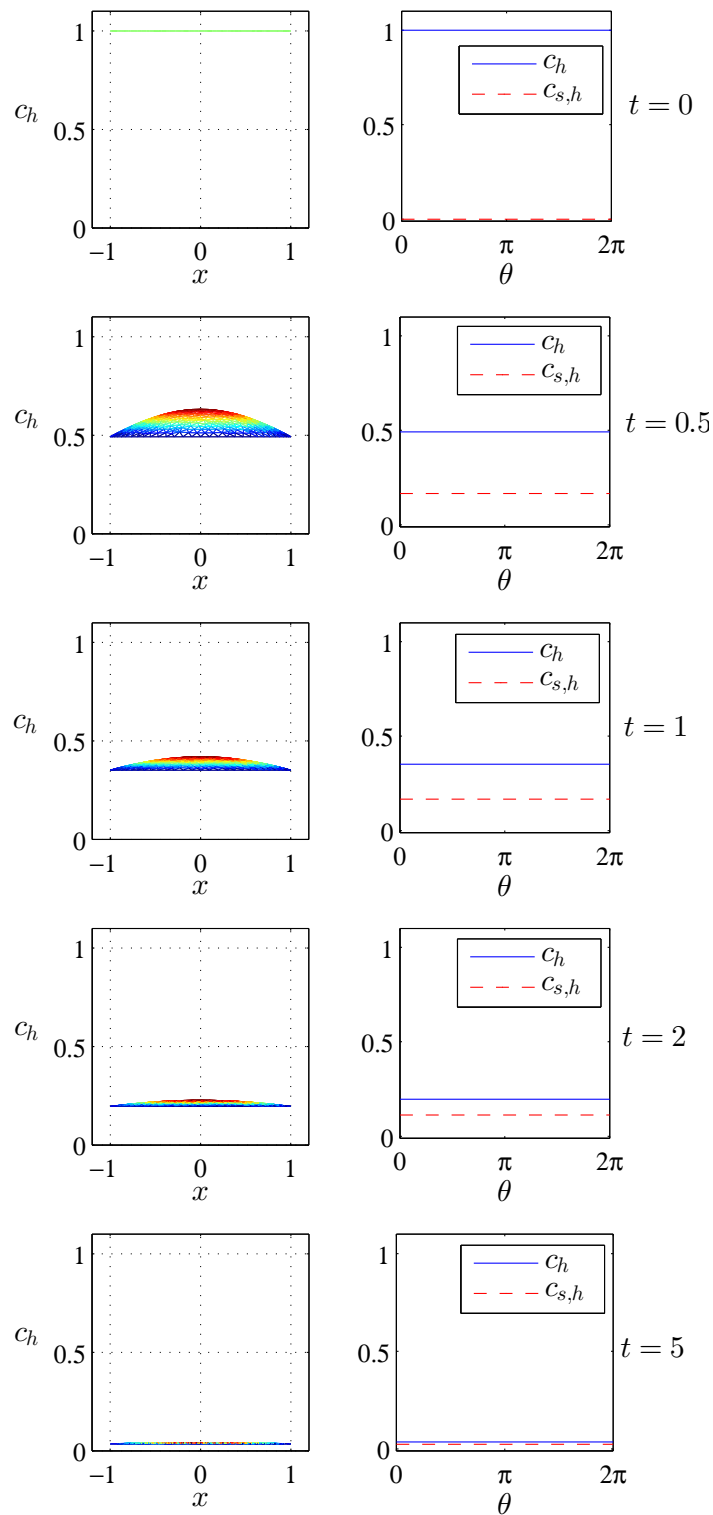


Figure 5.4: Plots of surface and bulk concentrations when  $k_1 = k_{-1} = k_2 = 1$ ,  $s_{tot} = 1$  at  $t = 0, 0.5, 1, 2$  and  $5$ . The mesh used has a maximum edge length of  $h = 0.08$  and  $NT = 1000$  time steps were used. The plots on the left hand side demonstrate how the bulk concentration varies with time. The right hand plots show that, at the surface, the bulk concentration  $c_h$  is continuously decreasing whereas  $c_{s,h}$  increases initially before decreasing.

Figure 5.4 shows plots of the bulk concentration of reactant (left hand side) and the concentration of the unbound reactant and concentration of the bound reactant at the boundary plotted against the angular coordinate of the boundary (right hand side). We can see initially that molecules of the bulk species adsorb onto the boundary where they react to form the product. Due to the time taken for bulk molecules to diffuse to the boundary, this results in a spatially inhomogeneous distribution of the bulk concentrations. As time progresses, the bulk concentration decreases and becomes increasingly flat. The right hand side plots of Figure 5.4 show that both concentrations at the boundary are approximately flat. This is due to having initial conditions which are constant in space and having a radially symmetric domain.

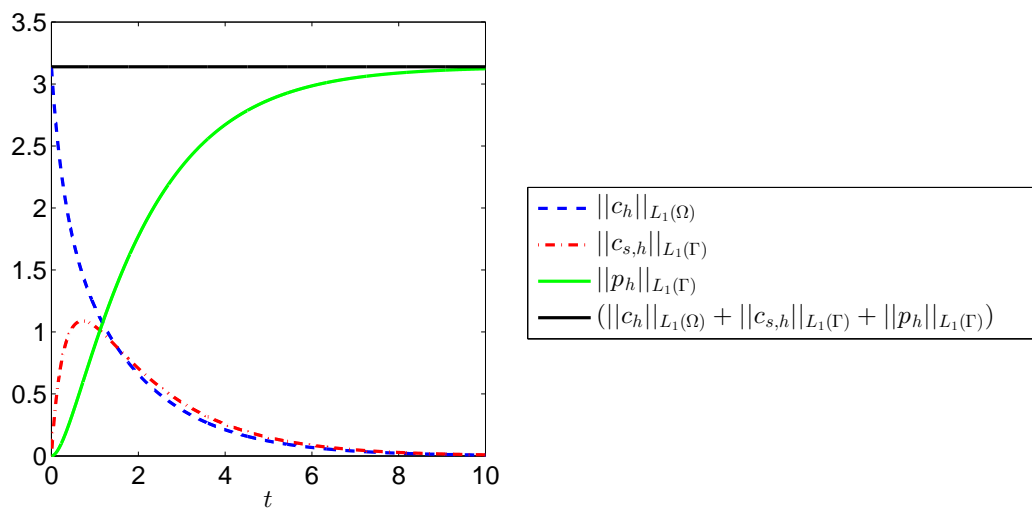


Figure 5.5: Plot showing the total concentration of reactant in the bulk ( $\|c_h\|_{L_1(\Omega)}$ ) and on the surface ( $\|c_{s,h}\|_{L_1(\Gamma)}$ ), the total concentration of product formed ( $\|p_h\|_{L_1(\Gamma)}$ ) as well as the sum of all three concentrations ( $\|c_h\|_{L_1(\Omega)} + \|c_{s,h}\|_{L_1(\Gamma)} + \|p_h\|_{L_1(\Gamma)}$ ).

By integrating  $c_h$  over the entire domain we can calculate the total amount of  $c_h$  in the system, which we define as  $\|c_h\|_{L_1(\Omega)}$ . Similarly, by integrating  $c_{s,h}$  and  $p_h$  over the boundary we can calculate the total amount of bound reactant and the total amount of reactant converted into product, which we will define as  $\|c_{s,h}\|_{L_1(\Gamma)}$  and  $\|p_h\|_{L_1(\Gamma)}$ , respectively. Figure 5.5 shows the total amount of

$\|c_h\|_{L_1(\Omega)}$ ,  $\|c_{s,h}\|_{L_1(\Gamma)}$  and  $\|p_h\|_{L_1(\Gamma)}$  against time, along with the total combined amount of reactant and product (  $\|c_h\|_{L_1(\Omega)} + \|c_{s,h}\|_{L_1(\Gamma)} + \|p_h\|_{L_1(\Gamma)}$  ). The plot demonstrates that the numerical method does an excellent job of mass conservation in this example. Note that Figure 5.5 is qualitatively very similar to the plot of the one-dimensional intermediate case in Figure 2.28.

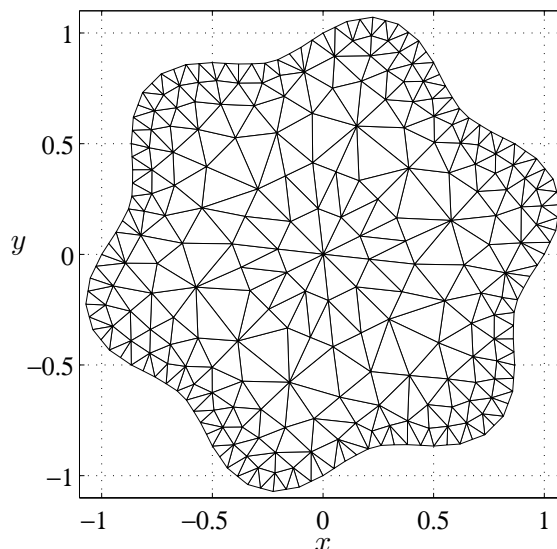


Figure 5.6: An example of a mesh produced using the MESH2D tool [7] after the boundary points have been equidistributed and a new interior mesh is found.

### 5.5.1.2 Non-circular domain

We now consider a non-circular domain, where the boundary is defined by the equation  $r(\theta) = 1 + 0.1 \sin(\theta)$ , and  $r$  and  $\theta$  are polar coordinates. We again assume the same initial conditions as in the previous example. Similarly, we use the same parameters as those used in the previous simulation. As in the previous example, our results are not sensitive to small changes in parameter values. As the boundary is not radially symmetric in this example, it will take longer for molecules of the bulk species to diffuse to certain parts of the boundary. This will result in the concentrations of  $c$  and  $c_s$  not remaining constant in space. Figures 5.7 and 5.8

were produced with identical kinetic parameters to those used previously.

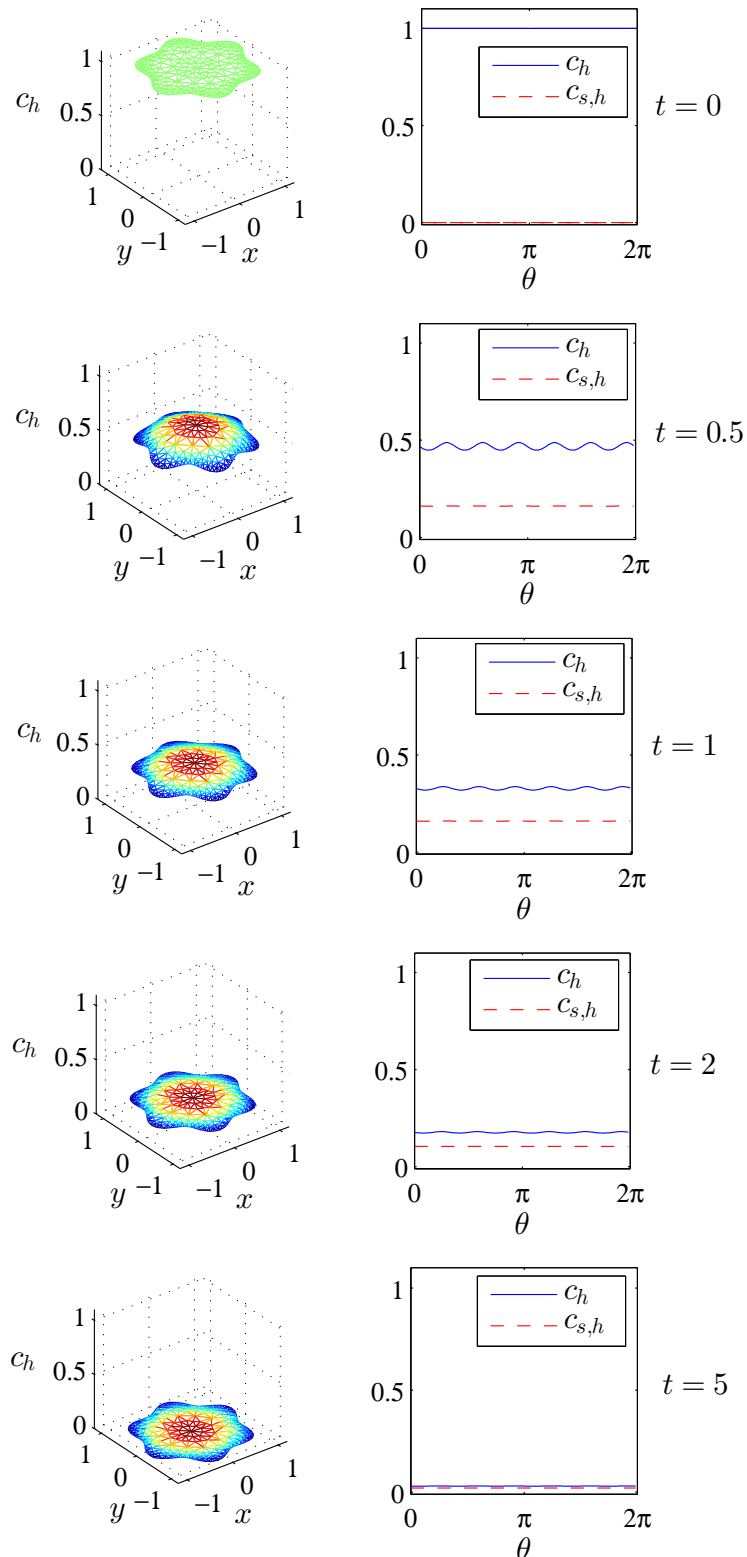


Figure 5.7: Plots of surface and bulk concentrations when  $k_1 = k_{-1} = k_2 = 1$ ,  $s_{tot} = 1$  at  $t = 0, 0.5, 1, 2$  and  $5$ . The mesh used has an approximate maximum edge length  $h = 0.3$  and  $NT = 5000$  time steps were used. The plots on the left hand side demonstrate how the bulk concentration varies with time. The right hand plots show that, at the surface, the bulk concentration  $c_h$  is continuously decreasing whereas  $c_{s,h}$  increases initially before decreasing. Simultaneously, the surface concentration profile of  $c_h$  is gradually becoming flatter.

The mesh used to approximate the domain is shown in Figure 5.6. The mesh was produced using the automatic mesh generation tool MESH2D [7]. The software allows a user to specify a number of boundary points and creates a mesh based on these specifications. We produced an initial mesh using MESH2D. This mesh does not necessarily have a good distribution of points along the boundary. Hence, we used the method described in Section 5.3.2, without expanding the boundary, to reposition the boundary points to ensure that they equidistribute the arc-length of the boundary. Using the newly defined boundary points as Dirichlet boundary conditions, the method described in Section 5.3.1, using the initial mesh produced using MESH2D, is used to solve for new interior mesh points. The mesh used for the simulations has a maximum edge length  $h = 0.308$  and  $NT = 5 \times 10^3$  time steps were used.

We can see from Figures 5.7 and 5.8 that the results are qualitatively and quantitatively very similar to the previous case considered. The plots on the right hand side of Figure 5.7 show that the bulk concentration at the surface is not spatially uniform. The plots in Figure 5.7 at  $t = 0.5$  show that  $c_h$  at the surface is not spatially uniform. The peaks in this plot are due to certain points of the boundary being closer to the centre of the domain. When molecules of the bulk species are adsorbed onto surface sites, the concentration of bulk species will decrease at the surface. For points on the surface closer to the centre of the domain, molecules of the bulk species will be more quickly transported to the boundary to replenish any molecules which have been adsorbed. Hence, we find that  $c_h$  at the surface becomes more spatially uniform as  $t$  increases. Due to assuming that the bound species  $c_{s,h}$  will diffuse along the domain, we have that  $c_{s,h}$  remains approximately spatially constant throughout the simulation.

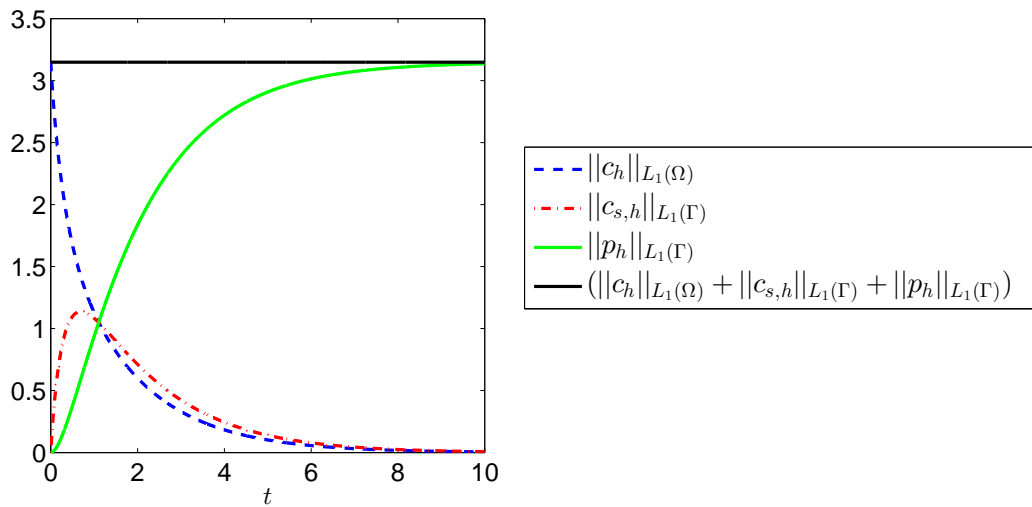


Figure 5.8: Plot showing the total concentration of reactant in the bulk ( $\|c_h\|_{L_1(\Omega)}$ ) and on the surface ( $\|c_{s,h}\|_{L_1(\Gamma)}$ ), the total concentration of product formed ( $\|p_h\|_{L_1(\Gamma)}$ ) as well as the sum of all three concentrations ( $\|c_h\|_{L_1(\Omega)} + \|c_{s,h}\|_{L_1(\Gamma)} + \|p_h\|_{L_1(\Gamma)}$ ).

### 5.5.2 Expanding circular domains

We next consider an example where we expand the circular boundary at a constant rate, so that  $r(t) = 1 + 4t$ . The parameters used in this case are the same as the previous two cases, except  $k_2$  has been reduced from 1 to 0.1. The reason for reducing  $k_2$  was to replicate the qualitative behaviour of the results presented in the previous section. In this case, the concentration of surface bound species will be reduced due to the expanding boundary, hence to ensure that the concentration of boundary species wasn't approximately zero, we set  $k_2$  to be smaller to limit the amount of bound species being converted to reactant. As in previous simulations, the results presented in this section are not sensitive to small changes in parameter values. The initial mesh used in this case is identical to the previous circular case considered. Instead of solving for our outer boundary mesh points at each time step and then solving for the interior points, we will simply expand all points radially outwards at a constant rate.

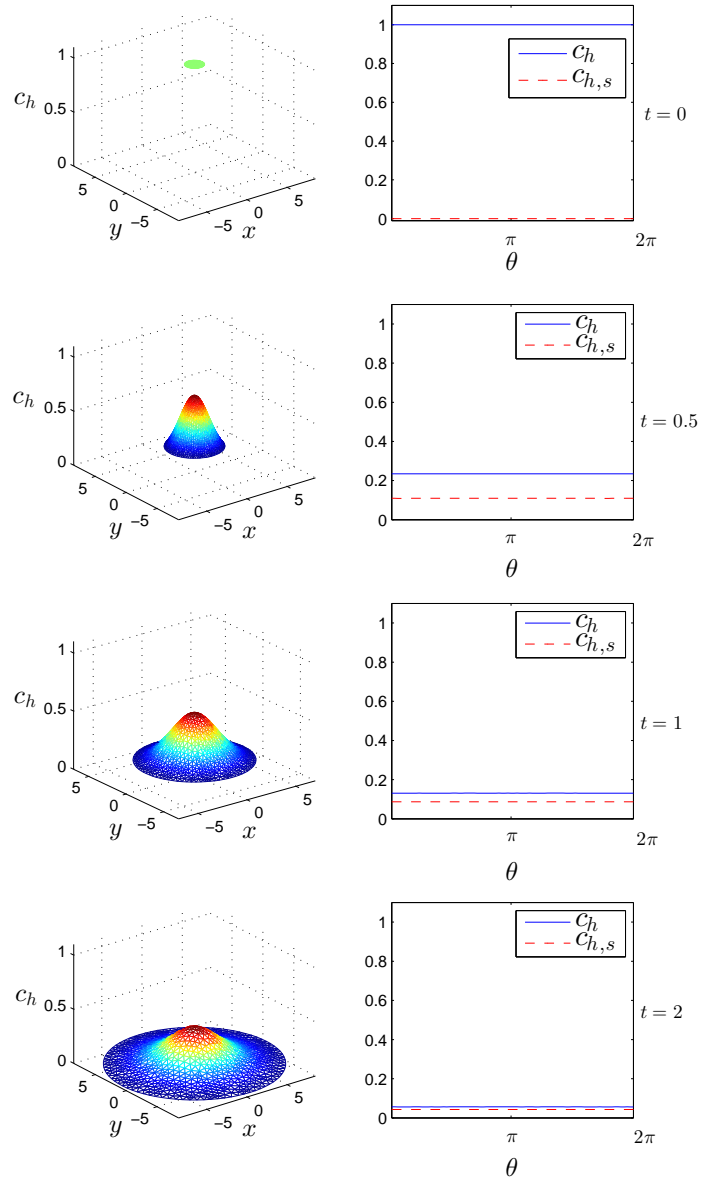


Figure 5.9: Plots of surface and bulk concentrations when  $k_1 = 1, k_{-1} = 1, k_2 = 0.1, s_{tot} = 1$  at  $t = 0, 0.5, 1$  and  $2$ . The mesh used has a maximum edge length  $h = 0.08$  and  $NT = 5000$  time steps were used. The plots on the left hand side show how the bulk concentration varies with time as the domain expands. The right hand plots show that, at the surface, the bulk concentration  $c_h$  is continuously decreasing, whereas  $c_{s,h}$  remains close to zero throughout.

Figure 5.9 shows how the bulk and boundary concentrations behave when the domain expands at a substantial rate. We can see that  $c_h$ , close to the boundary,

decreases far more quickly than at the centre of the domain. This is due to the reaction taking place at the boundary, but also because the domain is expanding making it more difficult for bulk reactant molecules to replenish molecules adsorbed onto the surface.

As was mentioned previously, for this example we are not solving for a new domain, or solving for a new mesh. Hence when applying the algorithm given in Section 5.4, step 1 will not be necessary. Throughout the following simulations we will consider two methods. Method 1 involves performing steps 2 (a) - 2 (c) at each time step, and Method 2 involves performing steps 2 (a) - 2 (d). In practice, we would not propose using Method 1 over Method 2 as step 2 (d) is relatively cheap to perform. However, Method 1 is included here for comparative purposes.

Figure 5.10 shows temporal convergence of  $c_h$  and  $c_{s,h}$  when  $k_1 = 1, k_{-1} = 1, k_2 = 0.1, s_{tot} = 1$  at  $t = 2$ . Throughout the simulations we used  $h = 0.1$ . As an approximation of the exact solution we used  $NT = 8000$  and to compare with this solution we used  $NT = 160, 320, 640$  and  $1280$ . We denote the maximal node errors in  $c_h$  and  $c_{s,h}$  as  $E_{c_h} = \|c - c_h\|_{l_\infty}$  and  $E_{c_{s,h}} = \|c_s - c_{s,h}\|_{l_\infty}$ , respectively. The plots show that Method 2 is second-order convergent (in terms of  $c_h$  and  $c_{s,h}$ ) while Method 1 is only first-order convergent; this demonstrates the advantage of performing step 2 (d) in Section 5.4.

For spatial convergence tests we used  $NT = 8000$ . For our exact solution we used  $h = 0.02$  and to compare with this exact solution we used  $h = 0.1, 0.2, 0.4$  and  $0.8$ . Figure 5.11 shows that second-order spatial convergence for our method still holds when we have an expanding domain.

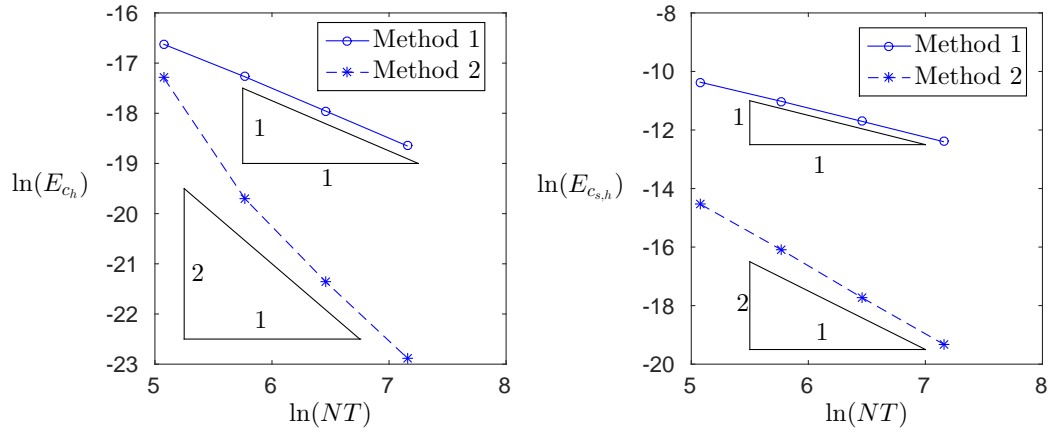


Figure 5.10: Temporal convergence of bulk-surface FEM on a time-dependent domain. Kinetic parameters are  $k_1 = 1, k_{-1} = 1, k_2 = 0.1, s_{tot} = 1$  and the final time is  $T = 2$ . The left hand plot shows convergence of the error in  $c_h$  and the right hand plot shows convergence of the error in  $c_{s,h}$ . Both plots show that Method 2 is second-order convergent in time, while Method 1 is only first-order.

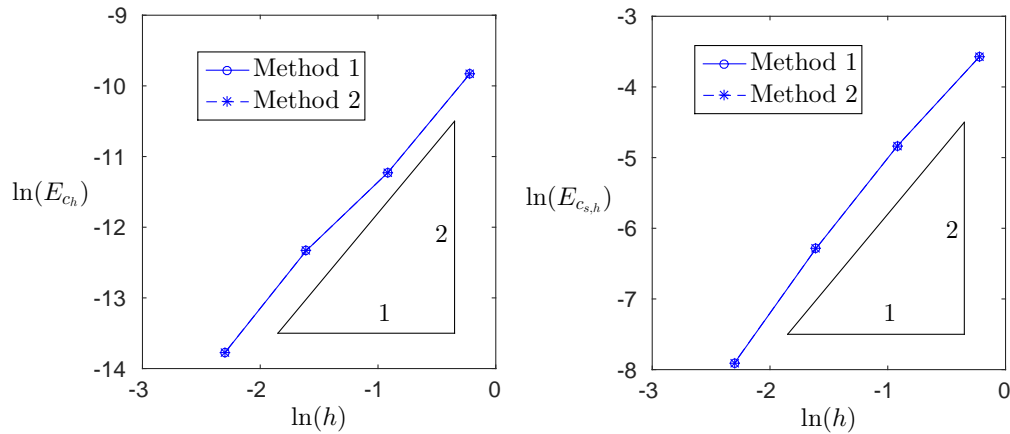


Figure 5.11: Spatial convergence of bulk-surface FEM on a time-dependent domain. Kinetic parameters are  $k_1 = 1, k_{-1} = 1, k_2 = 0.1, s_{tot} = 1$  and the final time is  $T = 2$ . The left hand plot shows convergence of the error in  $c_h$  and the right hand plot shows convergence of the error in  $c_{s,h}$ . Both plots show that both methods are second-order convergent in time.

We now consider an example where the domain expands due to the reaction taking place at the boundary. We will assume that the outer boundary expands outwards in the normal direction at a velocity of  $k_2 c_s$ . The following parameters are used;  $k_1 = 1, k_{-1} = 1, k_2 = 10, s_{tot} = 1, T = 2, h = 0.1$  and  $NT = 1 \times 10^3$ . In this case we increased  $k_2$  substantially to ensure that the expansion of the boundary

was not happening over a particularly large time-scale. The simulation results in this case are not sensitive to small changes in the chosen parameter values. The initial conditions are as in the previous case and we again use an initial isotropic mesh. Figure 5.12 shows plots of the bulk concentration  $c_h$ , as well as the surface concentrations  $c_h$  and  $c_{s,h}$  at  $t = 0, 0.5, 1, 1.5$  and  $2$ . Due to the finite amount of bulk reactant initially in the system, there is a limit to how far the boundary can expand. Figure 5.12 shows the results when the same parameters as the previous example are used. For this example, a new mesh is generated at each time step. A temporal smoothing parameter of  $\tau = 1 \times 10^{-3}$  was used for the simulation.

The plots show that the boundary is expanding. Due to the circular initial boundary and initial conditions we have that the domain will remain circular throughout the simulation. Other than the slight expansion of the boundary, the results are very similar to those obtained from the stationary circular domain problem. Note that  $c_{s,h}$  remains close to zero throughout due to  $k_2$  being significantly larger than  $k_1$  and  $k_{-1}$ .

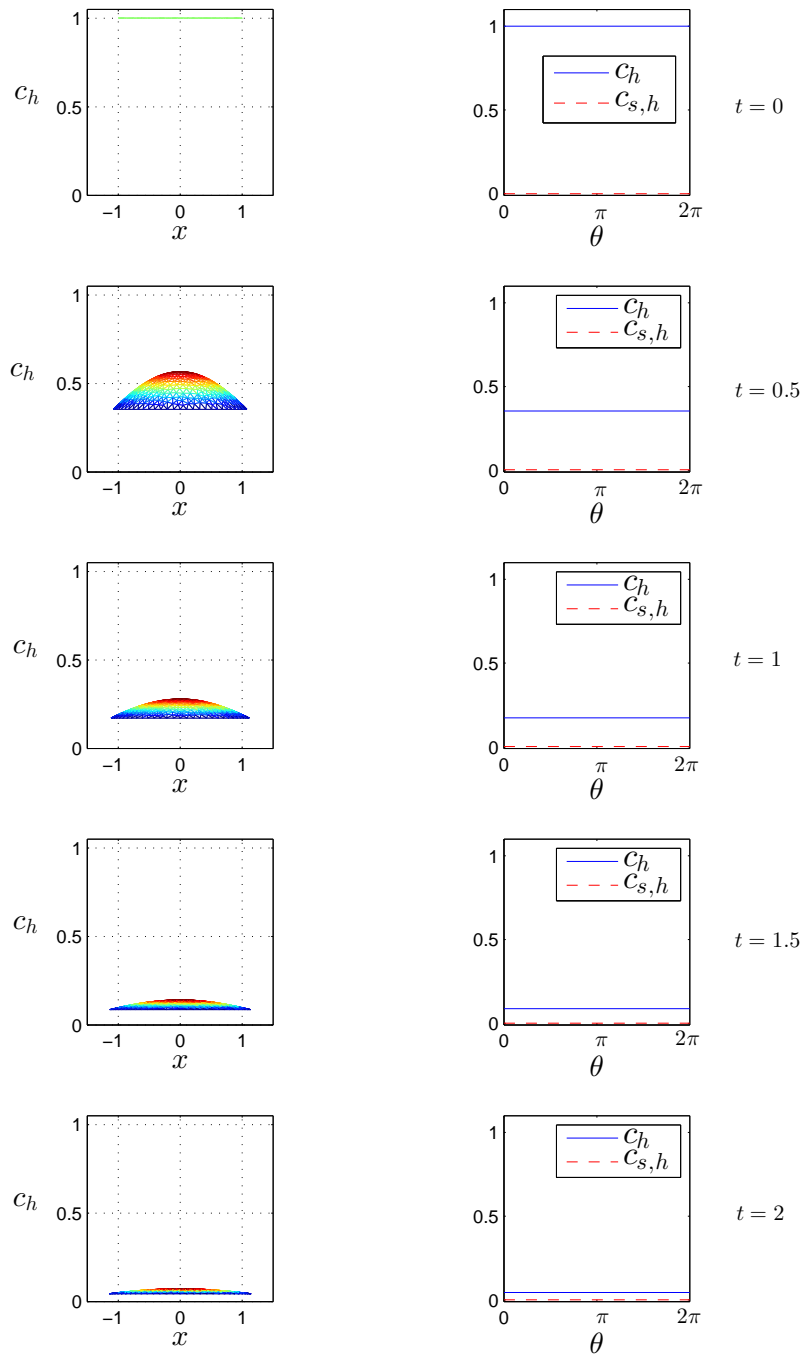


Figure 5.12: Plots of surface and bulk concentrations when  $k_1 = 1, k_{-1} = 1, k_2 = 10, s_{tot} = 1$  at  $t = 0, 0.5, 1, 1.5$  and  $2$ . The mesh used has a maximum edge length  $h = 0.1$  and  $NT = 1000$  time steps were used. When generating the moving meshes, a temporal smoothing parameter of  $\tau = 1 \times 10^{-3}$  was used. The plots on the left hand side demonstrate how the bulk concentration varies with time as the domain expands. The right hand plots show that, at the surface, the bulk concentration  $c_h$  is continuously decreasing whereas  $c_{s,h}$  remains close to zero throughout.

### 5.5.3 Expanding domain with boundary source of reactant

Finally, we consider a problem where we have a localised source of reactant. The location of this source is represented in this example by a fixed circular inner boundary in the middle of the domain. This means that we now have two boundaries in our system. As the inner boundary represents a constant source of reactant, the concentration of reactant at this inner boundary is kept constant throughout the simulation. In our FEM this is represented with constant Dirichlet boundary conditions at the inner boundary. This system is designed to be a two-dimensional equivalent of the system solved in Section 4.3 [67]. If we applied our model to such a system we would have that the inner boundary represents the source of hydroxyl radicals which will diffuse to the outer boundary and react with soot/dirt and cause the gap to expand.

The mesh used to cover the initial domain is shown in Figure 5.13 and was again produced using the automatic mesh generation tool MESH2D [7]. The outer and inner boundaries are defined by the equations  $r_1(\theta) = 1 + 0.1 \sin(\theta)$  and  $r_2(\theta) = 0.1$ , respectively, where  $r_{1,2}$  and  $\theta$  are polar coordinates. Using MESH2D we were able to specify the number of boundary points on both the inner and outer boundaries. A relatively fine initial mesh was chosen to allow us to expand the domain while still maintaining an acceptable mesh. We deliberately chose to have a large number of grid points at the inner boundary as, for the example considered, this is where we see the steepest gradients in the bulk concentration field. As with the example discussed in Section 5.5.1, we equidistributed the points on the outer boundary and solved for a new mesh. The initial mesh used for the following simulation had a maximum edge length  $h = 0.1439$  (shown in Figure 5.13) and  $NT = 5 \times 10^3$  time steps were used. The following parameters are used;  $k_1 = 5, k_{-1} = 1, k_2 = 0.5, s_{tot} = 1$  and  $T = 4$  and the following results are not sensitive to small changes in the parameter values used. Notice that the  $k_1$  to  $k_{-1}$  ratio is large, which allows reactant to easily bind to reaction sites. By setting  $k_2$  to be relatively small, we

limit the rate that the boundary can expand. If  $k_2$  was large, due to the constant supply of reactant, we would see the boundary expand more quickly.

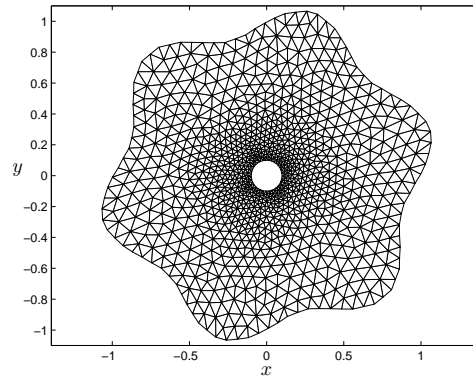


Figure 5.13: The initial mesh used to simulate diffusion in the bulk coupled to surface reactions at the domain boundaries.

The following plots demonstrate typical behaviour of such a system. Figure 5.14 shows plots at  $t = 0, 1, 2, 3$  and 4. The plots show that as the domain expands the outer boundary becomes more and more circular. This is unsurprising considering the source of reactant is circular. Reactant will be transported to the points of the boundary which are closer to the source more quickly than the points which are further away. This increased supply of reactant allows these points to expand more quickly and causes the outer boundary to eventually resemble a circle.

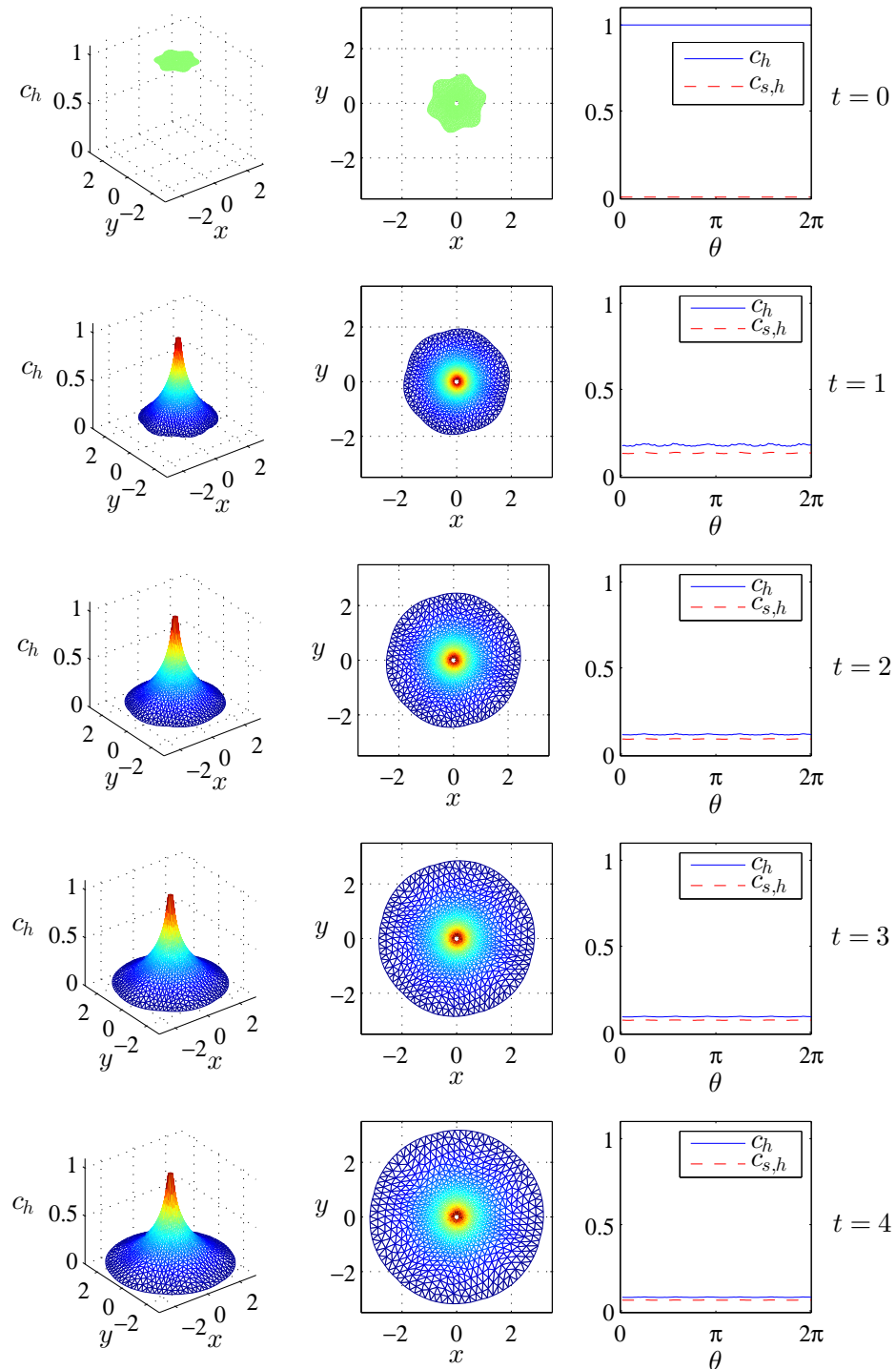


Figure 5.14: Plots of surface and bulk concentrations when  $k_1 = 5, k_{-1} = 1, k_2 = 0.5, s_{tot} = 1$  at  $t = 0, 1, 2, 3$  and 4. The mesh used has a maximum edge length of  $h = 0.14$  and  $NT = 5000$  time steps were used. Additionally, a temporal smoothing parameter of  $\tau = 1 \times 10^{-3}$  was used. The plots on the left hand side demonstrate how the bulk concentration varies with time as the domain expands and the plots in the centre show how the domain is gradually becoming more circular. The right hand plots show that, at the surface, the bulk concentration  $c_h$  is gradually decreasing whereas  $c_{s,h}$  initially increases, and remains relatively constant throughout the simulation.

## 5.6 Conclusions

In this chapter, we have presented a computational framework for the solution of coupled bulk- surface reaction-diffusion equations in two dimensions. The proposed algorithm is based on a conservative finite element ALE scheme to approximate the solution of the PDEs. A MMPDE approach has been used to simulate a curve moving in the normal direction that also allows control of the tangential distribution of mesh points. The overall algorithm has been shown to work well when applied to a model problem with a known analytical solution. The method has been applied to a system motivated by semiconductor photocatalysis and could be used for a range of different problems.

# Chapter 6

## Conclusion

### 6.1 Summary of main contributions

In Chapter 2 we introduced a numerical method for solving a system which models a reactant diffusing throughout a domain and reacting exclusively at a photocatalyst surface. This resulted in a coupled system of equations, where the bulk species was coupled to the surface species via a non-linear boundary condition. We proposed a method which involved explicitly solving for the concentration of surface species present at the boundary, before solving for the concentration of the bulk species using a Crank-Nicolson method. Once the bulk concentration has been approximated, we correct our initial approximation of the concentration of surface species using a Crank-Nicolson method. We demonstrated that our proposed technique was second-order convergent in space and time for a range of different parameter regimes. Throughout this thesis we used this numerical method, with slight modifications when required, and demonstrated that, for a range of different systems, our method was second-order convergent in space and time.

In Chapter 2, after presenting a general mathematical model, we considered a chemical system used to assess the activity of self-cleaning glass. We were able to replicate experimental data and use our model to explain the reason behind observed experimental results. In particular, we provided an explanation as to

why the initial reaction rate is inversely proportional to the thickness of the films considered.

For several of the systems considered in this thesis we explored the validity of the quasi-steady state assumption (QSSA). For every system where we considered the QSSA we were able to give examples of regimes where the QSSA was not valid. It is common practice to assume that the QSSA is valid for semiconductor photocatalyst systems as it can often significantly simplify the system. By showing that the QSSA is often not valid, our research suggests that care should be taken when invoking this assumption. Similarly, when modelling semiconductor photocatalysis systems it is often assumed that diffusion is quick enough to ensure that the transport of reactant is not rate-limiting. This assumption, along with the QSSA, is often used to simplify systems. However, for systems where these assumptions are not valid, more sophisticated methods will need to be considered. Throughout this thesis we have presented how the equations arising from various models can be solved without making either of these assumptions.

Chapter 3 focused on systems where reactions were taking place throughout the domain, as opposed to exclusively at the boundary, which was the case in Chapter 2. For two different systems we considered how the initial reaction rate varied with film thickness. For one of the systems considered we identified a regime where the initial reaction rate was inversely proportional to film thickness. Using our model we were able to rationalise this observed result. Interestingly, for an alternative system considered, we identified a distinct regime where the initial reaction rate was inversely proportional to the film thickness raised to the power of 0.72. Further work could involve additional consideration of the reason behind this dependence.

Many semiconductor photocatalyst systems involve the destruction of organics at a photocatalyst surface. This can lead to systems where the domain being considered is either expanding or contracting in size. In Chapter 4 we presented a numerical method which can be applied to systems where the domain is expand-

ing or contracting and a reaction is taking place at a boundary. We considered three models proposed by Ollis [67], and, for each model, we presented a more general model which makes fewer assumptions than the models proposed by Ollis. We demonstrated that our models could replicate the results presented by Ollis. Furthermore, we gave examples of situations where our general models could be applied, but the simple models proposed by Ollis would not be applicable.

In Chapter 5 we expand the work presented in Chapter 4 by considering surface catalysed reactions in two-dimensional time-dependant domains. We presented a computational framework for the solution of coupled bulk-surface reaction-diffusion equations in two dimensions. We showed that our approach works well by applying our method to a model problem with known solution. We went on to demonstrate, for several different regimes, that our proposed method was second-order convergent in space and time. The final simulations presented in this chapter gave an example of how our proposed method could be applied to a system where we have a source of hydroxyl radicals at an inner boundary which diffuse and react with soot/dirt at an outer boundary causing the outer boundary to expand.

## 6.2 Future work

For many of the systems considered, and some regimes in particular, there are periods of time where the solution varies rapidly with time. By adapting the size of the time step in line with how quickly the solution is varying, the methods we proposed could be made more efficient. For example, if we introduced a measure of how quickly the solution was changing between each time step we could decide to reduce the size of time step until the change in solution between two time steps was lower than some predefined tolerance. This would avoid a situation where we may be forced to use extremely small time steps throughout a simulation due to behaviour which is occurring exclusively at the start of the simulation.

Similarly, at times there are parts of the domain where the gradient of the

solution is very steep. This is particularly apparent when a solution decreases rapidly at a boundary. By determining the position of grid points based on the solutions being calculated, the efficiency of the proposed numerical methods could be improved.

In addition to exploring adaptive grids and adaptive time steps, our numerical method could potentially be improved by considering alternatives to the Crank-Nicolson method. Throughout the work presented in this thesis, the Crank-Nicolson method is used frequently as was our predictor-corrector approach. There are a range of other schemes which could be explored.

We did not consider the desorption kinetics of any product formed and its potential diffusion back into the bulk in any of the models we proposed in this thesis. Instead, we assumed that once a product had been formed, it no longer plays a role in any subsequent reactions. Furthermore, we have assumed that the reaction binding sites become available for further reactions. Potential enhancements to our models could involve considering what impact allowing reactant to desorb into the bulk would have on the overall kinetics of the systems we considered. Another interesting expansion of our work could involve considering a source of reactant at an outer boundary which is able to diffuse throughout a domain and react with a substance present at an inner boundary. It would also be interesting to consider two-dimensional systems where we have reactions occurring throughout the domain as opposed to exclusively at an outer boundary. This could be used to create two-dimensional models based on the systems considered in Chapter 3.

In all systems considered we assumed that any transport of reactant was entirely due to diffusion and ignored any potential convective transport. This would be particularly important were we to consider the ability of photocatalytic tiles and paint to remove airborne pollutants such as nitrogen oxides.

The final model presented in Chapter 3 was motivated by preliminary experimental results for a system where gas diffuses into a polymer film before reacting with a dye throughout the film. With more complete experimental data we would

aim to use our proposed model, with physically realistic parameters, to replicate experimental results before making predictions about the underlying system. Although this would be particularly useful for the material considered in Chapter 3, making use of additional experimental data would be beneficial for all models proposed. Throughout this thesis we have given an indication of how experimental results could be used to further validate our proposed models. In particular, we have suggested that if existing experiments could be reperformed using films that were substantially thicker than initial films used in experiments, the diffusion process would potentially become rate-limiting. This would allow us to further validate our proposed models which allowed for diffusion of reactant. Similarly, if experiments could be performed where the intensity of light applied to the photocatalyst is varied over a wide range of values, our models could potentially be used to replicate results ranging from reaction-limited (when the intensity of light is low, resulting in a slow surface reaction rate) through to diffusion-limited (when the intensity of light is high, the surface reaction rate will be quick).

In Chapter 5 we presented a numerical method for the solution of coupled bulk-surface reaction-diffusion equations in two dimensions which were motivated by the final case considered in Chapter 4. Numerical experiments carried out in this chapter suggest second-order spatial and temporal convergence. It would be useful to establish these rates theoretically. Consideration should be given with regards to how our model and the numerical technique proposed can be applied to a range of real life chemical systems. Again, experimental data would be helpful in helping to validate our proposed model and to make further enhancements and improvements.

# Appendix A

## Colour prediction

In Chapter 2 we considered a resazurin-based intelligent ink, which, under UV illumination, changed colour when applied to self-cleaning glass. In this appendix we demonstrate how experimental data can be analysed to predict what colour a material may be based on its absorbance spectrum.

An absorbance spectrum shows the fraction of incident radiation absorbed by a material at a certain frequency. This spectrum determines what colour we see when looking at a particular material. Using a standard formula we can convert an absorbance spectrum into CIE  $XYZ$  tristimulus values which can, in turn, be converted into RGB values which can be easily displayed by a computer [84]. The Commission internationale de l'éclairage (International Commission on Illumination, i.e. the CIE) has published selected colorimetric tables [4] which we make use of to predict what colour a material will be at a particular time based on its absorbance spectrum.

### A.1 Calculating CIE tristimulus values

The CIE originally defined the tristimulus values in terms of the integrals

$$X = k \int_{\lambda} S(\lambda) \bar{x}(\lambda) \beta(\lambda) d\lambda, \quad (\text{A.1})$$

$$Y = k \int_{\lambda} S(\lambda) \bar{y}(\lambda) \beta(\lambda) d\lambda, \quad (\text{A.2})$$

$$Z = k \int_{\lambda} S(\lambda) \bar{z}(\lambda) \beta(\lambda) d\lambda. \quad (\text{A.3})$$

Here,  $S(\lambda)$  is the spectral concentration of the radiant power of the source illuminating the object,  $\bar{x}(\lambda)$ ,  $\bar{y}(\lambda)$  and  $\bar{z}(\lambda)$  are the CIE 1931 standard colorimetric observers (shown in Figure A.1), where  $\int_{\lambda} \bar{x}(\lambda) d\lambda = \int_{\lambda} \bar{y}(\lambda) d\lambda = \int_{\lambda} \bar{z}(\lambda) d\lambda$  [2]. This means that, if an object has a completely flat absorbance spectrum, then  $X = Y = Z$ . The spectral reflectance of the illuminated and viewed object is represented by  $\beta(\lambda)$ , and  $k$  is a normalising factor given by

$$k = \frac{100}{\int_{\lambda} S(\lambda) \bar{y}(\lambda) d\lambda}. \quad (\text{A.4})$$

Equations (A.1)-(A.4) also apply when a material is transmitting instead of reflecting radiant power. This allows us to use the spectral transmittance  $T(\lambda)$  of an object instead of the reflectance factor  $\beta(\lambda)$  in (A.1)-(A.4). The transmittance of an object is the fraction of incident light that passes through a sample at a particular wavelength and can be written as

$$T(\lambda) = \frac{I(\lambda)}{I_0(\lambda)}, \quad (\text{A.5})$$

where  $I_0(\lambda)$  is the intensity of the incident light and  $I(\lambda)$  is the intensity of the light coming out of the object. Both  $I$  and  $I_0$  have units measured in the form of power divided by area. The definition of  $k$  makes the  $Y$  tristimulus value equal 100 exactly when the material is a *perfect reflecting diffuser* (i.e.  $\beta(\lambda) = 1$  at all wavelengths  $\lambda$ ). If an object is transmitting radiant power the *perfect reflecting diffuser* is replaced with the *perfect transmitting diffuser* (where  $T(\lambda) = 1$  at all wavelengths  $\lambda$ ) [91]. The  $XYZ$  values will be largest when we have a perfect reflecting/transmitting diffuser, leading to maximum values of  $X = 95.04$ ,  $Y = 100$  and  $Z = 108.85$ .

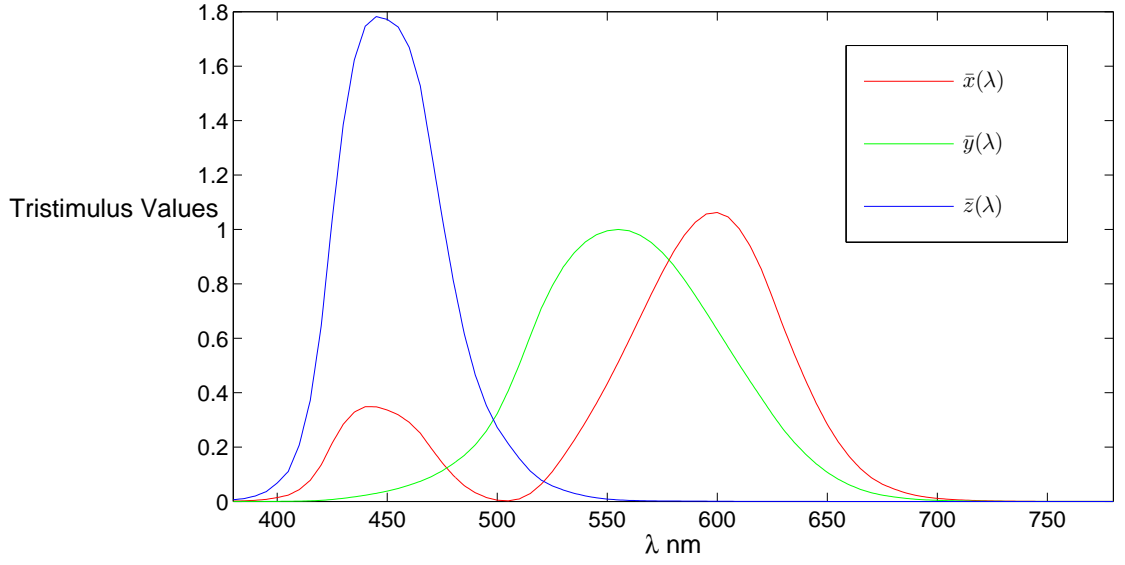


Figure A.1: The CIE 1931 standard colorimetric observers  $\bar{x}(\lambda)$ ,  $\bar{y}(\lambda)$  and  $\bar{z}(\lambda)$  [2].

From [83] we have that the relationship between the absorbance  $Ab(\lambda)$  and the transmittance  $T(\lambda)$  is given by

$$Ab(\lambda) = -\log_{10} \frac{I(\lambda)}{I_0(\lambda)},$$

which, making use of (A.5), can be re-arranged to give

$$T(\lambda) = 10^{-Ab(\lambda)}. \quad (\text{A.6})$$

The absorbance of an object is usually given in a discrete form at unit wavelength intervals. Hence we can substitute (A.6) into (A.1)-(A.4) and approximate the integrals with sums so that

$$X = k \sum_{\lambda=\lambda_a}^{\lambda_b} S(\lambda) \bar{x}(\lambda) 10^{-Ab(\lambda)} \Delta\lambda, \quad (\text{A.7})$$

$$Y = k \sum_{\lambda=\lambda_a}^{\lambda_b} S(\lambda) \bar{y}(\lambda) 10^{-Ab(\lambda)} \Delta\lambda, \quad (\text{A.8})$$

$$Z = k \sum_{\lambda=\lambda_a}^{\lambda_b} S(\lambda) \bar{z}(\lambda) 10^{-Ab(\lambda)} \Delta\lambda, \quad (\text{A.9})$$

$$k = \frac{100}{\sum_{\lambda=\lambda_a}^{\lambda_b} S(\lambda) \bar{y}(\lambda) \Delta\lambda}. \quad (\text{A.10})$$

The visible spectrum of wavelengths is  $(\lambda_a, \lambda_b)$ , where we assume that  $\lambda_a = 380$  nm and  $\lambda_b = 780$  nm [91].

The CIE have published data [4] that allows us to calculate (A.7)-(A.9). The data includes the colour-matching functions of the 1931 standard observer ( $\bar{x}(\lambda)$ ,  $\bar{y}(\lambda)$  and  $\bar{z}(\lambda)$ ) and standard illuminant data for D<sub>65</sub> (which simulates average daylight conditions with a correlated colour temperature of approximately 6504 K) which is  $S(\lambda)$  in this case. There are various other standard illuminants which are used to simulate different lighting conditions and are widely available on the internet. However D<sub>65</sub> is the main standard illuminant recommended by the CIE.

Using the built-in Matlab function `xyz2rgb`, it is straightforward to convert the 1931 CIE  $X, Y$  and  $Z$  values into RGB values and ultimately display the predicted colours.

## A.2 Making colour predictions using published data

Mills [50] published plots of the absorbance spectra of a typical Rz photocatalyst film indicator ink coated onto Activ<sup>TM</sup> self-cleaning glass at 16 uniformly distributed times throughout a 15 minute period of illumination with UVA light ( $3.3 \text{ mW cm}^{-2}$ ). It should be noted that the experiment was carried out under anaerobic conditions (i.e. without oxygen). This data is shown in Figure A.2.

At time  $t = 0$  there is a clear absorbance peak at approximately 608 nm. However, as time increases the peak at 608 nm gradually decreases, while a new

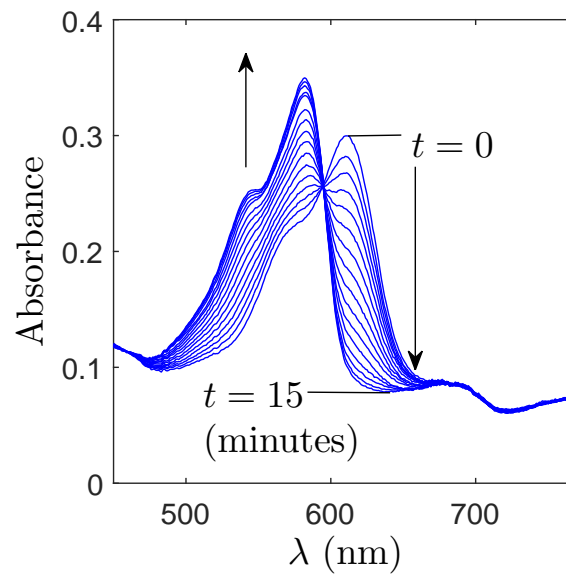


Figure A.2: UV/Visible absorbance spectra of a typical Rz photocatalyst indicator ink coated onto Activ<sup>TM</sup> self-cleaning glass at 16 uniformly distributed times throughout a 15 minute period of illumination with UVA light ( $3.3 \text{ mW cm}^{-2}$ ).

peak is simultaneously formed at approximately 580 nm. The initial spectrum corresponds to the Rz ink before the reaction has occurred whereas the spectrum after 15 minutes corresponds to the reduced form of the ink resorufin (Rf). As Rz is reduced to Rf there is a distinct colour change from blue to pink which corresponds to the change in absorbance spectra. Note that the spectra shown in Figure A.2 are qualitatively very similar to the spectra presented in Figures 2.33 - 2.39 from Section 2.2.

Using (A.7)-(A.10) we calculate the CIE  $X$ ,  $Y$  and  $Z$  co-ordinates corresponding to the 16 absorbance spectra shown in Figure A.2 and calculate the RGB values. Figure A.3 shows the colours predicted from the 16 absorbance spectra plotted in Figure A.2. There is a very clear colour change from light blue to pink. Mills [58] published pictures of the indicator ink applied to plain glass and Activ glass after 3 minutes of UV irradiation. Although the images were not obtained under the exact same experimental conditions as the data we have used to make our colour predictions, the pictures give us a qualitative idea of what kind of colours

we should be expecting to see as the ink changes colour throughout the reaction. The predictions in Figure A.3 are good estimates of what the colour change looks like in reality.

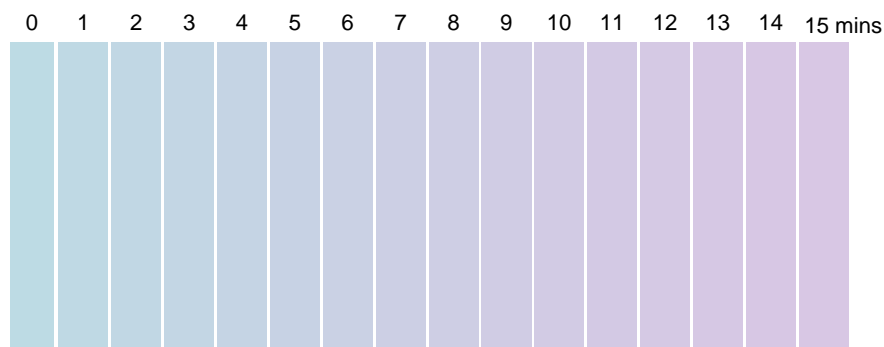


Figure A.3: The gradual colour change predicted using the 16 absorbance spectra from Figure A.2 with the initial colour at the far left and the colour after 15 minutes at the far right.

Brian Reid [1] has also designed an applet which predicts what colour a material should be based on its absorbance spectrum. A screenshot of the application is shown in Figure A.4, where the background colour of the graph is the colour which the application predicts that the absorbance spectrum corresponds to. Using the image manipulation programme *GIMP* we can easily extract the RGB values from the colour predicted by the application.

To compare the predictions made using Reid's applet with our own code we used two sets of absorbance data published on the internet [3]. Figures A.5 and A.6 show the comparison between the colours we predict from two different absorbance spectra and the colours predicted by the applet. The colours predicted are almost identical to look at, which would suggest that the method used to make our predictions is very similar to that used to make the predictions on the website.

For further comparison we entered the absorbance spectra shown in Figure A.2 into the applet and compared the colours with those which we predicted from our own calculations. The colours predicted by the applet are shown in Figure A.7 and are very similar to those predicted using our method, although they do appear to

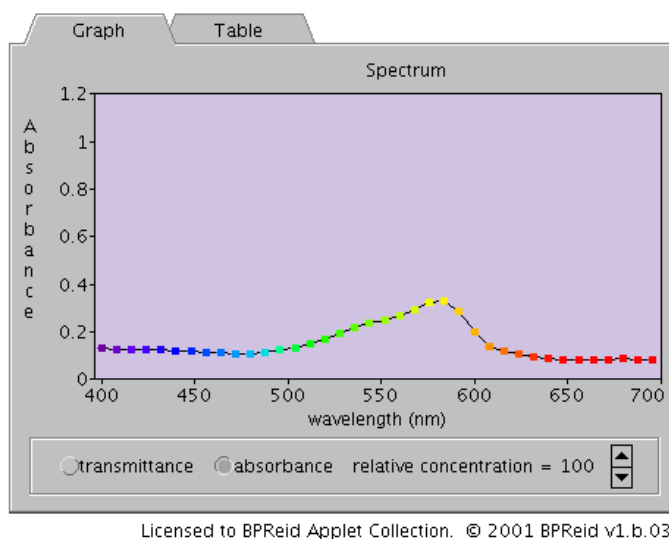


Figure A.4: A screenshot taken of Reid's website showing the application which predicts what colour a material will be based on its absorbance spectrum [1].

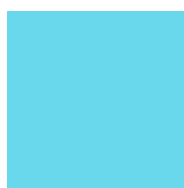


Figure A.5: Comparison of the colour predicted from the absorbance spectrum of the dye Malachite Green using our code (on the left) and the applet from Reid's website [1] (on the right).



Figure A.6: Comparison of the colour predicted from the absorbance spectrum of Rose bengal using our code (on the left) and the applet from Reid's website [1] (on the right).

be slightly darker. Figure A.8 shows the RGB values obtained from our Matlab code (solid lines) and from the website application (dashed lines). The behaviour of both sets of RGB values is very similar, although the values obtained from the applet are slightly lower throughout, which is the reason why the colours appear to be slightly darker.

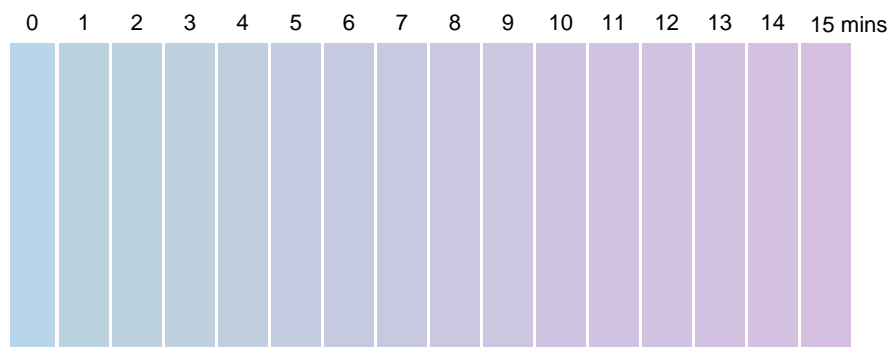


Figure A.7: The gradual colour change predicted using the applet [1] corresponding to the 16 absorbance spectra from Figure A.2. The initial colour is at the far left and the colour after 15 minutes is at the far right.

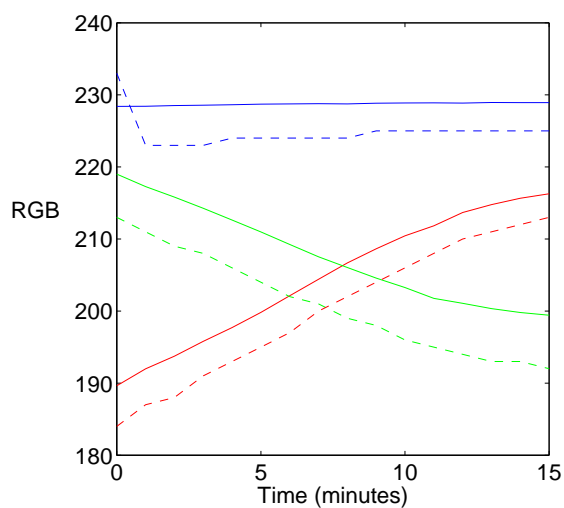


Figure A.8: The RGB values taken from the colour prediction made using our method (solid lines) and from the Reid website application [1] (dashed lines).

### A.3 Making colour predictions using experimental data

We performed the same colour predictions on the absorbance spectra we presented earlier in Figures 2.33 - 2.39 from Section 2.2. We will focus on three films; the thickest, the thinnest and an intermediate film.

Figures A.9 - A.11 show that for the thinnest film the colour predictions look pale in comparison to published photographs [58] and earlier predictions (Figure A.3). The change from blue to pink is visible, but very weak. For the middle film we see a far more convincing colour change which looks similar to the colour prediction made earlier. For the thickest film we see a far stronger colour change, however, the change is similar to the middle film.

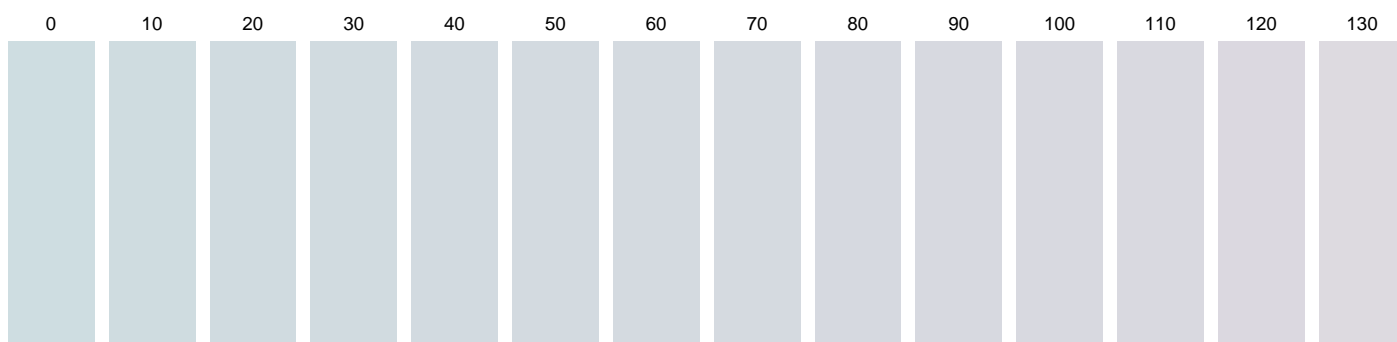


Figure A.9: The gradual colour change predicted with the initial colour at the far left and the colour after 1800 seconds at the far right from the absorbance spectra from a 549 nm thick film.

From the RGB plots we can see that qualitatively the R, G and B values are fairly similar for all three films, although quantitatively there is a significant difference. The overall absorbance is far higher for the thickest of films considered. This is unsurprising, as the Beer-Lambert law states that absorbance is proportional to path length (i.e. film thickness in this case) [83]. Our results suggest that thicker films will give a stronger colour change. Again, this is not surprising as thicker films will have a greater total number of dye molecules.

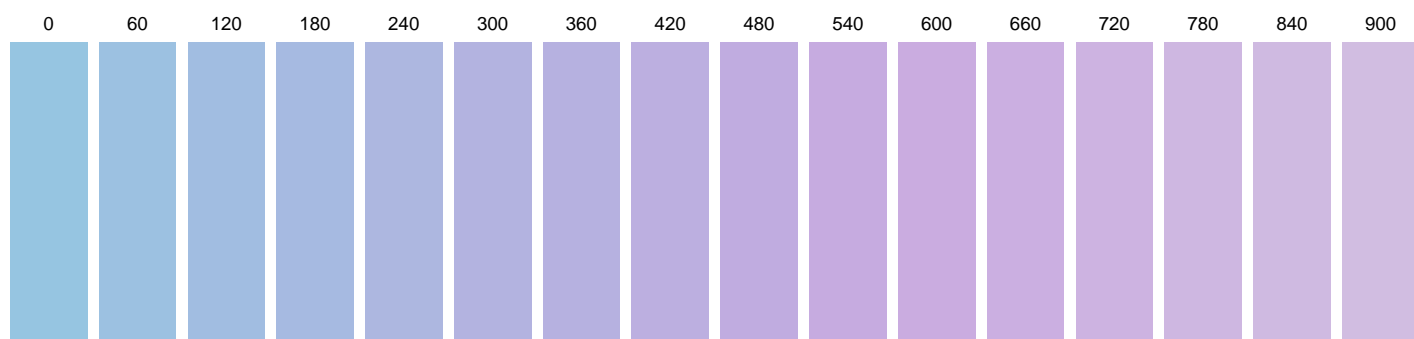


Figure A.10: The gradual colour change predicted with the initial colour at the far left and the colour after 900 seconds at the far right from the absorbance spectra from the 2140 nm thick film.

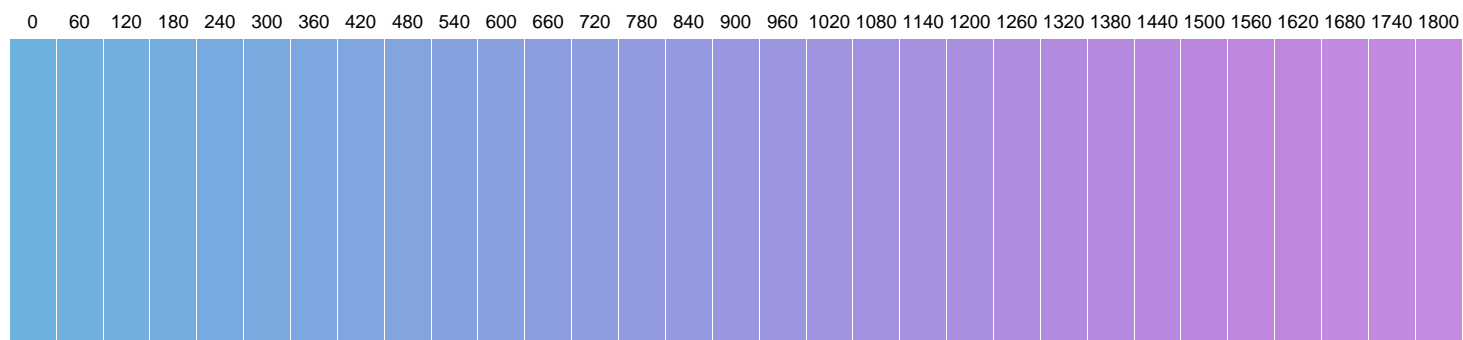


Figure A.11: The gradual colour change predicted with the initial colour at the far left and the colour after 1800 seconds at the far right from the absorbance spectra from the 4014 nm thick film.

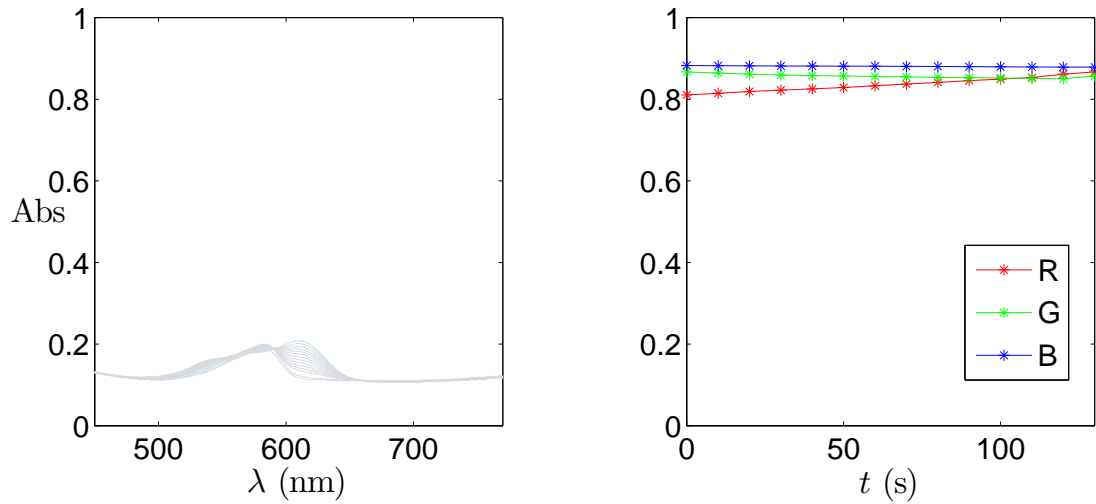


Figure A.12: Absorbance spectra for the 549 nm film (where spectra are plotted in our predicted colours) and the corresponding RGB values.

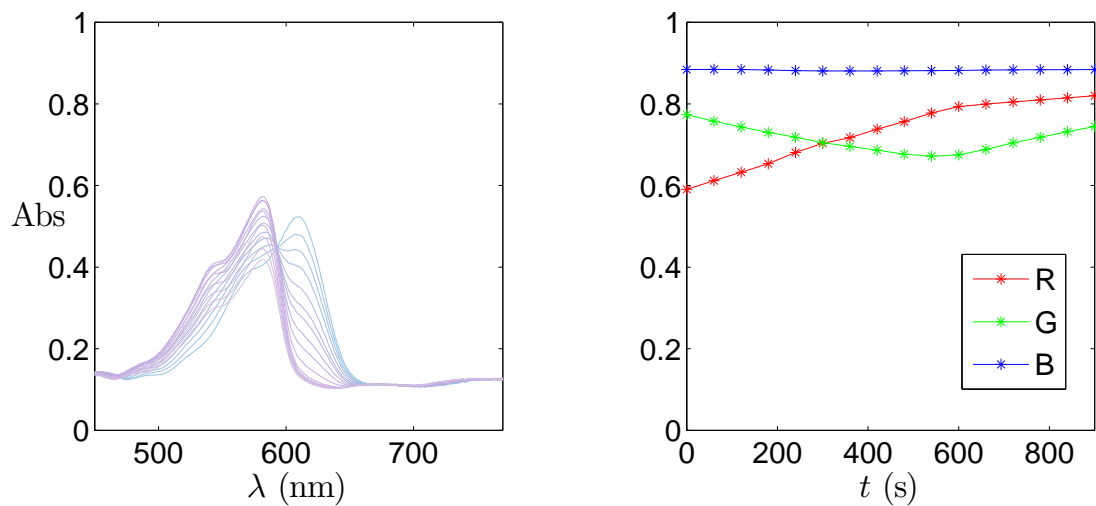


Figure A.13: Absorbance spectra for the 2140 nm film (where spectra are plotted in our predicted colours) and the corresponding RGB values.

## A.4 Conclusions and further work

We have demonstrated that we can predict the colour of a substance based purely on its absorbance spectrum. Our predictions are very similar to published pho-

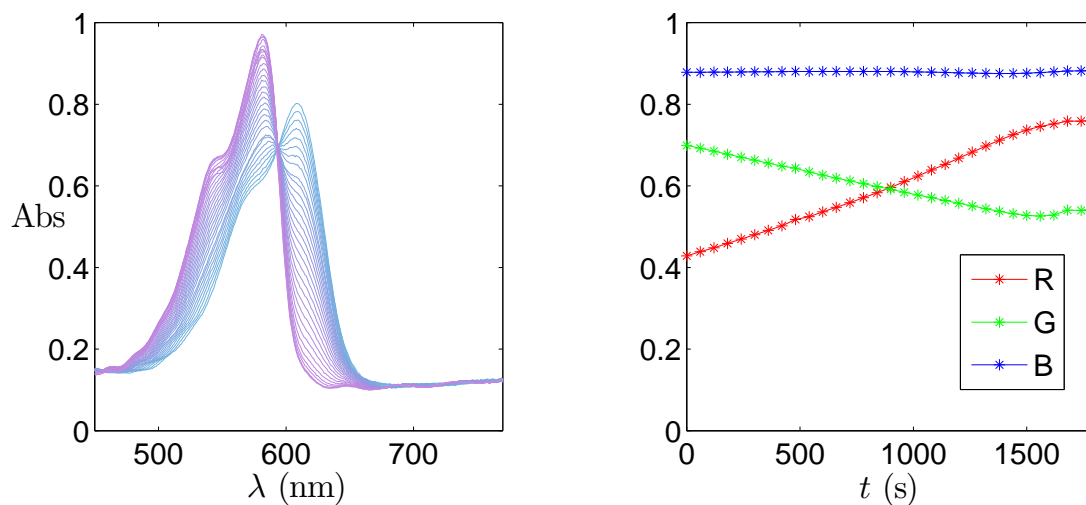


Figure A.14: Absorbance spectra for the 4014 nm film (where spectra are plotted in our predicted colours) and the corresponding RGB values.

tographs. We have also shown that the strength of the colour change is dependent on film thickness. This is due to thicker films containing more dye molecules and hence showing a stronger colour.

It can be noted from Figures A.13 and A.14 that the red RGB value changes most dramatically throughout the reaction process. This observation has been used in [52] and [61] to develop a cheap and quick means to determine quantitatively the activity of photocatalytic films via resazurin-based intelligent inks. Using either a digital scanner [52] or a mobile phone app [61] RGB data can easily be acquired and the R channel plotted as a function of time. The time taken for the R channel to reach 90% of its final maximum value,  $t_{tb}(90)$ , has been shown to correlate well with the inverse of the rate of the surface reaction. This follows if the reaction is approximately zeroth order in time up to the time  $t_{tb}(90)$ . Using the algorithm presented here we can further analyse the correlation between the absorbance data and the change in colour estimates. In particular, the algorithm could be used to identify dominant colour channels or combinations of channels whose dynamics are an accurate reflection of reaction rates deduced from changes to absorbance data.

# Bibliography

- [1] bpreid software for science and mathematics - spectroscopy: Spectral colors. <http://www.bpreid.com/spectral.php>, accessed June 2011.
- [2] H32: Putting numbers to colour: Cie xyz. <http://www.colour4free.org.uk/Books/H32ColourByNumbersCIEXYZV01.pdf>, accessed June 2011.
- [3] Oregon medical laser centre: Photochemcad spectra by category. <http://omlc.ogi.edu/spectra/PhotochemCAD/html/index.html>, accessed May 2011.
- [4] Selected colorimetric tables. [http://www.cie.co.at/index.php/LEFTMENUE/index.php?i\\_ca\\_id=298](http://www.cie.co.at/index.php/LEFTMENUE/index.php?i_ca_id=298), accessed May 2011.
- [5] How self-cleaning glass works. <http://www.pilkingtonselfcleaningglass.co.uk/how-it-works/default.htm>, accessed December 2013.
- [6] Science background and FAQ's. <http://www.catalytic-clothing.org/faq.html>, accessed September 2014.
- [7] MESH2D automatic 2d mesh generation. [http://people.sc.fsu.edu/~jburkardt/m\\_src/mesh2d/mesh2d.html](http://people.sc.fsu.edu/~jburkardt/m_src/mesh2d/mesh2d.html), accessed January 2015.
- [8] E. Allain, S. Besson, C. Durand, M. Moreau, T. Gacoin, and J Boilot. Transparent mesoporous nanocomposite films for self-cleaning applications. *Adv. Funct. Mater.*, 17:549–554, 2007.

- [9] A Ambrazevicius. Solvability of a coupled system of parabolic and ordinary differential equations. *Cent. Eur. J. Math*, 8(3):537–547, 2010.
- [10] G. Beckett, J.A. Mackenzie, A. Ramage, and D.M. Sloan. Computational solution of two-dimensional unsteady PDEs using moving mesh methods. *J. Comput. Phys.*, 182(2):478–495, 2002.
- [11] R. Blossey. Self-cleaning surfaces-virtual realities. *Nat. Mater.*, 2(5):301–306, 2003.
- [12] G. P. Boswell and F. A. Davidson. Diffusion fronts in enzyme-catalysed reactions. *J. Engrg. Math.*, 59(2):157–169, 2007.
- [13] S. Brosillon, L. Lhomme, C. Vallet, A. Bouzaza, and D. Wolbert. Gas phase photocatalysis and liquid phase photocatalysis: Interdependence and influence of substrate concentration and photon flow on degradation reaction kinetics. *Appl. Catal., B*, 78(34):232–241, 2008.
- [14] M. Chapwanya, J. M. S. Lubuma, and R. E. Mickens. Nonstandard finite difference schemes for Michaelis-Menten type reaction-diffusion equations. *Numer. Methods Partial. Differ. Equ.*, 29(1):337–360, 2013.
- [15] R.M. Corless, G.H. Gonnet, D.E.G. Hare, D.J. Jeffrey, and D.E. Knuth. On the Lambert-W function. *Adv. Comput. Math.*, 5(1):329–359, 1996.
- [16] J. Crank. *The Mathematics of Diffusion*. Oxford Science Publications. Clarendon Press, 1979.
- [17] M. E. Davis and R. J. Davis. *Fundamentals of chemical reaction engineering*. McGraw-Hill Higher Education, 2003.
- [18] S. de Niederhuser, M. Bondi, and F. Bondioli. Self-cleaning and antibacteric ceramic tile surface. *Int. J. Appl. Ceram. Tech.*, 10(6):949–956, 2013.

- [19] O. Deutschmann, H. Knzinger, K. Kochloeff, and T. Turek. *Heterogeneous Catalysis and Solid Catalysts*. Wiley-VCH, 2000.
- [20] J. Donea, S. Giuliani, and J.P. Halleux. An Arbitrary Lagrangian-Eulerian finite element method for transient dynamic fluid-structure interactions. *Comp. Meth. Appl. Mech. Engrg.*, 33(1-3):689–723, 1982.
- [21] J. Douglas and T. Dupont. Galerkin methods for parabolic equations with nonlinear boundary conditions. *Numer. Math.*, 20(3):213–237, 1973.
- [22] A.S. Dvinsky. Adaptive grid generation from harmonic maps on Riemannian manifolds. *J. Comput. Phys.*, 95(2):450–476, 1991.
- [23] C. M. Elliott and T. Ranner. Finite element analysis for a coupled bulk-surface partial differential equation. *IMA J. Numer. Anal.*, 33(2):377–402, 2013.
- [24] E. V. Emeline, A. V. Rudakova, V. Ryabchuk, and N. Serpone. Photostimulated reactions at the surface of wide band-gap metal oxides ( $ZrO_2$  and  $TiO_2$ ): Interdependence of rates of reactions on pressure-concentration and on light intensity. *J. Phys. Chem. B*, 102:10906–10916, 1998.
- [25] E. V. Emeline, V. Ryabchuk, and N. Serpone. Factors affecting the efficiency of a photocatalyzed process in aqueous metal-oxide dispersions: Prospect of distinguishing between two kinetic models. *J. Photochem. Photobiol. A*, 133:89–97, 2000.
- [26] E. H. Flach and S. Schnell. Use and abuse of the quasi-steady-state approximation. *Syst. Biol. (Stevenage)*, 153(4):187–191, 2006.
- [27] A. Fujishima and X. Zhang. Titanium dioxide photocatalysis: present situation and future approaches. *C. R. Chim.*, 9(5):750–760, 2006.

- [28] M. Hadnadjev, J. Ranogajec, S. Petrovic, S. Markov, V. Ducman, and R. Marinkovic-Neducin. Design of self-cleaning TiO<sub>2</sub> coating on clay roofing tiles. *Philos. Mag.*, 90(22):2989–3002, 2010.
- [29] J. Hagen. *Industrial Catalysis: A Practical Approach*. Wiley-VCH, 2006.
- [30] J. Herrmann. Heterogeneous photocatalysis: fundamentals and applications to the removal of various types of aqueous pollutants. *Catal. Today*, 53(1):115–129, 1999.
- [31] A. Hisaka and Y. Sugiyama. Analysis of nonlinear and nonsteady state hepatic extraction with the dispersion model using the finite difference method. *J. Pharmacokinet. Biopharm.*, 26(5):495–519, 1998.
- [32] M. R. Hoffmann, S. T. Martin, W. Choi, and D. W. Bahnemann. Environmental applications of semiconductor photocatalysis. *Chem. Rev.*, 95(1):69–96, 1995.
- [33] W. Huang. Practical aspects of formulation and solution of moving mesh partial differential equations. *J. Comput. Phys.*, 171(2):753–775, 2001.
- [34] W. Huang and R.D. Russell. Moving mesh strategy based on a gradient flow equation for two-dimensional problems. *SIAM J. Sci. Comput.*, 20(3):998–1015, 1999.
- [35] T.J.R. Hughes, W.K. Liu, and T.K. Zimmermann. Lagrangian-Eulerian finite element formulation for incompressible viscous flows. *Comp. Meth. Appl. Mech. Engrg.*, 29(3):329–349, 1981.
- [36] A. J. Kenneth. A century of enzyme kinetic analysis, 1913 to 2013. *FEBS Lett.*, 587(17):2753–2766, 2013.
- [37] H. Lachheb, E. Puzenat, A. Houas, M Ksibi, E. Elaloui, C. Guillard, and J. M. Herrmann. Photocatalytic degradation of various types of dyes (alizarin

- s, crocein orange g, methyl red, congo red, methylene blue) in water by uv-irradiated titania. *Appl. Catal., B*, 39(1):75–90, 2002.
- [38] K. Lawrie, M. Mills, and D. Hazafy. Simple inkjet-printed, UV-activated oxygen indicator. *Sens. Actuators B Chem.*, 176:1154–1159, 2013.
- [39] M. C. Lee and W. Choi. Solid phase photocatalytic reaction on the soot/TiO<sub>2</sub> interface: The role of migrating OH radicals. *J. Phys. Chem. B*, 106:11818–11822, 2002.
- [40] S. K. Lee, A. Mills, and A. Lepre. An intelligence ink for oxygen. *Chem. Commun.*, pages 1912–1913, 2004.
- [41] H. Levine and W. Rappel. Membrane-bound turing patterns. *Phys. Rev. E*, 72:061912, 2005.
- [42] G. MacDonald, J. A. Mackenzie, M. Nolan, and R. H. Insall. A computational method for the coupled solution of reaction-diffusion equations on evolving domains and manifolds: Application to a model of cell migration and chemotaxis. *J. Comput. Phys.*, 309:207–226, 2016.
- [43] M. Machida, K. Norimoto, and T. Kimura. Antibacterial activity of photocatalytic titanium dioxide thin films with photodeposited silver on the surface of sanitary ware. *J. Am. Ceram. Soc.*, 88(1):95–100, 2005.
- [44] J. A. Mackenzie and W. R. Mekwi. An analysis of stability and convergence of a finite-difference discretization of a model parabolic PDE in 1D using a moving mesh. *IMA J. Numer. Anal.*, 27:507–528, 2007.
- [45] A. Madzvamuse, A. H. W. Chung, and C. Venkataraman. Stability analysis and simulations of coupled bulk-surface reaction–diffusion systems. *Proc. R. Soc. A*, 471(2175):20140546, 2015.

- [46] P. Marek, J. J. Velasco-Velz, T. Haas, T. Doll, and G. Sadowski. Time-monitoring sensor based on oxygen diffusion in an indicator/polymer matrix. *Sens. Actuators B Chem.*, 178(0):254–262, 2013.
- [47] I. N. Martyanov and E. N. Savinov. Photocatalytic steady-state methylviologen oxidation in air-saturated TiO<sub>2</sub> aqueous suspension: Initial photonic efficiency and initial oxidation rate as a function of methylviologen concentration and light intensity. *J. Photochem. Photobiol. A*, 134:219–226, 2000.
- [48] A. Mills. Oxygen indicators and intelligent inks for packaging food. *Chem. Soc. Rev.*, 34(12):1003–1011, 2005.
- [49] A. Mills, M. Crow, J. Wang, I. P. Parkin, and N. Boscher. Photocatalytic oxidation of deposited sulfur and gaseous sulfur dioxide by TiO<sub>2</sub> films. *J. Phys. Chem. C*, 111:5520–5525, 2007.
- [50] A. Mills, A. Cusick, and J. Hepburn. The kinetics of semiconductor photocatalysis in activity-indicator films. *J. Adv. Oxid. Technol.*, 12:152–157(6), 2009.
- [51] A. Mills, D. Hazafy, and K. Lawrie. Novel photocatalyst-based colourimetric indicator for oxygen. *Catal. Today*, 161(1):59–63, 2011.
- [52] A. Mills, J. Hepburn, D. Hazafy, C. O'Rourke, J. Krysa, M. Baudys, M. Zlamal, H. Bartkova, C. E. Hill, K. R. Winn, et al. A simple, inexpensive method for the rapid testing of the photocatalytic activity of self-cleaning surfaces. *J. Photochem. Photobiol. A*, 272:18–20, 2013.
- [53] A. Mills and S. Le Hunte. An overview of semiconductor photocatalysis. *J. Photochem. Photobiol. A*, 108(1):1–35, 1997.
- [54] A. Mills and S-K. Lee. A web-based overview of semiconductor photochemistry-based current commercial applications. *J. Photochem. Photobiol. A*, 152:233–247, 2002.

- [55] A. Mills and M. McFarlane. Current and possible future methods of assessing the activities of photocatalyst films. *Catal. Today*, 129:22–28, 2007.
- [56] A. Mills and J. Wang. The kinetics of semiconductor photocatalysis: Light intensity effects. *Z. Phys. Chem.*, 110:49–58, 1999.
- [57] A. Mills, J. Wang, S. K. Lee, and M. Simonsen. An intelligence ink for photocatalytic films. *Chem. Commun.*, 21:2721–2723, 2005.
- [58] A. Mills, J. Wang, and M. McGrady. Method of rapid assessment of photocatalytic activities of self-cleaning films. *J. Phys. Chem. B*, 110(37):18324–18331, 2006.
- [59] A. Mills, J. Wang, and D. F. Ollis. Kinetics of liquid-phase semiconductor photoassisted reactions: Supporting observations for a pseudo-steady-state model. *J. Phys. Chem. B*, 110:14386–14390, 2006.
- [60] A. Mills, J. Wang, and D.F. Ollis. Dependence of the kinetics of liquid-phase photocatalyzed reactions on oxygen concentration and light intensity. *J. Catal.*, 243:1–6, 2006.
- [61] A. Mills and N. Wells. Indoor and outdoor monitoring of photocatalytic activity using a mobile phone app. and a photocatalytic activity indicator ink (paii). *J. Photochem. Photobiol. A*, 298:64–67, 2015.
- [62] A. Mills, N. Wells, J. A. Mackenzie, and G. MacDonald. Kinetics of reduction of a resazurin-based photocatalytic activity ink. *Submitted to Catal. Today*, 2016.
- [63] D. Monllor-Satoca, R. Gomez, M. Gonzalez-Hidalgo, and P. Salvador. The “direct-indirect” model: An alternative kinetic approach in heterogeneous photocatalysis based on the degree of interaction of dissolved pollutant species with the semiconductor surface. *Catal. Today*, 129:247–255, 2007.

- [64] A. Mukhopadhyay, S. Basak, J. K. Das, S. K. Medda, K. Chattopadhyay, and G. De. AgTiO<sub>2</sub> nanoparticle codoped SiO<sub>2</sub> films on ZrO<sub>2</sub> barrier-coated glass substrates with antibacterial activity in ambient condition. *ACS Appl. Mater. Interfaces*, 2(9):2540–2546, 2010.
- [65] I.L. Novak, F. Gao, Y.S Choi, D. Resasco, J.C. Schaff, and B. M. Slepchenko. Diffusion on a curved surface coupled to diffusion in the volume: Application to cell biology. *J. Comput. Phys.*, 226(2):1271–1290, 2007.
- [66] B. Ohtani. Preparing articles on photocatalysis – Beyond the illusions, misconceptions, and speculation. *Chem. Lett.*, 37(3):217–229, 2008.
- [67] D. Ollis. Kinetics of photocatalyzed film removal on self-cleaning surfaces: Simple configurations and useful models. *Appl. Catal., B*, 99:478–484, 2010.
- [68] D. F. Ollis. Kinetics of liquid phase photocatalyzed reactions: An illuminating approach. *J. Phys. Chem. B*, 109:2439–2444, 2005.
- [69] K. Page, R. G.. Palgrave, I. P. Parkin, M.I Wilson, S. L. P. Savin, and A. V. Chadwick. Titania and silver-titania composite films on glass-potent antimicrobial coatings. *J. Mater. Chem.*, 17:95–104, 2007.
- [70] I. P. Parkin and R. G. Palgrave. Self-cleaning coatings. *J. Mater. Chem.*, 15(17):1689–1695, 2005.
- [71] Y. Paz, Z. Luo, L. Rabenberg, and A. Heller. Photooxidative self-cleaning transparent titanium dioxide films on glass. *J. Mater. Res.*, 10:2842–2848, 1995.
- [72] M. Piispanen and L. Hupa. Comparison of self-cleaning properties of three titania coatings on float glass. *Appl. Surf. Sci.*, 258(3):1126–1131, 2011.
- [73] K. Qi, W. A. Daoud, J. H. Xin, C. L. Mak, W. Tang, and W. P. Cheung. Self-cleaning cotton. *J. Mater. Chem.*, 16(47):4567–4574, 2006.

- [74] A. Rätz and M. Röger. Symmetry breaking in a bulk–surface reaction–diffusion model for signalling networks. *Nonlinearity*, 27(8):1805, 2014.
- [75] V. Roméas, P. Pichat, C. Guillard, T. Chopin, and C. Lehaut. Degradation of palmitic (hexadecanoic) acid deposited on TiO<sub>2</sub>-coated self-cleaning glass: kinetics of disappearance, intermediate products and degradation pathways. *New J. Chem.*, 23:365–373, 1999.
- [76] A. A. Samarskii. *The Theory of Difference Schemes*. Marcel Dekker, 2001.
- [77] S. Schenll and P. K. Maini. A century of enzyme kinetics: Reliability of the  $k_m$  and  $v_{max}$  estimates. *Comments Theor. Biol.*, 8:169–187, 2003.
- [78] L. A. Segel and M. Slemrod. The quasi-steady-state assumption: A case study in perturbation. *SIAM Rev.*, 31(3):446–477, 1989.
- [79] M. Singh, J. A. Lumpkin, and J. Rosenblatt. Mathematical modeling of drug release from hydrogel matrices via a diffusion coupled with desorption mechanism. *J. Control. Release*, 32(1):17–25, 1994.
- [80] V. Skakauskas and P. Katauskis. Numerical solving of coupled systems of parabolic and ordinary differential equations. *Nonlinear Anal. Model. Control*, 15(3):351–360, 2010.
- [81] V. Skakauskas and P. Katauskis. On the kinetics of the Langmuir-type heterogeneous reactions. *Nonlinear Anal. Model. Control*, 16(4):467–476, 2011.
- [82] V. Skakauskas and P. Katauskis. Numerical study of the kinetics of unimolecular heterogeneous reactions onto planar surfaces. *J. Math. Chem.*, 50(1):141–154, 2012.
- [83] B.C. Smith. *Quantitative spectroscopy: theory and practice*. Academic Press, 2002.

- [84] M. Stokes, M. Anderson, S. Chandrasekar, and R. Motta. A standard default color space for the internet - srgb. <http://www.w3.org/Graphics/Color/sRGB.html>, November 1996.
- [85] S. Q. Sun, B. Sun, W. Zhang, and D. Wang. Preparation and antibacterial activity of Ag-TiO<sub>2</sub> composite film by liquid phase deposition (LPD) method. *Bull. Mater. Sci.*, 31(1):61–66, 2008.
- [86] D. Synnott, N. Nolan, D. Ryan, J. Colreavy, and S. C. Pillai. Self-cleaning tiles and glasses for eco-efficient buildings. In *Nanotechnology in Eco-Efficient Construction*, pages 327–342. Woodhead Publishing, 2013.
- [87] C. S. Turchi and D. F. Ollis. Photocatalytic degradation of organic water contaminants: Mechanisms involving hydroxyl radical attack. *J. Catal.*, 122(1):178–192, 1990.
- [88] R. A. Vijayendran, F. S. Ligler, and D. E. Leckband. A computational reaction-diffusion model for the analysis of transport-limited kinetics. *Anal. Chem.*, 71(23):5405–5412, 1999.
- [89] C. H. T. Vu and K. Won. Novel water-resistant UV-activated oxygen indicator for intelligent food packaging. *Food Chem.*, 140(12):52–56, 2013.
- [90] D. Wu, M. Long, J. Zhou, W. Cai, X. Zhu, C. Chen, and Y. Wu. Synthesis and characterization of self-cleaning cotton fabrics modified by TiO<sub>2</sub> through a facile approach. *Surf. Coating Tech.*, 203(24):3728–3733, 2009.
- [91] G. Wyszecki and W. S. Stiles. *Color Science: Concepts and Methods, Quantitative Data and Formulae*. Wiley-Interscience, second edition, August 2000.
- [92] Y. Xu and C. H. Langford. Variation of Langmuir adsorption constant determined for TiO<sub>2</sub>-photocatalyzed degradation of acetophenone under different light intensity. *J. Photochem. Photobiol. A*, 133:67–71, 2000.

- [93] T. Yuranova, T. Mosteo, J. Bandara, D. Laub, and J. Kiwi. Self-cleaning cotton textiles surfaces modified by photoactive  $\text{SiO}_2/\text{TiO}_2$  coating. *J. Mol. Catal. A*, 244(12):160–167, 2006.